Newcastle University
Faculty of Science, Agriculture and Engineering
School of Engineering

UAV photogrammetry ground control reductions using GNSS

Ben Grayson

Thesis submitted for the degree of
Doctor of Philosophy

August 2019

Abstract

Unmanned aerial vehicles (UAVs) are now well-established as platforms for photogrammetric data acquisition. Their advantages, particularly over conventional manned aerial platforms, relate to their low cost, ease of use, rapid deployability and low-level flying for the collection of centimetre-level spatial resolution imagery. Coupled with recent innovations in photogrammetry and computer vision, UAVs equipped with consumer grade digital cameras are now frequently used to generate centimetre-resolution and accuracy mapping products, such as dense point clouds, digital elevation models and orthomosaics. Despite the efficiency of UAV data acquisition, the continued need for ground control implementation for photogrammetric image orientation remains a substantial workflow constraint. In addition to the associated costs, ground control must be implemented strategically, and usually extensively, to ensure photogrammetric products meet the accuracy requirements of large scale mapping, which may or may not be possible given constraints of the intended application.

This research uses high precision, UAV-based GNSS (Global Navigation Satellite System) positioning techniques to substantially reduce ground control requirements by directly determining UAV image positions with centimetre-level accuracy and precision. The Precise Point Positioning (PPP) technique is applied and can yield centimetre-level planimetric and decimetre height accuracy photogrammetric mapping without GCPs, whilst the height accuracy can be improved to the centimetre-level using a single GCP. Unlike the standard relative GNSS positioning technique, PPP alleviates all spatial operating constraints associated with the installation and use of a local ground-based GNSS reference station, or the need to operate within the bounds of a permanent GNSS reference station network. Such a workflow simplifies operational logistics, and enables large-scale photogrammetric mapping from UAVs in even the most remote and challenging geographic locations globally. The approach was tested on 11 fixed wing UAV datasets, acquired at two sites in Northumberland, north-east England, which had varying ground control configurations. UAV flight durations, meaning time between launch and landing, were 12-42 minutes. It is shown that the main limitation of UAV-based PPP application is the inherent possibility of GNSS cycle slips and limited observation spans that inhibit the convergence of float ambiguity estimates. Although

PPP camera position estimates were biased in such cases, GCPs were still minimised due to the retained precision of the PPP camera position estimates and constraints on the image block.

Acknowledgements

This research was funded by a UK Engineering and Physical Sciences Research Council (EPSRC) Doctoral Training Award (reference NH/110088211).

First and foremost, I would like to thank my supervisory team for their persevering support of my research at Newcastle University over the last four years. I am very grateful to my principal supervisor, Dr Nigel Penna, for his invaluable guidance, advice and patience throughout my research, and for helping me develop as a researcher. I am also grateful to Prof Jon Mills and Dr Darion Grant for their continued support and helpful discussions at supervisory meetings. Many thanks goes to Martin Robertson for his invaluable help during fieldwork and data collection and general enthusiasm all-round.

I am also very thankful to Maria Valasia Peppa for her helpful ad hoc discussions (and calming) with regards to photogrammetry problem solving and also to Majid Abbaszadeh and Chen Yu for their discussion on GNSS aspects. Many thanks goes to the Geomatics team, including Maria, Majid, Pippa, Chris, Craig, Magda, Aun, Majid, Miles, Elias, Less-lee, Ahmed, Katerina, Kaizer, Tom, Yasir, Jess, Grant, Chen, Zheng and Jiajun, who have made G.19 a pleasant memory. Thanks also goes to QuestUAV for their provision of UAV data and support of this research.

Behind the scenes, I have also had invaluable support from friends and family. My running and triathlon friends (I could list many) have done an amazing job at lifting me up after long days and hard weeks in the office. I am ever grateful for the support of my family, in particular my mum, Liz, and sister, Claire, and grandparents. My late dad, Tony, has also been supporting from above, and will always be a huge source of inspiration and motivation.

A special thanks goes to my partner, Daisy, who has been there from the beginning, picking up the pieces after difficult weeks, cooking endless late evening meals, and generally teleporting myself back from PhD land. She has helped me bear the load.

My PhD experience has been exhilarating, full of ups and downs, new experiences, and wonderful people! I will never forget it.

Contents

List of Figures

List of Tables

Abbreviations

ARP	Antenna Reference Point
BBA	Bundle Block Adjustment
CPF	Cockle Park Farm
CODE	Centre for Orbit Determination in Europe
CV	Computer Vision
DOY	Day of Year
DEM	Digital Elevation Model
DSO	Direct Sensor Orientation
EOP	Exterior Orientation Parameter
GCP	Ground Control Point
GLONASS	Global'naya Navigatsionnaya Sputnikovaya Sistema
GNSS	Global Navigation Satellite System
GPS	Global Positioning System
GSD	Ground Sample Distance
ICP	Iterative Closest Point
IGS	International GNSS Service
INS	Inertial Navigation System
InSO	Indirect Sensor Orientation
ISO	Integrated Sensor Orientation
IMU	Inertial Measurement Unit
IOP	Interior Orientation Parameter
LiDAR	Light Detection And Ranging
LoD	Level of Detection
LH	Low Hauxley
MEMS	Micro Electro Mechanical System
OSGB36	Ordnance Survey Great Britain 1936
PANDA	Positioning And Navigation System Data Analyst
PPK	Post Processed Kinematic
PPP	Precise Point Positioning

RANSAC	RANdom SAmple Consensus
RMSE	Root Mean Squared Error
RTK	Real Time Kinematic
SfM	Structure-from-Motion
SIFT	Scale Invariant Feature Transform
Std Dev	Standard Deviation
TLS	Terrestrial Laser Scanning
TM	Trajectory Matching
UAV	Unmanned Aerial Vehicle
UPD	Uncalibrated Phase Delays
UTC	Coordinated Universal Time
ZTD	Zenith Tropospheric Delay

Chapter 1. Introduction

1.1 Introduction

The majority of worldwide topographic mapping has been performed through the measurement of imagery for around 60 years, whilst scientific and commercial practitioners have been determining basic object information from imagery for around 150 years (Fryer *et al.*, 2007). Photogrammetry may be defined as the '*applied science of taking reliable measurements from photographs*' (Read and Graham, 2002) and whilst the fundamental principles and objectives have remained unchanged over time, the last three decades have witnessed substantial developments with regards to sensors, processing techniques and most recently, platforms (Colomina and Molina, 2014; Toth and Jozkow, 2016).

1.2 Platforms

Image acquisition platforms are an important consideration of any topographic mapping application, with a substantial influence on the cost, spatial resolution and feasible temporal resolution of mapping products. Terrestrial data acquisition offers significant benefits in terms of spatial resolution because of the small object-to-sensor range. Cameras may be mounted on tripods or simply be hand-held to enable the acquisition of highly detailed imagery whilst conveniently minimising equipment costs (James and Robson, 2012; Stumpf *et al.*, 2015). However, terrestrial image acquisition often suffers from data occlusion issues, for example on upward facing surfaces, whilst geographic coverage is typically limited to only a few hundred metres (Achille *et al.*, 2015; Murtiyoso and Grussenmeyer, 2017).

Aerial platforms such as satellites and manned aircraft offer greater geographical coverage of topographic mapping, but at a much lower spatial resolution due to the larger object-to-sensor range. For example, the RapidEye satellite constellation comprises five satellites at an altitude of 630 km in the same orbital track, each producing imagery with a 6.5 m pixel size and 80 km swath. Despite the lower spatial resolution, operating as a constellation enables a sub-daily revisit time (Tyc *et al.*, 2005). The WorldView-3 and WorldView-4 satellite platforms produce imagery with an improved 30 cm pixel size (at nadir) and 13.1 km swath, but in contrast to RapidEye, revisit times are at least 4.5 days (DigitalGlobe, 2018). Again, this temporal resolution is slightly improved on by GeoEye-1 with a 3 day revisit time, but at a slightly compromised 40 cm image pixel size (DigitalGlobe, 2018). A more recent innovation is the so-

called nano-satellite constellation, operated by PlanetLabs (2018) since 2014, which comprises 175 so-called *Dove* satellites providing daily coverage with a 3 m pixel size from the standard, continuous acquisition mode, and a 0.7 m pixel size through a commissioned acquisition (PlanetLabs, 2018).

Manned aerial platforms, including small, single- or twin-engined aircraft and helicopters obtain imagery with a higher spatial resolution to satellites, typically with pixel sizes of 10 cm or better (Yuan, 2009). This is mostly because of their substantially smaller object-to-sensor ranges (flying heights above ground level) of around 500-1,000 m and, consequently, higher spatial resolution topographic mapping products can be supported. Before the arrival of light aircraft in the early 1900s (Toth and Jozkow, 2016), aerial techniques began through experimentation with hot-air balloons (e.g. the first aerial imagery of Paris was acquired by Tournachon in 1958; Read and Graham, 2002) and kites (e.g. English meteorologist, Archibald, in 1882; Toth and Jozkow, 2016). However, to date, manned aerial flights remain expensive to undertake and require careful planning with regards to use of the airspace and runways. Image acquisition from manned aerial platforms can thus be un-economical for small area or highly temporal surveys, and although such imagery improves on the spatial resolution of satellite imagery, it does not improve on that of terrestrial image acquisition.

1.3 UAV photogrammetry

Unmanned aerial vehicles (UAVs) have recently emerged as highly efficient and effective platforms for photogrammetric data acquisition. Also named *unmanned aerial systems* and *remotely piloted aircraft systems* or simply *drones*, they have evolved primarily from their use in military reconnaissance applications (Toth and Jozkow, 2016). UAVs have presented the opportunity to obtain both aerial and close range (10-150 m) imagery with pixel sizes at the centimetre to sub-centimetre level (Harwin and Lucieer, 2012; Nex and Remondino, 2014; Achille *et al.*, 2015; Eltner *et al.*, 2015; Murtiyoso *et al.*, 2018). In addition, compared to manned aerial platforms, UAV advantages include (1) a reduced possibility of interference from low cloud cover during image acquisition, (2) on-site and short-notice deployment without use of airports and runways, thus facilitating time critical and repeat survey applications (Berni *et al.*, 2009) and (3) substantially lower economic costs, thus facilitating topographic mapping with a low budget (Sauerbier *et al.*, 2011; Westoby *et al.*, 2012).

One of the first photogrammetric applications of a UAV occurred in 1980, when images were acquired from a radio controlled model helicopter holding a medium format camera for the observation of a construction project (Wester-Ebbinghaus, 1980). This system incorporated a

polystyrene box to dampen motor vibrations, whilst navigation was performed by observing two targets fixed at a known distance apart on the helicopter through a vertically aligned millimetre grid. Since then, however, UAVs have evolved in design and performance, making them a practical solution to photogrammetric data acquisition. Developments include the use of autopilots for the pre-programming of flight paths and autonomous navigation (e.g. Haala *et al.*, 2011; Baiocchi *et al.*, 2013), the use of agile camera gimbals for greater control of the camera pointing and image footprint (e.g. Achille *et al.*, 2015), and a transition in power source from the use of internal combustion engines (e.g. Eisenbeiss, 2004; Scholtz *et al.*, 2011) to lithium polymer battery power, resulting in a large reduction in system weight to as little as 500 g (Kung *et al.*, 2011; Goncalves and Henriques, 2015). In addition to optical cameras, UAVs have also been utilised to carry other imaging sensors such as range cameras (Kohoutek and Eisenbeiss, 2012), multi and hyperspectral sensors (Berni *et al.*, 2009; Matese *et al.*, 2015) and infrared sensors (Scholtz *et al.*, 2011). Another emerging technology is UAV-based LiDAR (Light Detection And Ranging) (Yang and Chen, 2015; Wallace *et al.*, 2016). LiDAR applications pose great challenges because of the need for real-time orientation sensors, such as high precision inertial measurement units (IMUs), whereas photogrammetry determines equivalent information during post processing (a thorough comparison may be found in Baltsavias, 1999).

With these advantages in mind, UAVs have become heavily integrated into a wide variety of applications. Relating to their temporal and close range advantages, such applications include landslide monitoring (e.g. Niethammer *et al.*, 2010; Peppa *et al.*, 2016), coastal erosion monitoring (e.g. Gonçalves and Henriques, 2015), glacier studies (e.g. Immerzeel *et al.*, 2014) and lake monitoring (e.g. Kohv *et al.*, 2017), as well as in time critical operations such as rapid disaster response (e.g. Zhou, 2009; Adams and Friedland, 2011) and post-seismic damage assessment (e.g. Baiocchi *et al.*, 2013). Relating to their unique viewpoints, applications also include heritage documentation (e.g. Murtiyoso and Grussenmeyer, 2017) and archaeological survey (e.g. Verhoeven *et al.*, 2012).

Regarding the user requirements of UAV-based workflows, it must be ensured that the accuracy of topographic mapping products meets that of the intended application and scenario. The required accuracy of point determination typically varies with intended mapping scale, where mapping scale here refers to that of the output drawing (and not area coverage) and is typically denoted by a scale ratio. For example, the RICS guidance notes for large scale topographic mapping stipulate that drawing scales of 1:50 require point determination with a 2 cm and 4 cm accuracy in plan and height respectively, whereas these values are both only 50 cm for 1:2500

mapping scales (RICS, 2014). Example 1:50 scale applications include measured building surveys and utility tracing whereas 1:2000 scale applications include general boundary and asset mapping.

User requirements are also dictated by the phenomena being observed. In landslide monitoring, surface displacements could be c. 10 cm between epochs, as seen for the rock glacier monitoring of Dall'Asta *et al.* (2017), whereas for soil erosion studies, surfaces changes could be only 1-2 cm as seen in Eltner *et al.* (2015). Therefore, to observe and derive such metrics, the accuracy of object point determination per epoch must, at least, improve on these values. A number of further applications are presented in Table 1-1, with details of the environmental scenario as well as the achieved accuracy of point determination. In geomorphological studies, where digital elevation models (DEMs) derived at different epochs are often differenced for surface change detection, an associated *level of detection* (LoD) threshold is often derived which accommodates the (variable) uncertainty of point determination in each DEM. Any surface change statistics derived between two epochs that do not exceed such a LoD can thereafter be discarded. For example, using archived aerial imagery from epochs between 1967 and 2012, Micheletti *et al.* (2015) achieved DEM uncertainties of c. 0.4-0.9 m over eight epochs which, when differenced, enabled associated LoD thresholds of (90% confidence limit) of c. 1.5-2.2 m. Peppa *et al.* (2016), however, obtained smaller area DEMs with smaller height errors of 2-3 cm, which resulted in an associated LoD threshold of c. 9 cm. Therefore, smaller magnitudes of change require a higher accuracy of point determination if they are to be detected.

In addition to survey accuracy (and precision), feasible survey coverage is also an important consideration. In geomorphology, in particular for bedland erosion (Smith and Vericat, 2015) and river bed erosion (Javemick *et al.*, 2014) studies, erosion rates must be determined over areas frequently exceeding many square kilometres. In such cases, small area and fine resolution survey techniques, such as terrestrial laser scanning (TLS) and terrestrial photogrammetry, become impractical (Smith and Vericat, 2015). UAV photogrammetric workflows, however, can be used to extend survey coverage, whilst still obtaining a centimetre-level point cloud accuracy and resolution (Smith and Vericat, 2015).

The advent of UAVs has therefore presented the opportunity to collect timely and highly detailed imagery. In turn, this has facilitated the production of photogrammetric products, such as dense point clouds, DEMs and orthomosaics with centimetre-level accuracy and resolution (e.g. Lucieer *et al.*, 2014; Reshetyuk and Martensson, 2016; Peppa *et al.*, 2016; Murtiyoso and Grussenmeyer, 2017).

Study	Application	Environmental considerations	Achieved accuracy / precision	Survey method
Micheletti *et al.* (2015)	Quantifying climate forcing of alpine landscapes	Large area DEMs (5x2.5 km). Mountainous terrain.	Error = 30-50 cm Prec. = 40-90 cm	Archival aerial imagery (from manned aerial platform)
Stumpf *et al.* (2015)	Monitoring landslide deformation and erosion	Large area site (600x800 m). 1-3 cm of movement per day.	Height error = 5-10 cm	Terrestrial photogrammetry
Goncalves and Henriques (2015)	Topographic monitoring of coastal erosion	Large area DEMs (c. 900 m long). Coastal erosion observed at 0.2-6 m / year.	Height error = 3.5 cm and 5 cm	Fixed wing UAV imagery
Lucieer *et al.* (2014)	Landslide monitoring	Small area site (125x60 m). High temporal resolution. Landslide horizontal displacements of up to c. 7 m.	Plan/height error = 7/6 cm	Rotary wing UAV imagery with image correlation techniques
Peppa *et al.* (2016)	Landslide monitoring	Small area site (290x230 m)	Error = 3-5 cm Prec. = 1-3 cm	Fixed wing UAV imagery
Dall'Asta *et al.* (2017)	Rock glacier monitoring	Small area site (400x300 m). Expected movement 10 cm / month.	Plan/height error = 5/7 cm	Fixed wing UAV imagery
Eltner *et al.* (2015)	Quantifying rill and interrill erosion	Small area site (20x30 m) Change in rill width/depth (Jun-Jul 2013) of 17-23 / 2-4 cm	Height error = 0.4-0.8 cm	Rotary wing UAV imagery
Immerzeel *et al.* (2014)	Glacier monitoring	Large area site (500x3500 m). Glacier ablation (May-Oct 2013) = -0.08 to -2.23 m	N/A	Fixed wing UAV imagery
James *et al.* (2017)	Landslide monitoring	Large area site (850x250 m). Landslide movement of 5-30 mm per day	Plan/height error = 1.9/2.0 cm	Rotary wing UAV imagery

Table 1-1. Details of topographic mapping application scenarios

The problem. Despite the efficiency of UAVs, UAV photogrammetric workflows typically still require a potentially large number of ground control points (GCPs) to determine the coordinate system of photogrammetric products. For large scale mapping, here meaning scale ratios smaller than 1:200 and thus centimetre-level point accuracy requirements, GCPs must be surveyed with high, typically centimetre-level accuracy, incurring the need for high precision terrestrial survey techniques. Historically, these have involved theodolites but more recently total stations and high precision ground-based Global Navigation Satellite System (GNSS) techniques. Moreover, for repeat applications, it is also usually paramount to re-survey existing GCPs before each survey due to possible disturbances that may have occurred during the intervening time period (e.g. Dall'Asta *et al.* 2017). A good example scenario, to justify the rationale, is the James *et al.* (2017) analysis of the Super Sauze landslide in the southern French Alps. Over the 850 m x 250 m active part of the landslide, 291 GCPs were implemented using high precision ground-based GNSS techniques, representing a substantial amount of ground survey effort. A large number (c. 47) of these GCPs were than discarded because of their lack of stability, relative to the others, whilst remaining GCPs were assumed to have a best accuracy of only 5 cm.

GCP implementation can thus be considered one of the greatest economic costs associated with the UAV photogrammetric workflow, whilst being a large hindrance on the flexibility now commonly associated with UAV platforms. GCP implementation is also often impeded for applications where survey area access is not possible or dangerous, such as on glaciers (e.g. Immerzeel *et al.*, 2014) and landslides (e.g. Peppa *et al.*, 2016; Dall'Asta *et al.*, 2017).

1.4 GNSS application

The use of on-board GNSS techniques in aerial photogrammetry from manned aerial platforms has been well-researched (e.g. Ackermann and Schade, 1993; Gruen *et al.*, 1993) where it has been shown that GCP requirements can be substantially reduced. The practical operation of UAVs has indeed depended on the availability of UAV-compatible GNSS antennas and receivers, in addition to IMU technology, for the purpose of on-board navigation systems and autopilots, but in this case, positioning accuracy requirements are typically only at the 5-10 m level. It has been shown that these outputs, therefore, have limited use when trying to minimise GCP requirements in large scale UAV photogrammetric mapping (e.g. Kung *et al.*, 2011; Turner *et al.*, 2012).

More recently, UAV-compatible high precision GNSS antennas and receivers have become available (Baumker *et al.*, 2013), and are now being utilised in UAV photogrammetric

workflows (e.g. Rehak and Skaloud, 2015; Gerke and Przybilla, 2016; Benassi *et al.*, 2017; Dall'Asta *et al.*, 2017; Rehak and Skaloud, 2017). However, the use of such GNSS positioning techniques usually incur the need to operate a local GNSS reference station or to operate within the bounds of a permanent GNSS reference station network. Consequently, as with GCPs, such requirements also translate to additional ground or location-based constraints which may again impede the flexibility now commonly associated with UAV platforms.

1.5 Aim and objectives

The aim of this research is to *eliminate or reduce GCP requirements in large scale UAV-based photogrammetric mapping using high precision GNSS positioning*. A particular focus is on the application of the GNSS Precise Point Positioning (PPP) technique, because it presents the opportunity to eliminate the ground-based GNSS reference station whilst still obtaining high precision GNSS positioning. Ultimately, it is expected that this combination offers the ability to perform UAV photogrammetric mapping with complete independence of any ground-based infrastructure (either GCPs or that associated with GNSS data processing) so that large scale UAV-based photogrammetric mapping may be performed in even the most remote geographic locations globally.

This aim will be achieved through the following objectives:

1. To review state-of-the-art digital photogrammetric techniques for UAV image processing and the requirements of external photogrammetric control information

2. To examine existing, standard techniques for applying GNSS (camera) positions in the photogrammetric workflow

3. To implement GNSS PPP on a UAV platform and determine achievable positioning accuracies and precisions given the limitations of UAV-acquired GNSS data

4. To use UAV PPP positions as external photogrammetric control information in the photogrammetric workflow

5. To assess the mapping accuracy obtained when using GNSS PPP position control and improvements (or degradations) with respect to standard workflows using GCPs

1.6 Thesis outline

Chapter 1 provides background information on large scale mapping techniques followed by the research context in UAV-based mapping. The aim and objectives of this research are then presented.

Chapter 2 provides a review of state-of-the-art photogrammetric workflows, including algorithmic aspects and details regarding UAV image processing. Close attention is paid to the roles and requirements of control information and the pros and cons of GCP-based and GNSS-based (on board the UAV) control implementation.

Chapter 3 reviews the theory of (high precision) GNSS positioning techniques that may be implemented on UAVs for photogrammetric control. The PPP technique is then introduced with discussion of its requirements and accuracy achievements to date (on other dynamic platforms).

Chapter 4 overviews the UAV PPP-based workflow, the design of experiments and the datasets used for investigation.

Chapter 5 deals with the implementation of UAV-based GNSS PPP experiments. The employed GNSS software packages are firstly introduced, along with their respective parameterisations. GNSS PPP experiments are then implemented to reveal obtainable positional accuracies, along with inherent limitations of UAV platforms. Final solutions are selected for subsequent use as photogrammetric control.

Chapter 6 integrates the selected GNSS PPP solutions (Chapter 5) with the photogrammetric workflow. The employed photogrammetric software packages are introduced and baseline (GCP-based) workflows are discussed and implemented. Camera positions are then determined from GNSS PPP solutions and implemented as photogrammetric control observations. Such GNSS PPP-supported workflows are then evaluated with respect to reference data (check points) and results of the baseline solutions. Finally, an alternative approach to overcome GNSS-camera synchronization issues is introduced, implemented and assessed with respect to the same reference data and former workflow results.

Chapter 7 discusses the findings of Chapters 5 and 6 together and summarizes the overall performance of the desired GNSS-PPP supported UAV photogrammetric workflow with comparison to results presented in recent literature. The initial aim and objectives are revisited and future work is proposed.

Chapter 2. Towards GCP reductions for UAVs

Chapter 1 introduced UAVs as photogrammetric platforms, and discussed their advantages over terrestrial, manned aerial and satellite platforms for photogrammetric data acquisition. Also discussed were the constraints and drawbacks associated with GCP implementation, particularly relative to the ease and low cost of UAV deployment. This chapter discusses developments in photogrammetric workflows that have facilitated UAV photogrammetry, including some basic photogrammetric theory and algorithmic aspects, and typical achievements regarding mapping accuracy to date using GCPs. Established methods for the reducing GCP requirements are examined, through the use of board GNSS and IMU techniques. Chapter 3, then discusses GNSS position techniques for use on UAVs, after which the research gap is identified.

2.1 Photogrammetry background

As a geomatics discipline, photogrammetry has existed for many years and aims to obtain the highest possible accuracy of object point reconstruction. Photogrammetry has transitioned through phases of plane table, analogue, analytical and digital processing (Luhmann *et al.*, 2006; Linder, 2009). *Plane table* photogrammetry was used until around 1930 (Luhmann *et al.*, 2006) and involved the simultaneous observation and plotting of maps using a flat, levelled table and telescope. The introduction of hard copy imagery recorded on film or plate mediums, led to *analogue* methods, involving the use of optical-mechanical stereo plotters to physically reconstruct the viewing conditions of stereo analogue image pairs (McGlone, 2004; Luhmann *et al.*, 2006). Though more accurate than plane table photogrammetry, analogue approaches were considered to be particularly laborious as the stereo plotting equipment was heavy, expensive and required specialist training to operate (Fryer *et al.*, 2007). *Analytical* methods commenced in light of computing advances and dispensed with stereo plotters by relying on mathematical rather than physical sensor modelling. Computing power was essential because the solution of large sets of non-linear equations would otherwise take many days to solve by hand (Fryer *et al.*, 2007). The additional possibility of considering greater numbers of image observations enabled improvements to mapping accuracy and precision through greater redundancy as well as statistical error analysis.

The last three decades have seen the arrival of *digital photogrammetry* (Mikhail *et al.*, 2001; Linder, 2009), which now entails a fully digital workflow from image acquisition using charge couple device (CCD) sensor technology to data processing on digital photogrammetric workstation (e.g. Buyuksalih and Li, 2003). Substantial developments in large CCD sensor technology have also led to the production of digital cameras that are capable of producing imagery with comparable quality and resolution as taken by analogue film cameras and consequently, digital cameras are now considered standard alternatives (McGlone, 2004; Jacobsen, 2011). Digital cameras have alleviated workflow costs associated with film development and scanning (Buyuksalih and Li, 2003; Ip *et al.*, 2007; Micheletti *et al.*, 2015). A particular advantage of the digital environment are increased levels of automation, particulary regarding image measurement (Gruen, 2012), resulting in a dramatic reduction in image processing times and reduced demands on the photogrammetric practitioner (Heipke, 1997; Schenk, 1997; Gruen, 2012). Currently, the highest metric accuracy of object point reconstruction has been typically achieved using (1) specialist, pre-calibrated metric digital cameras, (2) considering image network configurations and (3) carefully handling systematic and gross errors through quality control procedures and use of rigorous mathematical models.

As with digital photogrammetry, the arrival of digital imagery and video has facilitated the computer vision (CV) discipline which shares the same objective of determining object point coordinates (structure) from a displaced camera (motion) but with less focus on metric accuracy and more emphasis on automation and computational efficiency (Stamatopoulos and Fraser, 2014; Granshaw and Fraser, 2015). These goals have been achieved in CV by advances in automatic image measurement and correspondence determination, and the use of linear mathematical models. Although CV initially focused on the processing of low quality and resolution imagery, such as video frames (Pollefeys *et al.*, 2008), quality improvements, for example with regard to resolution and signal-to-noise ratio, have led to enhancements in reconstruction accuracy and thus a natural convergence between CV and photogrammetry has occurred (Deseilligny and Clery, 2011). The CV technique for reconstructing object points from digital imagery is generally referred to as structure-from-motion (SfM) (Ullman, 1979). Applications have included the creation of 3D visualisations of objects from diverse internet imagery, described in the Photo Tourism project of Snavely *et al.* (2008) and the real time reconstruction of urban scenes from video frames for 3D city modelling (Pollefeys *et al.*, 2008). A further distinctive feature of SfM is the processing of massive image datasets, in some cases using up to 100 million photos (Heinly *et al.*, 2015), and hence the prerequisite to develop computationally efficient reconstruction algorithms at the cost of reconstruction accuracy. SfM

reconstruction processes also yield camera pose information without prior knowledge of the scene, which is also the interest of Simultaneous Location And Mapping (SLAM) with the goal of real time autonomous robotics navigation. For example, the workflow of Weiss *et al.* (2011) used imagery to build a 3D model, determine camera pose with respect to the model and then navigate through the model in the absence of GNSS signals. The high computational efficiency of SfM techniques is particularly beneficial to real-time applications (Nister *et al.*, 2006).

Despite the differing aims of CV and Photogrammetry, modern photogrammetric workflows typically combine the advantages of both disciplines, namely the accuracy advantages of photogrammetry with the automation and robustness of CV (SfM) workflows, and for this reason, the term SfM-photogrammetry is often adopted.

2.2 Photogrammetric problem outline

Photogrammetry involves the derivation of object point coordinates from image feature correspondences (tie points). Key requirements are (1) knowledge of image orientations and (2) the appearance and measurement of objects of interest in two or more images, which therefore form key objectives in photogrammetric processing.

Image orientations are defined by interior and exterior orientation parameters (IOPs, EOPs respectively). IOPs express the internal structure of the camera, minimally comprising focal length and principal point coordinates, whilst EOPs express the position and attitude of the imaging camera. Moreover, as the coordinate frame of EOPs defines the coordinate system of object points, EOPs must be determined in the desired mapping frame.

Observed image point coordinates (x, y) may be related to the object point coordinates (X, Y and Z) through the following colinearity condition equations (Wolf *et al.*, 2014):

$$x = x_o - f\left[\frac{m_{11}(X - X_0) + m_{12}(Y - Y_0) + m_{13}(Z - Z_0)}{m_{31}(X - X_0) + m_{32}(Y - Y_0) + m_{33}(Z - Z_0)}\right] + dx \quad (2\text{-}1)$$

$$y = y_o - f\left[\frac{m_{21}(X - X_0) + m_{22}(Y - Y_0) + m_{23}(Z - Z_0)}{m_{31}(X - X_0) + m_{32}(Y - Y_0) + m_{33}(Z - Z_0)}\right] + dy \quad (2\text{-}2)$$

These include IOPs of focal length: f and principal point coordinates: x_o and y_o, and EOPs of image (perspective centre) position coordinates: X_0, Y_0 and Z_0 and image orientation angles: ω, ϕ and κ contained within rotation elements m_{11} to m_{33}. Such equations stipulate that the image (perspective centre) position, image point and the object point fall on the straight line path of a

ray of light. The additional terms, dx and dy are included to further account for image perturbing effects that cause deviations from the assumed colinearity condition, including lens distortion and CCD irregularities. The same colinearity condition can also be inferred through the projection matrix, P, which is typically adopted in CV as follows (Hartley and Zisserman, 2003):

$$\begin{bmatrix} x \\ y \\ 1 \end{bmatrix} = P \begin{bmatrix} X \\ Y \\ Z \\ 1 \end{bmatrix} \tag{2-3}$$

where

$$P = \begin{bmatrix} f & s & x_o \\ 0 & f & y_o \\ 0 & 0 & 1 \end{bmatrix} [R \quad T] \tag{2-4}$$

which is commonly expressed in the form:

$$P = k[R|T] \tag{2-5}$$

Here, P is the 3x4 projection matrix, k is a 3x3 upper triangle camera calibration matrix, R is a 3x3 rotation matrix and T is a 3x1 translation (image position) vector. The projection matrix thus has 11 degrees of freedom: six EOPs (image position coordinates in T and rotation angles held in R) and five camera parameters: focal length, three principal point coordinates, and a skew parameter (s). For the projection matrix, image point coordinates are expressed as homogeneous coordinates, i.e. image and object point coordinates as 3x1 and 4x1 vectors respectively, unlike the Euclidean coordinates used in the colinearity standard photogrammetric condition equations.

These are commonly known as camera pinhole models (e.g. Grussenmeyer and Al Khalil, 2002). A photogrammetric network requires the solution of the (two) colinearity condition equations, or a projection matrix per object point and per image in which that object point is seen. The determination of EOPs and IOPs (hereafter termed image orientation) remains the fundamental task of photogrammetric processing (Grussenmeyer and Al Khalil, 2002).

The acknowledged standard method for solving the image orientation problem is the bundle block adjustment (BBA), as described by Granshaw (1980), in which a globally optimum estimate of image orientations is achieved on the basis of all observed image tie points and

object space information in a nonlinear least squares adjustment. The BBA is formulated under the principle that all observations contain a residual error as follows:

$$\bar{l} = \check{l} + \bar{v} \tag{2-6}$$

where $\bar{l}$ is the true (least squares) value of the image point (x, y), $\check{l}$ is the image point observation and $\bar{v}$ is the image point observation residual. Accordingly:

$$\bar{l} = p(\bar{x}) \tag{2-7}$$

where p is the projective function of image positions (X_0, Y_0 and Z_0), attitudes (ω, ϕ and κ), object point coordinates (X, Y and Z) and camera model (f, x_o and y_o). Denoting these parameters under $\bar{x}$, the least squares solution aims to determine corrections dx to the approximate parameter values x_o as follows:

$$\bar{x} = x_o + d\bar{x} \tag{2-8}$$

Linearizing the nonlinear projective function with respect to each unknown term and equating to $\bar{l}$ gives:

$$f(x_o \dots \dots) + \left(\frac{dp}{d\bar{x}}\right)_o . d\bar{x} \dots \dots = \check{l} + \bar{v} \tag{2-9}$$

which may be arranged to:

$$A . d\bar{x} = \check{l} - p(x_o \dots \dots) + \bar{v} \tag{2-10}$$

where A is Jacobean matrix of partial derivatives, evaluated with respect to each unknown parameter. The least squares corrections obtained are then obtained as:

$$d\bar{x} = (A^T . W . A)^{-1} . A^T . W . b \tag{2-11}$$

where

$$b = \check{l} - p(x_o \dots \dots) \tag{2-12}$$

W is the observation weight matrix which contains weightings for all included observations. With least squares corrections estimated, approximate parameter values can be improved and the solution iterated until the least squares correction values become negligible (i.e. solution convergence).

Upon solution convergence, the estimated parameters (typically image orientations and object point coordinates) are optimum with regards to all (weighted) observations. Observation residuals may finally be calculated as:

$$\overline{v} = A.d\overline{x} - b \tag{2-13}$$

which may used for the detection of outlying observations. The BBA may be solved on the basis of image tie points only, provided arbitrary constraints on the image block scale, rotation and translation (i.e. 7 parameters) are implemented, for example by fixing EOPs. This result is also known as a *free network adjustment* in which tie points determine the shape (relative accuracy, or precision) of reconstructed object points and image orientations (Granshaw, 1980). However, when observed object space information is also included, external constraints also contribute to the image block shape, which may otherwise be deformed by errors in the camera model.

2.3 Aerial Triangulation

The traditional processing technique for aerial photogrammetric surveys is usually referred to as aerial triangulation (AT). AT operates under assumptions of normal case imagery (i.e. parallel, near-vertical axes), as would be conventionally taken from manned aerial platforms, which is advantageous to the formulation of the BBA. For example, it can be assumed that rotation angles between images are small, such that null value approximations can be used for camera rotation angles in the least squares estimation, whilst approximate camera positions can be determined from just a few imaged GCPs (Kraus, 2007; Wolf *et al.*, 2014). In addition, AT workflows usually adopt intensity and/or feature-based matching schemes for automated measurement of image tie points (e.g. Liang and Heipke, 1996; Heipke, 1997; Buyuksalih and Li, 2003). Such schemes typically match conjugate points on the basis of their image grey values, for example, by similarity comparisons through cross correlation and least squares matching (Gruen, 2012). These schemes therefore assume minimal geometric or radiometric transformation between overlapping images (Schmid *et al.*, 2000; Kasser and Egels, 2002).

UAV images, on the other hand, are rarely vertical and are usually regarded as convergent (Haala *et al.*, 2011; Rosnell and Honkavaara, 2012). As a result, geometric and radiometric transformation of image features due to perspective effects (e.g. scale variation) can result in failures at the tie point matching stage (Buyuksalih and Li, 2003; Lingua *et al.*, 2009; Rosnell and Honkavaara, 2012). AT workflows also usually assume the use of metric aerial cameras (e.g. Lichti *et al.*, 2008; Jacobsen, 2011b; Jacobsen, 2011a). Such cameras have known interior geometries and high quality lenses (with minimal, or well-modelled lens distortion) such that IOPs can be fixed with high accuracy in the BBA. UAVs however, are typically limited by payload to small format, consumer grade digital cameras (Colomina and Molina, 2014; Toth and Jozkow, 2016), which usually exhibit unknown and/or unstable IOPs. This therefore induces the requirement for potentially accuracy-limiting camera self-calibrations in the BBA (e.g. Goncalves and Henriques, 2015; Benassi *et al.*, 2017).

For these reasons, conventional AT-based workflows, from purely photogrammetric origins are generally limited with regards to their applicability to UAV imagery (a direct comparison can be found in Rosnell and Honkavaara, 2012). However, the processing and orientation of UAV imagery has been facilitated by more recent developments in feature based matching and CV algorithms.

2.4 UAV photogrammetric workflows

In contrast to the AT procedures used for manned aerial platforms, UAV workflows have been largely facilitated by a combination of the use of descriptor-based feature matching algorithms (for tie point detection) and direct determination of image orientations without need for approximate EOP values. In addition, image orientations and object points are generally reconstructed incrementally to avoid the possibility of divergences in the BBA.

Descriptor-based matching. Traditional intensity-based matching approaches determine feature correspondences on the basis of their (similar) grey values, and thus their applicability is limited to only short baseline imagery (Lingua *et al.*, 2009). The matching of convergent imagery, however, has been reliably facilitated by descriptor-based matching algorithms. These devise and utilise feature descriptors that are invariant to grey value changes between images, to allow the matching of detected image features (Lowe, 2004; Mikolajczyk *et al.*, 2005; Lingua *et al.*, 2009). Popular descriptor-based matching algorithms include the Scale Invariant Feature Transform (SIFT) algorithm of Lowe (2004) or Speeded Up Robust Features (SURF) algorithm of Bay *et al.* (2008). The use of SIFT, or a variant of SIFT, is particularly common in UAV-based literature.

SIFT detects scale and orientation invariant features (interest points) by searching over all image scales using a difference-of-Gaussian function, before assigning orientations to detected features based on local pixel gradients for additional rotation invariance (Lowe, 2004). The feature descriptors themselves are then based on neighbouring pixel gradients to the transformed (scaled and rotated) image features using so-called orientation histograms. Final descriptors comprise 128-element vectors which are normalised about intensity values to achieve further illumination invariance. Feature matching can then be performed on the basis of the Euclidean length of descriptor vectors in the descriptor database to establish a level of correspondence, using a so-called nearest neighbour search (Stamatopoulos and Fraser, 2014).

The colloquial features produced by descriptor-based image matching algorithms are typically vast in number, but also prone to descriptor matching errors, meaning paired features do not always correspond to the same object point (Schonberger and Frahm, 2016). This is particularly the case when repetitive scene patterns exist (Lingua *et al.*, 2009; Stamatopoulos and Fraser, 2014). Therefore, in conjunction with descriptor-based matching, geometric filtering is usually performed to filter incorrectly determined feature correspondences (Schonberger and Frahm, 2016). This involves the estimation of a transformation that maps each feature point to its corresponding location on the overlapping image (Stamatopoulos and Fraser, 2014; Schonberger and Frahm, 2016). The estimation typically uses a RANdom SAmple Consensus (RANSAC) approach (Fischler and Bolles, 1981) which, rather than estimating the transformation based on all presented tie points and performing outlier detection through analysis of residuals, uses the smallest tie point dataset possible (given the degrees of freedom of the transformation) to determine an initial model solution before enlarging the dataset based on the fit of data points to the current transformation. Tie points are then excluded should their fitting error exceed a predefined threshold. RANSAC performs well when at least half of the input tie points are inliers (Stamatopoulos and Fraser, 2014).

Incremental BBA. With (geometrically verified) image tie points, the next step is typically to reconstruct EOPs and object points (Schonberger and Frahm, 2016). As discussed, AT-based BBAs are usually formulated around the availability of suitable approximations for unknown EOPs, which may have been calculated from available GCPs, assumptions of vertical imagery or using GNSS or inertial sensor techniques. Whilst such assumptions are rarely possible for UAV applications, CV offers strategies to directly determine (without approximations) relative image orientations on the basis of image tie points alone. This is achieved through computation of the Fundamental or Essential matrix, which are commensurate to the traditional photogrammetric coplanarity model used in photogrammetry (McGlone, 2004). These may be

computed on the basis of five image correspondences (e.g. as presented in Nister, 2004, Stewenius *et al.*, 2006 and McGlone, 2004) although typically thousands will be typically used to achieve a more reliable and robust result by minimizing some cost function (examples may be found in Hartley and Zisserman, 2003). The Fundamental and Essential matrices transform points from one image (x_i) to another image ($x_i^{'}$) for uncalibrated or calibrated images respectively, as follows (Hartley and Zisserman, 2003):

$$x_i^{'T}.F.x_i = 0 \tag{2-14}$$

$$x_i^{'T}.E.x_i = 0 \tag{2-15}$$

where F and E are the Fundamental and Essential matrices respectively (both 3x3 element matrices) which are valid for all i. Image points are expressed as 3x1 dimensional homogeneous image coordinate vectors. From the Fundamental and Essential matrices, relative image translation and orientations may be derived (for example, using Singular Value Decomposition, McGlone, 2004) and with consecutive relative image orientations, all EOPs may be reconstructed in a consistent coordinate system. The coordinate system, however, is typically defined by arbitrarily fixing the EOPs of one image to null values (i.e. defining the origin), along with the baseline vector of the first image pair (defining the scale) (Snavely *et al.*, 2008; Deseilligny and Clery, 2011; Stamatopoulos and Fraser, 2014). However, due to the limited accuracy of initial relative orientation estimates, relating to possible tie point blunders and the use of linear models (Weng *et al.*, 1993; El Hazzat *et al.*, 2018), a BBA is typically carried out prior to each relative orientation step (equivalent to a multistation relative orientation as described by Granshaw (1980)). Reconstructed image orientations and object point coordinates are thus optimised with the addition of each image by minimising global reprojection error in the BBA (Triggs *et al.*, 1999).

The workflow comprising (1) descriptor-based image matching, (2) geometric filtering, (3) direct initialisation and (4) incremental SfM (Schonberger and Frahm, 2016; El Hazzat *et al.*, 2018) is key to the orientation of a UAV image block, which is otherwise challenging with conventional workflows based on AT (e.g. Rosnell and Honkavaara, 2012). However, at this stage, the reconstruction coordinate system remains arbitrary. In order to realise the mapping datum and optimise the reconstruction with respect to known, real-world dimensions, the BBA must be optimised with object space control information (Granshaw, 1980).

2.5 Bundle block adjustment control

The role of control information in photogrammetry may be considered two-fold: firstly it defines the mapping datum, meaning the real-world scale and coordinate system of the image block (here *image block* refers to the image orientations and object point coordinates), and secondly it contributes to the image block precision or shape (e.g. Nex and Remondino, 2014; James and Robson, 2014). For example, Figure 2-1 illustrates the effects of deteriorated EOP elements on final model height coordinates (Kraus, 2007).

Control information comprises observed object space information, sometimes in the form of known object space distances, but more usually in the form of either absolute object point coordinates corresponding to image tie points (i.e. GCPs) or absolute image orientations. Workflows can be differentiated by whether control information is considered within the BBA (i.e. the rigorous approach) or only used afterwards to determine an independent datum transformation (i.e. the non-rigorous approach) (James and Robson, 2014; Eltner and Schneider, 2015).

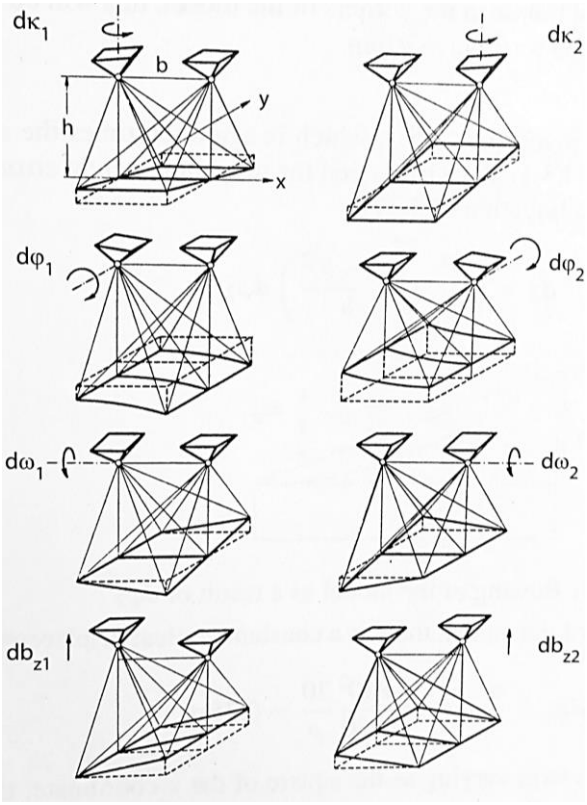

Figure 2-1. Model deformations in height with deteriorated EOPs (Kraus, 2007). The solid-line and dashed-line surfaces represent the erroneous and error free model surfaces respectively.

In the non-rigorous approach, control information is used to determine a similarity (3D conformal) transformation to transform the arbitrary image block, as produced by the free

network adjustment, into the mapping datum. From a photogrammetric standpoint, this process is suboptimal because control information does not contribute to the image block precision or shape (Nex and Remondino, 2014), whilst any error in the image block shape will propagate linearly into the final output with magnitude depending on the project scale (James and Robson, 2012). For example, using such an approach, Eltner and Schneider (2015) showed reconstruction doming errors of 14 mm when modelling a 4 m x 15 m planar building floor, whilst James and Robson (2014) indicated larger reconstruction doming errors of 0.2 m over horizontal distances of 100 m. Such reconstruction doming errors were incurred from an inaccurate estimation of lens distortion in the self-calibrating BBA with parallel axes imagery. Although it can be desirable to pre-calibrate and fix lens distortion prior to the BBA (Eltner and Schneider, 2015), the self-calibrating BBA is usually necessitated when using a consumer grade camera.

The more conventional photogrammetric approach to handling image block deformations is by appropriate implementation of control information within the BBA. When control information is considered within the BBA, it represents external observations that constrain the shape of the computed image block, and thus it may be used to minimise systematic errors resulting from reduced tie point quality or camera model errors (including lens distortion). However, should the weighting assigned to tie point and control observations through the stochastic model be over optimistic, image block deformations can prevail due to an over fitting of the image block to the tie point or control observations respectively (James *et al.*, 2017). Granshaw (1980) clarified that control information may improve the precision of photogrammetrically derived points only should it improve image orientation estimates.

2.5.1 Indirect Sensor Orientation

GCPs represent the traditional form of control information, enabling the indirect determination of absolute image orientations, and hence the approach is known as *Indirect Sensor Orientation* (InSO) (e.g. Wolf *et al.*, 2014). Observation equations for the inclusion of GCPs directly relate the surveyed GCP coordinates (effectively observations) to the unknown object point coordinates corresponding to tie points observations as follows:

$$\begin{bmatrix} X_i^{gcp} \\ Y_i^{gcp} \\ Z_i^{gcp} \end{bmatrix} = \begin{bmatrix} X_i^{op} \\ Y_i^{op} \\ Z_i^{op} \end{bmatrix} + \begin{bmatrix} vX_i^{op} \\ vY_i^{op} \\ vZ_i^{op} \end{bmatrix} \tag{2-16}$$

This is in the form of equation (2-6), where for GCP i, X_i^{gcp}, Y_i^{gcp} and Z_i^{gcp} are the observed GCP coordinates, X_i^{op}, Y_i^{op} and Z_i^{op} are the estimated object point coordinates and vX_i^{op}, vY_i^{op} and vZ_i^{op} are the associated observation residual errors.

When included in the BBA, the image block is optimised so that light rays (defined by the image orientations and image measurement) intersect at the GCP coordinates. In the non-rigorous approach, GCPs may be used to determine a similarity transformation on the basis of their corresponding arbitrary model coordinates (Turner *et al.*, 2012; Fonstad *et al.*, 2013). Focusing on the rigorous approach where GCPs are employed within the BBA, the minimum requirement is at least three GCPs, along with their manual image measurement, to orientate the image block. However, best practice suggests that GCPs should encompass the full survey area extent (Kraus, 2007; Goncalves and Henriques, 2015; Harwin *et al.*, 2015; Reshetyuk and Martensson, 2016), be sufficiently dense with regards to the survey area size (especially when large topography height variations are present: Harwin and Lucieer, 2012; Eltner *et al.*, 2016; Luhmann *et al.*, 2006), be appropriately sized with respect to the ground sample distance (GSD) (Reshetyuk and Martensson, 2016), and be located on stable terrain (Goncalves and Henriques, 2015). For UAV applications, Harwin and Lucieer (2012) suggested a general rule-of-thumb of adopting a GCP spacing of between a fifth and tenth of the camera-to-object distance. However, because every UAV survey varies in terms of terrain, illumination conditions, image configurations, flight characteristics and image quality, it is argued here that optimal GCP configurations can only be determined through controlled experiments. Therefore, the effect of GCP configurations and weighting in the BBA should be examined with respect to independent check points (CPs), as per James *et al.* (2017) and Harwin *et al.* (2015).

Although GCP-based image orientation in UAV photogrammetric workflows is frequently shown to result in mapping errors at the one-GSD level (e.g. Eltner and Schneider, 2015; Goncalves and Henriques, 2015; Gerke and Przybilla, 2016; Dall'Asta *et al.*, 2017), problems are often encountered when GCPs are insufficient with regards to their numbers or distribution. For example, Goncalves and Henriques (2015) achieved overall 3D mapping errors of 3.2-4.5 cm with 12-13 GCPs over two study areas. However, they also showed check point errors to degrade by 2-3 times outside GCP-containing regions, which is suggestive of unconstrained image orientation errors. Moreover, it was also speculated that GCP errors were induced due to soil instability during the control survey. Similarly, Gerke and Przybilla (2016) achieved mapping errors of around 2.5 cm in plan and 8 cm in height using 18 well-distributed GCPs. However, when reduced to only four GCPs, one located in each corner of the image block, these degraded to c. 5 cm (c. 2 pixels) and 20 cm (c. 7 pixels) respectively. When analysing the

distributions of mapping errors, they showed substantial level of deformation in the centre of the image block. Although these results were only experimental, this study highlights the nature of potential mapping errors when GCP distributions are sparse. Further to this, Turner *et al.* (2015) used a variable number of GCPs (between 16 and 56) over the eight epochs of their landslide survey, such that mapping errors varied between 3-8 cm in plan and 3-9 cm in height. This also highlights the dependence of mapping quality on the employed GCP numbers, as well as distribution, and could be particularly problematic for such a time series analysis, where differing mapping errors might be interpreted as landslide movement. On larger scale, Immerzeel *et al.* (2014) performed two fixed wing UAV surveys of the 3.5 km by 500 m Lirung Glacier in Nepal, for which 18 and 20 GCPs were deployed for two epochs. However, glacial dynamics necessitated the placement of these GCPs on the stable terrain surrounding the glacier. As was shown by Gerke and Przybilla (2016), such GCPs distributions were likely to result in central image block deformation errors, although the authors made no mapping error assessment on the glacier itself. This study highlights a situation where the nature of the applications might result in suboptimal mapping results.

Overall, these studies indicate that using GCP control in the BBA can facilitate UAV topographic mapping with centimetre- or one pixel-level accuracy. However, best survey practices must be adhered to if image block deformations (e.g. Gerke and Przybilla, 2016) are to be suppressed. Best survey practices may, however, be prevented by survey area restrictions (e.g. Immerzeel *et al.*, 2014) or limited availability of resources (Turner *et al.*, 2015). Some applications also make GCP implementation impossible, or dangerous (e.g. Dall'Asta *et al.*, 2017), whilst GCP visibility issues with regards to the UAV imagery have been frequently reported (Immerzeel *et al.*, 2014; Dall'Asta *et al.*, 2017).

2.5.2 GNSS supported AT

The advent of civilian GPS (Global Positioning System) use in the 1980s led to the technique of *GNSS-supported AT* for the reduction of GCP requirements in traditional aerial photogrammetry (Ackermann and Schade, 1993; Gruen *et al.*, 1993). It should be noted that 'GPS' is often used, rather than 'GNSS' to denote the use of the GPS constellation satellites only. However, for consistency, distinction if not made in this section and 'GNSS' is retained. Rather than relying solely on GCPs, GNSS-supported AT includes GNSS-determined camera positions in the BBA, whilst retaining the benefits of AT by the continued inclusion of image tie points. Additional observation equations for GNSS-supported AT directly relate the GNSS-determined camera position to the corresponding unknown camera position coordinates as follows (modified from Ackermann and Schade, 1993):

$$\begin{bmatrix} X_i^{gps} \\ Y_i^{gps} \\ Z_i^{gps} \end{bmatrix} = \begin{bmatrix} X_i^{pc} \\ Y_i^{pc} \\ Z_i^{pc} \end{bmatrix} + \begin{bmatrix} vX_i^{pc} \\ vY_i^{pc} \\ vZ_i^{pc} \end{bmatrix} \quad (2\text{-}17)$$

This is in the form of equation (2-6), where X_i^{gps}, Y_i^{gps} and Z_i^{gps} are the observed GNSS camera position coordinates, X_i^{pc}, Y_i^{pc} and Z_i^{pc} are the estimated camera position coordinates and vX_i^{pc}, vY_i^{pc} and vZ_i^{pc} are the associated residual errors. To account for the offset between the camera position and the GNSS antenna on the aircraft, these are usually modified to include the lever arm offsets as follows:

$$\begin{bmatrix} X_i^{gps} \\ Y_i^{gps} \\ Z_i^{gps} \end{bmatrix} = \begin{bmatrix} X_i^{pc} \\ Y_i^{pc} \\ Z_i^{pc} \end{bmatrix} + R(\omega, \varphi, k). \begin{bmatrix} lX_i^{pc} \\ lY_i^{pc} \\ lZ_i^{pc} \end{bmatrix} + \begin{bmatrix} vX_i^{pc} \\ vY_i^{pc} \\ vZ_i^{pc} \end{bmatrix} \quad (2\text{-}18)$$

where lX_i^{pc}, lY_i^{pc} and lZ_i^{pc} are the lever arm offsets in the (local) body frame, and R is the rotation matrix comprised of rotation angles between the body frame and georeferenced coordinate system. The lever arm offset parameters (lX_i^{pc}, lY_i^{pc}, lZ_i^{pc}, ω, φ, k) may either be pre-determined (and fixed) or estimated in the BBA.

Initial manned aircraft practices usually encountered systematic GNSS positioning errors as a result of increasing distances from the GNSS reference station or GNSS signal interruptions during flight turns, which resulted in shift errors in the GNSS camera positions (Ackermann and Schade, 1993; Gruen *et al.*, 1993). In response, Curry and Schuckman (1993) suggested attempting to limit bank angles on aircraft turns to prevent GNSS signal interruption, but at the expense of an extensive turning radius. Alternatively, Ackermann and Schade (1993) suggested to accept the presence of the systematic GNSS positioning errors and estimate shift error corrections on a strip-by-strip basis using a small number of GCPs. The advantage of the latter approach was that all constraints on the flight (e.g. banking, distance from GNSS reference station) were removed, albeit at the expense of a few GCPs. For this, the observation equations are extended to include GNSS shift error parameters, as follows (modified from Ackermann and Schade, 1993):

$$\begin{bmatrix} X_i^{gps} \\ Y_i^{gps} \\ Z_i^{gps} \end{bmatrix} = \begin{bmatrix} X_i^{pc} \\ Y_i^{pc} \\ Z_i^{pc} \end{bmatrix} + R(\omega, \varphi, k). \begin{bmatrix} lX_i^{pc} \\ lY_i^{pc} \\ lZ_i^{pc} \end{bmatrix} + \begin{bmatrix} sX_i^{pc} \\ sY_i^{pc} \\ sZ_i^{pc} \end{bmatrix} + \begin{bmatrix} vX_i^{pc} \\ vY_i^{pc} \\ vZ_i^{pc} \end{bmatrix} \quad (2\text{-}19)$$

where sX_i^{pc}, sY_i^{pc} and sZ_i^{pc} are the GNSS shift parameters, which may either be valid for the whole image block or only for individual strips, and should be estimated with the same accuracy as that required of the object points to sufficiently accommodate GNSS biases.

Gruen *et al.* (1993) showed that using four GCPs, one in each corner of the image block, and solving for a global shift of the whole block could result in the same object point accuracy as when using a complete set of GCPs, although solving shift errors on a strip-by-strip basis could worsen the overall image block accuracy. This strategy of using four GCPs has now become the accepted norm for manned aerial photogrammetry. For example, Lichti (2002) undertook GNSS-supported AT with image blocks of scale 1:5000 and 1:7500. Solving for shift errors on a strip-by-strip basis, object point accuracies of 3 cm and 5 cm in planimetry and height respectively were achieved for the 1:5000 block, whilst these values were 6 cm and 10 cm for the 1:7500 image block. Similarly, Yuan *et al.* (2009) computed GNSS positioning errors of 1.4 m, 0.5 m and 0.9 m in easting, northing and height respectively. However, under the same GCP configuration, object point accuracies of 0.15 m in both planimetry and height were achieved for a 1:2500 image block.

The advent of UAV-compatible GNSS receivers and antennas over the last decade has naturally led to the implementation of GNSS-supported workflows with UAV platforms. However, unlike the traditional GNSS-supported AT workflow, modern SfM-photogrammetric software (e.g. PhotoScan or Pix4D) typically do not allow the estimation of block or strip-wise GNSS shift corrections. This is likely due to their design for close range photogrammetric applications where image strips are not always defined. Consequently, the integration of GNSS camera position observations to such a workflow is hereafter referred to as a GNSS- or GPS-supported bundle block adjustment (GNSS-BBA, GPS-BBA). A major factor influencing the accuracy of UAV mapping from GNSS-BBAs in the absence of GCPs is the quality of GNSS-based camera positions.

When UAV applications are limited to the use of low quality GNSS with typical accuracies of c. 5-10 m (e.g. Haala *et al.*, 2011), GNSS-determined camera positions are also limited to such an accuracy, such that only metre-level mapping accuracies are obtainable (Kung *et al.*, 2011; Turner *et al.*, 2012; Shahbazi *et al.*, 2015). For example, Kung *et al.* (2011) used low quality GNSS camera positions (and without GCPs) in the BBA for three missions with flying heights

of 130 m, 262 m and 900 m in Pix4D software. Final mapping errors of 0.50-2.45 m, 0.65-4.40 m and 0.58-1.29 m were achieved in easting, northing and height respectively. No report was made on any parameterisations of the BBA, such as assigned GNSS camera position weights (*a priori* standard deviations) or *a posterior* statistics such as camera position or image observation residuals. Similarly, Turner *et al.* (2012) used low quality GNSS camera positions, but this time in conjunction with Bundler software which does not allow consideration of GNSS camera positions in the BBA. Having applied a similarity transformation for two image blocks, final mapping errors for two different datasets of 1.247 m and 0.665 m were achieved, with standard deviations of 0.184 m and 0.459 m respectively. These studies indicate that camera positions determined using low quality GNSS cannot facilitate mapping accuracies equivalent to that achieved with GCP-based image block orientation.

The recent advent of UAV-compatible carrier phase-based GNSS receivers and antennas (Baumker *et al.*, 2013) has enabled determination of UAV-based GNSS camera positions with a higher level of accuracy and precision (Rehak *et al.*, 2013; Skaloud *et al.*, 2014; Dall'Asta *et al.*, 2017; Stöcker *et al.*, 2017). It should at this stage be noted that the umbrella terms of Post Processed Kinematic (PPK) or Real Time Kinematic (RTK), are often used in literature to cover specifically the use of onboard carrier phase-based GNSS receivers, although these will be defined and distinguished in Chapter 3. For example, Rehak *et al.* (2013) implemented GNSS-BBAs using carrier phase-based GNSS camera positions using a self-developed rotary wing UAV. Also using a single GCP, mapping Root Mean Squared Errors (RMSEs) of 3.6 cm, 2.2 cm and 19 cm were achieved in easting, northing and height respectively. This was, however, only evaluated on six check points over an 8 m x 8 m test area, and only for a flying height of 8 m, which reduces implications for larger scale studies. Similarly, Turner *et al.* (2014) included carrier phase-based GNSS camera positions in a GNSS-BBA implemented in PhotoScan. Despite expected camera position accuracies of 10-20 cm, orthomosaic accuracies of 2.9 cm and 10.8 cm were achieved in easting and northing respectively with a 2D precision of 2.1 cm. Again parameterisations of the GNSS-BBA were not given. In such a workflow, the accuracy of GNSS camera positions was concluded to be most limiting factor.

More recently, Gerke and Przybilla (2016) used carrier phase-based GNSS camera positions to implement GNSS-BBAs in PhotoScan for a 1100 m x 600 m stockpile survey. With the addition of four GCPs, mapping errors of c. 3 cm and c. 8 cm in plan and height respectively were achieved, which improved on the values of 10 cm and 30 cm when using the same four GCPs only. Furthermore, the inclusion of more GCPs showed little further enhancement in addition to the GNSS camera positions. When eliminating GCPs completely and using the GNSS camera

positions only, check point RMSEs of c. 7 cm and 6.5 cm were achieved in plan and height respectively. This study illustrates the possibility of improving the image block precision by the inclusion of GNSS camera positions in the BBA, in support of GCP reductions or even complete GCP elimination. The authors concluded that the use of carrier phase-based GNSS camera positions may deliver superior results to conventional GCP-based workflows, especially when GCP distributions are sparse.

Further to this, Dall'Asta *et al.* (2017) also implemented (fixed wing) UAV-based GNSS-BBAs with carrier phase-based GNSS camera positions to survey of a rock glacier. This time however, in a second step, the GNSS-optimised image block was shifted to minimise the residual error at the single GCP. Subsequently, they achieved check point RMSEs of 4.0 cm, 3.1 cm and 7.2 cm in easting, northing and height respectively. This second step seems similar to the traditional approach of using GCPs to solve for a global image block shift, but in light of SfM-photogrammetric software limitations. Such check point errors were concluded to be sufficient for the periodic monitoring of the rock glacier, which moved at a decimetre per month.

2.5.3 Direct and integrated sensor orientation

In GNSS-supported AT, image tie points allow the estimation of image orientation angles in the BBA with sufficient accuracy, providing a regular image block containing multiple overlapping image strips exists. However, using an inertial measurement unit (IMU), camera orientation angles may also be observed directly. IMUs measure linear acceleration and incremental angular motion using gyroscopes and accelerometers (i.e. inertial sensor assembly), such that relative position, attitude and velocity can be estimated in order to calculate coordinate differences relative to a start point (Curey *et al.*, 2004; Yastikli and Jacobsen, 2005a). IMU and GNSS behaviours are considered complementary, whereby IMUs have good short-term accuracy but substantially drift with time, whereas GNSS observations have a good long-term accuracy but may exhibit short term degradations, for example, due to cycle slips (Yastikli and Jacobsen, 2005a; Waegli *et al.*, 2010). Therefore, such observations are frequently integrated in a Kalman filter for an optimised trajectory. However, with accurate IMU-determined camera orientation angles, tie points can potentially be eliminated though *Direct Sensor Orientation* (DSO).

DSO involves the direct measurement of image orientation angles in addition to camera positions, which are subsequently fixed (i.e. treated as constants) to determine object point coordinates by space intersection (Yastikli and Jacobsen, 2005a; Yastikli and Jacobsen, 2005b). Though mitigating the requirement for image tie points, DSO typically requires the

measurement of camera orientation angles with a 0.005-0.008 degree absolute accuracy using high grade IMUs (Ip *et al.*, 2007). To investigate the potential of DSO in traditional aerial photogrammetry from manned aerial platforms, an investigation was launched by the OEEPE (now EuroSDR) in 2002 which involved the distribution of aerial film imagery at scales of 1:5000 and 1:1000 and corresponding high-end GNSS and IMU outputs to over 50 organisations for post processing (Heipke *et al.*, 2002). Reported results indicated that DSO could achieve an object point accuracy of 5-10 cm in planimetry and 15-20 cm in height, which was deemed sufficient for applications with "less stringent" accuracy requirements. Similarly, Yastikli and Jacobsen (2005a) also performed flights with an image scale of 1:5000 and achieved improved check point errors (RMSE) of 6.6 cm, 4.0 cm and 8.6 cm in easting, northing and height respectively. Their main cause of concern however were "unacceptable" y-parallax errors.

The Integrated Sensor Orientation approach (ISO) involves the treatment of camera position and orientation measurements as observations (not constants) in the BBA with the inclusion of image tie points as per GNSS-supported AT (Yastikli and Jacobsen, 2005a). Compared to GNSS-supported AT, the additional IMU camera orientation angle observations reduce the need for a regular image block containing multiple overlapping image strips, whilst unlike DSO, the tie points enable a refinement of relative orientation and thus a reduction of y-parallax errors (Yastikli and Jacobsen, 2005a). Ip *et al.* (2007) investigated ISO performance under different GNSS and IMU performances on manned aerial platforms. It was concluded that with a lower accuracy GNSS and IMU, ISO with an image block configuration may enhance the object point accuracy to that of DSO with a higher accuracy system, thus enabling cost savings and reduced demands on the GNSS and IMU performance. Further to this, Yastikli and Jacobsen (2005a) showed almost a twofold improvement in horizontal check point errors (now 3.5 cm, 2.4 cm and 7.1 cm in easting, northing and height respectively) when employing ISO over DSO. Heipke *et al.* (2002) concluded the key advantage of ISO over GCP-supported AT were its greater applicability to projects such as corridor mapping.

The applicability of DSO and ISO to UAVs, however, is more limited due to payload limitations such that only low quality MEMs-type IMUs can be carried. Such devices typically exhibit accuracies at the 1-3 degree level due to sensor bias instability and noise (El-Sheimy, 2009; Pfeifer *et al.*, 2012), whilst UAV-based DSO typically requires camera orientation angle accuracies of around 0.01-0.017 degrees, assuming flying heights of 100-250 m (Rehak and Skaloud, 2015). A possible accuracy enhancement may be obtained by using so-called

redundant IMUs, which combine multiple MEMS-type IMUs into a single solution to increase the reliability of attitude determination (Waegli *et al.*, 2010; Rehak and Skaloud, 2015).

Rehak and Skaloud (2015) investigated the potential of UAV-based ISO using a redundant MEMS-type IMU for an image block comprising 521 images in five strips with a GSD of 3.8 cm. An initial GNSS-BBA (i.e. GNSS camera positions only) produced check point RMSEs of 3.3 cm, 2.9 cm, and 4.0 cm in easting, northing and height respectively, which were equivalent to c. 1 pixel. However, in the application of corridor mapping, here using a subset of 61 images in two strips, these values degraded to 5.9 cm, 3.3 cm and 7.0 cm because the block was weak in angular orientation. When performing ISO by including camera orientation angle observations in the BBA (with expected accuracies of 0.04 degrees in roll/pitch, and 0.14 degrees in yaw), the same image block (corridor) was strengthened such that check point RMSEs improved to 2.1 cm, 2.1 cm and 7.0 cm in easting, northing and height respectively. Therefore, it was concluded that camera orientation angle observations were only required for linear image block configurations, such as in corridor mapping applications.

Similarly, Stöcker *et al.* (2017) investigated the effect of camera orientation angle observations for a UAV image block of 32 strips, three cross strips over a 1.4 km^2 area of mixed terrain with 60 m height variation. The study used a fixed wing UAV, equipped with a coupled carrier phase-based APX-15 Applanix IMU and RGB sensor. When using four GCPs and carrier phase-based positions and camera orientation angles with low weightings, mean checkpoint errors were c. 1 cm in plan and c. 15 cm in height. However, when using camera orientation angles with high weightings, these values degraded to c. 60 cm and c. 50 cm respectively. In the same situation but without GCPs, for camera orientation angles with low weightings, mean check point errors were c. 20 cm in plan and c. 5 cm in height, but for camera orientation angles with high weightings, these values again degraded to c. 50 cm and c. 70 cm respectively. Further analysis of image residuals showed that giving high weightings to the camera orientation angles increased image residual errors compared to equivalent solutions with low-weighted camera orientation angles. Despite the use of a good block geometry (32 strips, 3 cross strips) it was concluded that applying high (optimistic) weightings to the attitude observations deforms the BBA result because of their low quality.

2.5.4 Relative aerial control

In contrast to absolute camera position and attitude control, Blázquez (2008) and Blázquez and Colomina (2012) introduced a concept of relative aerial control, where *relative* camera position and attitude observations are considered in the BBA. For manned aerial platforms, the primary

benefit of relative aerial control was conceived to be that GNSS shift errors and the boresight (camera-IMU relative orientation) parameters could be ignored under the assumption that the relative attitude and position of the IMU between two epochs is the same as that of the camera (Blázquez, 2008). This model is highly favourable in the event of GNSS cycle slips. For example, when Blázquez (2008) perturbed camera position observations for an image strip by 50 cm, check point errors were substantially degraded for conventional ISO (with absolute aerial control) but not for the relative aerial control method. For three image blocks at scales of 1:8000 to 1:14000 with 8-10 GCPs, Blázquez and Colomina (2012) showed improvements with relative aerial control of 17%, 8% and 2% over conventional ISO for three image blocks respectively.

As Blázquez (2008) and Blázquez and Colomina (2012) did for manned aerial platforms, Skaloud *et al.* (2014) applied relative aerial control for UAVs, but only in the form of relative camera position control with the aim of reducing the importance of absolute accuracy of the GNSS. Results showed that GCPs could be minimised to only three, for which check point RMSEs of 3.8 cm, 3.0 cm and 10.3 cm were obtained in easting, northing and height respectively. When using one GCP and the biased absolute camera positions (i.e. GNSS-BBA), object point accuracies degraded to 5.5 cm, 4.6 cm and 7.3 cm. However, when using one GCP, six 'good' camera positions and the relative aerial control (the latter being obtained from the same biased GNSS), these were improved to 2.9 cm, 2.2 cm and 3.8 cm. Rehak and Skaloud (2017a) further studied the benefits of relative aerial control with regards to a fixed wing UAV equipped with both single and dual frequency carrier phase-based GNSS receivers. Using a local GNSS reference station, the agreement (RMSE) between the single and dual frequency GNSS-determined camera positions was shown to be c. 10 cm. However, the agreement (RMSE) between relative camera position vectors from each GNSS solution was only c. 1 cm. Subsequently, using one GCP, six 'good' GNSS camera positions, and relative position control, check point errors were 5.9 cm, 2.7 cm and 6.4 cm in easting, northing and height respectively for the single frequency GNSS, which were considered indifferent to the values of 5.9 cm, 2.8 cm and 6.2 cm obtained with dual frequency GNSS. However, although this relative aerial control approach gives protection against GNSS positioning biases, it does not completely mitigate the requirement for GCPs or a few 'good' camera positions to solve for the mapping datum (Rehak and Skaloud, 2017a).

2.6 Relative errors

In order to compare GNSS-based workflows, Table 2-1 summarises 14 UAV-based studies employing GNSS for image block orientation, either without, or with a minimal number of

GCPs. As each study varies in characteristics, for example, regarding camera specification and flying heights, relative mapping errors, defined as the ratio of measured mapping errors to the object-to-camera distance (James and Robson, 2012; Smith and Vericat, 2015; Eltner *et al.*, 2016), have been calculated where possible to facilitate comparison (noting that flying heights are not reported in all cases). Here it can be seen that relative error values are quite distinguishable based on whether they employ low quality or carrier phase-based GNSS positioning for camera position determination. Where low quality GNSS is employed, typically metre-level mapping errors translate to relative errors of 1:7-1:265 in plan and 1:23-1:299 in height for flying heights of 50-990 m. However, where carrier phase-based GNSS is employed, typically centimetre-level mapping errors translate to improved relative errors of 1:137-1:3152 in plan and 1:189-1:1849 in height for flying heights of 8-145 m. Such higher relative errors provide confirmation of the improvements offered from carrier phase-based GNSS camera positions, as opposed to low quality GNSS with only metre-level accuracy.

2.1 Summary

This chapter has discussed state-of-the-art routines employed by SfM-photogrammetric workflows and best practices and challenges associated with GCP control implementation. Preceding this, discussion indicated that GNSS camera positions offer an attractive alternative to the use of GCP control in UAV photogrammetry as such observations facilitate definition of the mapping datum and contribute to the image block precision in the GNSS-BBA. To fulfil these roles, however, GNSS camera positions must have both a high, typically centimetre-level, accuracy and precision. Consequently, GNSS camera positions derived from consumer grade GNSS with a consequent metre-level of accuracy and precision, remain insufficient (e.g. Kung *et al.*, 2011). GNSS camera positions must also be included as observations in the BBA and not used to derive a simple similarity transformation, for example as used by Turner *et al.* (2014). Where GNSS camera positions lack absolute accuracy, yet retain high precision, the relative constraints approach may be adopted to reduce block deformations, but with the remaining requirement of a few ‘good’ control points in the form of either GCPs or GNSS camera positions, for example as used by Rehak and Skaloud (2017a). With a regular image block geometry, GNSS camera positions in GNSS-BBAs can be sufficient without the need for an IMU because the block orientation is sufficiently resolved, whilst tie points enable an accurate calculation of camera orientation angles. UAV-compatible MEMS-type IMUs, however, currently do not provide any additional information over the image tie points due to their limited accuracy (e.g. Rehak and Skaloud, 2017; Stöcker *et al.*, 2017) unless linear image block configurations exist (Rehak and Skaloud, 2015). Overall, it has been indicated that centimetre-

level camera positions are the key to mitigating or eliminating GCPs in the BBA (Gerke and Przybilla, 2016; Dall'Asta *et al.*, 2017) and therefore, the next section reviews GNSS positioning techniques that may be used to achieve this task.

Study author	UAV type	GNSS positioning strategy for camera. positions	GSD (cm)	Flying height (m)	No. of GCPs	No. of CPs	Image workflow (and software if specified)	Check point RMSE (m) (Plan | h)	Check point relative error
Kung *et al.* (2011)	Fixed wing	SF, pseudorange, standalone	33 8 6	990 260 130	0 0 0	13 19 12	GNSS-BBA (Pix4D)	5.036 | 5.420 1.830 | 1.290 0.871 | 1.760	178 | 183 142 | 201 149 | 100
Turner *et al.* (2012)	Rotary wing	SF, pseudorange, standalone, barometric height	1	50	0 0	43 61	Bundler + similarity transformation	1.218 0.633	41 78
Rehak *et al.* (2013)	Rotary wing	DF, carrier phase, PPK GNSS, local base	ng	8	1	6	GNSS-BBA	0.042 | 0.019	189 | 421
Turner *et al.* (2014)	Rotary wing	SF, carrier phase, PPK GNSS, local base	ng	ng	0 0 0	22 22 22	GNSS-BBA (PhotoScan, Pix4D, Bundler)	0.111 0.244 0.750 (varied software)	
Jozkow and Toth (2014)	Rotary wing	DF, carrier phase, PPK GNSS, local base	ng	135	0	31	GNSS-BBA	0.163 | 0.64	829 | 210
Skaloud *et al.* (2014)	Rotary wing	DF, carrier phase, PPK GNSS, local base	ng	10	1 3	22 22	GNSS-BBA, *abs.* control + 1GCP GNSS-BBA, *rel.* control + 3GCP	0.033 | 0.039 0.034 | 0.039 (*abs*. vs *rel*. aerial control)	299 | 256 292 | 256
Shahbazi *et al.* (2015)	Rotary wing	SF, pseudorange, differential GNSS, WAAS-enabled	ng	80	0 0	ng ng	DSO and GNSS-BBA	3.393 | 11.67 2.266 | 3.169 (DSO vs BBA)	23 | 7 35 | 25
Eling *et al.* (2015)	Rotary wing	DF, carrier phase, RTK GNSS, local base	ng	20	0 0	22 9	GNSS-BBA (Pix4D)	0.046 | 0.030 0.011 | 0.009 (two sites)	434 | 666 1849 | 2222

Rehak and Skaloud (2017a)	Fixed wing	SF, carrier phase, PPK GNSS, local base	4	145	0	23	GNSS-BBA (Pix4D)	0.077 | 0.046	1894 | 3152
Benassi *et al.* (2017)	Fixed wing	DF, carrier phase, RTK GNSS, local base	2.3	80	0	14	GNSS-BBA (APERO)	0.011 | 0.085 (abs. mean errors) 0.008 | 0.063 0.007 | 0.035 0.003 | 0.009	7155 | 941 9363 | 1270 10988 | 2285 25298 | 8888
Gerke and Przybilla (2016)	Fixed wing	DF, carrier phase, RTK GNSS, local base	2.5	105	0 0	35 35	GNSS-BBA (PhotoScan)	0.040 | 0.050 (cross strips) 0.070 | 0.070 (no cross strips)	2625 | 2100 1500 | 1500
Rehak and Skaloud (2015)	Fixed wing	DF, carrier phase, PPK GNSS, local base	3.8	ng	0 0 0	17 9 9	ISO (Pix4D)	0.043 | 0.040 0.067 | 0.070 0.029 | 0.070 (block, cam. pos. obs. only) (corridor, cam. pos. obs. only) (corridor, cam. pos + att. obs.)	
Dall'Asta *et al.* (2017)	Fixed wing	DF, carrier phase, PPK GNSS, local base	4	140	1	13	GNSS-BBA + block shift (PhotoScan)	0.040 | 0.031 | 0.072	2766 | 1944
Stöcker *et al.* (2017)	Fixed wing	DF, carrier phase, PPK GNSS, Virtual Reference Station	2.8	100	0 0	18 18	ISO (Pix4D)	0.217 | 0.186 | 0.053 0.156 | 0.502 | 0.727 (0 GCPs, low cam. att. weight) (0 GCPs, high cam. att. weight)	349 | 2000 190 | 137
Median values with pseudorange GNSS								1.760 | 1.830	163 | 149
Median values with carrier phase GNSS								0.050 | 0.057	1886 | 392

Table 2-1. Summary of case studies discussed in Chapter 2 employing GNSS-supported BBAs with calculated relative errors (i.e. the ratio of measured mapping errors to the object-to-camera distance). *DF/SF = dual/single frequency, ng = not given in text

Chapter 3. GNSS positioning for UAVs

3.1 Introduction

Chapter 2 discussed how GNSS-determined camera positions may be used to reduce GCP requirements through GNSS-supported AT in traditional aerial photogrammetry, and GNSS-BBAs in UAV photogrammetric applications. However, a major factor is the accuracy and precision of GNSS camera positions, which relates to the GNSS positioning strategy. Here, GNSS positioning strategies are discussed with relevant theory, for the purpose of determining UAV GNSS camera positions. Brief details are provided as well as the benefits and drawbacks of each. Strategies are broadly categorised into single point, differential pseudorange, carrier phase relative and precise point positioning.

3.2 GNSS overview

The Navigation Satellite Timing and Ranging (NAVSTAR) GPS has been designed to produce a global positioning service that can be accessed anywhere in the world, 24 hours a day (Leick *et al.*, 2015). As of 4th March 2018, the active GPS constellation consists of 31 satellites and a number of decommissioned residuals (GPS.gov, 2018). They orbit twice daily in medium earth orbits at inclinations of 55 degrees to optimise coverage over the USA. Of these satellites, 24 form the core constellation with seven held in reserve. The arrangement ensures at least four satellites are simultaneously visible at any one time globally, although many more are likely. Range measurements (as will be discussed in subsequent sections) are obtained from GPS satellite signals. The system is undergoing continuous modernization, with the launch of upgraded satellites (notably the Block III satellites) and announcement of new signals. Alongside the two legacy signals L1 and L2 , the US government plans for three new civil signals, L1C, L2C and L5, the latter intended for safety of life applications. This has good implications for the modelling of frequency-dependant atmospheric errors, especially due to the large frequency difference between L1 and L5, although receivers must be upgraded for their use and tracking.

In addition to GPS, the Russian GLONASS (Global'naya Navigatsionnaya Sputnikovaya Sistema) constellation was initiated in 1982, and now comprises 24 core satellites. GLONASS

satellites orbit in three planes at inclinations of 65 degrees and with orbital periods of approximately 11 hours 15 minutes, an arrangement that ensures four satellites are simultaneously visible at any time over 97% of the Earth's surface (IAC, 2018). The collective use of both GPS and GLONASS positioning is referred to as Global Navigation Satellite System (GNSS) positioning and has implications for the improvement in accuracy and availability of global positioning by increasing the number of observable satellites over GPS-only.

Though not yet complete, the European satellite positioning system, named Galileo, is also under development with a full constellation of 30 satellites planned for completion by 2020. Unlike GLONASS, Galileo is to be compatible with GPS, thus enabling the use of the same receiver components, by broadcasting signals on the same carrier frequencies as GPS L1 and L5, whilst also employing the same algorithms for satellite ephemeris determination (Leick *et al.*, 2015). Further GNSSs include the Chinese Beidou system and the regional Japanese Quasi Zenith Satellite System. It should be noted that although 'GNSS' has been used generically in previous chapters, it is hereafter used to denote the combined processing of multiple constellation data, whereas 'GPS' denotes GPS-only processing.

3.3 GNSS observables

GNSS positioning strategies are based on the observation of two primary signals; the pseudorange (code) and carrier phase, which can be made on multiple frequencies (Leick *et al.*, 2015). Their observational models, including contaminating error sources, are as follows:

$$P_r^s = R_r^s + c(d_r - d^s) + d_{orb} - d_{ion} + d_{tro} + d_{oth} \tag{3-1}$$

$$\Phi_r^s = \lambda\phi = R_r^s + c(d_r - d^s) + \lambda N + d_{orb} + d_{ion} + d_{tro} + d_{oth} \tag{3-2}$$

where R_r^s may be expressed as

$$R_r^s = \sqrt{(X^s - X_r)^2 + (Y^s - Y_r)^2 + (Z^s - Z_r)^2} \tag{3-3}$$

Here P_r^s is the pseudorange observation (m), Φ_r^s is the one-directional carrier phase observation (m), c is the propagation speed of radio waves in a vacuum (m/s), d_r is the receiver clock correction to GPS time (s), d^s is the satellite clock correction to GPS time (s), d_{orb} is the satellite orbit correction (m), d_{ion} and d_{tro} are the ionospheric and tropospheric delays (m)

respectively, λ is the carrier wavelength (m) and N is the integer number of carrier cycles between satellite and receiver, also termed 'integer ambiguity'.

3.4 Positioning with pseudorange observations

The pseudorange is computed in the receiver by multiplying the satellite-to-receiver travel time by its velocity as follows:

$$R_r^s = c(t_r - t^s) \tag{3-4}$$

where c is the propagation speed of radio waves in a vacuum (m/s), t_r is the signal transmission time from satellite (satellite clock) (s) and t^s is the signal reception time at receiver (receiver clock) (s). Here $t_r - t^s$ is determined from the temporal correlation of code-modulated carrier waves, transmitted by the satellite and replicated by the receiver. The GPS time frame is maintained by the receiver and satellite clock offset terms d_r and d^s respectively. d^s is supplied in the satellite navigation message, which is broadcasted directly from all satellites, whilst d_r is simultaneously estimated along with the receiver coordinates.

3.4.1 Single point positioning

The solution in which receiver positions are computed from pseudorange observations is known as Single Point Positioning (SPP) or sometimes the navigation solution (Leick *et al.*, 2015). SPP provides a standalone positioning solution because its only requirements are satellite orbits and clock values broadcast in the navigation message. The main limitations on positional accuracy are the quality of the broadcast satellite orbits, which have an accuracy of around 1 m (IGS, 2018), and contamination of pseudorange observations by metre-level multipath errors (Braasch and Van Dierendonck, 1999). As a result, most other error sources, including the ionosphere, troposphere and receiver clock, are relatively insignificant in magnitude and may be ignored (Hofmann-Wellenhof *et al.*, 2007). When at least four satellites are observed (three to solve for the trilateration, one to solve for the receiver clock offset) the 3D position of the antenna may be determined in a nonlinear least squares solution. SPP therefore provides a readily available, real-time and standalone positioning solution, but with an accuracy at the 5-10 m level, and is thus most suitable for navigation purposes. With pseudorange observations made on two frequencies, it is also possible to further improve the SPP positioning accuracy by forming linear observable combinations to mitigate first order ionospheric delays (Leick *et al.*, 2015).

3.4.2 Differential positioning

SPP may be extended to differential positioning (DGNSS), a strategy that applies range corrections (RCs) to pseudorange observations. RCs are calculated at a local GNSS reference station as the difference between the computed ranges (using precisely known reference station coordinates and broadcast satellite ephemeris) and observed pseudoranges for each satellite and epoch (Hofmann-Wellenhof *et al.*, 2007). In addition, range rate corrections (RRCs) are computed as the time derivative of the RCs, which enables the prediction of RCs at epochs intermediate to the known RCs. The RCs account for common error sources in observed pseudoranges, such as the ionosphere and troposphere. DGNSS thus improves the measured pseudoranges used for trilateration and thus the point positioning accuracy with respect to the local GNSS reference station(s) used to compute the RCs (Hofmann-Wellenhof *et al.*, 2007) and can achieve positional accuracy at the 0.5 to 1 m level (Chen *et al.*, 2009).

3.5 Positioning with carrier phase observations

To achieve positioning accuracies at the 0.01 m level or better, it is desirable to process carrier phase measurements. According to Braasch and Van Dierendonck (1999), phase measurements may be recorded with an accuracy between 2 and 5 degrees, depending on the signal to noise ratio, which corresponds to millimetre-accurate range measurements (owing to the 19.0 cm and 24.4 cm wavelengths of L1 and L2 respectively). However, the conversion of carrier phase measurements to precise range measurements requires the determination of carrier phase ambiguity parameters. These denote the integer number of wavelengths between each satellite and the receivers' antenna. There are two main techniques for doing this: (1) relative GNSS and (2) standalone Precise Point Positioning techniques. If ambiguity parameters can be fixed to their true integer values, they are removed from the least squares estimation along with associated parameter correlations to improve the precision of estimated receiver coordinates (Leick *et al.*, 2015).

3.5.1 Relative positioning

Relative GNSS positioning involves the differencing of carrier phase observations made at the rover (i.e. here the UAV) and a local GNSS reference station for the estimation of a baseline vector (in Cartesian coordinates) between the two receivers. Assuming the local GNSS reference station is fixed (i.e. has known coordinates) then estimating the baseline vector enables the positioning of the rover. The differencing of carrier phase observations enables the removal of spatially correlated non-integer error sources for the estimation and fixing of integer ambiguity parameters. Single differences involve the differencing of observations made by two

receivers to the same satellite for the cancelling out of both satellite clock and hardware biases as well as common atmospheric errors. Double differences involve differencing two single differences across a receiver for the cancelling of receiver clock and hardware biases (Hofmann-Wellenhof *et al.*, 2007; Leick *et al.*, 2015). In addition to positional vectors, relative GNSS estimates an integer double differenced ambiguity parameter per satellite pair.

Successful integer ambiguity resolution requires a sufficient cancellation of ionospheric and tropospheric refraction biases and consequently the rover must remain within 10-20 km of the GNSS reference station to ensure such errors are spatially correlated (Wanninger, 2004; Dai *et al.*, 2007). In such cases, relative GNSS positioning accuracies of c. 1-3 cm in planimetry and c. 1-5 cm in height are obtainable (Hu *et al.*, 2003). However, with increasing distance from the GNSS reference station, relative GNSS positioning accuracies degrade due to residual ionospheric and tropospheric refraction errors (Dai *et al.*, 2007).

Relative GNSS positioning can be applied in both real-time, known as the RTK approach, or in post processing mode, known as the PPK approach. For RTK, code and carrier phase observations are broadcast from the GNSS reference station to the rover using a communication link to perform the differences (e.g. Hu *et al.*, 2003). For PPK, code and carrier phase observations are logged at both the rover and GNSS reference station to perform the differences retrospectively (e.g. Stöcker *et al.*, 2017). The benefits of PPK over RTK are that more control is given in the parameterisation of the processing strategy to enable interrogation of parameterisations affecting positional quality (Stöcker *et al.*, 2017), whilst also eliminating the need for a communication link. The main drawbacks of relative GNSS positioning are therefore (1) the requirement to operate in close proximity to a local GNSS reference station (e.g. 5-10 km as per Dai *et al.*, 2007) and (2) the need to accurately determine the GNSS reference station as any error in its coordinate will propagate directly into those of the rover.

These constraints may be partly addressed through Network RTK, for example using the Virtual Reference Station (VRS) technique. In the VRS approach, observation data is generated for a non-existent GNSS reference station using a surrounding network of GNSS reference stations, before being transmitted to the rover (e.g. Hu *et al.*, 2003). Double differenced ambiguity resolution may then be performed with initialisation times (meaning times to first ambiguity fix) of c. 1.5-2 minutes (Dai *et al.*, 2007). This approach can yield a horizontal accuracy of up to 5 cm for baselines (to the reference station network) of up to 35 km with a height component of 1.5-2 times worse (Retscher, 2002). The drawback, however, along with the costs of a

network subscription, is the need to operate within the bounds of a permanent network of GNSS reference stations. Consequently, such an approach is not globally applicable.

Applications of relative GNSS to UAV-based GNSS-BBAs have been recently presented using both the local GNSS reference station (e.g. Gerke and Przybilla, 2016; Benassi *et al.*, 2017) and the VRS approach (e.g. Stöcker *et al.*, 2017). Though potentially minimising the use of GCPs (as was discussed in Chapter 2), such workflows incur costs associated with additional equipment (i.e. GNSS reference stations receiver/antenna and tripods) or VRS subscriptions, whilst in all cases, are spatially constrained for the purpose of effective error cancellation. These details, however, are usually overlooked, or else not discussed in substantial detail.

3.5.2 Precise Point Positioning

In the PPP technique, rather than differencing observations and estimating integer double differenced ambiguities, highly accurate satellite orbit and clock parameters are fixed so that a stand-alone position may be estimated directly, using dual frequency carrier phase and code GNSS data (Zumberge *et al.*, 1997). This has the substantial advantage over relative GNSS positioning in that it mitigates the need for a local GNSS reference station or the need to operate within the bounds of a permanent reference station network as for the Network RTK approach. It is therefore globally applicable.

The drawback of PPP is that integer ambiguity resolution is not possible in pure stand-alone mode without additional data from reference stations. This is because ambiguities are contaminated by non-integer hardware delays (e.g. Bertiger *et al.*, 2010), usually termed Uncalibrated Phase Delays (UPDs). Ambiguities must therefore be estimated as float values. Reliable estimation requires their separation from other estimated parameters, such as the tropospheric delay, receiver clock and coordinates. However, as long as float ambiguity values converge to accurate non-integer values, centimetre-level accuracy kinematic positioning becomes possible (Cai and Gao, 2013; Yu and Gao, 2017). In the PPP solution, the majority of ionospheric refraction (first order effects) can be eliminated by using the ionosphere free linear combination of dual frequency observations, because the effects of the ionosphere are frequency dependant (Hoque and Jakowski, 2007). Typically, the majority of the tropospheric delay is modelled and the residual tropospheric delay estimated.

At the time of writing and to the author's knowledge, the PPP technique has not been applied to UAV-based GNSS-BBAs. Eliminating the need to operate a ground-based GNSS reference station, or need to operate within the bounds of a network of permanent GNSS reference stations would be beneficial for remote UAV applications, whilst further minimising survey equipment

requirements. However, the extent to which PPP may be used to minimise GCP requirements in the UAV-based GNSS-BBAs depends on obtainable PPP accuracies, and thus these are hereafter reviewed for other dynamic platforms.

3.5.3 PPP convergence and attainable accuracies

Accurate PPP positioning can only be obtained when (float) ambiguity estimates converge to stable values, which requires a sufficient change in satellite geometries. PPP solutions therefore require longer GNSS observation durations if solutions are to converge, where GNSS *observation duration* here refers to the duration of continuously tracked satellite data without interruption. The *convergence time* is typically used to denote the GNSS observation duration required for solutions (coordinates) to reach a specified solution accuracy (Li and Zhang, 2014) or stable condition (Yu and Gao, 2017). Convergence times relate to the quality of the approximate values of the parameters used for the least squares estimation and the agreement of code and carrier phase observations (Kouba and Heroux, 2001). Convergence times for float ambiguity estimation are usually much longer than the initialisation time for ambiguity fixed solutions (Li and Zhang, 2014), but ambiguity fixed solution may only be obtained with additional information on non-integer UPDs (e.g. Bertiger *et al.*, 2010). Moreover, kinematic float ambiguities are usually slower to converge compared to static solutions because coordinates are estimated per epoch with a subsequent reduction in observation redundancy in the least squares adjustment (Li and Zhang, 2014). For dynamic platforms, the receiver environment also continually changes such that error sources do not remain constant for all data epochs (Cai and Gao, 2013).

Additional factors includes satellite observation redundancy, which influences the estimation of remaining errors in the GNSS signal (Bisnath and Gao, 2009; Cai and Gao, 2013). For this reason, combined GPS+GLONASS PPP is often a focus in PPP research. For example, Anquela *et al.* (2013) showed the inclusion of GLONASS satellites to result in a 27% improvement to the average positional dilution of precision (PDOP), whilst Cai and Gao (2013) showed that GLONASS increased the average number of satellites from eight to 14 and subsequently reduced the PDOP from 2.5 to 1.7. Ambiguity fixing for GLONASS is also considered more challenging because of the presence of inter-satellite and frequency UPDs in GLONASS carrier phase and pseudorange observations (Reussner and Wanninger, 2011; Wanninger, 2012; Li and Zhang, 2014). However, for float ambiguity estimation, such hardware biases may be absorbed by float ambiguity parameters (Cai and Gao, 2013).

Table 3-1 presents a summary of published PPP results to date involving float ambiguity estimation. Because studies vary by whether they focus on PPP convergence times, or attainable PPP accuracy, the analysis criteria per study are presented along with the used GNSS constellation(s). Anquela *et al.* (2013) processed GPS+GLONASS data acquired from eight IGS permanent reference stations in static PPP mode. For GPS-only solutions, they required 70-100 minutes of data to achieve a 1 cm positional accuracy, whereas GPS+GLONASS solutions required 20 minutes less. Two kinematic PPP trials were also performed: firstly a 30 minute car test and secondly a 30 minute walking trajectory test, with solutions evaluated against a relative GPS trajectory obtained over a (maximum) 5 km baseline. For the car test, coordinate RMSEs were at the c. 0.5-1 m level with precisions of c. 0.1-0.3 m. In this case, the inclusion of GLONASS satellites gave only improvements to the coordinate precisions, with a slight degradation in height RMSE. For the 30 minute walking trajectory test, coordinate RMSEs were similar at c. 0.5 m, again with precisions of c. 0.1-0.3 m. As before, the inclusion of GLONASS satellites primarily resulted in a reduction in coordinate precision (of 62% and 44% improvements in northing and height respectively) but no notable improvement to the coordinate RMSEs were observed. These results are suggestive of a lower obtainable PPP positioning accuracy on dynamic over static platforms, although in the context of UAV photogrammetry, such kinematic PPP positioning accuracies would improve on standalone SPP solutions with a 5-10 m accuracy.

Li and Zhang (2014) processed a week of data from 178 (stationary) IGS reference stations in two hour batches. Defining convergence time as the time to reach a 10 cm positioning accuracy, in static PPP mode, they showed GPS-only solutions to converge in an average of 22.9 minutes, whereas this was 12.4 minutes for GPS+GLONASS, representing an improvement of 45.9%. They also showed that at least four GLONASS satellites were required to have a 20% or greater improvement in convergence time, whilst more than four satellites did not always guarantee a further improvement. Further to this, they showed that benefits from GLONASS increase with fewer available GPS satellites. For example, a 47.6 minute convergence time reduction was observed with only four available GPS satellites, whereas this was only 15 minutes with 13 GPS satellites. When processing in kinematic PPP mode, average convergence times were 40.6 minutes for GPS-only solutions, which improved to 17.7 minutes with the inclusion of GLONASS satellites, representing a 57.9% improvement. In contrast to Anquela *et al.* (2013), these results are suggestive of a higher obtainable PPP positioning accuracy (of at least 10 cm) for kinematic PPP processing. It is expected that if such positioning accuracies could be obtained on a UAV, PPP could be effectively leveraged in the UAV-based GNSS-BBA (for

example they are commensurate with the Turner *et al.* (2014) camera position accuracies). The 17.7 minute convergence time with GPS+GLONASS processing is also in range of typical UAV flight durations.

Cai and Gao (2013) performed kinematic PPP on a land vehicle with a longer GNSS observation durations of around two hours. Solutions were again evaluated against a relative GNSS trajectory obtained using a local GNSS reference station. For GPS-only processing, they achieved coordinate RMSEs of 18.2 cm, 2.8 cm and 9.1 cm in easting, northing and height respectively, whilst these were improved to 5.0 cm, 2.6 cm and 9.2 cm with the inclusion of GLONASS. Although a similar two hour UAV flight duration is generally not currently possible, such PPP positioning accuracies are large improvements on standalone SPP solutions, whilst the latter, with GPS+GLONASS processing, are of the same order of magnitude as those obtainable with relative GPS and hence they would be highly useful as control information in the UAV-based GPS-BBA.

Yu and Gao (2017) also performed kinematic PPP on a land vehicle with a GNSS observation duration of around two hours. Solutions were again evaluated against a relative GNSS trajectory obtained using a local GNSS reference station (baseline length not given). For this study, converge criteria were defined as the GNSS observation duration required to reach a 10 cm accuracy. Convergence times were 64 minutes for GPS-only processing, and 52.4 minutes for GPS+GLONASS processing. Again, such convergence times exceed typical UAV flight durations to date, although solutions indicate the possibility of a 10 cm kinematic PPP positioning accuracy on a highly dynamic platforms (in this case travelling at 20 m/s). Moreover, both the Yu and Gao (2017) and Cai and Gao (2013) studies were undertaken in urban environments and thus likely incurred GNSS signal obstructions from buildings, which would not be the cause for UAV platforms. Yuan *et al.* (2009) performed kinematic PPP on a manned aerial platform with a flight duration of 5 hours 14 minutes. The solution was evaluated against a relative GPS trajectory processed over a c. 29 km baseline. Accordingly, kinematic PPP positioning accuracies were c. 0.5 m, 0.3 m and 0.6 m in easting, northing and height respectively. Based on the results of Yu and Gao (2017) and Cai and Gao (2013), a higher kinematic PPP accuracy could be expected. However, as the relative GPS trajectory was processed over a c. 29 km baseline, similar errors could be expected in the reference solution due to residual atmospheric errors (e.g. Dai *et al.*, 2007). In this case, the kinematic PPP solutions were used to implement GPS-supported AT, in which four GCPs were used to compensate for these errors. Moreover, they also noted variable PPP positioning errors between each strip and hence camera position shift corrections were estimated on a strip-by-strip basis.

The only application of kinematic PPP on a UAV was presented by Gross *et al.* (2016), but as a first trial of UAV-based kinematic PPP, and not for further photogrammetric use. Gross *et al.* (2016) undertook three fixed-wing UAV flights of duration c. 2.6, 5.7 and 4.4 minutes. Solutions were again evaluated against a relative GNSS trajectory obtained using a local GPS reference station (baseline length not given). Over all flights, kinematic PPP positioning accuracies ranged between 0.61 m and 1.39 m. Such accuracies were attributed to the lack of ambiguity convergence over the short (c. 5 minute or less) duration flights. The kinematic PPP position precision, however, was at the centimetre-level for all flight and thus they suggested that the coordinate bias could have been resolved by starting the UAV from a known location.

Study	Platform	Study focus	Satellites, solution type	Conv. time (minutes)	Accuracy (cm) Precision (cm)
Yu and Gao (2017)	Ground based vehicle (> 2 hours)	Time until solution remained within 10 cm of reference	GPS, kinematic	**64.2**	**4.5 | 8.5 (E | N)** 6.7 | 9.1
			GPS+GLO, kinematic	**52.4**	**4.0 | 8.0 (E | N)** 6.2 | 8.1
Anquela *et al.* (2013)	8 stat. IGS stations (1 day)	Time until solutions reached a 1 cm /10 cm accuracy	GPS, static GLO, static GPS+GLO, static	**70-100 / 48-45** **130-160 / 70-95** **60-85 / 33-38**	
		Accuracy achieved	GPS, kinematic	-	**3.6 | 4.2 | 11.3** 3.2 | 3.1 | 9.9
			GPS+GLO, kinematic	-	**2.9 | 3.1 | 6.9** 2.6 | 2.8 | 6.3
Anquela *et al.* (2013)	Ground based vehicle (32 mins)	Accuracy achieved	GPS, kinematic	-	**55.2 | 64.6 | 82.4** 9.0 | 8.2 | 33.2
			GPS+GLO, kinematic	-	**40.9 | 89.1 | 98.4** 8.0 | 7.7 | 19.0
Anquela *et al.* (2013)	Walking trajectory (30 mins)	Accuracy achieved	GPS, kinematic	-	**12.5 | 19.8 | 67.9** 10.1 | 4.5 | 15.7
			GPS+GLO, kinematic	-	**22.0 | 76.3 | 9.5** 4.5 | 3.7 | 8.8
Cai and Gao (2013)	Ground based vehicle (> 2 hours)	Accuracy achieved	GPS, kinematic	-	**18.2 | 2.8 | 9.1**
			GPS+GLO, kinematic	-	**5.0 | 2.6 | 9.2**
Li and Zhang (2014)	178 static IGS stations in two hour segments	Time until solution reached a 10 cm accuracy	GPS, static GPS+GLO, static	**22.9** **12.4**	-
			GPS, kinematic	**40.6**	-
			GPS+GLO, kinematic	**17.7**	-

Yuan *et al.* (2009)	Manned aerial platform (5 hours 14 mins)	Accuracy achieved	GPS, kinematic	-	**c. 140 | 50 | 90** c. 10 | 10 | 10
Gross *et al.* (2016)	Unmanned aerial vehicle	Accuracy achieved	GPS, kinematic	**2.6** **5.7** **4.4**	**0.61 and 0.91 (L/R antenna)** (0.038 and 0.02) **0.63 and 0.99 (L/R antenna)** (0.03 and 0.82) **1.39 and 1.33 (L/R antenna)** (0.029 and 0.026) **Units = Metres**

Table 3-1. Convergence in PPP applications with float ambiguity estimation. *GLO = GLONASS

3.6 The research gap

This chapter has presented a review of GNSS positioning strategies that may be applied for kinematic UAV positioning. SPP (i.e. single frequency pseudorange GNSS) has the advantage of enabling standalone UAV positioning without the need of supporting GNSS infrastructure, but is generally limited to a c. 5-10 m positioning accuracy. This is suitable for UAV navigation, but as indicated in Chapter 2, has limited utility for reducing GCPs in the GNSS-BBA where centimetre-accuracy camera positions are required. In contrast, carrier phase-based relative GNSS (either as PPK or RTK) facilitates a UAV positioning accuracy of around 2-3 cm and therefore has much improved implications for eliminating GCPs in UAV-based GNSS-BBAs. However, relative GNSS requires the use of a local GNSS reference station (or equivalent VRS) for double difference ambiguity resolution. Therefore, despite the inherent flexibility of UAV platforms and potential to eliminate GCPs, such workflows incur (1) additional GNSS equipment requirements and associated costs, (2) the need to accurately determine the GNSS reference station coordinates, and (3) the need to perform UAV flights in close proximity to the local GNSS reference station. The alternative Network RTK approach also incurs (1) the need to operate within the bounds of a permanent network of GNSS reference stations and (2) the cost of a subscription to a Network RTK correction network. Such workflows based on relative GNSS are therefore inherently complicated and not globally applicable.

In contrast to relative GNSS, the PPP technique offers the potential to eliminate the GNSS reference station, whilst still achieving a similar kinematic positioning accuracy (e.g. Cai and Gao, 2013; Yu and Gao, 2017). Accurate PPP positioning, however, can only be obtained when (float) ambiguity estimates converge to stable values, which requires a sufficient change in satellite geometries, which can only be ensured with longer GNSS observation durations. To date, PPP has been applied to GNSS-supported AT from a manned aerial platforms with flight durations of several hours and incorporating GCPs to compensate for GNSS PPP biases. The PPP technique has once been applied on a UAV, but resulted in metre-level PPP positioning accuracies due to the limited (c. 3-6 minute) duration of the UAV flights. Such positioning accuracies would also have limited use for eliminating GCPs had they been applied to a UAV-based GNSS-BBA. As PPP has not yet applied to UAV photogrammetry, this thesis investigates whether accurate PPP positioning of a lightweight UAV platform is possible, to eliminate the need for GCPs, a local GNSS reference station or flying within the bounds of a Network RTK correction network in UAV-based photogrammetric mapping. Previous studies of kinematic PPP on other dynamic platforms have indicated that achieving solution convergence may be

challenging given the generally short duration of UAV flight durations, although it has also been indicated that GLONASS may reduce convergence times to facilitate such a UAV application. The next chapter provides an overview of the PPP-BBA methodology, the datasets used for investigation and considerations that were made to improve the performance of kinematic PPP on the UAV.

Chapter 4. PPP-BBA methodology and datasets

4.1 Introduction

Chapter 2 provided background information on the evolution of close range photogrammetric workflows with the integration of CV techniques to facilitate the orientation of UAV imagery. Discussion also related to the roles and requirements of control information in the bundle block adjustment (BBA), whereby GNSS-determined camera positions can be used to constrain image orientation estimates directly in a GNSS-supported bundle block adjustment (GNSS-BBA). Should camera positions entail centimetre-level accuracy, such an approach offers the potential to eliminate or minimise the use of GCPs. For this purpose, Chapter 3 discussed feasible UAV-based GNSS positioning strategies and how dual frequency carrier phase GNSS data can be processed to yield centimetre-accuracy positions (and subsequently camera positions). For the purpose of ambiguity estimation and error reduction, the relative GNSS positioning technique is usually adopted, and to date, has been successfully applied to UAV-based GNSS-BBAs. However, such a technique incurs either the inconvenient requirement of a local GNSS reference station for a PPK or an RTK-based workflow, or the need to operate within the bounds of a permanent GNSS reference station network for the Network RTK approach. In contrast, it was discussed that the PPP technique may provide an alternative UAV-based positioning solution without the requirement of a GNSS reference station (or equivalent). For the PPP technique, satellite orbits and clocks are fixed to pre-determined values, whilst ambiguity parameters, zenith tropospheric delays, receiver coordinates and clocks are directly estimated. The main additional requirement (over PPK), however, is the need for longer GNSS observation durations, to improve the estimation of PPP ambiguities. To the best of the author's knowledge, kinematic PPP has only been tested once on a UAV with only a metre-level positioning accuracy achieved, and without further photogrammetric application.

This research methodology therefore involves two aspects; (1) undertaking kinematic PPP trials on a lightweight fixed wing UAV platform and (2) implementing PPP-supported bundle block adjustments (PPP-BBAs) to eliminate or minimise the use of GCPs. The overall goal is to obtain large scale (one GSD-level accuracy and precision) UAV photogrammetric mapping, but without the need for either GCPs or a ground-based GNSS reference station (or equivalent).

4.2 Methodology

The proposed research methodology comprises four main tasks:

Task 1. *Assessing the accuracy and precision of kinematic PPP positions on a fixed wing UAV.* To undertake UAV-based GPS PPP positioning, dual frequency (L1/L2) carrier phase and code GPS observations are acquired on a number of fixed wing UAV flights. To maximise flight durations, necessary to improve the estimation of PPP ambiguities, the UAVs were manually piloted after completion of the automated flight plan and not landed until battery voltage readings dropped to a critical level. In addition, to extend GPS observation durations beyond the respective flight durations, ground-based GPS logging periods were implemented when possible, both before and after the UAV flight, with seamless transition. PPP processing is undertaken in PANDA software. To assess the accuracy of the PPP positions on the UAV, reference trajectories are computed by processing the data from each mission in PPK mode, relative to a local GNSS reference station. PPK processing is undertaken in Leica Infinity software. PPP control experiments are also performed at the local GNSS reference station by processing the static (ground-based) data as per the UAV flights and comparing solutions to the pre-determined reference station coordinates.

Task 2. *Setting up of optimum reference GCP-supported bundle block adjustments (GCP-BBA).* Optimal reference GCP-BBA workflows are set up for each flight by evaluating the effect of GCP numbers, distributions and observation weights on the mapping error. This is important given the variable dataset characteristics and limitations.

Task 3. *Determining camera positions from kinematic PPP (and PPK) positions*. GPS (both PPP and PPK) camera positions are determined through (1) GPS-camera time synchronisation and interpolation and (2) the derivation and application of lever arm corrections. For GPS-camera time interpolation, linear and spline interpolation schemes are assessed, and the possibility of GPS-camera time synchronisation errors is evaluated by comparing GPS camera position solutions with those indirectly estimated in reference GCP-BBAs.

Task 4. *Assessing the accuracy and precision of UAV photogrammetric mapping obtained through PPP-BBAs and comparison to the equivalent PPK-supported bundle block adjustment (PPK-BBA) solutions and standard GCP-BBAs*. GPS-BBAs (PPP-BBAs and reference PPK-BBAs) are implemented in both PhotoScan and APERO software, with investigation of GPS camera position observation weight settings. The achieved accuracy of object point determination from the PPP-BBAs is compared to that of the PPK-BBAs and GCP-BBAs to

determine whether, and under what conditions, GCPs may be largely reduced or eliminated through PPP-BBAs.

In addition to the GPS-BBA workflows, a different approach for GPS-based image orientation was developed, named trajectory matching (TM). This method uses an iterative closest point (ICP) adjustment to register arbitrary camera positions estimated in the free network adjustment with a corresponding UAV GPS (either PPP or PPK) trajectory. The TM approach overcomes some dataset limitations, namely missing image time stamps, with only a small reduction in mapping accuracy.

4.3 Datasets

Data for this work was collected over the period March 2017 to August 2017. In total, 11 flights were undertaken at two different sites involving two fixed wing UAV systems. The UAVs were designed and piloted by QuestUAV, a small company based in Amble, Northumberland, UK. Details of each site and dataset are given in the following.

4.3.1 Quest DATAhawk PPK Flights, Low Hauxley, Northumberland

Flights. In March 2017, four flights (three on 3/03/17 and one on 10/03/17) were undertaken with QuestUAV at a test site near Low Hauxley (LH), Amble, Northumberland, UK. These are hereafter referred to as LH2 Flights 1-4. These were performed with a Quest DATAhawk fixed wing UAV (Figure 4-2a) and flight specifications are given in Table 4-1. The DATAhawk is designed for a PPK workflow, enabling raw GPS data to be logged for post processing. The DATAhawk also has the capability to log GPS data on the ground for the implementation of ground logging periods and thus such periods of 10-15 minutes were implemented before and after each flight. Exact flight timings and durations in Coordinated Universal Time (UTC) are detailed in Table 4-2. However, because these flights were also for the experimental purpose of QuestUAV, image overlap was varied for each. Weather conditions on 3/3/17 for LH2 Flights 1-3 were overcast and fairly dim with wind speeds of 10 mph at 12 pm (Flight 1), which increased gradually to 13 mph by 3 pm (Flight 3). Weather conditions on 10/3/17 for LH2 Flight 4 were similar but with wind speeds staying at 10 mph.

GNSS reference station and ground target survey. A local GNSS reference station (*lhx0* – shown in Figure 4-2b) was set up about 300 m from the launch site for the GCP survey and generation of UAV GPS PPK positions. The coordination of the local GNSS reference station and processing of UAV GPS PPK positions is discussed in Chapter 5.

In total, 39 ground targets were surveyed on 10th March 2017 for use as either GCPs or check points. Targets comprised a mixture of spray-painted crosses on roads with c. 24 cm diameter (e.g. Figure 4-2c), plastic targets on grass with c. 40 cm diameter (e.g. Figure 4-2d) and painted targets on stone surfaces with c. 60 cm diameter (e.g. Figure 4-2e-f). Targets were surveyed using a relative GPS positioning strategy and Leica Infinity version 2.0 software and processed relative to the fixed coordinates of *lhx0* (as was also used for the processing of UAV PPK trajectories to ensure reference frame compatibility) resulting in baseline lengths of no more than 700 m. All ground targets were occupied for 3 minutes with a roving Leica GS10 receiver and AS10 antenna. GPS data was logged in 'static+kinematic' mode to ensure a continuous, long GPS observation duration and thus reliable integer ambiguity estimation. Rover data was thus continually logged for c. 5-hour duration (10:09 to 15:25 on 03.03.17). Five targets were re-occupied to provide a check at the end of the main survey with a 3D RMSE coordinate difference of 28 mm.

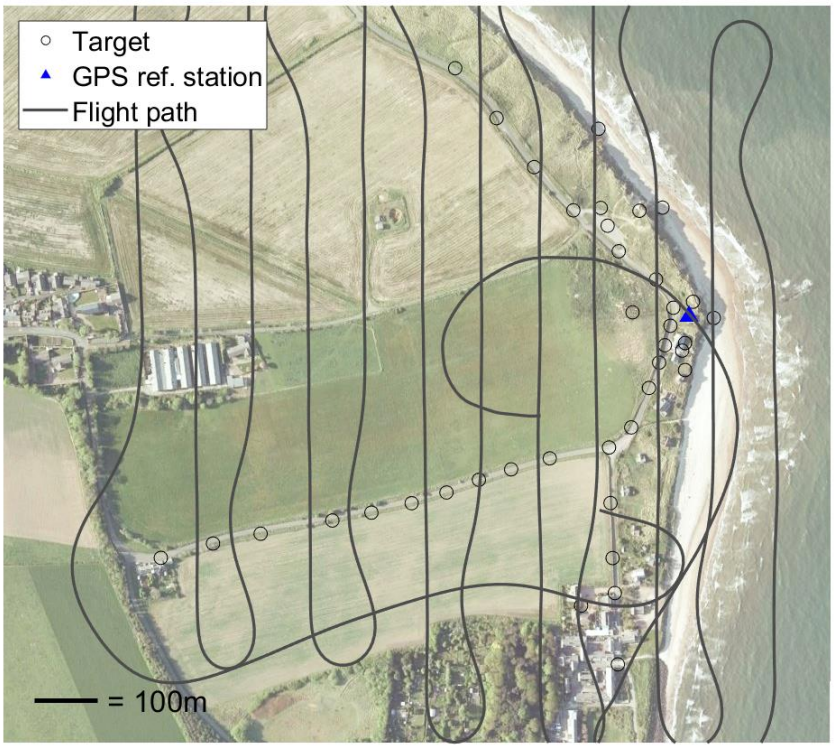

Figure 4-1. Low Hauxley site showing location of ground targets and the local GNSS reference station (with OS National Grid coordinates of E: 428660 m, N: 603143 m).

(a) Quest DATAhawk UAV

(b) lhx0

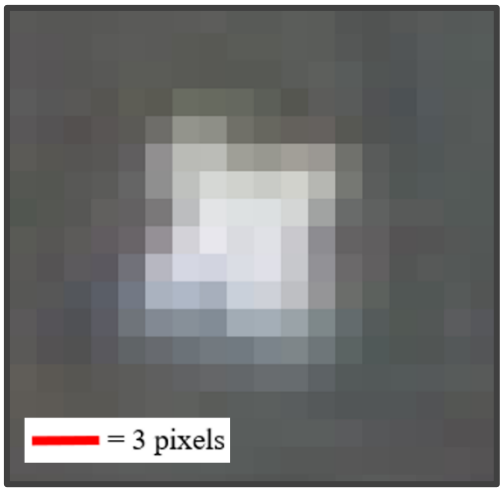

(c) Road cross

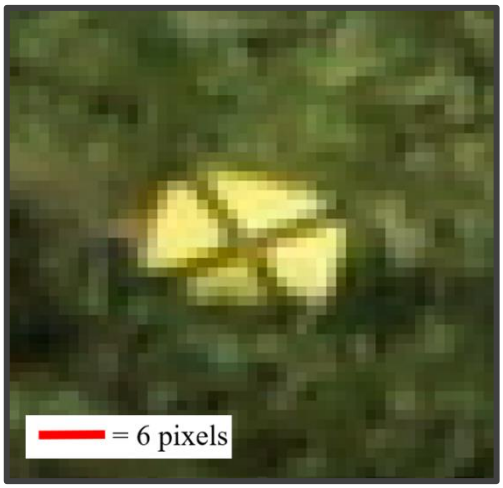

(d) Plastic target

(e) Painted target (beach)

(f) Painted target (wall)

Figure 4-2. The (a) UAV, (b) local GNSS reference station and (c-f) image projection of GCP targets at Low Hauxley.

Flight	CPF Flight 1	CPF Flight 2	CPF Flight 3	CPF Flight 4	LH1 Flight 1	LH1 Flight 2	LH1 Flight 3	LH2 Flight 1	LH2 Flight 2	LH2 Flight 3	LH2 Flight 4
Date	16/08/17	16/08/17	16/08/17	16/08/17	02/09/16	22/08/16	18/08/16	03/10/17	03/10/17	03/10/17	10/10/17
Flight duration	00:30:26	00:25:10	00:29:14	00:31:58	00:20:40	00:18:39	00:42:04	00:14:42	00:13:21	00:12:20	00:12:19
Overlap % (side / end)	80/70	80/70	80/70	80/70	80/70	80/70	80/70	80/60	80/50	80/40	80/50
GSD (cm)	3.0	3.0	3.0	3.0	3.0	3.0	3.0	3.2	3.2	3.2	3.2
Log rate	10 Hz	10 Hz	10 Hz	10 Hz	2 Hz	2 Hz	2 Hz	2 Hz	2 Hz	2 Hz	2 Hz
Images	691	663	732	826	476	423	505	340	277	197	233
Long / cross strips	18/1	18/1	18/2	18/2	15/0	16/0	12/4	14/0	11/0	8/0	13/0
Camera	ILCE6000	ILCE6000	ILCE6000	ILCE6000	ILCE6000	ILCE6000	ILCE6000	RX100M2	RX100M2	RX100M2	RX100M2
F (mm)	16	16	16	16	16	16	16	10.8	10.8	10.8	10.8
Lever arm vec. (cm)	[0 0 -12]	[0 0 -12]	[0 0 -12]	[0 0 -12]	[0 0 -12]	[0 0 -12]	[0 0 -12]	[0 0 -5]	[0 0 -5]	[0 0 -5]	[-6 -10 -5]
Acquired by	Newc. Uni	Newc. Uni	Newc. Uni	Newc. Uni	Quest	Quest	Quest	Newc. Uni	Newc. Uni	Newc. Uni	Newc. Uni
Comments	Missing images			Missing images	No IMU data					Missing images	

Table 4-1. Flight details

Flight	CPF Flight 1	CPF Flight 2	CPF Flight 3	CPF Flight 4	LH1 Flight 1	LH1 Flight 2	LH1 Flight 3	LH2 Flight 1	LH2 Flight 2	LH2 Flight 3	LH2 Flight 4
Date	16/08/17	16/08/17	16/08/17	16/08/17	02/09/16	22/08/16	18/08/16	03/10/17	03/10/17	03/10/17	10/10/17
Initiation time	07:44:00	09:09:40	10:23:45	11:41:30	-	-	-	13:12:13	14:20:13	15:24:13	12:10:43
Ground log 1	00:20:56	00:15:00	00:19:45	00:21:02	-	-	-	00:18:05	00:17:21	00:16:04	00:18:26
Flight duration	00:30:26	00:25:10	00:29:14	00:31:58	00:20:40	00:18:39	00:42:04	00:14:42	00:13:21	00:12:20	00:12:19
Ground log 2	00:13:51	00:18:35	00:15:46	00:19:08	-	-	-	00:14:05	00:16:30	00:45:32	00:23:48
Total log period	01:05:45	00:59:20	01:05:15	01:12:30	00:20:40	00:18:39	00:42:04	00:47:30	00:48:00	01:15:00	00:55:00

Table 4-2. Flight GNSS logging times in UTC time frame

4.3.2 Quest Q200 PPK Flights, Low Hauxley, Northumberland

Flights. In addition to the March 2017 datasets, QuestUAV also provided three archive datasets (acquired on 18/08/16, 22/08/16 and 02/09/16 by Quest UAV pilots) collected at the same test site. These are hereafter referred to as LH1 Flights 1-3. These flights were performed with a Quest Q200 fixed wing UAV and ground logging periods were not implemented. Weather conditions for LH1 Flight 1 (on 02/09/16) were clear skies with a 20 mph wind speed, for LH1 Flight 2 (on 22/08/16) were overcast with a 24 mph wind speed and for LH1 Flight 3 (on 18/08/16) were overcast with a 12 mph wind speed.

GNSS reference station and ground target survey. GNSS reference stations for these flights were operated by QuestUAV. For LH1 Flights 1 and 2, the reference station was located on the roof of the QuestUAV headquarters in Amble, Northumberland at c. 2 km away, whereas for LH1 Flight 3, it was located in approximately the same position as *lhx0*. The local GNSS reference stations were used only for the processing UAV GPS PPK positions as discussed in Chapter 5. Because ground targets were permanently marked, the surveyed coordinates determined in March 2017 were used.

4.3.3 Quest Q200 PPK Flights, Cockle Park Farm, Northumberland

Flights. In August 2017, four flights were undertaken at Cockle Park Farm (CPF), Northumberland, UK. Unlike the former datasets, these were acquired purely for the GPS PPP tests (and not also for QuestUAV experimentation). These were again performed with a Quest Q200 fixed wing UAV and flight specifications are given in Table 4-1. Ground logging periods of at least 15 minutes were included before and after each flight and pilots were instructed not to stand over or obstruct the UAV antenna as far as possible. Unfortunately, standard procedures still required the UAV to be launched at a high inclination (as shown in Figure 4-4f). Although all batteries were fully charged before each flight, flight durations varied from c. 25 - 32 minutes due the variable condition of each battery. Weather conditions for the flights were blue skies with broken cloud and wind speeds of 4 mph in the morning (Flight 1) which increased gradually to 13 mph by 12 pm (Flight 4).

GNSS reference station and ground target survey. A local GNSS reference station (*basb* – shown in Figure 4-4b) was again set up about 100 m from the launch site for the GCP survey and generation of UAV GPS PPK positions, as well as PPP control experiments. The coordinate of the local GNSS reference station and processing of UAV GPS PPK positions is discussed in Chapter 5.

In total, 40 ground targets were surveyed for use as either GCPs or check points. Targets consisted of rigid white, circular plastic plates, each 270 mm in diameter with a solid black, round inner target of 90 mm diameter. These were mounted on wooden stakes to ensure temporal stability and clear visibility above the grass surface (as seen in Figure 4-4a, and as appearing in the UAV imagery in Figure 4-4e-f). The ground targets were coordinated twice using a relative GPS positioning strategy and Leica Infinity version 2.0 software, once pre-flight on 15th August 2017 and again, as a check, post-flight on 16th August 2017. The rover data was processed relative to the fixed coordinates of the local GNSS reference station *basb*, resulting in baseline lengths of no more than 300 m. Rover data was continually logged for each c. 3-hour survey duration (10:35 to 14:29 on 15.08.17 and 13:42 to 15:39 on 16.08). The 3D RMSE coordinate difference for the 40 ground targets between the two surveys was 12 mm.

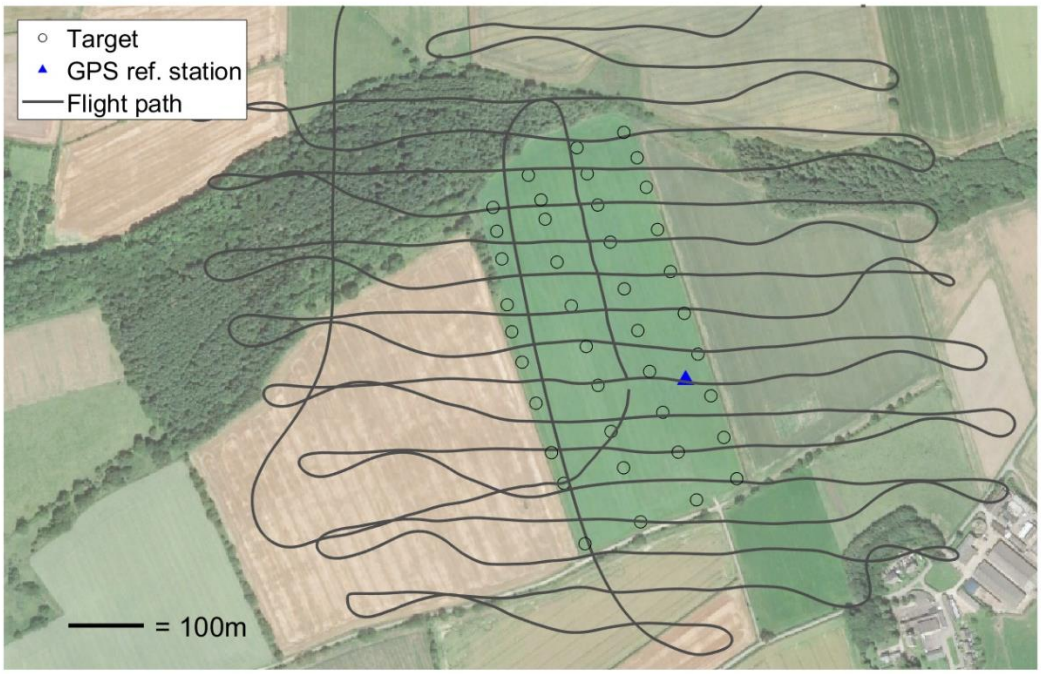

Figure 4-3. Cockle Park Farm site showing location of ground targets and the local GNSS reference station (with OS National Grid coordinates of E: 419811 m, N: 591465 m).

4.4 Summary

This chapter has overviewed the design of experiments for the implementation and assessment of the PPP-based photogrammetric workflow, along with the 11 fixed wing UAV datasets collected for investigation. To follow, Chapter 5 focuses solely on UAV-based PPP investigations, and Chapter 6 on the implementation of PPP-supported bundle block adjustments.

(a) Quest Q200 UAV

(b) basb

(c) Target design

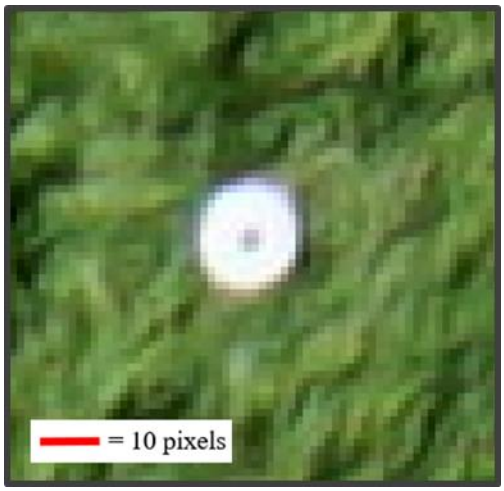

(d) UAV image projection (good)

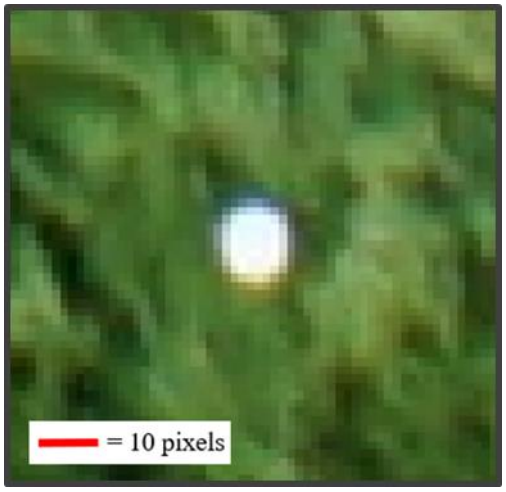

(e) UAV image projection (poor)

(f) UAV launch inlcination

Figure 4-4. The (a) UAV, (b) local GNSS reference station, (c) GCP target design, (d-e) image projection of targets and (d) Quest Q200 launch procedure at Cockle Park Farm.

Chapter 5. GNSS PPP UAV trajectory computation

5.1 Introduction

Chapter 4 overviewed the PPP-based workflows for the undertaking of large scale UAV photogrammetric mapping along with the GNSS datasets collected on board the 11 fixed wing UAV flights. This chapter focusses solely on UAV-based PPP investigations and aims to answer the following questions:

1. What PPP positional accuracies and precisions are achievable on short duration fixed wing UAV flights and what GNSS observation durations are required to achieve these?

2. Can ground logging periods assist PPP convergence for short duration UAV flights?

3. What improvements come with the processing of additional GLONASS observations?

These questions were investigated by assessing the accuracy of UAV PPP trajectories directly against reference PPK solutions. Experiments include (1) the processing of full UAV flight durations, (2) the processing of partial UAV flight durations, (3) the additional processing of pre and post-flight ground logging periods, and finally (4) repeats of (1) and (2) with the addition of GLONASS observations, as opposed to GPS-only. PPP control experiments are also performed for (1) and (3) at the CPF GNSS reference station for comparison.

This chapter first describes the employed PPP software, processing inputs and used settings, followed by the setup of PPK reference trajectories for PPP accuracy assessment. Coordinate systems are also discussed to ensure reference frame compatibility. Following this, the above experiments are implemented and discussed for the UAV datasets.

5.2 Determination of UAV PPP positions

5.2.1 Positioning And Navigation System Data Analyst (PANDA) software

Kinematic GNSS PPP processing was undertaken using the Positioning And Navigation System Data Analyst (PANDA) scientific software (Liu and Ge, 2003), developed at Wuhan University, China. The PANDA procedure for the estimation of rover (antenna) coordinates,

receiver clock, ambiguity and zenith tropospheric delay (ZTD) parameters on the basis of precise satellite orbit and clocks is as follows:

1. PANDA first marks GNSS observations of cycle slips using the TurboEdit approach of Blewitt (1990), which uses epoch differences of combinations of dual frequency carrier phase and P code pseudorange observations (wide lane and IF free, which are independent of non-dispersive delay errors).
2. Input satellite orbit and clock data are then temporally interpolated from their pre-tabulated values to the times corresponding to data epochs.
3. A least squares adjustment is then performed for parameter estimation in which interpolated orbit and clocks are fixed. This involves two sub-steps; firstly the estimation of time constant parameters by pre-eliminating the time varying parameters, and secondly, the back substitution of (estimated) time constant parameters for the estimation of time-varying parameters, hereafter referred to as back smoothing. These two steps comprise a single solution iteration. Time constant parameters include the ZTD and an ambiguity parameter per satellite. Additional ambiguities are included for satellites where respective cycle slips were found by the TurboEdit approach. Time varying parameters include the coordinates per epoch and receiver clock. Initial values for parameters are determined using GNSS code solutions.
4. After each solution iteration, the carrier phase residuals are screened for outliers, before re-iteration. The carrier phase outlier tolerance was initially set to be very relaxed, at 10 m, and thereafter reduced between subsequent solution iterations to 5 cm as parameter estimates improve. This prevents the early elimination of inlying carrier phase observations due to low accuracy parameter estimates.

This estimation approach ensures that all GNSS observations from the dataset contribute to the determination of parameters at each epoch, thus maintaining a similar accuracy throughout the computed trajectory. This aspect is important from a photogrammetric viewpoint, as it enables the determination of camera positions with a homogenous accuracy so that all such (camera position) observations may be weighted equally in the BBA.

The performance of PANDA has been documented in several recent studies, in both kinematic and static modes, in which the positioning results have been promising. Li *et al.* (2014) processed data from eleven, globally distributed, (static) reference stations in GPS-only static PPP mode (float ambiguity estimation is assumed as pre-calculated UPDs were not used). Processing in 24 hour batches, positioning accuracies better than 1 cm in all coordinate

components were achieved (average E|N|h errors were 0.50|0.29|0.89 cm over all stations). When further processing data from one of the GPS reference stations in kinematic PPP mode, mean coordinate accuracies over seven days of processing (i.e. mean of the seven RMSE statistics) were 1.99 cm, 1.21 cm and 6.11 cm in easting, northing and height coordinate components respectively. Convergence plots did not appear to show solutions to converge (i.e. stabilise) before 3-5 hours of data processing, although some improvement was indicated when processing both GPS and BeiDou data. Furthermore, although the authors did not indicate real time processing, the application of back smoothing was not specified, which could have improved the initial positioning accuracy. In another example, Penna *et al.* (2018) processed 13 days of GNSS data observed on an unmanned (dynamic) Wave Glider platform in kinematic PPP mode and achieved agreements (standard deviations) of 5-6 cm with ocean dynamic topography and geoid models. For control, 14 days of data from two onshore static GNSS reference stations were also processed in kinematic PPP mode, for which height precisions of c. 2 cm were achieved.

PANDA has also been employed with ambiguity fixing, in which cases UPDs (pre-calculated from processing a network of ground GNSS reference stations) are employed during PPP processing. Fang *et al.* (2014) processed 30 minutes of (1 Hz) data collected at four permanent GPS reference stations surrounding an earthquake event. Data was processed in PANDA in real time kinematic PPP mode and assessed against relative GPS solutions. Achieved standard deviations were 5.4-8.9 mm in horizontal and 23.1-26.6 mm in vertical coordinate components, which were concluded sufficient for the detection of seismic waves with an amplitude of 1 cm in plan and 2-3 cm in height. Geng *et al.* (2010a) also performed kinematic PPP with PANDA on a remote marine platform, where six hours of 1 Hz GPS data were processed over a 250 km trajectory. Using a relative GPS trajectory as reference, agreements (RMSEs) of 1.7-1.9 cm, 0.8-1.3 cm and 1.8-5.0 cm in easting, northing and height coordinate components respectively were achieved with float ambiguity estimation, whilst these values were improved to 0.6-0.8 cm, 0.5-1.0 cm and 2.6-3.2 cm with successful integer ambiguity resolution. However, for the latter, UPDs were pre-computed using a varied GNSS reference station network radius (i.e. 900 km, 2000 km and 3600 km) around east Asia. Results showed UPD estimates varied due to the different spatial coverage of each, which subsequently influenced the accuracy of kinematic PPP solutions at the centimetre-level. Ambiguity fixed PPP can thus be considered a more complex problem, compared to float ambiguity estimation.

These examples indicate the potential of PANDA software to perform both static and kinematic PPP with centimetre-level accuracy on a variety of platforms, thus confirming it as a suitable

software for UAV-based investigations with subsequent photogrammetric application. Ambiguity fixed applications, however, remain more complex given the requirement of UPDs to be pre-calculated from an extensive GNSS reference station network (e.g. Geng *et al.* (2010a)), in addition to the possibility of fixing ambiguities to incorrect integer values.

5.2.2 Orbits and clocks

In this work, 5 second clocks from the Centre for Orbit Determination in Europe (CODE) IGS Analysis Centre were used. 5 second over 30 second clocks were selected to reduce satellite clock interpolation (and subsequent positioning) errors, as was indicated by Bock *et al.* (2009) for kinematic applications. Guo *et al.* (2010) also showed improvements of 30-50% in some coordinate components when using 5 second over 5 minute clock rates. IGS clock products now typically entail an accuracy of 75 picoseconds, equivalent to a user range of c. 2 cm (IGS, 2018).

To be consistent with the CODE satellite clocks, 15 minute CODE final satellite orbits were used. As with the IGS final orbit product, they have an expected accuracy of 2.5 cm which is superior to the 3-5 cm accuracy of the Ultra-Rapid orbit product (IGS, 2018). The use of CODE products was further justified by their inclusion of both GPS and GLONASS data at the same rates, as opposed to GPS-only for the standard IGS products.

5.2.3 Antenna phase centre models

Antenna phase centre variation (PCV) models are used to account for the offset between the physical antenna reference point (ARP) and the electronic phase centre which varies with satellite elevation and azimuth (Hofmann-Wellenhof *et al.*, 2007). The antenna phase centre model itself comprises a constant offset value and an azimuth and elevation-dependent phase centre variation component. Unfortunately, antenna PCV models were not available for the UAV antennas. This was expected to predominantly influence the height component, with the potential for coordinate errors of up to 10 cm as detailed in Mader (1999). Such errors would likely propagate directly into the height component of photogrammetric object point determination in the absence of GCPs.

5.2.4 Ionospheric error

The ionosphere is a dispersive medium and its effects on the satellite signal are frequency dependent. The ionosphere causes an advance of the carrier phase (giving a shorter range estimation), and delay of the pseudorange (giving a longer range estimation) but by equal magnitude (Hofmann-Wellenhof *et al.*, 2007).

Ionospheric effects were mitigated in PANDA using the ionosphere-free (IF) linear combinations (LC) of dual frequency code and carrier phase observations, which eliminates first order signal delays in the carrier phase and pseudorange respectively. This is as follows (Leick *et al.*, 2015):

$$P_{if}^{s} = P_{l1}^{s}\left[\frac{f_{l1}^{2}}{f_{l1}^{2} - f_{l2}^{2}}\right] - P_{L2}^{s}\left[\frac{f_{l2}^{2}}{f_{l1}^{2} - f_{l2}^{2}}\right] \tag{5-1}$$

$$\Phi_{if}^{s} = \Phi_{l1}^{s}\left[\frac{f_{l1}^{2}}{f_{l1}^{2} - f_{l2}^{2}}\right] - \Phi_{L2}^{s}\left[\frac{f_{l2}^{2}}{f_{l1}^{2} - f_{l2}^{2}}\right] \tag{5-2}$$

Where P_{if}^{s} and Φ_{if}^{s} are the IF pseudorange and carrier phase observations respectively, f_x is the frequency of carrier signal x (i.e. L1 and L2) and P_x and Φ_x are the pseudorange and carrier phase observations respectively.

Thus, the observation equation becomes:

$$P_{if}^{s} = \sqrt{(X^s - X_r)^2 + (Y^s - Y_r)^2 + (Z^s - Z_r)^2} + c.d_r + T_j^i + d_{oth} \tag{5-3}$$

$$\Phi_{if}^{s} = \sqrt{(X^s - X_r)^2 + (Y^s - Y_r)^2 + (Z^s - Z_r)^2} + c.d_r + \lambda N + T_j^i + d_{oth} \tag{5-4}$$

as per, for example, Kouba and Heroux (2001), noting that the ionospheric delay, satellite orbit and satellite clock terms have been neglected due to their elimination (ionosphere) or modelling (orbits).

5.2.5 Tropospheric error

The tropospheric delay on a range measurement is modelled by the scaling of the zenith tropospheric delay (ZTD) by a satellite-elevation dependant mapping function. The ZTD comprises two components: a wet delay, accounting for 10% of the ZTD and a dry (or hydrostatic) delay accounting for 90% of the ZTD (Hofmann-Wellenhof *et al.*, 2007). The dry delay can be approximated by a model with a sufficient accuracy which prevents the need to estimate. The wet delay however, is more spatially and temporally variable, making it difficult to model and thus it is typically estimated as a parameter in the least squares adjustment (Herring, 1992; Lagler *et al.*, 2013). The ZTD is expressed as (Herring, 1992):

$$T_j^i = Tz_{dry}.M_{dry}\left(el_j^i\right) + Tz_{wet}.M_{wet}\left(el_j^i\right) \tag{5-5}$$

where Tz_{dry} and Tz_{wet} are the dry (modelled) and wet (estimated) zenith delay components (units are m), el_j^i is the elevation angle corresponding to satellite i at epoch j and M_{wet} and M_{dry} are the wet and dry mapping functions specific to the selected model. The Global Pressure and Temperature (GPT2) model of Lagler *et al.* (2013), together with the Global Mapping Function (GMF) of Boehm *et al.* (2006) was employed in PANDA with ZWD estimated as a constant for the duration of each (sub 1-hour) UAV flight, as it typically only varies by a few centimetres per hour (according to Kouba and Heroux, 2001). Additionally, only hourly ZWD parameters were estimated by Penna *et al.* (2018) for a dynamic ocean-based platform.

5.3 Summary of processing parameters

Final processing parameters used in PANDA are detailed in Table 5-1. It should be noted that satellite elevation cut-off angles are varied during PPP experiments, whilst for the troposphere delay, only the wet component was estimated, and the dry component modelled. The process noise on the coordinates was set to be very 'loose' at 25 m/$\sqrt{s}$ so their estimation between adjacent epochs was not constrained.

Parameter / Setting	**PPP (PANDA)**	**PPK (Leica Infinity)**
Sat. elevation cut off angle	5-15 degrees	5 degrees
Processing rate	CPF flights - 10 Hz LH1 flights - 2 Hz LH2 flights - 2 Hz	CPF flights - 10 Hz LH1 flights - 2 Hz LH2 flights - 2 Hz
Antenna phase centre model	IGS14 (but none for the UAV)	IGS14 (but none for the UAV)
Tropospheric delay	Estimated	VMF with GPT2 model
Ionospheric delay	Ionosphere free LC	Automatic
Precise orbit / clock product	CODE	CODE (orbits only)
Ambiguity solution	Float	Fixed
Process noise	Coordinates: 25 m/$\sqrt{s}$ Receiver clock: white noise	n/a
Observation weights (phase/code)	GPS: 2 cm / 2 m GLONASS (when used): 2 cm / 2 m	n/a

Table 5-1. GNSS processing parameters

5.4 Determination of reference UAV PPK positions

5.4.1 Leica Infinity software

To assess the accuracy of the GNSS PPP positions on the UAV, reference trajectories were computed by processing the GNSS data from each flight in GPS PPK mode, relative to the local GNSS reference station. A local GNSS reference station was therefore established in each

survey area, ensuring short baselines, in all cases not exceeding 1 km, to facilitate the differencing away of tropospheric and ionospheric refraction and the fixing of integer double differenced ambiguities. GPS PPK processing was undertaken in Leica Infinity commercial software with the processing settings listed in Table 5-1. Although the Leica Infinity algorithms are proprietary, routines employed are assumed to be as discussed in Chapter 3. It should also be noted that Leica Infinity allows the output of positions at the full UAV logging rate, despite having a lower logging rate at the GNSS reference station. For example, for the CPF flights, the local GNSS reference station only logged at 5 Hz, whilst the UAV logged at 10 Hz. From correspondence with Leica, this is because Leica Infinity applies an interpolation scheme based on the original RINEX data (and not the processed positions), although the exact algorithmic details are proprietary and were not shared. This is also discussed in Grayson *et al.* (2018).

5.4.2 Setup of local GNSS reference stations

The PPK positioning coordinate reference frame is defined by the frame of the fixed GNSS reference station. This differs from the PPP approach, whereby the frame is defined by the fixed satellite orbits. As satellite orbits were in IGS14, the GNSS reference stations also needed to be positioned in IGS14. This could be done by determining GNSS reference station coordinates also by PPP, as per the UAV, but because GNSS reference station observation durations were limited to between one and eight hours, this would likely result in PPP solutions being biased by time-of-day satellite geometry effects (e.g. Marques *et al.*, 2018) which vary over the course of a sidereal day (approximately 23 hours 56 minutes). GNSS reference station observation durations were, however, long enough to enable the convergence of PPP ambiguities (e.g. Cai and Gao, 2013).

The approach applied here was to process long term observations in kinematic GPS PPP mode (and hence in the same IGS14 reference frame) for the closest IGS reference station (MORP) to ensure the averaging out of sidereal day repeat geometry effects. Subsequently, processing each local reference station relative to the determined IGS reference station coordinates would ensure that each was coordinated in IGS14 without biasing the reference coordinates by any time-of-day satellite geometry effects.

Cockle Park Farm Reference Station. For the CPF flights, a local GNSS reference station named *basb* (comprising a Leica GS10 receiver with AS10 antenna logging both GPS and GLONASS observations) was established in the central grass field (see Figure 4-2), logging at 5 Hz from 09:12 to 13:36 UTC on 15th August 2017 and then from 07:01 to 15:08 UTC on 16th August 2017. The eight hours of observed reference station GNSS data acquired at *basb* on 16th

August 2017 were processed with Leica Infinity relative to IGS reference station MORP, conveniently located only 600 m away. As discussed in the above paragraph, the coordinates of MORP were themselves determined by averaging 48 hours of kinematic GPS PPP positions processed by the same method as used for the UAV (and hence in the same IGS14 reference frame defined by the CODE satellite orbits). Thus *basb* was coordinated in the frame of the satellite orbits, and using the same kinematic processing method as for the UAV (rather than the conventional static approach) ensured complete compatibility with the UAV GNSS kinematic PPP positions for evaluation purposes. Unlike for the UAV, PCVs were modelled for the Leica AS10 antenna, according to the IGS14 models.

Low Hauxley Reference Station – 3rd and 10th March 2017. For the Low Hauxley flights, a local GNSS reference station named *lhs0* (again comprising a Leica GS10 receiver with AS10 antenna logging both GPS and GLONASS observations) was established to the east of the test site (see Figure 4-1) logging at 5 Hz from 10:07 to 15:09 UTC on 3rd March 2017 and then from 09:26 to 15:27 UTC on 10th March 2017. The c. 5 and 6 hours of reference station GNSS data acquired on 3rd and 10th March 2017 respectively were again processed with Leica Infinity relative to IGS reference station MORP, this time located c. 35 km away. The coordinates of MORP were themselves determined by a similar method to before, but this time averaging eight days of kinematic GPS PPP positions spanning the intervening time period between the two *lhs0* occupations (i.e. 00:00 to 24:00 UTC on 3-10th March 2017). The coordinates determined for the two *lhs0* occupations were then averaged. This ensured *lhs0* was also coordinated in the IGS14 reference frame defined by the CODE satellite orbits. Unlike the UAV, PCVs were modelled for the Leica AS10 antenna, according to the IGS14 models.

Low Hauxley Reference Station – 2nd September, 22nd and 18th August 2016. Unlike the 2017 Low Hauxley flights, the three 2016 datasets were acquired solely by QuestUAV, using their own local GNSS reference stations. For LH1 Flights 1 and 2 (on 2nd September and 22nd August, respectively) the local GNSS reference station, named *ambl*, was located on the roof of the QuestUAV headquarters in Amble, Northumberland, creating baselines of c. 1.9 km to the UAVs. These local GNSS reference stations were logged at 5 Hz from 11:11 to 16:32 UTC on 2nd September 2016 (c. 5h 21m) and from 09:56 to 13:28 UTC on 22nd August 2016 (c. 3h 52m). For LH1 Flight 3 (on 18th August 2016), the local GNSS reference station, named *lhxs*, was located at approximately the same location as *lhs0* and logged from 14:59 to 15:49 UTC on 18th August 2016.

The c. 1, 4 and 5 hours of local GNSS reference station data (i.e. acquired on 18th and 22nd August and on 2nd September 2016 respectively) were processed with Leica Infinity relative to IGS reference station MORP located c. 35 km away. However, rather than reprocessing the coordinates of MORP, the same kinematic GPS PPP-determined coordinates were used as for the March 2017 flights because the same GCP coordinates were to be used during subsequent photogrammetric processing. This again ensured *lhs0* was coordinated in the IGS14 reference frame defined by the CODE satellite orbits, albeit with a slightly reduced accuracy (noting the expected X/Y/Z MORP coordinate velocities of 1.3/1.6/1.0 cm/year due to European plate tectonic movement in the IGS14 reference frame). Furthermore, as with the UAV, PCVs were not modelled as they possessed the same antenna as the UAV, for which no IGS PCV models were available.

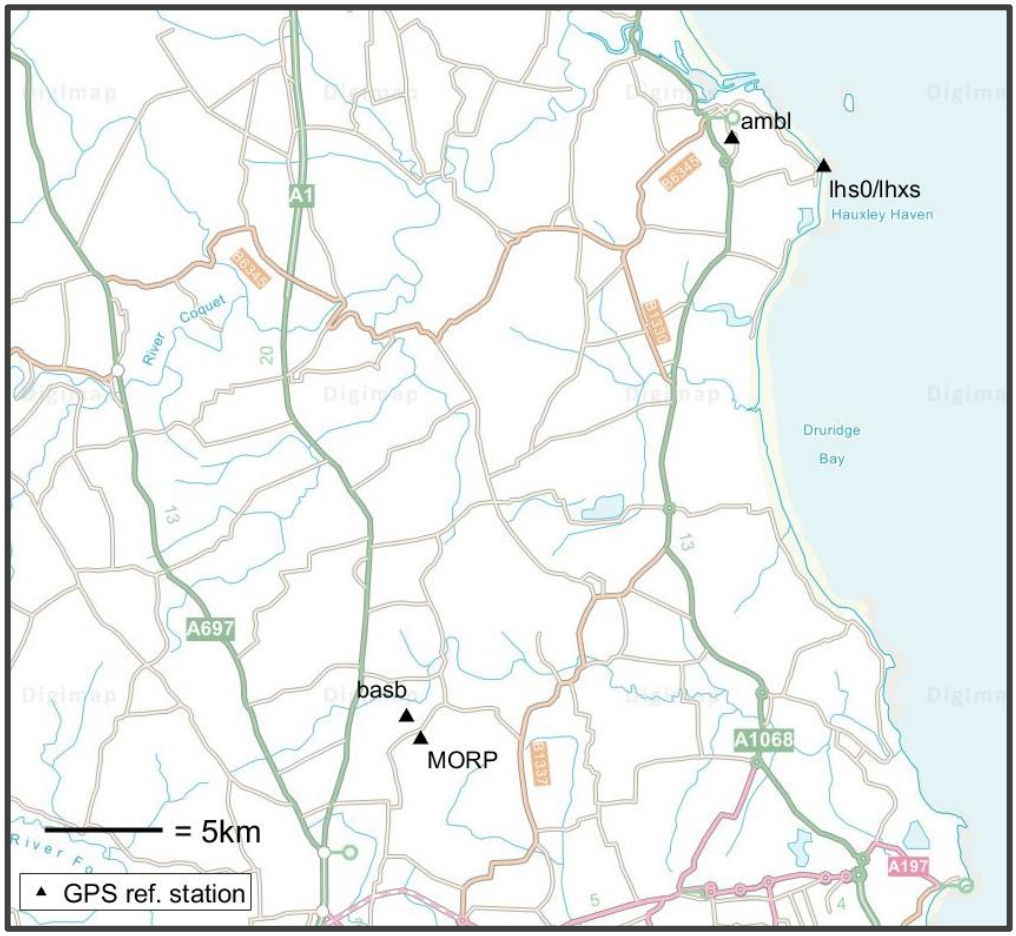

Figure 5-1. GNSS reference station locations in Northumberland

5.4.3 Local map projection

Rather than evaluating trajectories in IGS14 Cartesian geocentric coordinates, trajectories were projected into a local coordinate system for analysis in local easting, northing and height. Because all data collection was undertaken in the UK, coordinates were projected into the

British National Grid with use of the Grid Inquest tool provided by the Ordnance Survey (OS, 2018). This projection was also consistent with later photogrammetric analysis.

5.4.4 Reference station coordinates

To verify the local reference station coordinates for all sites for quality control purposes, the GPS data was processed in kinematic GPS PPP mode (as per the UAV). Final reference station PPP-PPK coordinate differences are presented in Table 5-2, with different occupations of the same reference station denoted by their respective occupation day of year (DOY). Values are generally c. 1-2 cm in all coordinate components. However, exceptions include offsets of c. 12 cm and 15 cm in the easting and height coordinates of GNSS reference station *lhxs* on DOY 231. Because only one hour of GNSS reference station data was held for *lhxs* this was likely to result from a bias in the PPP solution.

Ref. stn. (DOY)	**Obs. duration (hours)**	**PPP minus rel. GPS difference (m)**		
		E	**N**	**h**
lhxs (231)	1.0	0.124	0.030	-0.159
ambl (235)	5.4	-0.054	-0.009	-0.002
ambl (246)	5.9	-0.010	-0.012	0.014
ambl (062)	4.7	-0.009	-0.006	0.015
lhs0 (062)	5.0	-0.014	-0.012	-0.022
lhs0 (069)	6.0	-0.017	-0.009	-0.013
basb (228)	11.4	0.015	0.001	0.003

Table 5-2. Final reference station PPP-PPK coordinate differences for quality control

Additionally, a c. 5 cm offset exists in the easting of *ambl* on DOY 235, which is again likely to result from a bias in the PPP solution (also noting that comparing the *ambl* DOY 235 coordinates to both the PPP and PPK coordinates for *ambl* DOY 246 yielded a difference of only c. 4 cm in easting coordinate). Due to the similarity of solutions for *ambl* on DOY 235 and 246, these were combined. The *ambl* GNSS reference station receiver monument is shown in Figure 5-2.

Figure 5-2. Monument for GNSS reference station *ambl* located at the QuestUAV headquarters in Amble

5.5 DOP measures of satellite geometries

As PPP ambiguity estimation is highly impacted by receiver-satellite geometries, Dilution of Precision (DOP) values are used in subsequent investigations to quantify such effects over processed epochs (Leick *et al.*, 2015). DOP values were calculated as functions of the coordinate precision estimates from the covariance matrix of the parameters and may be separated into horizontal (HDOP), vertical (VDOP) and positional (PDOP) DOP values as follows (Leick *et al.*, 2015):

$$VDOP = \sqrt{\sigma_h} \tag{5-6}$$

$$HDOP = \sqrt{\sigma_e + \sigma_n} \tag{5-7}$$

$$PDOP = \sqrt{\sigma_e + \sigma_n + \sigma_h} \tag{5-8}$$

where σ_e, σ_n and σ_h are the estimated easting, northing and height coordinate precisions respectively, obtained from the covariance matrix of the parameters. DOP is strongly related to the number and spatial distribution of satellites (Zhang *et al.*, 2014; Marques *et al.*, 2018). As satellite geometries get weaker (e.g. closer together), elements of columns of the design matrix become increasingly linearly dependent and subsequently DOP values increase as coordinate precision estimates degrade.

5.6 Results: Flight only processing

5.6.1 GPS control tests

Before processing the UAV flights, a control experiment was undertaken using GNSS reference station data collected at Cockle Park Farm. Firstly, as a check on the PPP processing, the full duration of observed reference station (*basb*) data (c. 4.5 hours on DOY 227 and c. 8 hours on DOY 228) was processed in kinematic PPP mode using GPS observations only, and compared to the known coordinates, determined with relative GPS as discussed in Section 5.4.2. Following this, to mimic the shorter, c. 30 minute UAV flights, the same data was processed in 30 minute blocks. Figure 5-3 shows the coordinate errors for the full duration processing (red line) and 30 minute blocks (blue line) for solutions on both DOY 227 and 228, as well as indicating the GNSS observation windows for CPF Flights 1-4 with dashed lines. Further to this, Table 5-3 presents the mean coordinate differences (from the known reference station coordinates) and standard deviations for both PPP solutions. Solutions were calculated with a 5 degree satellite elevation cut-off angle.

From Figure 5-3 and Table 5-3, it is evident that processing the full duration of observed reference station data results in only a very small solution bias (mean coordinate difference from the known reference station coordinates) of 14 mm, 3 mm and 2 mm in easting, northing and height coordinates respectively. Full duration standard deviations are also only c. 1 cm and c. 2 cm in plan and height coordinates respectively, whilst Figure 5-3 shows that coordinate error magnitudes do not exceed 5 cm in any component. This confirms the good performance of PANDA PPP with observation durations of many hours.

When processing the same data in 30 minute blocks to mimic the UAV flight durations, coordinate error magnitudes show greater variation, and now peak at c. 60 cm, c. 20 cm and c. 70 cm in easting, northing and height coordinates respectively (Figure 5-3). The variation between each block, shown by the coordinate jumps, is reflected in the overall standard deviations, which, compared to the full duration processing, increase from 0.9-20.1 cm, 1.0-8.5 cm and 1.8-18.1 cm in easting, northing and height coordinates respectively (Table 5-3). The solution bias, however, remains at the centimetre-level, and whilst some coordinate errors now exceed 60 cm (e.g. 10.5 to 11 hours on DOY 227 and 228), many are better than 5-10 cm (e.g. 8.5 to 9 hours on DOY 228).

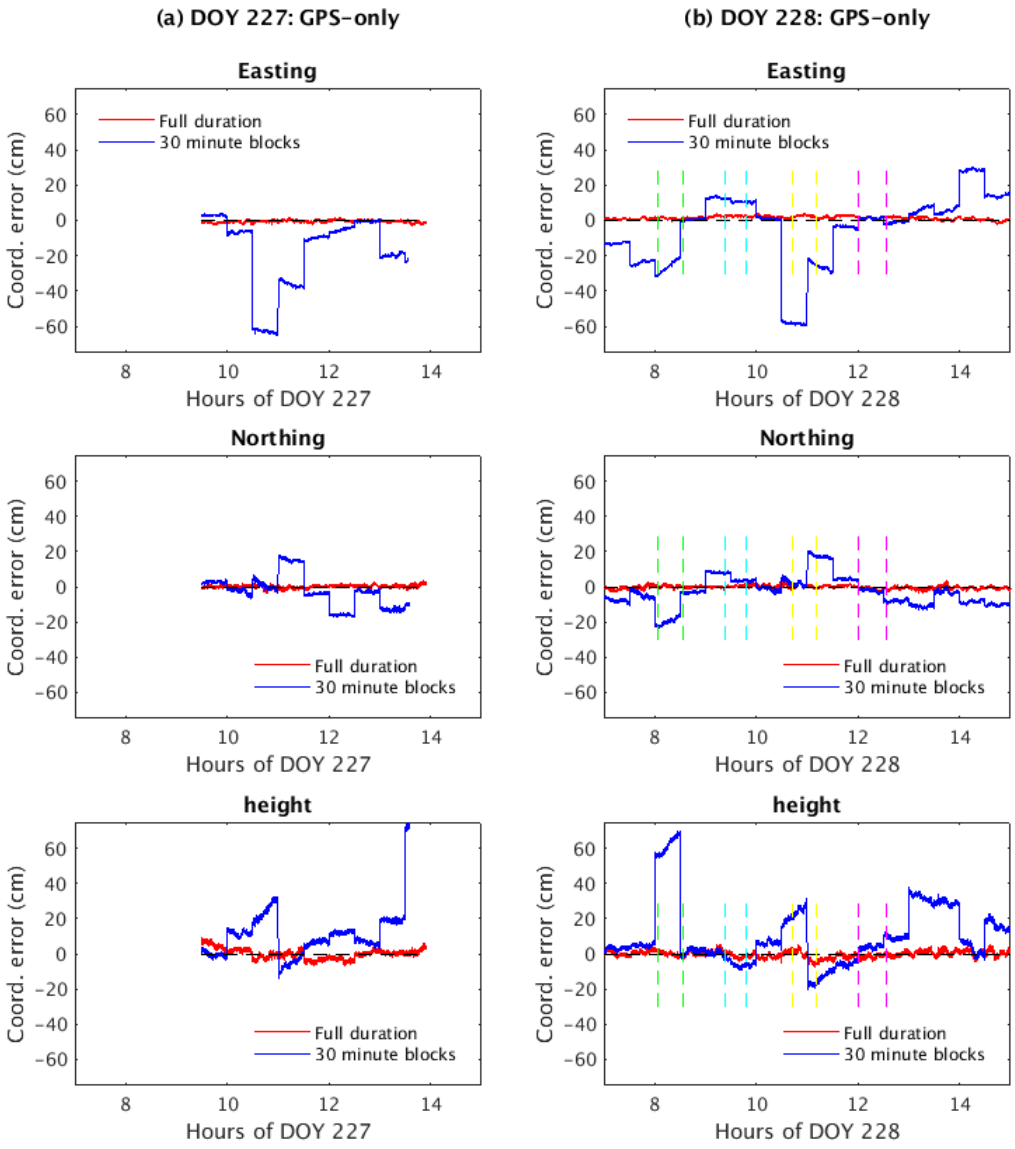

Figure 5-3. GPS PPP errors for the CPF reference station on (a) DOY 227 and (b) DOY 228. Processed as the full duration (red line) and in 30 minute blocks (blue line), with a satellite elevation cut-off angle of 5 degrees. GNSS observation windows for CPF Flights 1-4 are indicated by the green, cyan, yellow and magenta dashed lines, respectively.

Proc. Strat.	Mean diff. (cm)				Std Dev (cm)			
	E	N	h	3D	E	N	h	3D
Full	1.4	-0.3	-0.2	2.5	0.9	1.0	1.9	1.0
30 min	-4.5	-2.7	10.4	24.4	20.3	8.6	18.2	18.8

Table 5-3. Mean and standard deviation of the GPS PPP errors for the CPF reference station, processed as the full duration ('Full') and in 30 minute blocks ('30 min').

To help explain the variable coordinate errors for the 30 minute blocks, Figure 5-4 presents the number of satellites and DOP values throughout the CPF reference station observation period. This shows the number of satellites and DOP values to be interdependent. For example, at c. 10.5 hours on both DOY 227 and 228, satellite numbers drop to less than 9 whilst the PDOP exceeds a value of 2. When comparing Figure 5-4 with Figure 5-3, it is further seen that this PDOP spike (and drop in satellite numbers) at c. 10.5 hours corresponds with greater coordinate errors for the 30 minute block processing, for example exceeding 60 cm in the easting coordinate component. This is attributed to the estimation of the ambiguities not having fully converged to their correct values (as is discussed in section 5.6.3) when there are lower numbers of satellites and higher PDOPs and only 30 minutes of data.

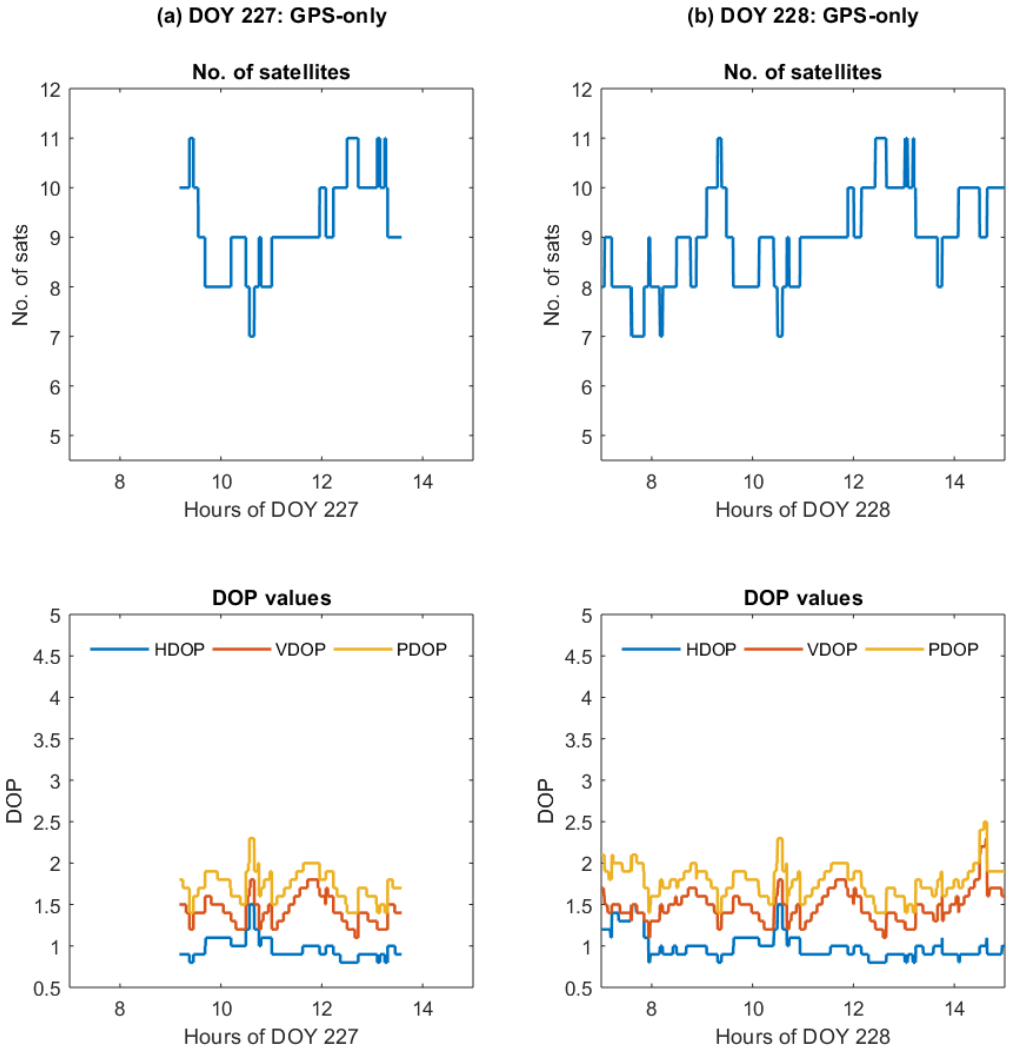

Figure 5-4. Satellite numbers and DOP values for observations made at the CPF reference station on DOY 227 and 228. Calculated in RTKlib software with a 5 degree satellite elevation cut-off angle.

The 30 minute blocks, however, do perform well when there is a higher number of visible GPS satellites. For example, from c. 9-10 hours on both DOY 227 and 228, coordinate errors are c. 10 cm or less, which coincides with 9-11 satellites being in view. Additionally, from c. 12-13 hours on both DOY 227 and 228, coordinate errors are again c. 10 cm or less which coincides with 9-10 satellites being in view. In these case, the estimation of the ambiguities have fully converged to their correct values due to there being higher numbers of satellites and higher PDOPs. Comparing the trends in Figure 5-4 (and Figure 5-3) on DOY 227 and 228 indicates that the DOP values and satellite numbers repeat themselves, which provides confirmation of expected repeat GPS satellite geometry effects. As the GNSS observation windows for CPF Flights 1-4 in Figure 5-3 correspond with variable error magnitudes at the reference station (and thus variable satellite geometries), it is expected that results for the c. 30 minute or less UAV flight will be equally susceptible to the effects of time-of-day GPS satellite geometry effects.

In summary, these control experiments suggest that for kinematic GPS PPP to provide decimetre-level, converged solutions from 30 minutes of data, then nine or more satellites and/or a PDOP of under 2 are needed.

5.6.2 Full flight processing

Having analysed data at the static reference station, the full duration of each UAV flight was processed in GPS PPP mode and coordinate differences were calculated with respect to reference GPS PPK trajectories. Figure 5-5 illustrates these differences per epoch for CPF Flights 1 to 4. In addition, the mean and standard deviation of the GPS PPP minus PPK differences for all datasets are presented in Figure 5-6 with satellite elevation cut-off angles of 5, 10 and 15 degrees.

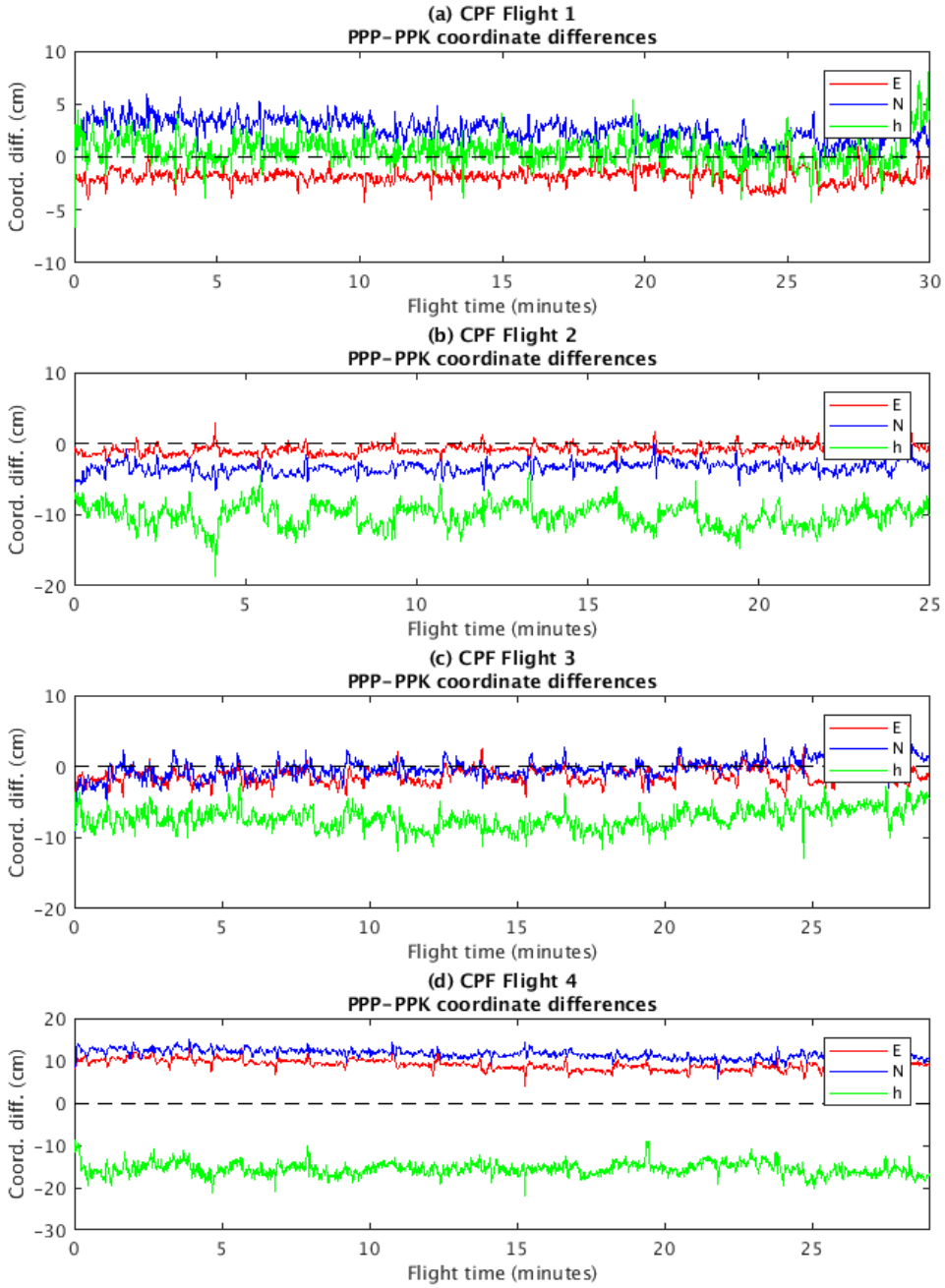

Figure 5-5. GPS PPP minus PPK coordinate differences for antenna trajectories from CPF Flights 1-4. Shown for a satellite elevation cut-off angle of 5 degrees.

As GPS PPK trajectories are assumed to exhibit a 2-3 cm accuracy, the GPS PPP minus PPK differences are assumed to represent GPS PPP coordinate errors. Figure 5-5 shows that coordinate errors are at most c. 20 cm in any component and for any CPF flight (results for CPF Flights 2 and 3 are also presented in Grayson *et al.* (2018)). For all flights, coordinate errors are seen to fluctuate by around 5 cm with no obvious outliers. Such coordinate errors are thus suggestive of GPS PPP coordinate biases. Similar-natured results are also shown for the other flights in Figure 5-6. For example, coordinate errors for solutions with a 5 degree satellite elevation cut-off angle range between c. 2 cm and c. 30 cm in planimetry and c. 1 cm and

c. 50 cm in height. However, median values are 0.9 cm, 1.6 cm and 10.3 cm in easting, northing and height respectively which is quite promising. The small magnitude of coordinate precisions, typically c. 1-2 cm and 1-4 cm in plan and height respectively, relative to the respective mean coordinate errors, is again suggestive of GPS PPP coordinate biases, as illustrated in Figure 5-5.

Figure 5-6 shows that increasing the satellite elevation cut-off angle from 5 to 10 degrees has little effect on coordinate errors, with variable improvements and degradations of c. 1 cm among different flights. This indicates that such a transition results in little change to the processed observations (or in some cases no change). However, when increasing the satellite elevation cut-off angle further to 15 degrees, the effects on coordinate errors are more substantial, particularly in the height coordinate. For LH2 Flight 4, the height coordinate error undergoes a two-fold increase (to c. 90 cm) compared to corresponding values with a 5 and 10 degree satellite elevation cut-off angle. Additionally, for CPF Flight 1, the transition from a 10 to 15 degree value results in a height coordinate error increase from c. 1 cm to c. 19 cm. Plan coordinate errors, however, are relatively unaffected by this change. These results are indicative that smaller satellite elevation cut-off angles should be used to reduce height coordinate errors, and hence a value of 5 degrees is adopted hereafter. The UAV receiver environment lends itself to such a processing strategy because of its open environment.

DOP values. Changing the satellite elevation cut-off angle has the effect of changing the observed satellite geometries, to which the accuracy of kinematic PPP solutions is known to be highly sensitive (e.g. Zhang *et al.*, 2014; Marques *et al.*, 2018) and as was indicated by the CPF GPS control experiment at the reference station. This can explain the varied coordinate errors per satellite elevation cut-off angle in Figure 5-6.

To compare observed satellite geometries between flights, satellite numbers and DOP values per epoch (computed in RTKlib software with a 5 degree elevation cut-off angle) are presented in Figure 5-7, Figure 5-8 and Figure 5-9 for CPF, LH1 and LH2 flights respectively. The generally larger height than plan coordinate errors among all flights can be attributed to the inherent satellite geometric distribution for which range errors directly propagate into the estimated heights. This is reflected by the substantially (c. 2 times or more) larger VDOP over HDOP values illustrated in Figure 5-7 to Figure 5-9. These figures also indicate the high sensitivity of DOP values to changes in satellite numbers (as was also shown by the CPF GPS control experiment), which occur frequently throughout each flight. Comparing the DOP values to Figure 5-5, the slightly larger PDOP for CPF Flight 4 (of c. 1.8 after launch compared to c. 1.5-1.6 for the other three flights) may explain the slightly larger coordinate errors for this flight.

However, Figure 5-6 shows substantially larger PDOP values for LH1 Flight 1 (of c. 2.3) compared to those of LH1 Flight 2 (of c. 1.5), yet coordinate errors are much smaller (i.e. c. 3 cm compared to c. 25 cm). Consequently, such DOP values do not explain the difference between coordinate errors over all flights.

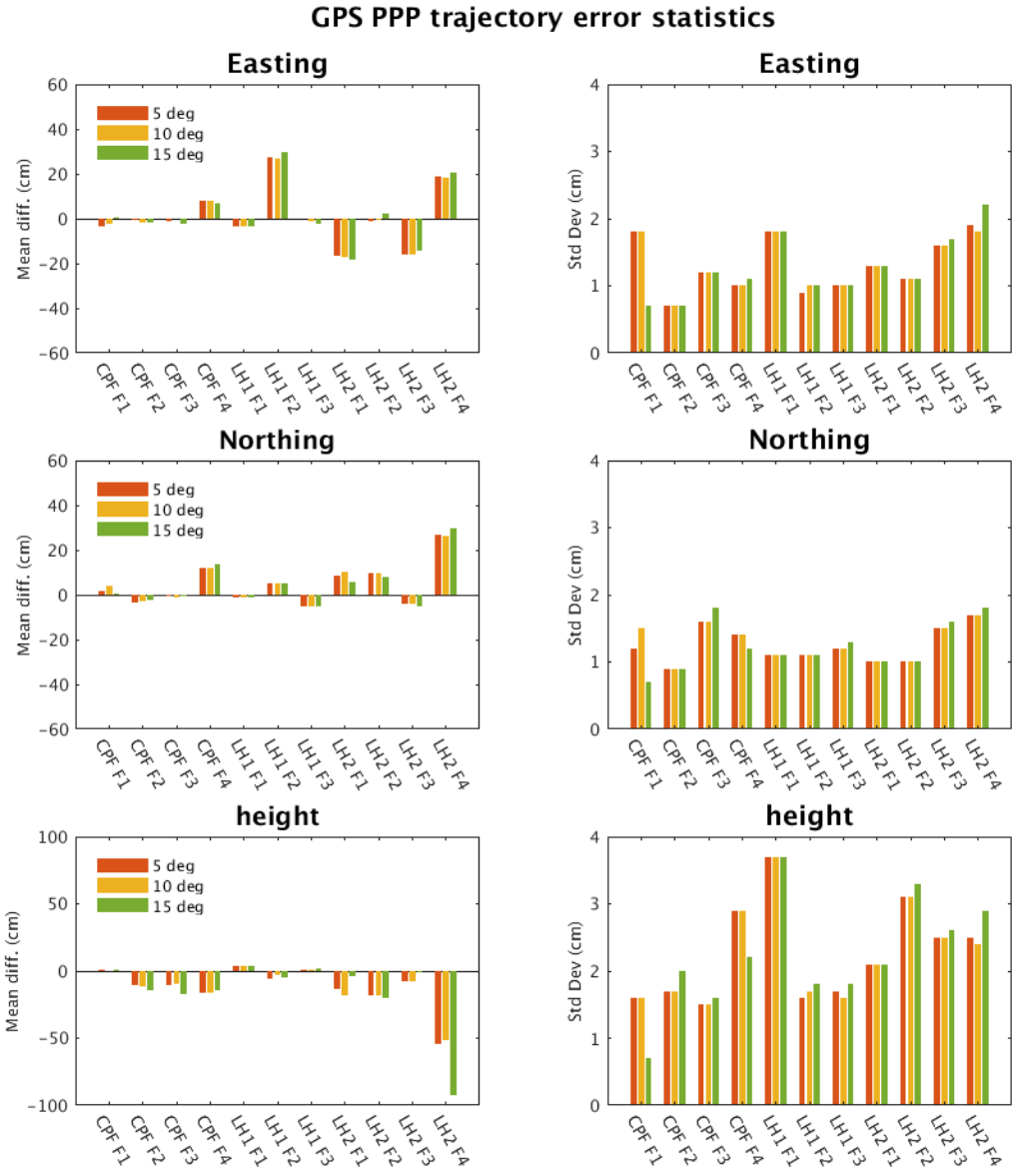

Figure 5-6. Mean and standard deviation of the GPS PPP minus PPK differences with satellite elevation cut-off angles of 5, 10 and 15 degrees.

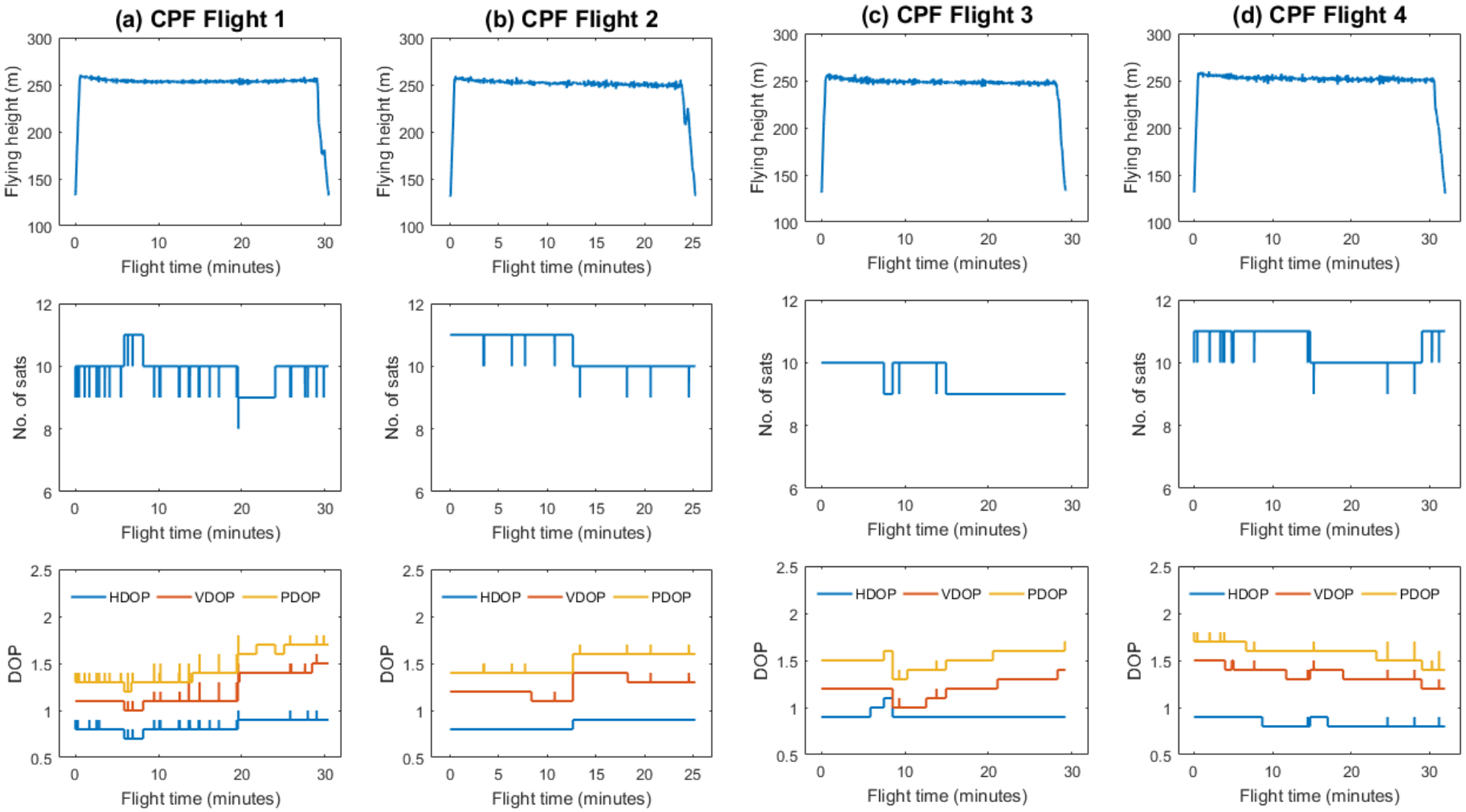

Figure 5-7. Satellite numbers and DOP values for CPF Flights 1-4. Calculated in RTKlib software with a 5 degree satellite elevation cut-off angle.

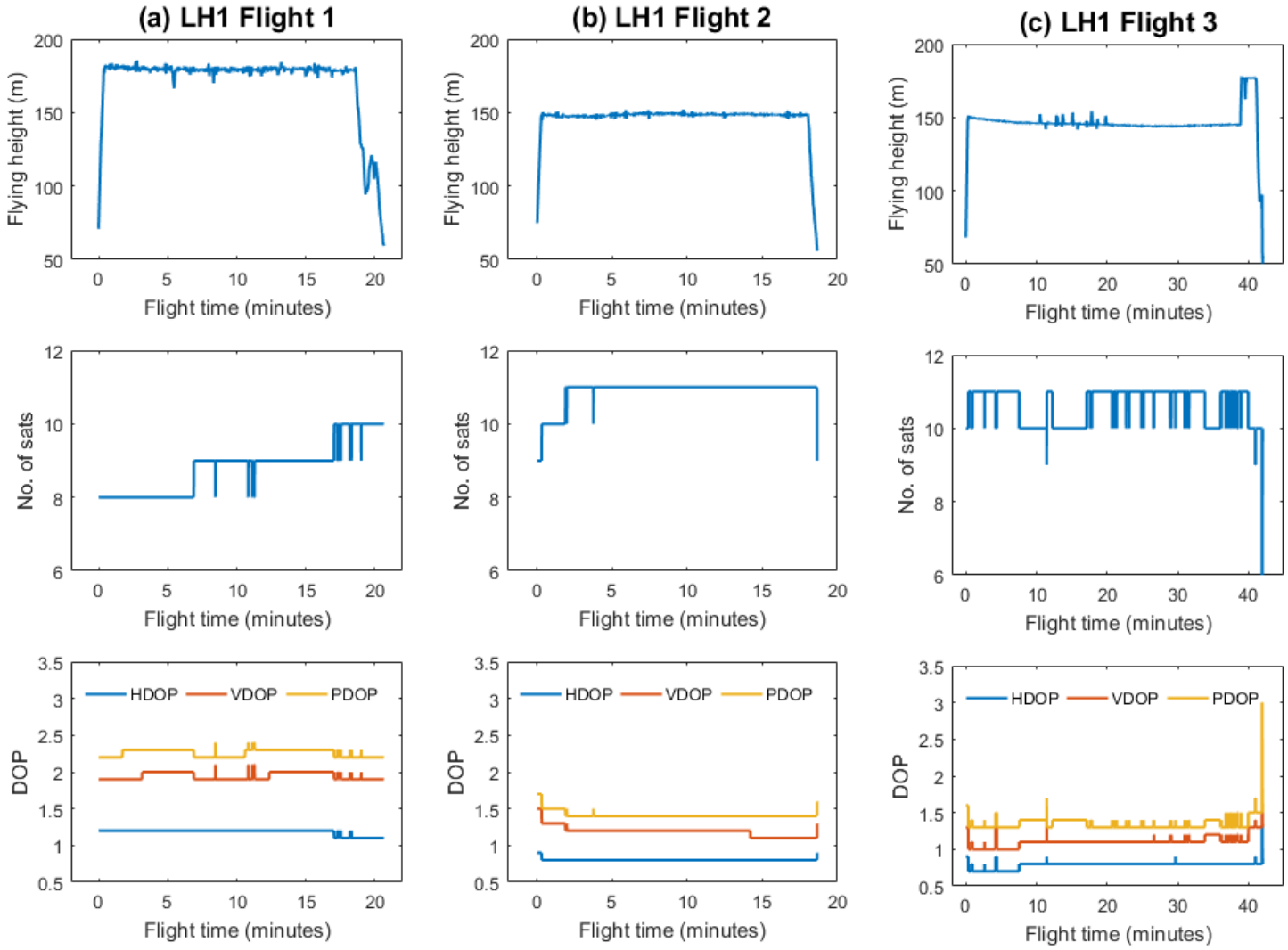

Figure 5-8. Satellite numbers and DOP values for LH1 Flights 1-3. Calculated in RTKlib software with a 5 degree satellite elevation cut-off angle

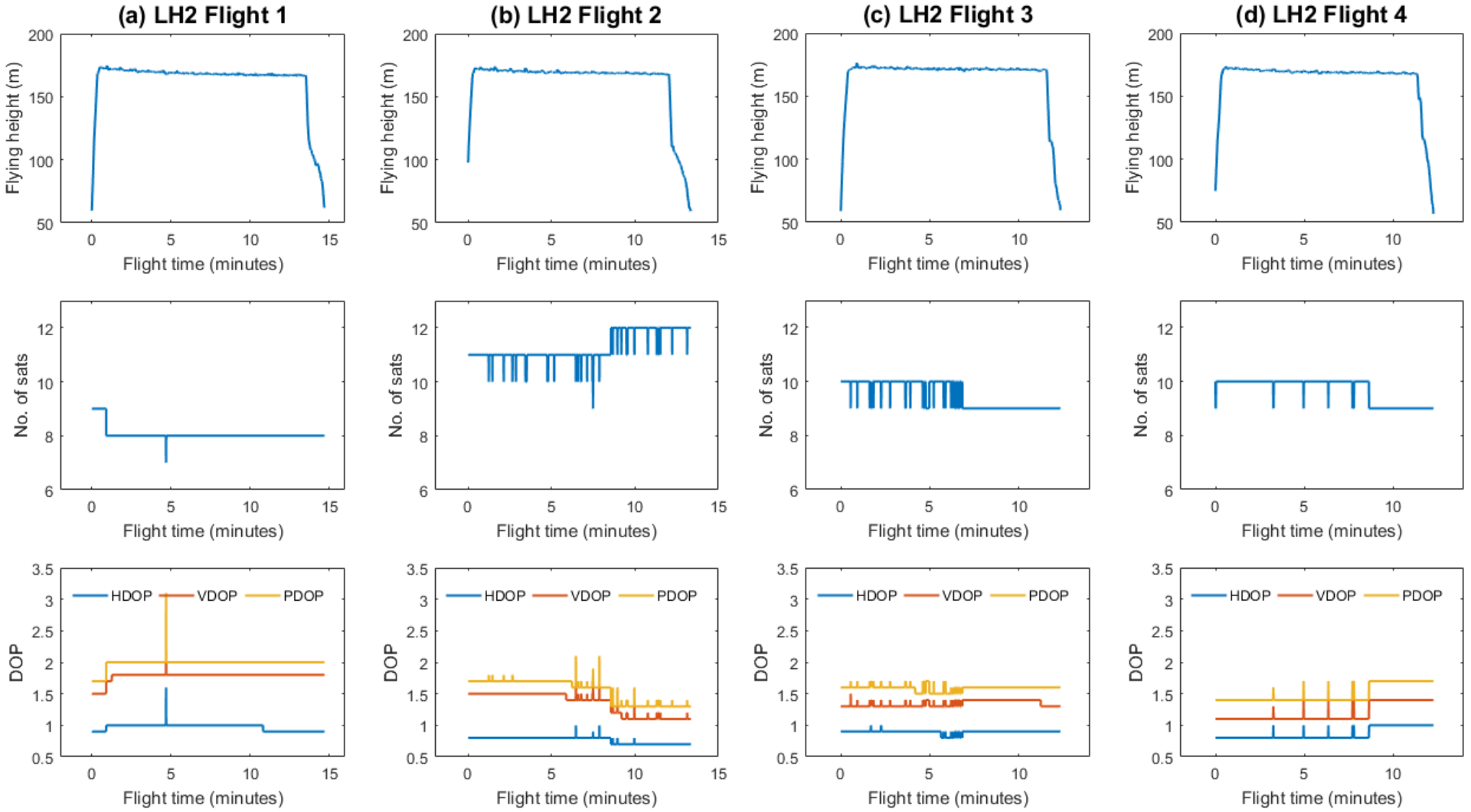

Figure 5-9. Satellite numbers and DOP values for LH2 Flights 1-4. Calculated in RTKlib software with a 5 degree satellite elevation cut-off angle

Observation duration. It is also known that the accuracy of kinematic PPP solutions highly depends on satellite geometries changing sufficiently such that ambiguity parameters can be accurately estimated. Figure 5-10 plots the mean coordinate errors (as presented in Figure 5-6 with a 5 degree satellite elevation cut-off angle) against the respective duration of GPS observations used for their computation. The term *processing duration*, is hereafter used to denote the duration of continuously tracked satellite data without interruption that has been processed in the final trajectory solution. This could be equivalent to the complete flight duration, as below in Figure 5-10, or a specified processing window within, as seen in the next section. Figure 5-10 shows a general trend of increasing coordinate errors with reducing flight durations (and thus GPS processing duration). However, variation in coordinate errors still remains for flights of a similar duration. Referring back to the DOP plots in Figure 5-7 to Figure 5-9, each flight presents unique observation conditions with respect to the satellite geometry evolution and the number of observed satellites which may contribute to the varied performance among similar duration flights. However, unlike the coordinate errors, Figure 5-10 suggests coordinate precisions are much less dependent on the respective flight duration, with a variation of only 1-4 cm over all coordinate components.

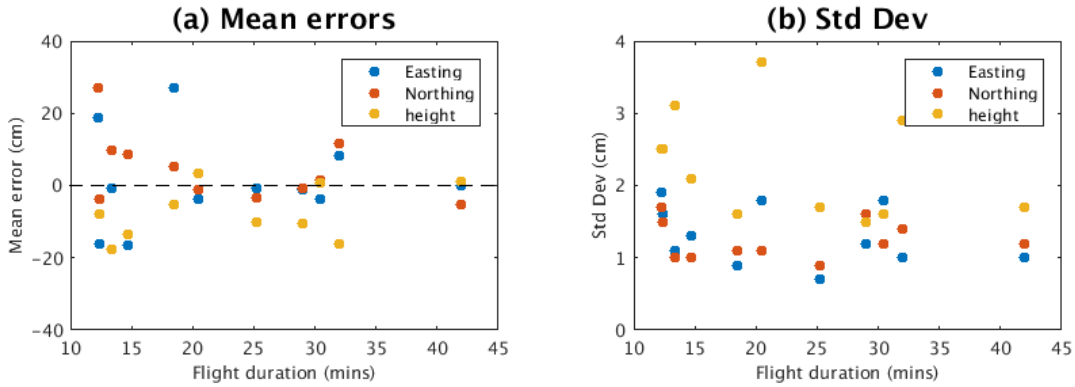

Figure 5-10. All UAV flights: mean coordinate errors and standard deviations vs flight duration

Summary. Regarding the CPF GPS control experiment at the reference station, PPP coordinate errors are typically much larger compared to those at the UAV flights. This is counterintuitive considering the dynamics of the UAV and that some flights are less than c. 30 minutes in duration with negative implications for ambiguity convergence. As the CPF GPS control experiment revealed the importance of the number of satellites and their geometries, Figure 5-11 compares the number of GPS satellites and DOP values at both the UAV and CPF reference station during the observation windows of CPF Flights 1-4.

From Figure 5-11 it can be seen that, generally, more satellites are observed by the UAV with lower PDOP values compared with the reference station during the same observation window. At the reference station, typically only 7-9 satellites are seen with PDOP values of up to 1.9, in which cases large coordinate errors of up to 60 cm can occur, as shown in Figure 5-3 (i.e. from the 30 minute block runs at the reference station). Conversely, typically 9-11 satellites are observed on the UAV, with PDOP values of up to 1.5, resulting in decimetre-level UAV positioning accuracies. Thus, even though there are increased dynamics on the UAV compared with the reference station, decimetre level PPP positioning can arise in instances when larger errors occur at the reference station because of the improved satellite visibility and geometry.

So far, these results provide important insights into the variable accuracy of GPS PPP positions that may be obtained on a UAV. Results show the sensitivity of GPS PPP solutions to satellite geometries, thereafter suggesting that low satellite elevation cut-off angles should be used when possible. However, due to the uniqueness of each flight with respect to observation conditions and their effect on coordinate errors, the next section moves on to assess the influence of GPS processing duration on a flight-by-flight basis.

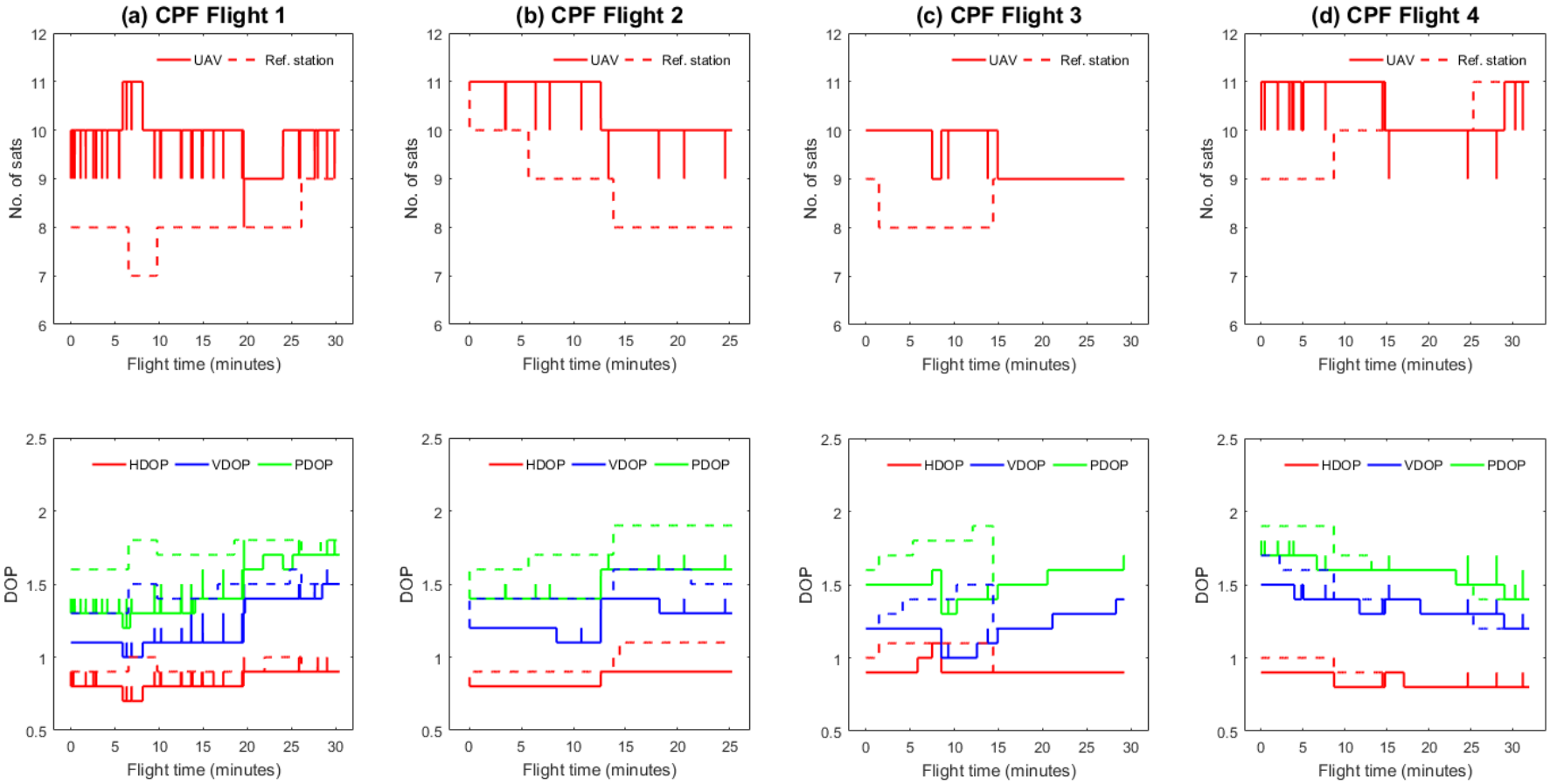

Figure 5-11. Comparison of satellite numbers and DOP values for observations made at the CPF reference station (on DOY 228) and during CPF flights 1-4, plots (a)-(d), respectively. Calculated in RTKlib software with a 5 degree satellite elevation cut-off angle.

5.6.3 GPS processing duration tests

To assess the influence of the GPS data span on coordinate errors on a flight-by-flight basis, flights were processed with GPS processing durations ranging between three minutes and the full (respective) flight duration with 30-second increments. To ensure a fair comparison for each GPS processing duration, coordinate errors were only evaluated over the first three minute period of each flight, enabling the same GPS data (window and number of epochs) to be assessed per test. Coordinate RMSEs per test (GPS processing duration) are presented in Figure 5-12 for CPF Flights 1-4 and Figure 5-13 for LH1 Flights 1-3. For reference, the dotted line on each plot denotes a 10 cm RMSE statistic value. The X axis scale (GPS processing duration) has also been maintained throughout each plot to facilitate an inter-comparison between flights. These tests were not performed for the LH2 flights, however, because of their relatively short overall flight durations of c. 12-15 minutes. As the additional processed GPS observations (beyond the first three minute evaluation period) were used only to improve estimated ambiguity and ZTD parameters (as detailed in the PANDA software description in Chapter 5.1.1), ambiguity correction values estimated over the three minute evaluation period as well as ZTD correction values are also presented in Figure 5-14 for each GPS processing duration of CPF Flights 1-4, and Figure 5-15 for LH1 Flights 1-3.

In Figure 5-12, CPF Flight 1 generally reflects the expected result where RMSEs in all three coordinates gradually improve with increasing GPS processing duration. With a processing duration beyond 25 minutes, the RMSEs for all coordinates fall below 10 cm, and after 28 minutes, improve to c. 1-2 cm. Referring to Figure 5-14, it can be seen that both ambiguity and ZTD values are initially quite variable for shorter GPS processing durations (and hence explaining the greater variation in coordinate errors) before stabilising (especially the ZTD values) with increasing GPS processing durations. The reducing coordinate errors thus suggest that the additional GPS observations being processed improve the accuracy of the estimated ambiguity and ZTD parameters.

For CPF Flights 2 and 3, the situation is different as coordinate RMSEs reach 10 cm for, and beyond, a shorter GPS processing duration of c. 8 minutes. With a further increase in GPS processing duration, coordinate errors fluctuate around c. 5 cm. However, for CPF Flight 2, the height coordinate is seen to diverge beyond a GPS processing duration of c. 15 minutes to around 10 cm without recovering. This may be suggestive of the occurrence of a cycle slip in the extended GPS observation processing (i.e. beyond c. 15 minutes), or else a change in satellite geometries occurring from the loss of a GPS satellite. Again, referring to Figure 5-14 it can be seen for CPF Flight 2 and 3 that ambiguities stabilise for GPS processing duration

beyond c. 10-15 minutes and hence the faster convergence of coordinates. For CPF Flight 2, however, ZTD values show a rapid increase for GPS processing durations beyond 15 minutes, which may explain the increased height coordinate error.

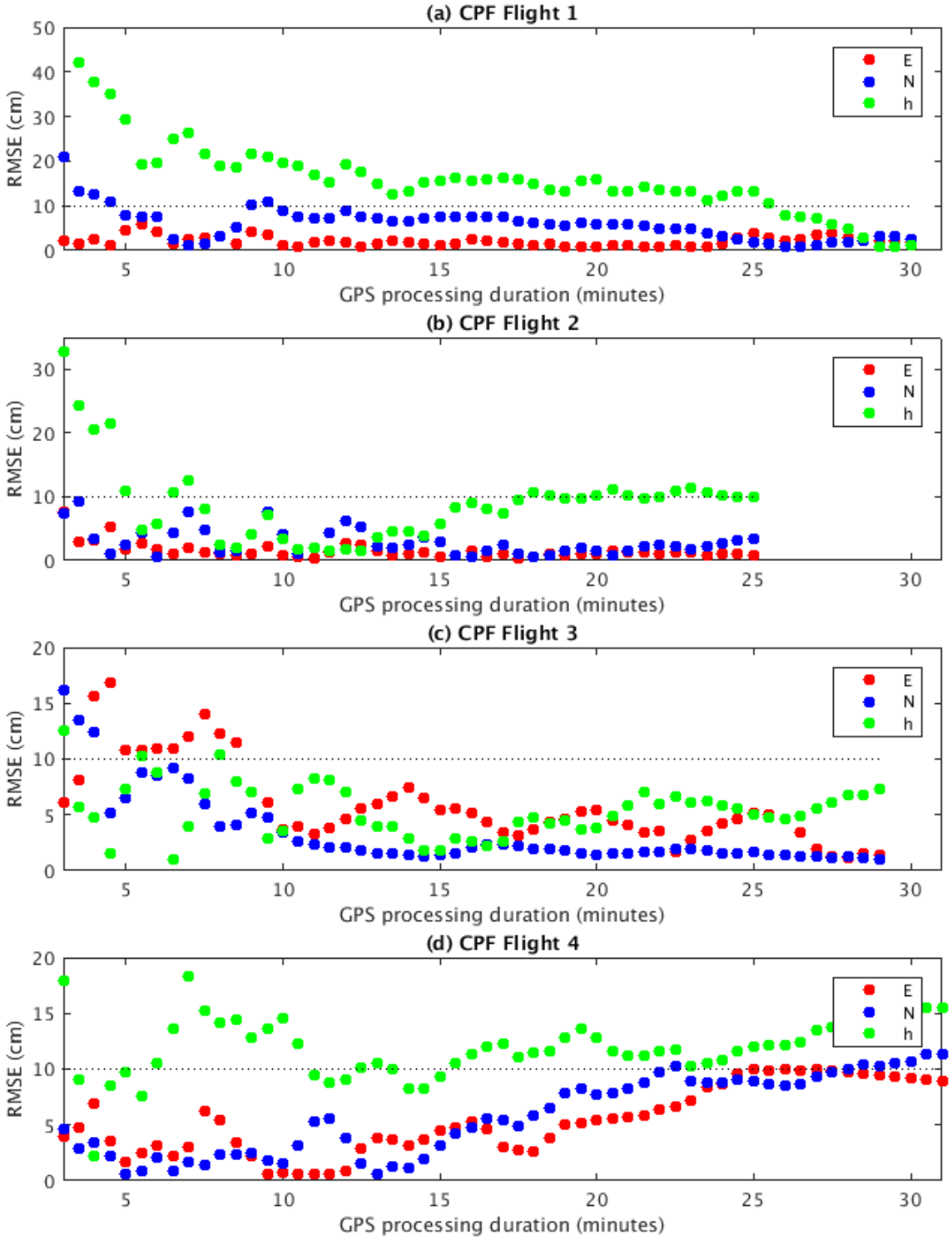

Figure 5-12. GPS PPP coordinate RMSEs (evaluated over the first 3 minute window) for GPS processing durations between 3 minutes and the full flight duration of each flight respectively with 30 second increments for CPF Flights 1-4. Processed with a 5 degree satellite elevation cut-off angle for flight-based GPS observations only.

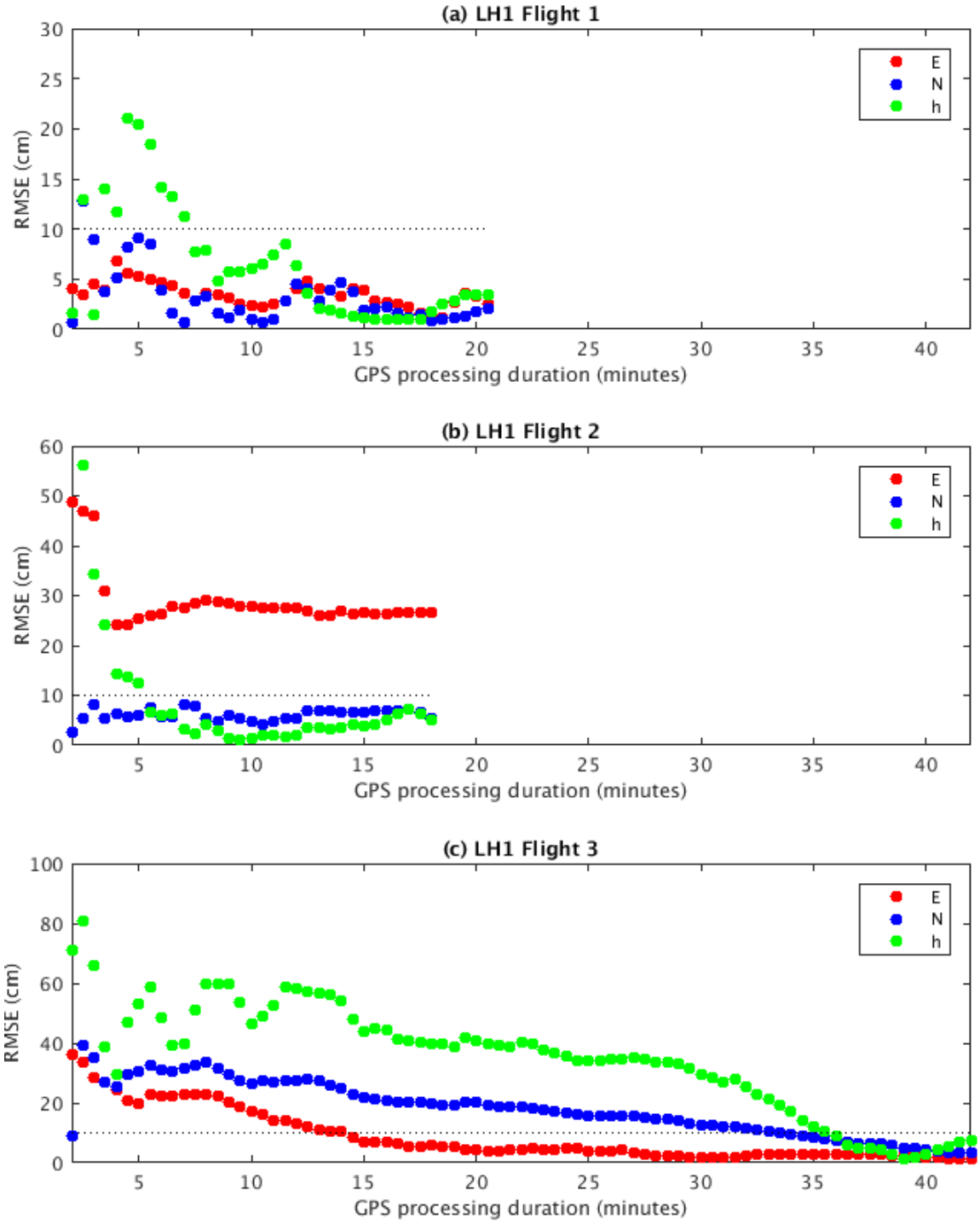

Figure 5-13. GPS PPP coordinate RMSEs (evaluated over the first 3 minute window) for GPS processing durations between 3 minutes and the full flight duration of each flight respectively with 30 second increments for LH1 Flights 1-3. Processed with a 5 degree satellite elevation cut-off angle for flight-based GPS observations only.

Compared to the other CPF flights, CPF Flight 4 entails the worst final coordinate RMSEs, despite being the longest in duration. Here, coordinate errors of better than 10 cm in plan are obtained for GPS processing durations of 3-5 minutes, before diverging beyond GPS processing

durations of c. 15 minutes. Figure 5-14 again shows ambiguities to stabilise beyond GPS processing durations of c. 10-15 minutes. ZTD parameters, however, are shown to be more unstable, with rapid value decreases beyond a GPS processing duration of c. 10 minutes, which may explain the coordinate divergences beyond GPS processing durations of c. 15 minutes.

Regarding LH1 Flights 1-3, Figure 5-12 shows that coordinate errors vary in a similar manner to the CPF flights. Coordinate errors for LH1 Flight 1 are shown to converge to better then 10 cm beyond a GPS processing duration of c. 8 minutes, as per CPF Flights 2 and 3, whilst beyond a GPS processing duration of c. 15 minutes, all coordinate errors are below c. 5 cm. For this flight, Figure 5-15 shows that ambiguity values stabilise after c. 8 minutes, and ZTD values after c. 15 minutes, which is similar to CPF Flight 1. In contrast, LH1 Flight 2 exhibits an easting coordinate bias of c. 25 cm which does not reduce with an extended GPS processing duration (as per LH1 Flight 1). This is perhaps unexpected as the HDOP value is not particularly worse than those for LH1 Flights 1 and 3. LH1 Flight 3 shows the same trend as CPF Flight 1 where, with the exception of some initial fluctuations in the height coordinate errors, coordinate errors gradually improve with increasing GPS processing duration, reaching 10 cm at c. 35 minutes and 5 cm for at c. 40 minutes. For this flight, Figure 5-15 again shows both ambiguity values and ZTD values to stabilise after 15-20 minutes. However, had this flight been cut short to 18 minutes, as per LH1 Flight 2, the final northing and height coordinate errors would have remained at c. 30 cm and c. 50 cm.

Overall, these results indicate that estimated ambiguity and ZTD parameters, and hence coordinate values, are highly influenced by the amount of GPS data processed. Whilst all GPS observations are used to compute the (time-constant) ZTD parameter, the number of GPS observations used for the computation of each ambiguity parameter depends on the presence of cycle slips and subsequent ambiguity re-initialisation. Therefore, in the next section, the number of ambiguities (and ambiguity resets) as well as the duration of GPS observations used to compute each, is investigated.

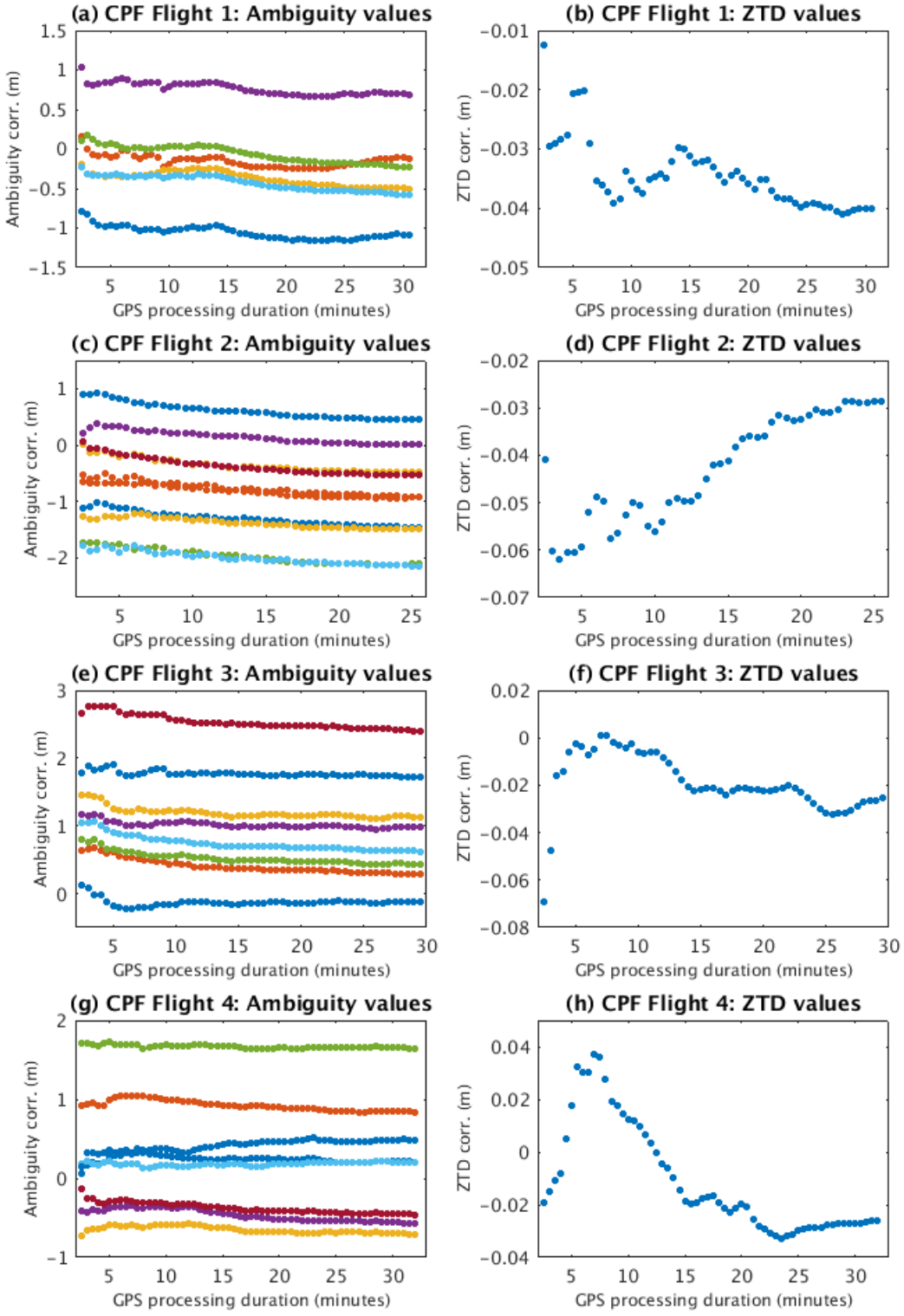

Figure 5-14. Estimated ambiguity (a, c, e) and ZTD (b, d, f) correction values per GPS processing duration test for CPF Flights 1-4. Each colour represents a different satellite ambiguity (left).

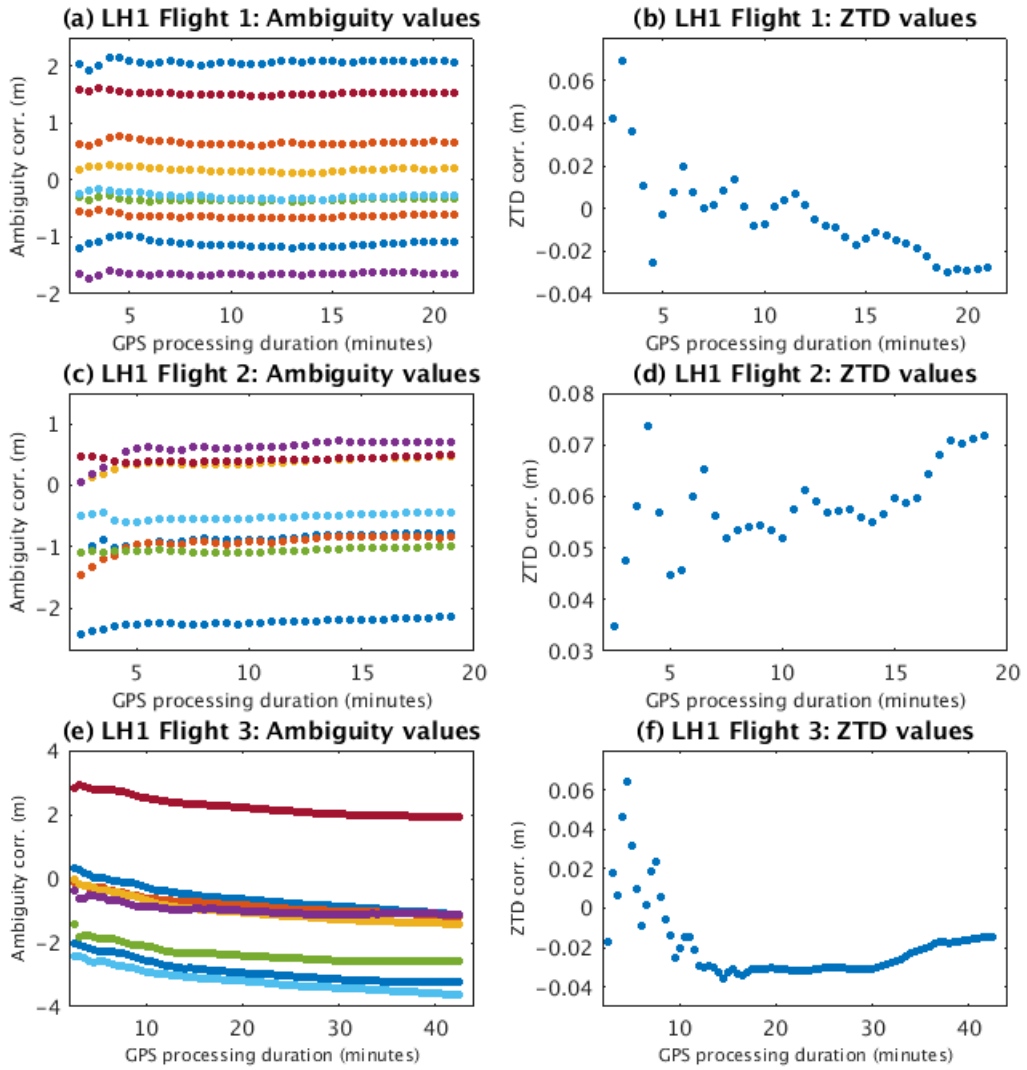

Figure 5-15. Estimated ambiguity (a, c, e) and ZTD (b, d, f) correction values per GPS processing duration test for LH1 Flights 1-3. Each colour represents a different satellite ambiguity (left).

5.6.4 Ambiguity durations and resets

As discussed in Chapter 3, accurate coordinate estimation requires the separation of (float) ambiguity estimates from coordinate estimates, which in turn requires a sufficient change in satellite geometries. An indication of poorly estimated ambiguities may therefore be gained from the duration of continuous phase measurements used to estimate each parameter, which depends on both the observability of the satellite and the occurrence of cycle slips.

To recover this information, Figure 5-16 displays the least squares ambiguity corrections (hereafter referred to simply as ambiguities) estimated per satellite for CPF Flights 1-4 along with the respective estimated values. This shows that there are 10-12 observable GPS satellites per flight, of which between 3-6 are observed continuously for the full flight duration without ambiguity resets or loss of view (4, 7, 6 and 5 satellites for CPF Flight 1-4 respectively). Continuous ambiguity resets are most evident for GPS satellite 7 for CPF Flight 3 and GPS satellite 30 for CPF Flight 4, where 6 and 7 ambiguities are estimated respectively. Remaining satellites, however, are only visible for part of each UAV flight or display multiple cycle slips, resulting in the re-initialisation of the ambiguity parameter (hereafter termed an *ambiguity reset*). For example, frequent ambiguity resets can be seen in Figure 5-16 for GPS satellite 9 during CPF Flight 2 and GPS satellite 7 during CPF Flight 3 where four and six ambiguities are estimated for the same satellites. When comparing to the coordinate differences per epoch, it can be see that coordinate jumps appear about the same time as each ambiguity reset. Coordinate jumps are most evident in the height of CPF Flight 2, but are only c. 5 cm or less.

When comparing these plots to Figure 5-12 (the GPS processing duration tests) it is possible to relate some of the changes in coordinate errors to the timings of ambiguity resets or the appearance (or loss of) of individual satellites. For example, approximately 16 minutes into CPF Flight 2, ambiguity resets occur on GPS satellites 10 and 23, whereas for GPS processing durations beyond 15 minutes (in Figure 5-12), height coordinate errors are seen to elevate. The continuous ambiguity resets seen on GPS satellites 7, 8 and 10 for CPF Flight 3 can also be related to the 5 cm coordinate error fluctuations (in Figure 5-12) for further incremented GPS processing durations. Fortunately for CPF Flight 3, six satellites are continually observed over the full flight duration and thus the coordinates remain somewhat constrained. For CPF Flight 4, ambiguity resets on GPS satellite 30 at around 15 minutes may explain the increase in height coordinate error for GPS processing durations beyond 15 minutes, whilst the six new ambiguity parameters estimated in the final 10 minutes of the same flight may explain the further increase in all coordinate errors.

These results suggest a high possibility of cycle slips and subsequent ambiguity resets on the fixed wing UAV flights, which limit the duration of continuous phase measurements used to estimate each ambiguity parameter. The effects are reflected by coordinate errors, but with further influence from total number of observed satellites. Regardless of these ambiguity resets, the processing duration tests (Figure 5-12 and Figure 5-14) have shown that the overall GPS processing duration remains a key factor regarding the accuracy of estimated coordinates. GPS PPP processing has so far been performed with flight-based GPS observation only, resulting in maximum GPS processing durations of c. 18 to 32 minutes for the CPF and LH1 flights but only c. 12-14 minutes for the LH2 flights. The latter resulted in larger GPS PPP position biases of 10-50 cm (Figure 5-6). From the CPF GPS control experiment at the reference station, it was clearly shown that GPS PPP position biases of only c. 1 cm, along with standard deviations of c. 1-2 cm are obtainable with c. 4.5 to 8 hours of data. However, using only 30 minutes of data increased the likelihood of obtaining larger coordinate biases (e.g. errors up to 60 cm), as seen here for the shorter LH2 flights. Therefore, in the next section, the potential for GPS PPP performance enhancements on the UAV through extended ground-based GPS observations is investigated.

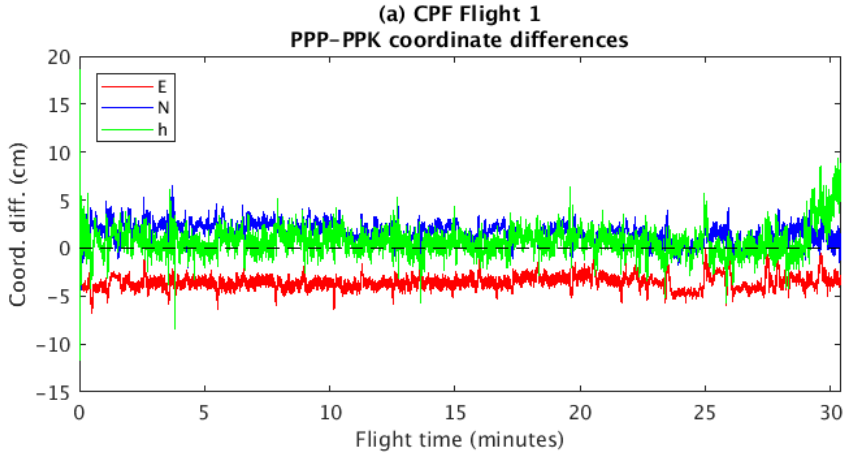
(a) CPF Flight 1
PPP-PPK coordinate differences
E
N
h
Coord. diff. (cm)
Flight time (minutes)

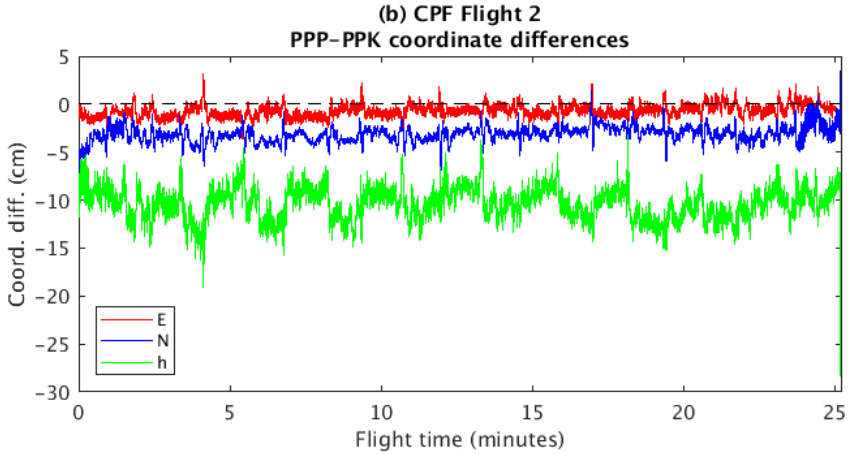
(b) CPF Flight 2
PPP-PPK coordinate differences
E
N
h
Coord. diff. (cm)
Flight time (minutes)

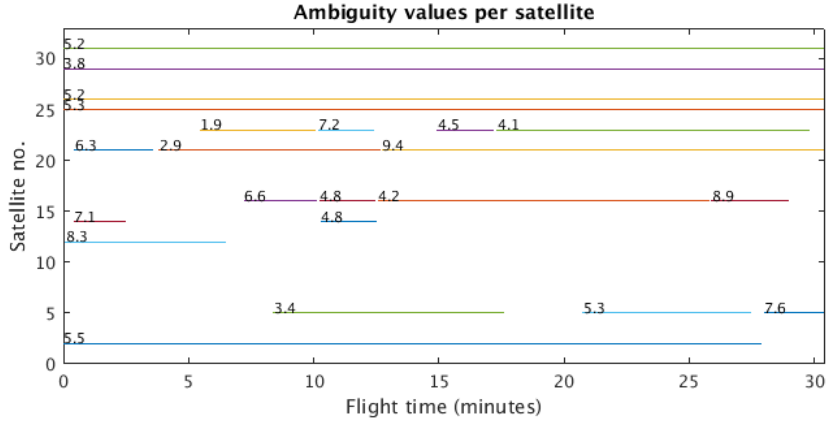
Ambiguity values per satellite
Satellite no.
Flight time (minutes)

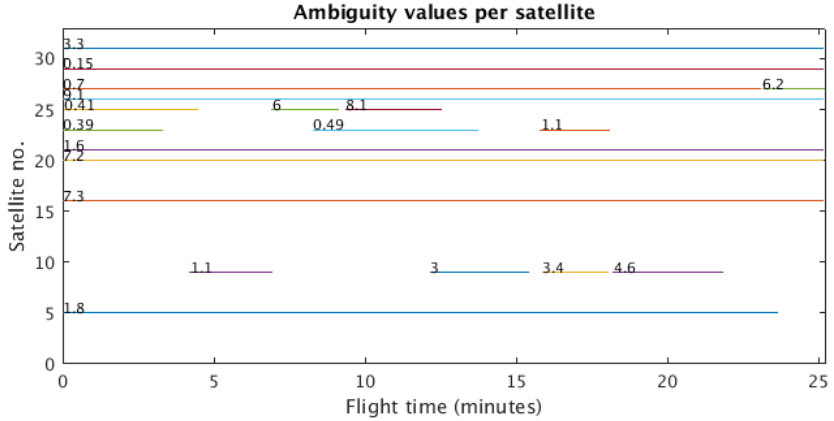
Ambiguity values per satellite
Satellite no.
Flight time (minutes)

Continued…

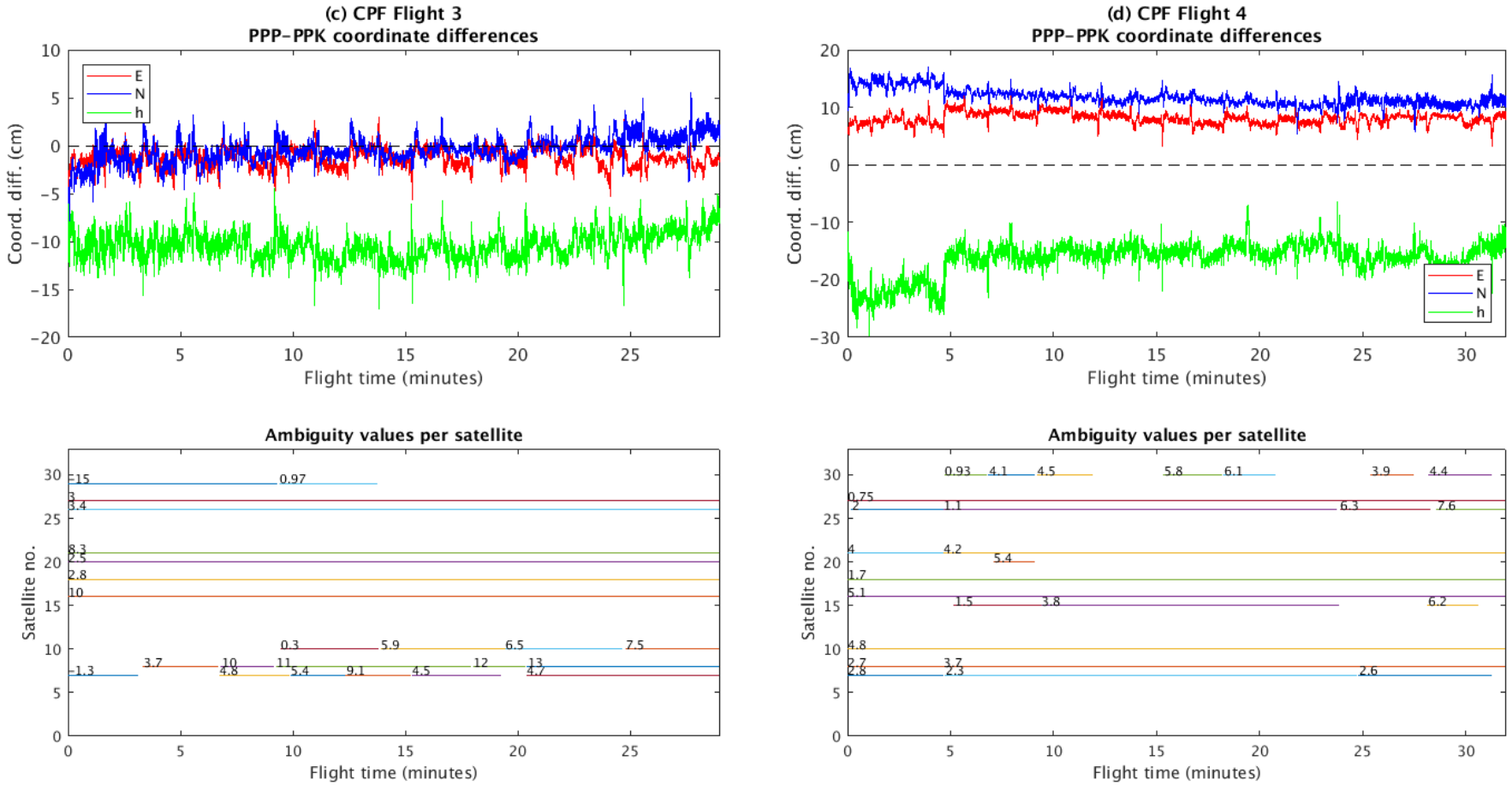

Figure 5-16. Duration of continuous phase measurements used to estimate IF ambiguities per satellite, with overlaid final values (in units of metres) for fight only GPS observations of CPF Flights 1-4

5.7 Results: Ground logging period tests

Although maximum flight durations depended on the UAV batteries, an attempt was made to extend GPS observation durations for CPF Flights 1-4 and LH2 Flights 1-4 by introducing ground-based GPS logging periods (GLPs) both before and after each flight (hereafter referred to as *pre-flight GLPs* and *post-flight GLPs* respectively). The intention was to increase the duration of continuous phase measurements (i.e. without cycle slips) to improve overall estimation of ambiguity parameters, and therefore coordinates.

Figure 5-17 presents coordinate RMSEs and standard deviations for solutions processed as flight-based GPS observations only (denoted 'no GLP'), as flight-based GPS observations plus the pre-flight GLP (denoted 'pre GLP') and as flight-based GPS observations plus the post-flight GLP (denoted 'post GLP'). In all cases, coordinate RMSEs and standard deviations were evaluated over the duration of each respective UAV flight only (and not the respective GLPs), such that the GLPs are only used to improve ambiguity and ZTD parameter estimates. From Figure 5-17, it is apparent that processing the pre and post-flight GLPs in addition to the flight observations does not give a consistent improvement to coordinate errors over processing the flight only GPS observations. For example, coordinate error reductions can be seen in all components for LH2 Flight 4 when processing the pre-flight GLPs in addition to the flight observations (with improvements of 52-89%) but northing and height coordinates are degraded for the equivalent post-flight GLP test. Overall, with pre-flight GLPs, easting, northing and height errors are improved for 3, 3 and 4 of the eight flight tests respectively, whilst with post-flight GLPs, these values are lower at 3, 1 and 2. However, regardless of the changing coordinate errors, the GLPs do not result in substantial changes to coordinate precisions, which are typically less than 1-2 cm per coordinate component, equivalent to 30-50% of their initial magnitudes. It is thus evident that the degrading effects of the pre and post-flight GLPs prevail as increased coordinate biases.

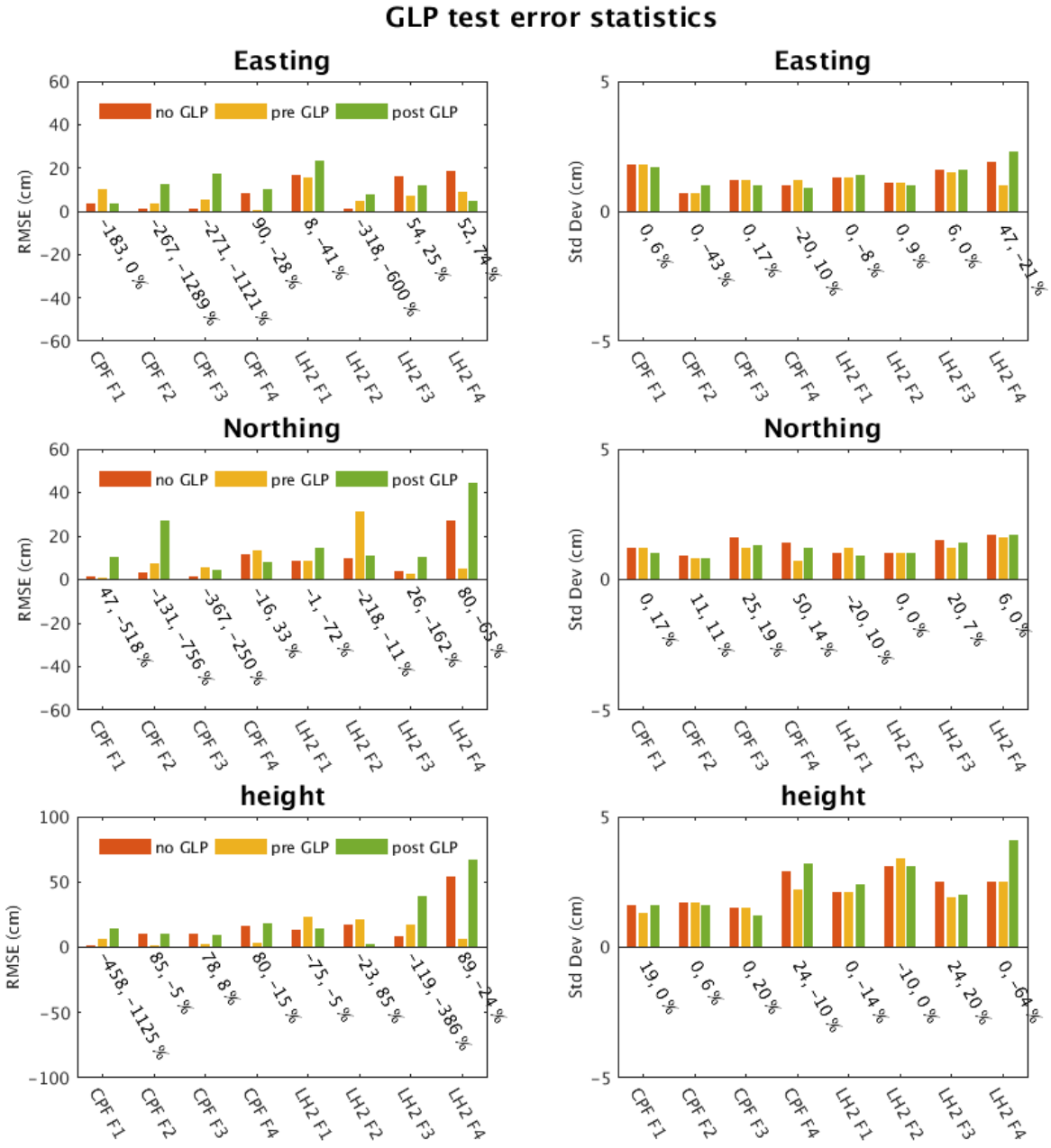

Figure 5-17. RMSE and standard deviation of the GPS PPP errors for solutions processed as flight-based GPS observations only ('no GLP'), as flight-based GPS observations plus the pre-flight GLP ('pre GLP') and as flight-based GPS observations plus the post-flight GLP ('post GLP'). Error statistics were evaluated over the duration of each respective UAV flight only (and not the respective GLPs). Displayed percentages indicate the improvements with pre-flight and post-flight GLPs respectively over processing flight-based GPS observations only.

As the sensitivity of coordinate errors to ambiguity resets has already been demonstrated, Figure 5-18 again displays ambiguities estimated per satellite for CPF Flights 1-4 along with the respective estimated values, but this time including both pre and post-flight GLPs. From these ambiguity plots, it is immediately evident that numerous ambiguity resets occur around the UAV launch and landing times. At the UAV launch times, these are likely to be caused by

tilting of the UAV antenna such that numerous observed satellites are obstructed (see UAV launch picture in Figure 4-4f). At the landing times, these are likely to be caused by the rapid deceleration of the UAV antenna as the UAVs are grounded into the short grass from flying speed.

Referring to the corresponding coordinate difference plots in Figure 5-18, it can be seen that large coordinate jumps also occur at the UAV launch and landing times. At the UAV landing times, such jumps are as large as c. 40 cm, whereas at the launch times they are substantially smaller at only c. 5-10 cm. The smaller jumps seen at the launch times can be explained by the fact that a subset of satellites (e.g. 4 and 7 for CPF Flights 2 and 3 respectively) are continually observed through the launch procedure (as no such ambiguity resets occur). Consequently, coordinate estimates remain somewhat constrained by these satellite observations. This may be contrasted to the landing times, where cycle slips are evident on all satellites. The complete loss of lock on all satellites at landing times may also explain the generally slightly worse performance of the post-flight GLPs over pre-flight GLPs in Figure 5-17. With complete loss of lock on all satellites, additional processed GPS observations made to the same satellites are disconnected from former ambiguity arcs and thus ambiguity estimations may not be further improved (as detailed the PANDA software description in Chapter 5.2.1).

Coordinate jumps resulting from loss of lock on multiple satellites has also been shown by, for example, Marques *et al.* (2018) in the context of cycle slips resulting from ionospheric scintillations. Consequently, the high likelihood of losing satellite lock during UAV launch and landing procedures currently suggests a limited utility of both the pre or post-flight GLPs towards improving ambiguity estimates, and thereafter the PPP performance.

5.7.1 Cycle slip fixing

The current approach to handle cycle slips in PANDA is to use the TurboEdit approach of Blewitt (1990) to flag each cycle slip for subsequent re-initialisation of ambiguities in the least squares adjustment. Furthermore, remaining observations containing undetected cycle clips are cleaned by analysing observational residuals between each least squares iteration, such that bad observations can be deleted. This approach is commonly applied in literature (e.g. Fang *et al.*, 2014; Zhang *et al.*, 2014) but does not make any attempt to repair observations. Compared to the UAV flights presented here, previously published applications of PPP usually entail longer observation durations for better estimation of (new) ambiguity parameters, in addition to a lower frequency of cycle slip occurrence. The occurrence of cycle slips, as well as the shorter

observation duration for UAV flights, makes cycle slips more critical to the PPP performance and thus it is more desirable to repair observations rather than simply discard.

Fixing cycle slips gives the possibility of maintaining the positioning accuracy during GNSS outages (Geng *et al.*, 2010b; Du and Gao, 2012; Zhang and Li, 2012; Li *et al.*, 2016). For the UAV flights, it is expected that fixing cycle slips would also improve the utility of both the pre- or post-flight GLPs, by effectively increasing the duration of continuous phase measurements, and hence the accuracy of ambiguity parameter estimation.

Cycle slips may be repaired if the size of each cycle slip can be determined, in addition the respective times. All subsequent phase observations made to the same satellite and on the same carrier signal can then be corrected by the determined cycle slip value (Hofmann-Wellenhof *et al.*, 2007). Although the TurboEdit implementation in PANDA does not currently fix cycle slips, numerous methods exist for doing so which typically involve further analysis of the test quantity used to initially detect a cycle slip (examples can be found in Zhang *et al.* 2012). As discussed in Section 5.2.1, the test quantity of the TurboEdit approach comprises a combination of dual frequency carrier phase and code observations, the value of which will jump between adjacent epochs in the event of a cycle slip (Blewitt, 1990). The value of the cycle slip may be further recovered by fitting a curve through the test quantity values before and after the cycle slip to estimate the magnitude of this jump (Hofmann-Wellenhof *et al.*, 2007). Such techniques are typically called interpolation methods. Further methods include predictive methods, whereby Kalman filters are used to fuse data from additional INS (Inertial Navigation System) sensors to predict cycle slip values. For example, Eling *et al.* (2014) showed how accelerometers, which provide independent information on the UAV motion, can be used to detect and fix cycle slips based on their agreement with the GPS observations in a tightly coupled Kalman filter for an RTK GPS application. For PPP, Du and Gao (2012) proposed a PPP GPS/INS integrated system where phase combinations (Wide Lane and Extra Wide Lane, due to their greater wavelength) are used to uniquely determine L1 and L2 cycle slips. In this case the IMU solution was used to remove the range information from the Wide Lane phase. Results gave improvements of c. 22 % and c. 31 % at times of cycle slips in plan and height coordinate components respectively (compared to not fixing). More recently, for an airborne dataset of c. 7 hours in duration, Gao *et al.* (2015) achieved a positioning RMSE of 6.6 cm, 8.9 cm and 6.6 cm in easting, northing and height respectively for a standalone (ionosphere-constrained) GPS PPP solution, whereas these values were improved to 3.2 cm, 4.8 cm and 5.5 cm in an equivalent (ionosphere-constrained) PPP-INS solution. However, rather than fixing cycle slips, erroneous GPS observations were only down-weighted (through their

associated covariance matrix) relative to the IMU measurements for the update of system state parameters. Building on this, Li *et al.* (2016) further developed an PPP-inertial aided cycle slip detection and repair methodology (i.e. rather than using PPP observations to estimate INS error states) to replace the need for ambiguity initialisation, and thus mitigate associated errors (e.g. coordinate jumps). The method was applied to a 30 minute vehicle test, in which cycle slips were simulated at four epochs, simultaneously on both L1 and L2. Using a relative GPS trajectory as reference, fixing the cycle slips (rather than simply reinitialising) improved coordinate RMSEs from 9.7 cm, 7.0 cm and 39.7 cm to 3.9 cm, 5.2 cm and 30.8 cm in easting, northing and height components respectively. Moreover, maximum coordinate errors were reduced from 15.5 cm to 8.1 cm in easting, 21.5 cm to 13.9 cm in northing and 78.6 cm to 68.0 cm in height. In this application, the focus of the cycle slip repair was to maintain the positional accuracy throughout the trajectory. This is relevant to the UAV tests as it was shown that some of the GPS in-flight observations were contaminated with cycle slips, resulting in frequent ambiguity re-initialization for the same satellites and thus shorter data spans for these ambiguities. However, in the case of the GLPs, cycle slip repair would further enable phase data arcs to be connected such that in-flight ambiguity and subsequently UAV positioning accuracies are improved. The in-GLP PPP positioning accuracy, however, is of less interest but would reflect the accuracy of ambiguity estimation.

The development of a full cycle slip fixing capability in PANDA is considered future work. It would also benefit from raw IMU data being available from the UAVs (although this is not always possible, as was the case for the commercial platforms used here), as it has been shown that INS-based cycle slip detection and repair methods can be applied using consumer grade IMU observations (e.g. Du and Gao, 2012).

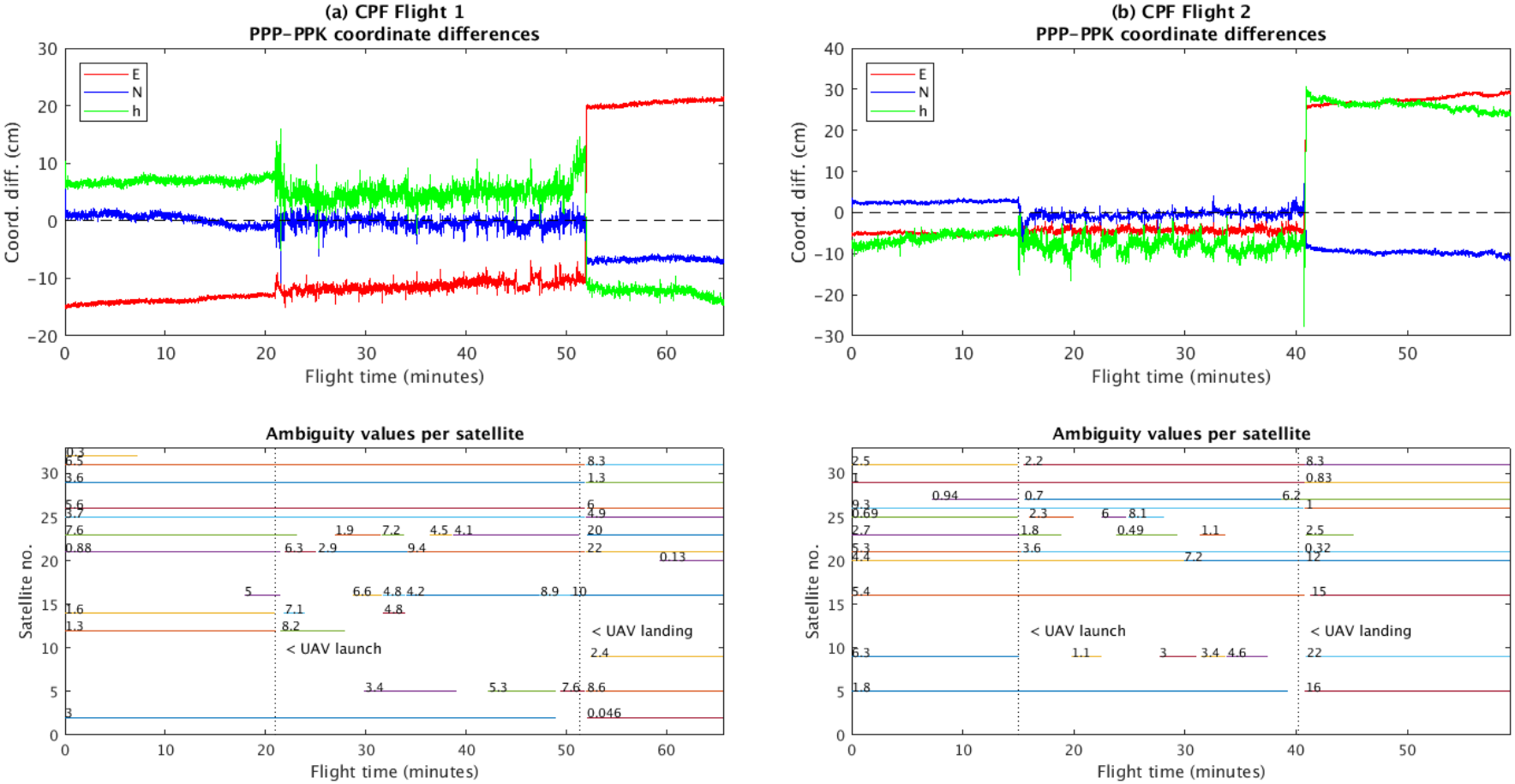
(a) CPF Flight 1
PPP–PPK coordinate differences
Coord. diff. (cm)
Flight time (minutes)
E
N
h
(b) CPF Flight 2
PPP–PPK coordinate differences
Coord. diff. (cm)
Flight time (minutes)
E
N
h
Ambiguity values per satellite
Satellite no.
Flight time (minutes)
< UAV launch
< UAV landing
Ambiguity values per satellite
Satellite no.
Flight time (minutes)
< UAV launch
< UAV landing

Continued…

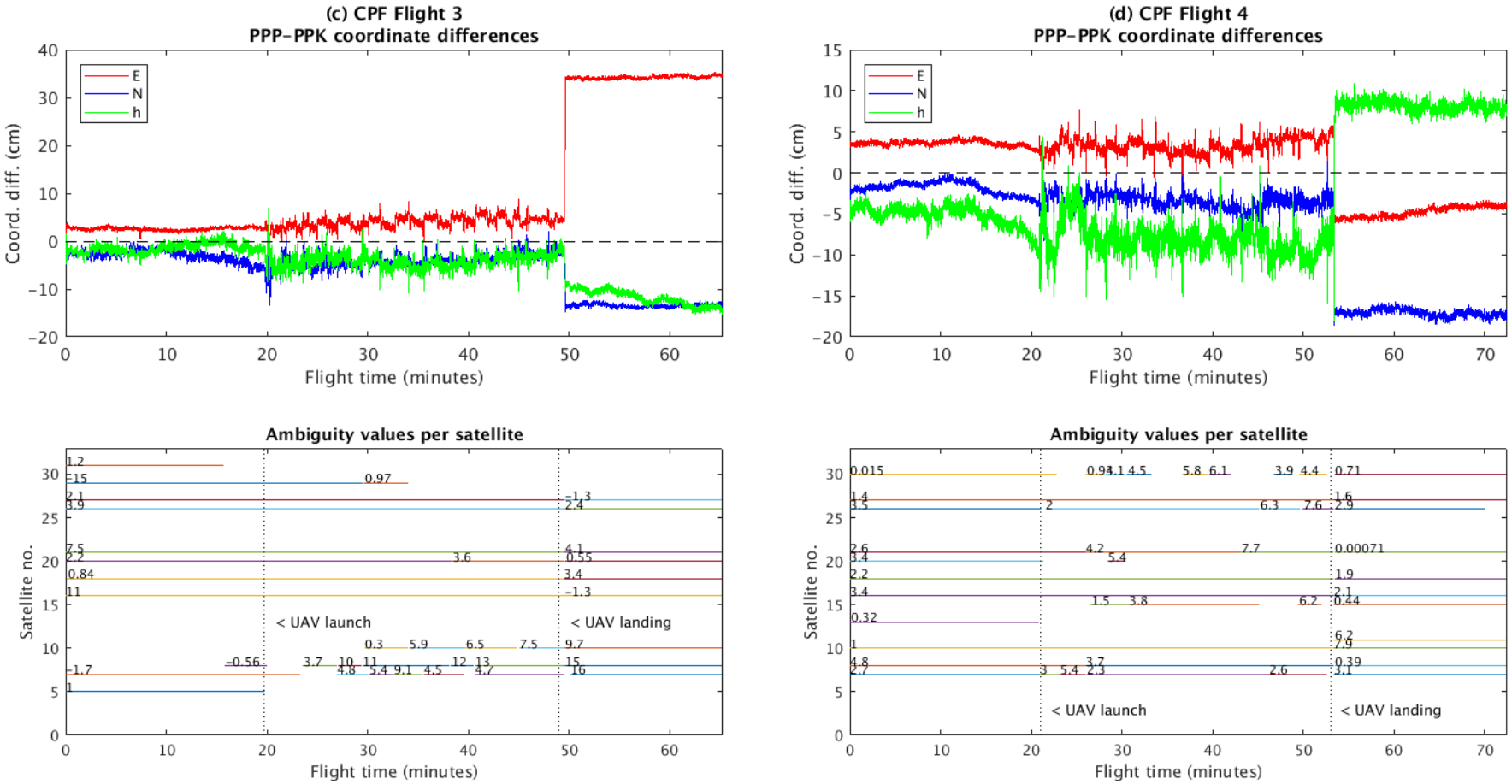

Figure 5-18. Duration of continuous phase measurements used to estimate IF ambiguities per satellite, with overlaid final values (in units of metres) for fight plus GLP-based GPS observations of CPF Flights 1-4

5.8 GPS+GLONASS processing

Discussion in Chapter 3 suggested the inclusion of GLONASS may offer improvements to PPP convergence times, and subsequently PPP coordinate accuracies due to an increased observation redundancy in the least squares adjustment. Further to this, Marques *et al.* (2018) showed that the inclusion of GLONASS satellites can reduce the effects of ambiguity resets in kinematic PPP solutions. The following section investigates the benefits of GPS+GLONASS PPP processing over equivalent GPS-only solutions. From Section 5.6.1, it is expected that at least 9 satellites are required to produce accurate results, and thus the inclusion of GLONASS satellites is expected to have positive implications for the UAV flights.

5.8.1 GPS+GLONASS control tests

Before reprocessing the UAV flights, the CPF GPS control experiment (as presented in Section 5.4.2) was repeated using both GPS and GLONASS observations (hereafter referred to as the CPF *GPS+GLONASS* control experiment). Equivalent to Figure 5-3 for the GPS-only processing, Figure 5-19 shows the coordinate errors for the full duration processing (red line) and 30 minute blocks (blue line) for solutions with GPS and GLONASS observations on both DOY 227 and 228. Further to this, Table 5-4 presents the mean coordinate differences (from the known reference station coordinates) and standard deviations for GPS+GLONASS PPP solutions, as well as the percentage improvement over the equivalent GPS-only solutions (in Table 5-3). Solutions were calculated with a 5 degree satellite elevation cut-off angle.

From Figure 5-19 and Table 5-4, it is evident, as with GPS-only, that processing the full duration of observed reference station data results in a very small solution bias, this time only 7 mm, 8.3 mm and 21.1 mm in easting, northing and height coordinates respectively. Coordinate error magnitudes again do not exceed c. 5 cm in any component. However, for the 30 minute block solutions, and in contrast to the GPS-only solutions in Figure 5-3, coordinate jumps are less pronounced, and typically only 10-15 cm. The more limited variation between each 30 minute block solutions is reflected in the improved overall standard deviations, now only 4.8 cm, 16.3 am and 3.7 cm in easting, northing and height respectively, which represent improvements of 14-81 % over the GPS-only solutions. Moreover, the overall solution bias is improved by 96 %, 89 % and 97 % in easting, northing and height coordinate components respectively. With the additional GLONASS satellites now enabling centimetre-accuracy PPP at the ground-based CPF reference station, where sky visibility is more limited, further improvements might be expected for the UAV.

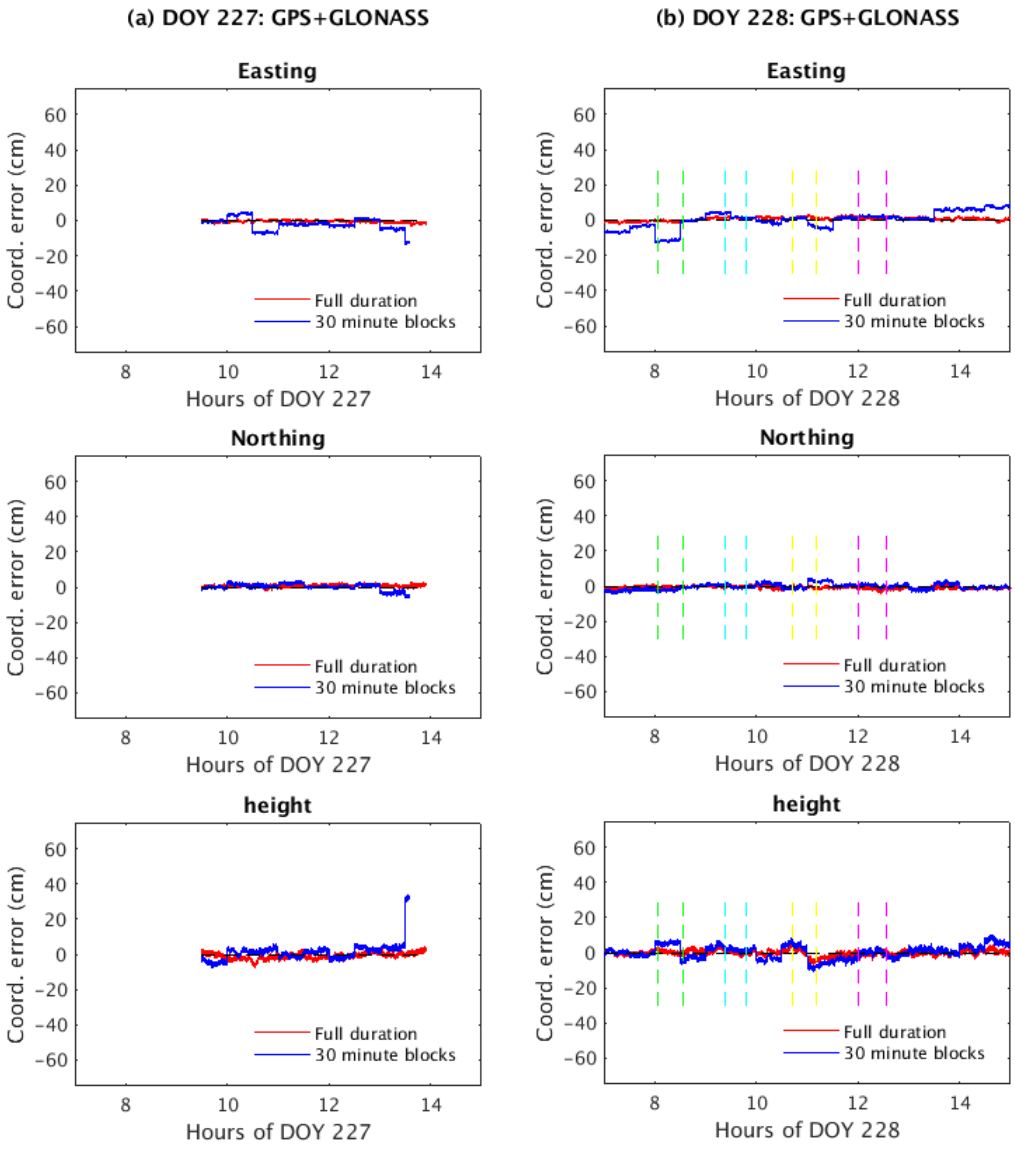

Figure 5-19. GPS+GLONASS PPP errors for the CPF reference station on (a) DOY 227 and (b) DOY 228. Processed as the full duration (red line) and in 30 minute blocks (blue line), with a satellite elevation cut-off angle of 5 degrees. GNSS observation windows for CPF Flights 1-4 are indicated by the green, cyan, yellow and magenta dashed lines, respectively.

Const.	Proc. Strat.	Mean diff. (cm)				Std Dev (cm)			
		E	N	h	3D	E	N	h	3D
GR	Full	0.7	-0.8	0.0	2.1	1.0	0.8	1.6	0.9
	30 min	0.2	-0.3	0.3	5.5	4.8	1.6	3.7	3.1
% imp. G-only	Full	50	-167	100	16	-11	20	16	10
	30 min	96	89	97	77	76	81	80	84

Table 5-4. Mean and standard deviation of the GPS+GLONASS ('GR') PPP errors for the CPF reference station, and % improvement over the equivalent GPS-only solutions in Table 5-3 ('% imp. G-only'), processed as the full duration ('Full') and in 30 minute blocks ('30 min').

5.8.2 Full flight processing

Following on from the CPF GPS+GLONASS control experiment at the reference station, the full duration of each UAV flight was processed in GPS+GLONASS PPP mode and coordinate differences were calculated with respect to reference GPS PPK trajectories. Figure 5-20 shows the mean and standard deviation of the PPP minus PPK differences for the CPF and LH2 flights processed with GPS-only and GPS+GLONASS observations. The LH1 flights, however, were not processed as GPS+GLONASS as the 5 second GLONASS orbit product was not available from CODE prior to 2017. The percentage (mean error magnitude) improvement of coordinate errors with GPS+GLONASS over GPS-only processing is presented above each bar plot. All solutions were processed with a 5 degree satellite elevation cut-off angle with flight only GPS/GPS+GLONASS observations.

From Figure 5-20, it can be seen that improvements with GPS+GLONASS over GPS-only processing are variable, but small in magnitude (i.e. typically only 5 cm) over all coordinate components and flights. Overall, with GPS+GLONASS processing, easting, northing and height errors are improved for five, six and two of the nine flight tests respectively. Incurred reductions in mean coordinate error magnitudes from GPS+GLONASS processing range from -300% to +96% in easting, -8% to +81% in northing and -414% to +63% in height. The best results can be seen for the easting and height coordinate errors of LH2 Flight 3 which reduce by 65% (i.e. from c. 19 cm to c. -5 cm) and 63% (i.e. from c. -50 cm to c. -20 cm) respectively. The small (centimetre-level) easting and northing biases for CPF Flight 1 are almost completely eliminated, although a c. 15 cm easting coordinate bias for LH2 Flight 2 and a c. 20 cm height coordinate bias for LH2 Flight 3 is introduced. The changes in coordinate standard deviations from GPS+GLONASS processing are also relatively small over all coordinate components and flights. Changes range from -20% to +22% in eastings, -10% to +35% in northings and -21% to +41% in height, which reflect changes at the 1 cm level only.

Generally, it can be seen that the inclusion of GLONASS satellites results in only relatively small changes to the UAV trajectory error compared with the GPS-only solutions. Some coordinate biases are reduced and some are increased, but for the majority of flights, the magnitude of bias change is typically only at the 5 cm level per componant. However, as was shown through the CPF GPS control experiment, and subsequent analysis of UAV satellite geometries at the UAV, sufficient numbers of GPS satellites, meaning 9 or more, are already available at the UAV. Such numbers were shown to facilitate PPP solutions with decimetre-level accuracy with c. 30 minutes of data at the reference station. Including GLONASS for the CPF reference station processing, however, remained beneficial as satellite numbers were

typically lower (i.e. fewer than 9) due to poorer sky visibility. For the UAV, sufficient GPS satellite numbers without GLONASS inclusion, appears to prevent GLONASS from being substantially beneficial and only slightly improve or degrade solutions depending on the time-of-day geometry implications (and cycle slips). In the context of PPP convergence times, Li and Zhang (2014) also showed that the benefit of including GLONASS satellites reduces with an increasing number of GPS satellites. They indicated a similar tipping point, at around 9-10 GPS satellites, where further improvements from the inclusion of GLONASS satellites were minimal.

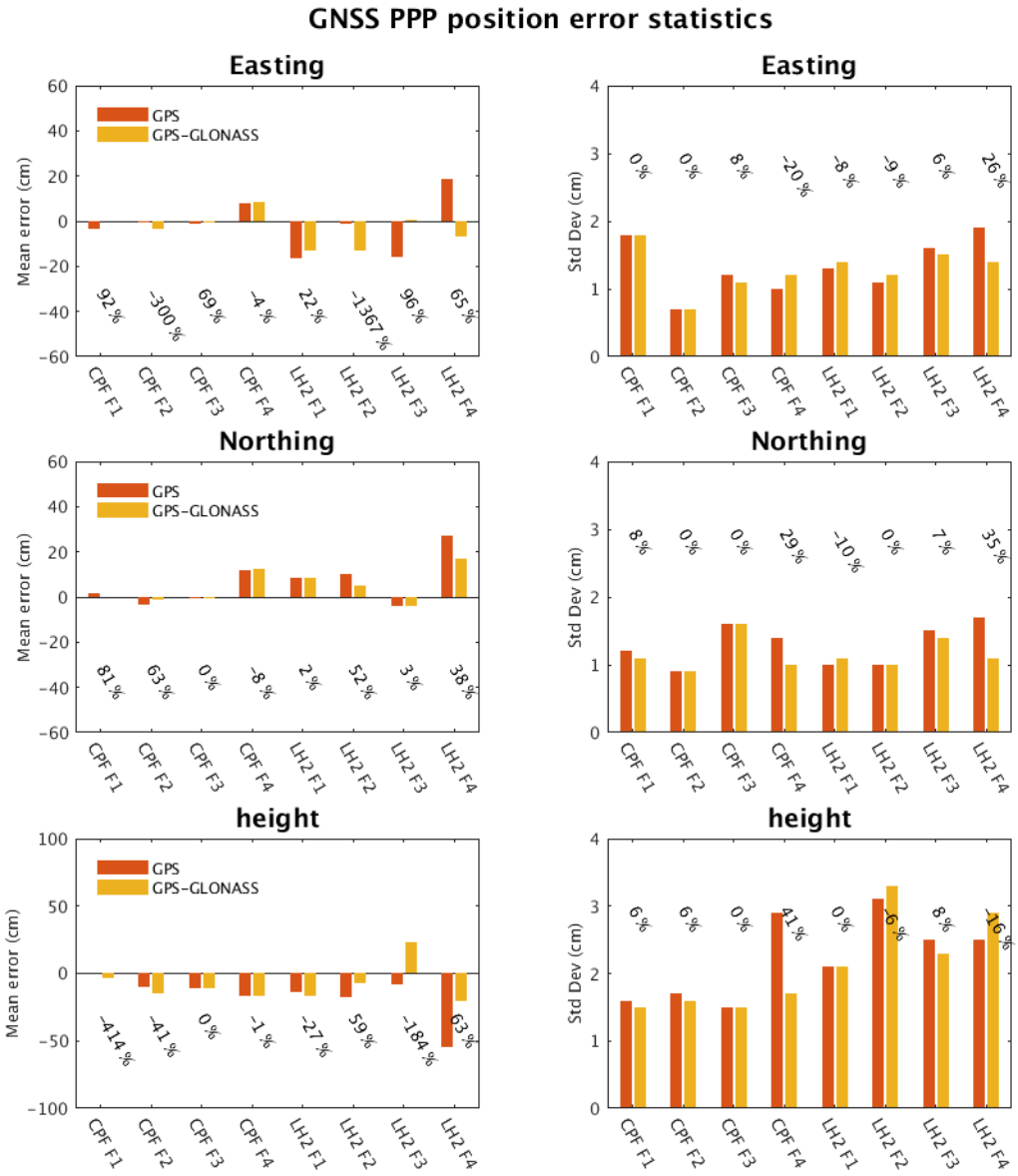

Figure 5-20. Mean and standard deviation of the GNSS PPP minus PPK differences for GPS-only (orange) and GPS+GLONASS processing. Percentages above/below the bars indicate the percentage (mean error magnitude) improvement of coordinate errors with GPS+GLONASS over GPS-only processing. Processed with a 5 degree satellite elevation cut-off angle for GNSS observations obtained during flights only.

A further consideration with GLONASS is that a receiver-dependent inter system time bias has to be estimated for each observed GLONASS satellite (time-constant) in the adjustment. This is to account for the relative offset between the GPS time frame and that of GLONASS, but has the potential to weaken the least squares solution (i.e. lower parameter precisions) due to the estimation of more parameters and subsequent reduction in observation redundancy (Dalla Torre and Caporali, 2015; Li *et al.*, 2015).

5.8.3 GPS+GLONASS processing duration tests

As improvements to PPP convergence time from GPS+GLONASS processing are well-documented (e.g. Li and Zhang, 2014) the session increment tests (as were presented in Figure 5-12 for GPS-only processing) were also repeated with GPS+GLONASS. The final coordinate RMSEs per GPS+GLONASS processing duration are presented in Figure 5-21 for CPF Flights 1-4, along with corresponding GPS-only results.

For CPF Flight 1, a noticeable faster convergence rate is evident with the height coordinate RMSE reaching 10 cm after a c. 13 minute GPS+GLONASS processing duration, compared to c. 25 minute GPS-only processing duration. The easting coordinate RMSE also settles below 10 cm after a c. 1 minute GPS+GLONASS processing duration, compared to a c. 9 minute GPS-only processing duration. However, after a c. 25 minute GPS+GLONASS processing duration, coordinate accuracies are seen to diverge, unlike the equivalent GPS-only solutions. In contrast, GPS+GLONASS processing does not offer any enhancements to the CPF Flights 2-4 results, rather it is seen that GPS+GLONASS processing degrades the accuracy of at least two coordinate components over the GPS-only solutions. In such cases, GPS-only processing provides the best solutions.

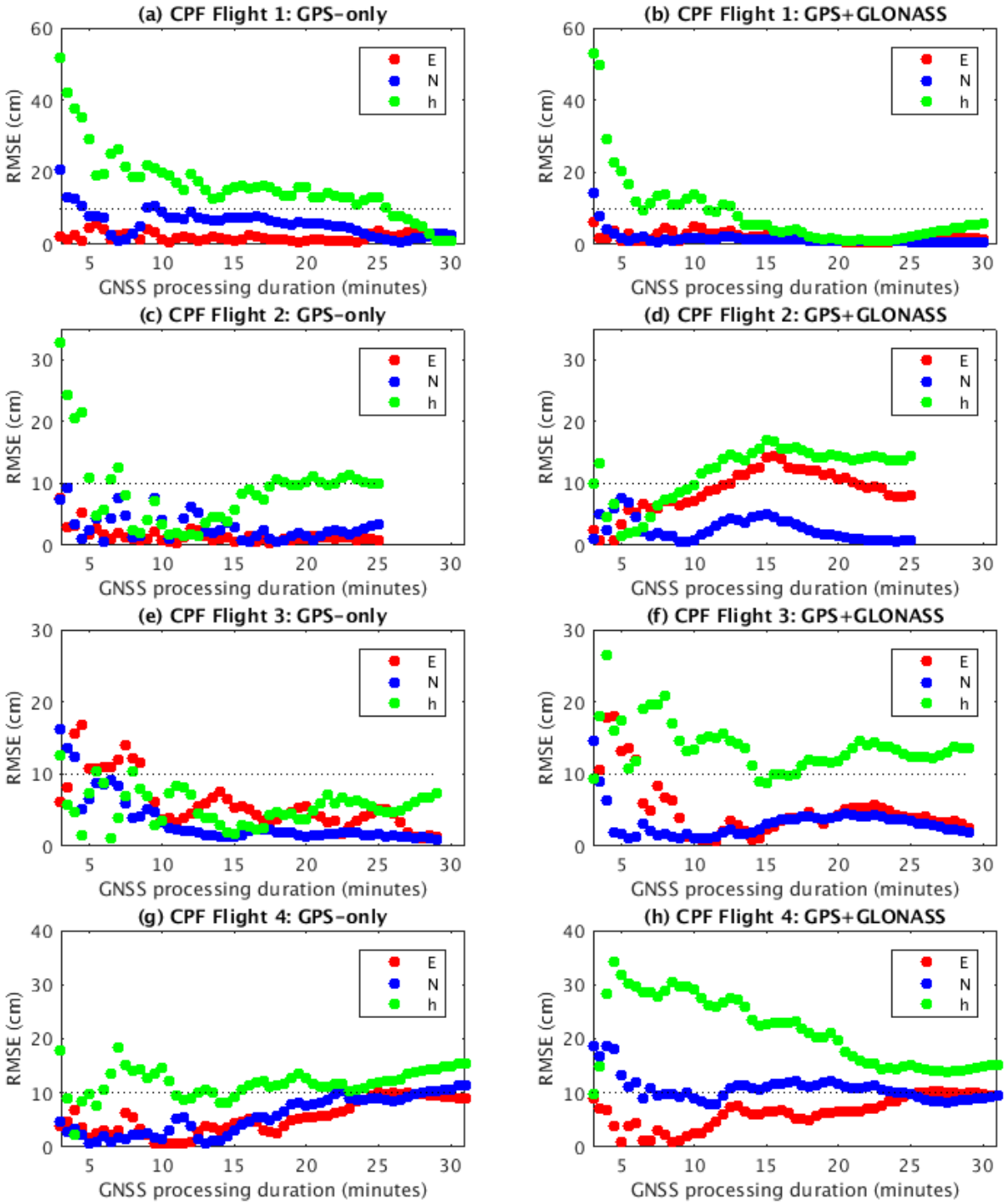

Figure 5-21. GPS-only and GPS+GLONASS PPP coordinate RMSEs (evaluated over the first 3 minute window) for processing durations between 3 minutes and the full flight duration of each flight respectively with 30 second increments for CPF Flights 1-4. Processed with a 5 degree satellite elevation cut-off angle for GNSS observations obtained during flights only.

5.9 Summary of findings and final solutions

Referring back to the research question presented in Section 5.1, this chapter firstly set out to determine *what PPP positional accuracies and precisions are achievable on short duration fixed wing UAV flights* and *what processing durations are required to achieve these*.

It has been shown that it is possible to achieve GPS PPP positions on the UAV with a 3D accuracy of 10 cm or better (agreement of GPS PPK positions) with GPS processing durations greater than c. 20 minutes, or 5 cm with GPS processing durations greater than c. 30 minutes (e.g. CPF Flight 1 and LH1 Flight 3 in Figure 5-12 and Figure 5-13 respectively). Moreover, the highest UAV PPP positioning accuracies are achieved when using low satellite elevation cut-off angles (i.e. 5 degrees). Compared to the ground-based GNSS reference stations, the UAV typically sees more satellites, resulting in better satellite geometries (lower DOP values), which improves the accuracy of coordinate estimation. Longer GPS processing durations generally give more repeatable GPS PPP positioning accuracies on the UAV, although for these tests, final coordinate accuracies remained variable with the flight due to different observation conditions. The weakest positioning accuracies, at decimetres in both planimetry and height, were obtained for the shortest duration flights, which was attributed to inaccurately estimated ambiguity parameters. Irrespective of final GPS PPP positioning accuracies on the UAV, positions are achieved with a precision of c. 1-4 cm for all UAV flights, which has good implications for use as photogrammetric control.

This chapter secondly set out to determine *if ground logging periods can assist PPP convergence for short duration UAV fights*. Results showed that cycle slips and subsequent ambiguity resets for all, or the majority of observed satellites during UAV launch and landing procedures prevented the effective use of pre and post-flight GLPs. Consequently, the highest GPS PPP positioning accuracies for the UAV are achieved when processing flight only GPS observations. It is expected that GLPs may be better implemented on rotary-wing UAVs, where the UAV remains upright and stable during launch and landing procedures, or else with improved treatment of cycle slips.

Finally, this chapter set out to determine *what improvements come with the processing of additional GLONASS observations*. Results showed that the processing of GLONASS observations, in addition to GPS, results in variable improvements and degradations in coordinate accuracies for the presented datasets. It is expected that this relates to there already being sufficient numbers of GPS satellites (i.e. 9 or more) observed by the UAV such that the inclusion of GLONASS satellites has limited influence on the accuracy of the PPP solutions.

In light of the above, for the implementation of PPP-BBAs (in the next chapter), UAV PPP positions obtained from the processing of flight only and GPS-only observations with a 5 degree satellite elevation cut-off angle are subsequently used. The mean coordinate errors and standard deviations for these solutions are presented in Table 5-5, which may be used as the final errors in UAV PPP positions, prior to the determination of GPS PPP camera positions in the next chapter. It can be expected that the presented GPS PPP position biases will propagate into photogrammetrically-derived mapping coordinates determined by GPS PPP-supported BBA in the absence of GCPs. It might also be anticipated that the centimetre-level precision of the GPS PPP positions may reduce systematic errors in the same BBA. Both of these aspects are key photogrammetric considerations and are thus investigated in the next chapter.

Solution	**Conv. Time (mins)**		**Mean error (cm)**				**Std Dev (cm)**			
	10 cm	*20 cm*	*E*	*N*	*h*	*3D*	*E*	*N*	*H*	*3D*
CPF Flight 1	26	10	-3.6	1.6	0.7	4.4	1.8	1.2	1.6	2
CPF Flight 2	7.5	5	-0.6	-3.3	-10.2	10.8	0.7	0.8	1.7	1.6
CPF Flight 3	8.5	1	-0.7	-0.5	-9.2	9.4	1	1.3	1.4	1.5
CPF Flight 4	*	1	8.1	11.7	-16.3	21.8	1	1.4	2.9	2.7
LH1 Flight 1	7.5	5	-3.6	-1.3	3.3	5.4	1.8	1.1	3.7	3.8
LH1 Flight 2	*	*	27.2	5.1	-5.4	28.2	0.9	1.1	1.6	1.1
LH1 Flight 3	35.5	33.5	0	-5.1	1.1	5.5	1	1.2	1.7	1.3
LH2 Flight 1	n/a	n/a	-16.7	8.5	-13.4	23.1	1.3	1	2.1	1.4
LH2 Flight 2	n/a	n/a	-0.9	9.9	-17.7	20.5	1.1	1	3.1	2.7
LH2 Flight 3	n/a	n/a	-16	-3.9	-8	18.6	1.6	1.5	2.5	1.3
LH2 Flight 4	n/a	n/a	18.8	27	-54.3	63.6	1.9	1.7	2.5	2

Table 5-5. Mean and standard deviations of the coordinate differences between GPS-only PPP and PPK trajectories, applying a 5-degree elevation cut-off angle. The '*' symbols indicate that solutions did not coverage to such an accuracy for the respective flights.

Chapter 6. GNSS PPP-supported photogrammetric bundle block adjustments

6.1 Introduction

Chapter 5 presented trials of PPP on eleven UAV flights, where it was found that positioning accuracies in the range of a few centimetres to a few decimetres could be obtained in both planimetry and height coordinate components. Corresponding precisions, however, were c. 1-4 cm for all flights. This chapter uses these solutions as photogrammetric control through PPP-supported bundle block adjustments (PPP-BBAs) and compares with equivalent PPK-based (PPK-BBA) and GCP-based (GCP-BBA) workflows as reference solutions. The layout of this chapter is as follows. Firstly the employed SfM-photogrammetric software packages are discussed as well as the measures used to assess each workflow. Reference GCP-BBA workflows are then presented along with experimental optimisation, with regards to camera calibration and GCP numbers. Dataset-specific limitations are also examined. Following this, camera positions are determined from UAV PPP and PPK trajectories through camera time synchronisation, interpolation and lever arm correction and errors associated with each step are also discussed. Reference PPK-BBAs are then presented with investigation of camera position weights. Finally, PPP-BBAs are presented and PPP-induced mapping errors are examined. Possible strategies to eliminate such error are also suggested and implemented. The trajectory matching (TM) approach is also implemented with both PPK and PPP positions and compared with standard PPK-BBA and PPP-BBA results.

6.2 Photogrammetry software

As different software packages can give different results due to the employment of different image matching algorithms and BBA routines (Jaud *et al.*, 2016; Murtiyoso *et al.*, 2018), photogrammetric workflows are implemented through two frequently software packages; (1) APERO (Deseilligny and Clery, 2011) and (2) PhotoScan (Agisoft, 2016), to provide a check on the repeatability of solutions.

APERO is a tool for image orientation that has been developed by the Institute Géographique National (IGN) as part of the MicMac software suite. It is operated through a combination of the command line and XML files and has been frequently applied to scientific research (e.g.

Rupnik *et al.*, 2013; Benassi *et al.*, 2017; Murtiyoso and Grussenmeyer, 2017; Murtiyoso *et al.*, 2018). In contrast, PhotoScan is a commercial software package, which has been developed by Agisoft LLC and is operated through a graphic user interface. PhotoScan is often commended for its ease of use and robustness when generating topographic models (Eltner *et al.*, 2016; Murtiyoso and Grussenmeyer, 2017) and is thus highly popular among non-photogrammetrists. For example, 36 of the 65 studies presented in Eltner *et al.* (2016) can be seen to use such a workflow. PhotoScan is also used here in conjunction with the PhotoScan-Monte Carlo approach of James *et al.* (2017) to assist in the determination of optimal GCP numbers for GCP-BBAs through repeat BBAs.

6.3 Workflow steps

APERO and PhotoScan adopt similar workflows, comprising: (1) tie point detection and matching, (2) free network adjustment with camera self-calibration, (3) similarity transformation and (4) BBA with control observations and refined camera self-calibration. These are illustrated in the schematic in Figure 6-1.

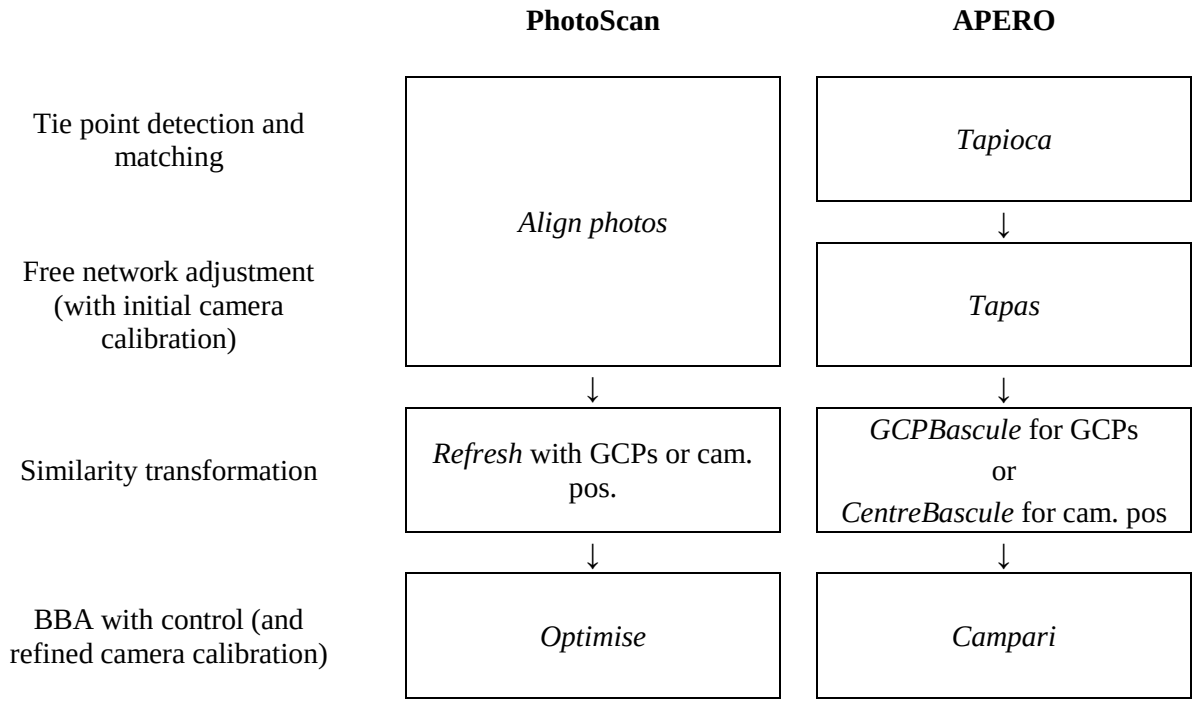

Figure 6-1. APERO and PhotoScan workflow comparison (italics are used to indicate software options/modules)

Tie point detection and matching. For tie point determination, APERO employs an implementation of the SIFT algorithms (through the TAIOPA module) in conjunction with RANSAC for geometric filtering. Although SIFT cannot be parameterised (e.g. to adjust feature

detection thresholds examined by Lingua *et al.*, 2009), image matching was performed at the full image resolution (i.e. the bottom pyramid level) so as not to reduce the localisation accuracy of image tie points from image down-sampling. Although the PhotoScan approach to tie point detection is not discussed in documentation, it is likely to adopt a similar SIFT-RANSAC algorithm. It does, however, allow the specification of a maximum number of key points and tie points per image, for which the values of 400,000 and 40,000 were used respectively. The 'High' accuracy setting was also selected. GPS camera positions were imported into both APERO and PhotoScan to aid the image matching process by indicating likely image pairs.

Free network adjustment. APERO implements the free network adjustment using Essential matrix computations and space resection to generate initial orientation values, followed by an incremental BBA with linearised collinearity condition equations in which global reprojection error is minimised (Deseilligny and Clery, 2011; Rupnik *et al.* 2017). For PhotoScan, details of the free network adjustment are not discussed in documentation, but it is treated as a single step along with tie point detection and matching through the *align photos* option. The free network adjustments also offer optional camera self-calibration.

Camera self-calibration. As the employed consumer grade digital cameras had unknown interior orientation parameters (with the exception of nominal focal length), 12 convergent images (90 degrees rotated) of a specifically designed camera calibration target were taken prior to each flight for an offline calibration in Photomodeler software (version 6.4.0, build 821). However, due to target focusing issues, the calibration imagery could not be used and thus a self-calibrating BBA was resorted to. On this subject, the internal geometry of consumer grade digital cameras is also usually regarded as unstable, particularly principal point and focal length due to the flexible lens alignments incurred from the use of variable zoom lenses (Fraser, 2013; Luhmann *et al.*, 2016; Carbonneau and Dietrich, 2017). Therefore, employing a camera self-calibration represents a practical and realistic scenario.

APERO and PhotoScan both implement the Brown (1971) camera model, comprising radial and tangential components, as well as Fraser's extended camera model, comprising differential axis scale (affine) and non-orthogonality (skew) parameters. These models are commonly used in the BBA and are expressed as follows (Fraser, 1997; Fraser, 2013):

$$dx = -\frac{\bar{x}}{f}\Delta f + \bar{x}K_1.r^2 + \bar{x}K_2.r^4 + \bar{x}K_3.r^6 + P_1(r^2 + 2\bar{x}^2) + 2P_2\bar{x}\bar{y} + b_1\bar{x} + b_2\bar{y} \quad (6\text{-}1)$$

$$dx = -\frac{\bar{y}}{f}\Delta f + \bar{y}K_1.r^2 + \bar{y}K_2.r^4 + \bar{y}K_3.r^6 + P_2(r^2 + 2\bar{r}^2) + 2P_1\bar{x}\bar{y} \quad (6\text{-}2)$$

where

$$r = (\bar{x}^2 + \bar{y}^2)^{-1/2} \quad (6\text{-}3)$$

Here dx and dy are the image point correction terms, $\bar{x}$ and $\bar{y}$ are the image point coordinates in the principal point coordinate system, Δf is the focal length correction term, K_1 to K_4 are the radial distortion coefficients, P_1 and P_2 are the tangential (decentring) distortion coefficients, b_1 and b_2 are correction terms for differential axis scale and non-orthogonality (skew) respectively.

Variations of the Brown (1971) camera model, with the Fraser (2013) extended parameters were implemented. In the self-calibrating BBA, focal length is initialised from the image metadata, principal point coordinates from the image centre, and distortion parameters are initialised as null. Whilst the self-calibrating BBA is implemented for all flights, a suitable camera model is determined on the basis of check point errors, as will be presented in Section 6.5.3.

Similarity transformation. After the (self-calibrating) free network adjustment, a similarity transformation is then computed in APERO using the *GCPBascule* or *CentreBascule* module, and PhotoScan, using the *update* option, by linking known model coordinates to real world values, for either camera positions or GCPs.

BBA with control. Control observations are then included in the BBA, using the *CAMPARI* module of APERO or *Optimise* option in PhotoScan. Control information comprised GCPs (for GCP-BBAs) or camera positions (for PPK or PPP-BBAs) depending on which method was being followed. Approximate values of the parameters were used from the free network adjustment. Tie points are assigned *a priori* standard deviations based on the final RMSE of the image residuals obtained from the free network adjustment.

In all cases, the BBA minimises the sum of the differences between the observations and their final estimated values, weighted according to the reciprocal of their squared *a priori* standard deviations, in consideration of all other weighted constraints. The relevant settings to

parameterise the stochastic model in APERO and PhotoScan are presented in Table 6-1. It should also be noted that in any least squares adjustment, parameter observations should be weighted according to their expected precision, despite PhotoScan options referring to the accuracy.

Observation	**PhotoScan (*Reference Settings*)**	**APERO (*Campari* – command line)**
Camera positions (m)	Camera accuracy = XYZ	EmGPS = [coordinate file, XY, Z]
Manual GCP image measurements (pix)	Marker accuracy = XY	GCP = [coordinate file, XYZ, image measurement file, XY]
GCP coordinates (m)	Marker accuracy = XYZ	
Tie point measurement (pix)	Tie point accuracy = XY	SigmaTieP = XY

Table 6-1. Setting of *a priori* standard deviations in APERO and PhotoScan. *XYZ, XY, Z refer to the (allowed) specified value in 3D, 2D and 1D respectfully.

6.4 Bundle block adjustment assessment

A number of measures were used to assess the quality of BBAs, which have been broken down into internal, referring to BBA statistics, and external referring to verification through independent solutions for parameters determined by the BBA, such as reference coordinates.

6.4.1 Internal quality measures

Bundle block adjustment residuals. Observation residuals are used as the first measure of orientation error, which denote the differences between the observation values and respective values according to the least squares estimated model. Tie point residual error, or *reprojection error* from the free network adjustment is used to indicate the quality of tie point matching (James *et al.*, 2017), whilst indicating tension between tie points and control observations, especially if the latter are optimistically weighted (Rupnik *et al.*, 2015; Stöcker *et al.*, 2017). The orientation of residuals at GPS camera positions is also used to highlight possible GPS or image tie tag errors (Rehak and Skaloud, 2017b).

Parameter standard deviations and correlations. Parameter precision estimates and correlations (as obtained from the covariance matrix of the parameters; Mikhail *et al.* 2001; Wolf and Ghilani, 2006) are used to evaluate over-parameterization, and hence the selection of a suitable camera model. For example, a parameter is excluded from the self-calibrating BBA

if it is deemed to be highly correlated with another parameter (Granshaw, 1980; Lichti *et al.*, 2008). Such correlations are now made available by PhotoScan (version 1.3.4), and thus PhotoScan is used to select the appropriate camera model for both workflows.

6.4.2 External quality measures

To determine the external accuracy of object points, independent reference data is used.

Check points. External accuracy assessment is carried out by comparing independently surveyed check points to their photogrammetrically-derived coordinates. Mean and standard deviation of the errors at independent check points can allow the detection of systematic shifts (datum) and block deformations (Stöcker *et al.*, 2017). As per James *et al.* (2017), check point errors are also used to assist in the selection of the camera model by selecting parameters that reduce the RMSE at the check points and GCPs. As was detailed in Chapter 4, independent check points were surveyed using high precision terrestrial GPS.

Reference point clouds. As check points only offer a sparse sample of the object point accuracy (albeit with a high reliability), reference point clouds such as those generated by TLS, can provide a denser overview of the object point error distribution, but with a lower reliability (Eltner and Schneider, 2015; Eltner *et al.*, 2016). Although TLS data was not acquired, relative accuracy (and error distribution) is assessed by comparing 3D tie point coordinates over the whole image block for each processing scheme (as per Stöcker *et al.*, 2017). This also negates the requirement for any error-inducing interpolation schemes due to different point distributions, as required when using TLS point cloud data (Eltner *et al.*, 2015; Smith and Vericat, 2015) because each 3D tie point will have a corresponding point in the reference point cloud (for example, when comparing PPP-BBAs against corresponding GCP-BBAs solutions). Relative accuracy is pursued for the detection of systematic error differences.

6.5 Optimising GCP-BBAs

Reference GCP-BBAs for each dataset were implemented in three steps to ensure optimal reliability. Firstly, to assess image measurement quality, image residuals from the free network BBAs, corresponding to both tie points and target measurements, were inspected and outlying observations removed. Secondly, to determine a suitable camera model, BBAs were optimised in PhotoScan with a number of camera models and with c. 50% of targets used as GCPs. The camera model was selected as that which reduced mapping errors assessed at remaining check points, whilst PhotoScan parameter correlations were also inspected for confirmation. Finally, to determine optimal GCP numbers, a PhotoScan-Monte Carlo approach was used for each dataset.

6.5.1 Image preparation

Prior to image processing, care was taken to remove images deemed unsuitable for image processing. Firstly, *blurry* images were removed from each dataset (for example, images in which ground targets could not be distinguished). For the Cockle Park Farm datasets which comprise flight paths spanning far outside the target field, only images acquired as part of the pre-defined image strips were retained (and those acquired during turning manoeuvres were discarded). For the Low Hauxley datasets, which border the coastline, images containing more than c. 40% water were also removed because of the potential for erroneous tie points corresponding to dynamic water features. Such a percentage was determined from experimentation.

6.5.2 Image observations

To assess image observations, PhotoScan and APERO free network adjustments were executed with self-calibration of a basic camera model, comprising focal length, principal point and three radial lens distortion parameters (K1-K3) as per James *et al.* (2017). PhotoScan tie points were first visually inspected and off-terrain (anomalous) solutions were discarded. This typically resulted in the removal of between 100 and 500 tie points per dataset. The *Gradual Selection* tool was also used to remove tie points with reprojection error exceeding three pixels, which resulted in the further exclusion of between c. 10,000 and c. 100,000 tie points per dataset (a maximum 99,690 for CPF Flight 2) although these still only accounted for c. 5% of all tie points. This step was not replicated in APERO because reprojection error per tie point could not be recovered. APERO does, however, provide the RMSE of the image residuals per image, and therefore images with larger values (typically greater than two pixels) were also excluded. For consistency among software packages, the same images were also excluded from the

corresponding PhotoScan workflow. At most, three images were excluded (from L2 Flight 2) from any dataset. The final RMSE of the image tie point residuals from APERO and PhotoScan are presented in Table 6-2 for each dataset. Values fall between 0.7 and 1.3 pixels in PhotoScan and c. 0.8 and 1.0 in APERO, which are approximately consistent in magnitude between flight and software. The average values over all datasets of c. 0.8 pixels and c. 1 pixel for APERO and PhotoScan respectively were used as *a priori* estimates of the image tie point precisions from respective software packages, and thus for weightings in subsequent BBAs.

Following on, image measurements of ground targets were made manually in PhotoScan and the free network adjustments were re-optimised (i.e. without importing target coordinates). Ground targets with larger reprojection errors were inspected and image measurements were amended (i.e. manually adjusted) to reduce respective reprojection errors. If this was not possible (i.e. reprojection error did not reduce), image measurements were excluded. The final RMSE of the target image measurement residuals per dataset are also given in Table 6-2, where values are seen to range between c. 0.7 and 1.6 pixels. Image measurements of ground targets were finally exported from PhotoScan for use in APERO.

Dataset	**APERO**	**PhotoScan**	
	TP image res.	**TP image res.**	**Target image res.**
CPF Flight 2	0.822	1.325	1.447
CPF Flight 3	0.807	1.329	1.563
LH1 Flight 1	0.765	0.976	1.338
LH1 Flight 2	0.951	1.026	1.244
LH1 Flight 3	0.742	0.739	0.867
LH2 Flight 1	0.883	1.054	1.112
LH2 Flight 2	0.781	0.976	0.651
LH2 Flight 3	0.829	1.007	0.765
LH2 Flight 4	0.740	0.761	0.815
Mean:	**0.813**	**1.021**	**1.089**

Table 6-2. Free network adjustment RMS image residuals for tie points (APERO and PhotoScan) and target image measurements (PhotoScan only). TP = Tie Points

6.5.3 Camera model selection

Having obtained estimates of tie point and target image measurement precision, surveyed ground coordinates of targets were imported into PhotoScan for the determination of a suitable

camera model. This step was again only performed in PhotoScan because of its ability to compute camera model parameter correlations to assess over-parametrisation. 50% of targets were assigned as GCPs and the remainder as check points. For each dataset, GCP-BBAs were run with the five camera models presented in Table 6-3. Image tie point and target image measurements were assigned *a priori* standard deviations of 1.0 pixels from the previous step.

Camera model	No of parameters
Focal length + principal point	3
Focal length + principal point + K1	4
Focal length + principal point + K1-K3	6
Focal length + principal point + K1-K3 + P1-P2	8
Focal length + principal point + K1-K3 + P1-P2 + affinity + skew	10

Table 6-3. Tested camera models

GCP residuals and check point errors obtained with each camera model are presented in Figure 6-2. This generally shows that all such values reduce with an increasingly complex camera model. The greatest improvement in both the GCP residuals and check point errors are seen with the additional estimation of K1 (over only focal length and principal point) and the additional estimation of P1-P2 (tangential lens distortion). On the contrary, the effects of estimating K1-K3 over K1 only are only visible for check point errors for CPF Flight 3, with negligible effects among remaining datasets. Moreover, the additional estimation of b1-b2 (affine and skew parameters) only improves check point errors for the CPF and LH2 flights, which coincidently share the same Sony camera.

In addition to the GCP residual and check error statistics, PhotoScan camera model parameter correlations are presented in Table 6-4. Here high correlations (exceeding 90%) are indicated between the K1-K2, K1-K3 and K2-K3 combinations for all datasets, whilst their lack of contribution in Figure 6-2 confirms their high projective coupling. K2 and K3 are therefore excluded from all camera models. P1 is also highly correlated with cx (the X principal point coordinate) for almost all datasets. However, because including P1 improves check point errors for all datasets (Figure 6-2), it is retained in final camera models. Table 6-4 also suggests high correlation of b1 with cy and also b2 with cx. As improvements to check point errors are seen for the CPF and LH1 flights, b1 and b2 are retained in the final camera model for these flights. However, with b1-b2 offering little improvement to check point errors of the LH2 flights

(coincidently, using a different camera), b1 and b2 are excluded for these datasets. The final selected camera models per flight are presented in Table 6-5.

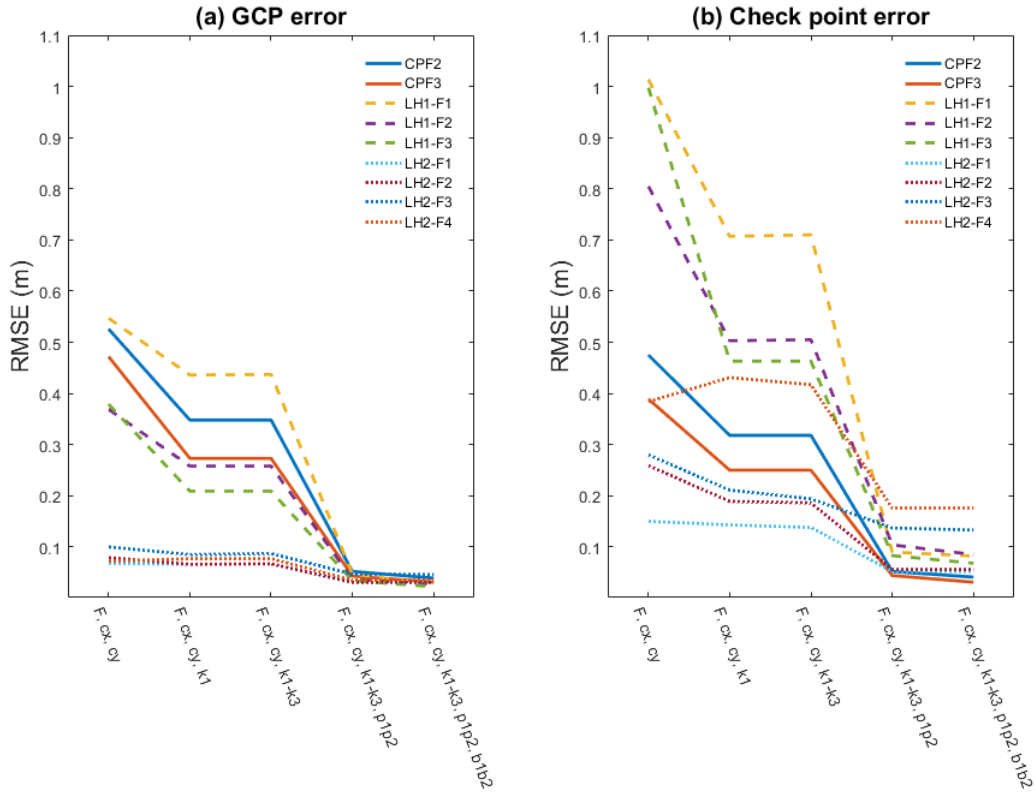

Figure 6-2. The effect of camera model on (a) GCP residuals and (b) check point error, using 50% of targets as GCPs and assigning all image tie and target point measurements an *a priori* standard deviation of 1.0 pixels.

Parameter combination	**Flight**								
	CPF F2	**CPF F3**	**LH1 F1**	**LH1 F2**	**LH1 F3**	**LH2 F1**	**LH2 F2**	**LH2 F3**	**LH2 F4**
F-cy	-0.48	-	-0.41	-0.51	-0.32	-0.53	-0.59	-0.55	-0.48
cx-b2	-	-	0.42	-	0.53	-	0.38	-	-
cx-p1	0.51	0.54	0.61	0.43	0.48	-	0.51	0.48	0.41
cy-b1	-	-	-0.45	-	-0.56	-0.50	-0.52	-0.55	-
cy-p2	-	0.44	0.52	-	0.38	0.45	0.48	0.48	-
k1-k2	-0.96	-0.96	-0.94	-0.95	-0.94	-0.96	-0.95	-0.94	-0.94
k1-k3	0.91	0.90	0.88	0.89	0.87	0.90	0.89	0.88	0.88
k2-k3	-0.98	-0.98	-0.98	-0.98	-0.98	-0.98	-0.98	-0.98	-0.98

Table 6-4. PhotoScan camera model parameter correlations for all datasets. Only showing values exceeding a 0.3 magnitude.

Camera model	Flights
Focal length + principal point + K1 + P1-P2 + affinity + skew	CPF and LH2 flights
Focal length + principal point + K1 + P1-P2	LH1 flights

Table 6-5. Final camera models

6.5.4 GCP numbers (PhotoScan-Monte Carlo approach)

With selected camera models and observation weights, the PhotoScan-Monte Carlo approach of James *et al.* (2017) was used to determine a suitable number of GCPs. This involved the execution of GCP-BBAs for a range of GCP numbers, with the latter being specified by a percentage of the total number of targets to be used as GCPs, hereafter referred to as the GCP percentage. 50 GCP-BBAs were run for each GCP percentage, each with randomly elected GCP distributions. GCP percentages were varied from 10-80% for the CPF datasets and 20-90% for the LH1 and LH2 flights with 10% increments. The higher GCP percentage range for the LH1 and LH2 flights was used due to the worse GCP distribution compared to that of the CPF flights. Figure 6-3 shows the distribution of plan and height coordinate RMSEs evaluated at remaining check points, as well as median values, for each of the 50 GCP-BBA iterations per GCP percentage for all flights.

For the CPF flights, Figure 6-3 shows that median plan and height coordinate RMSEs generally stabilise at around 5 cm with variations of c. +/- 1 cm for GCP percentages of 40% and greater. With the exception of LH1 Flight 1, the same can also be said for the LH1 and LH2 flights, but for GCP percentages of 50% and greater. Over all flights, it is generally seen that the spread of plan coordinate RMSEs is relatively small compared to those in height for each GCP percentage. This is particularly the case for LH1 Flights 1 and 2 as well as LH2 Flight 4, where, even for GCP percentages of 50% (equivalent to c. 20 GCPs), the spread of height RMSEs remains around 10 cm. Harwin *et al.* (2015) also showed that the vertical accuracy of GCP-BBAs is most susceptible to the GCP distribution (although in their case, only comparing 5- and 13-GCP configurations). Particularly for the lower GCP percentages, this is suggestive of a large dependence of mapping error on GCP distribution for these datasets. This an inherent limitation of relying on GCPs, and although a suitable number and distribution of GCPs can be selected here for an optimal workflow, in other applications where the placement of GCPs is more restricted, this may be a more serious problem. As median check point RMSEs (in plan and height) generally settle beyond GCP percentages of 40% for the CPF flights and 50% for the LH1 and LH2 flights, the equivalent GCP numbers (i.e. 16 GCPs and 19 GCPs, respectively) were selected for subsequent processing.

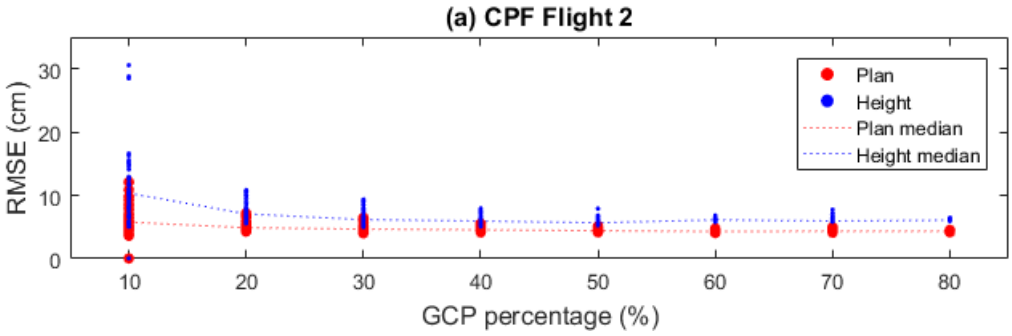
(a) CPF Flight 2
RMSE (cm)
GCP percentage (%)
Plan
Height
Plan median
Height median

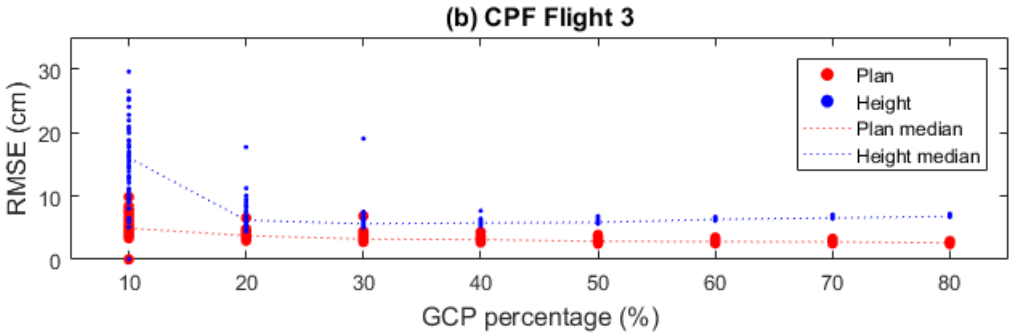
(b) CPF Flight 3
RMSE (cm)
GCP percentage (%)
Plan
Height
Plan median
Height median

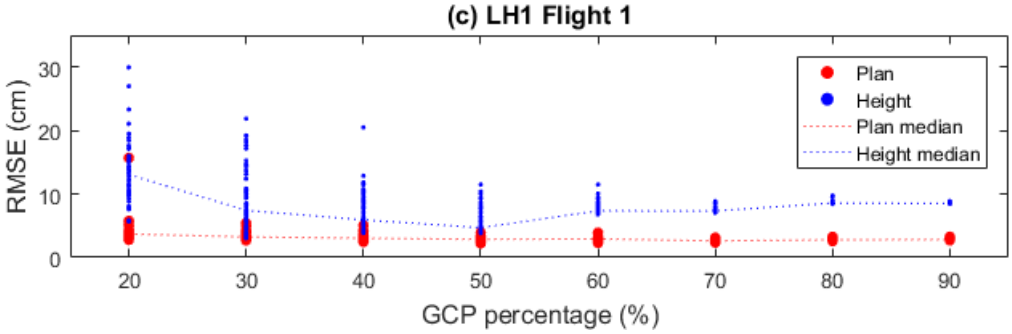
(c) LH1 Flight 1
RMSE (cm)
GCP percentage (%)
Plan
Height
Plan median
Height median

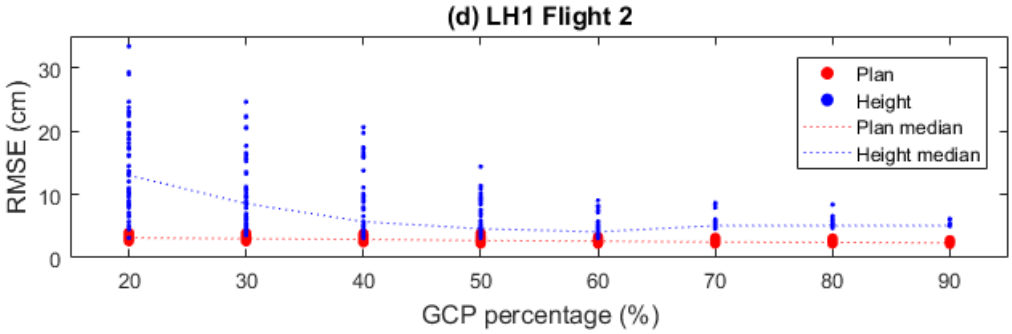
(d) LH1 Flight 2
RMSE (cm)
GCP percentage (%)
Plan
Height
Plan median
Height median

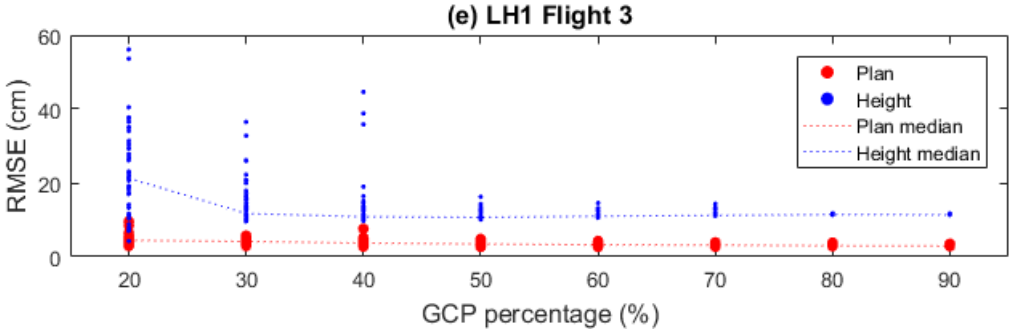
(e) LH1 Flight 3
RMSE (cm)
GCP percentage (%)
Plan
Height
Plan median
Height median

Continued…

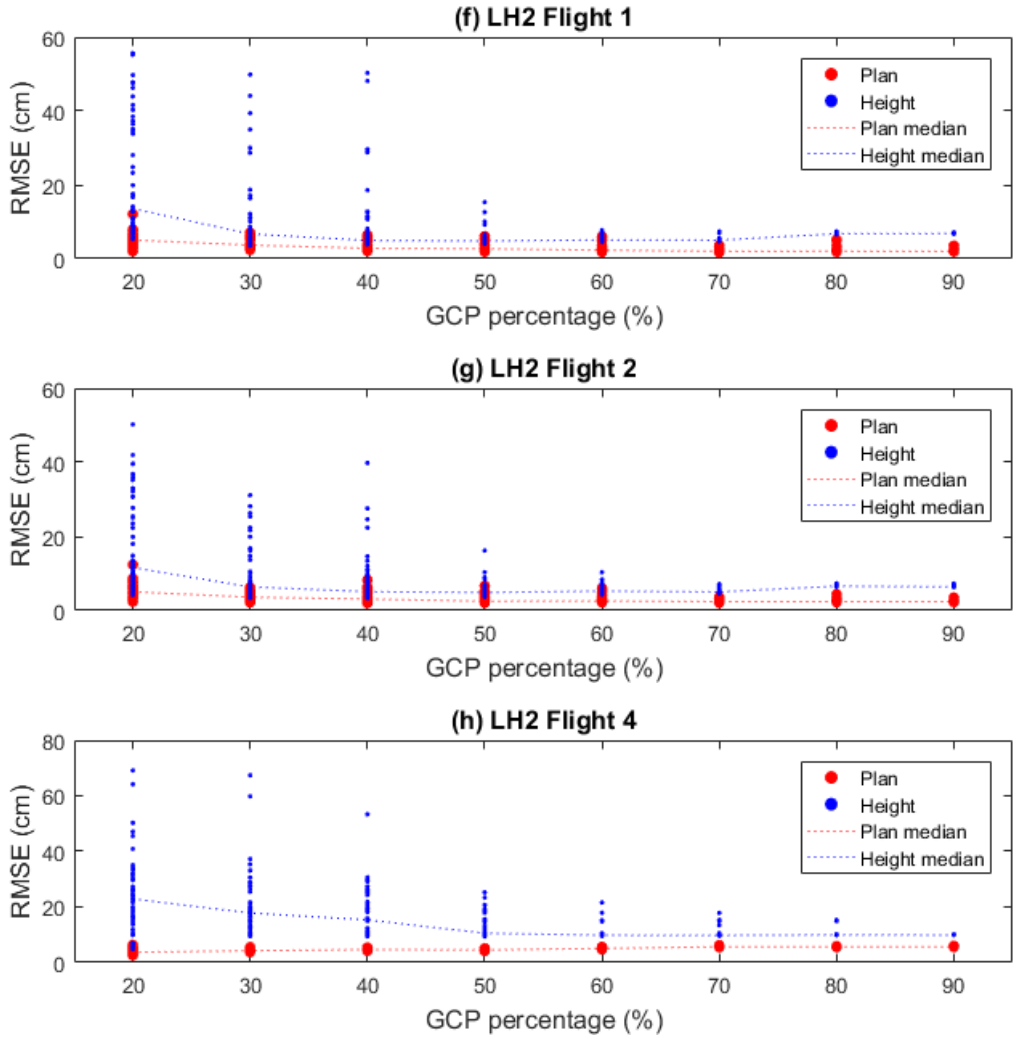

Figure 6-3. PhotoScan-Monte Carlo results: check point RMSE vs. GCP percentage. Each GCP percentage has one data point for each of the 50 BBA runs with random GCP allocation. Dotted lines link the respective median RMSE values for each GCP percentage.

6.5.5 Selected GCP distributions

Final GCP configurations were selected to ensure that (1) remaining check points fell within the convex hull formed from elected GCPs and (2) GCPs were evenly distributed throughout the target network. This also ensured that remaining check points (i.e. 24 and 20, respectively) conformed to a similar distribution. Final GCP and check point configurations are presented in Figure 6.4 and Figure 6.5 for the Cockle Park Farm and Low Hauxley datasets respectively. GCP-BBAs were finally optimised with the final GCP distributions. Figure 6-6 displays check point RMSEs and standard deviation obtained with APERO and PhotoScan respectively (the APERO results for CPF Flights 2 and 3 are also presented in Grayson *et al.* (2018)). With the exception of LH2 Flight 3, easting and northing coordinate RMSEs and standard deviations are better than 1 pixel for all flights and both software packages.

Figure 6-4. Final GCP and check point configurations at Cockle Park Farm

Figure 6-5. Final GCP and check point configurations at Low Hauxley

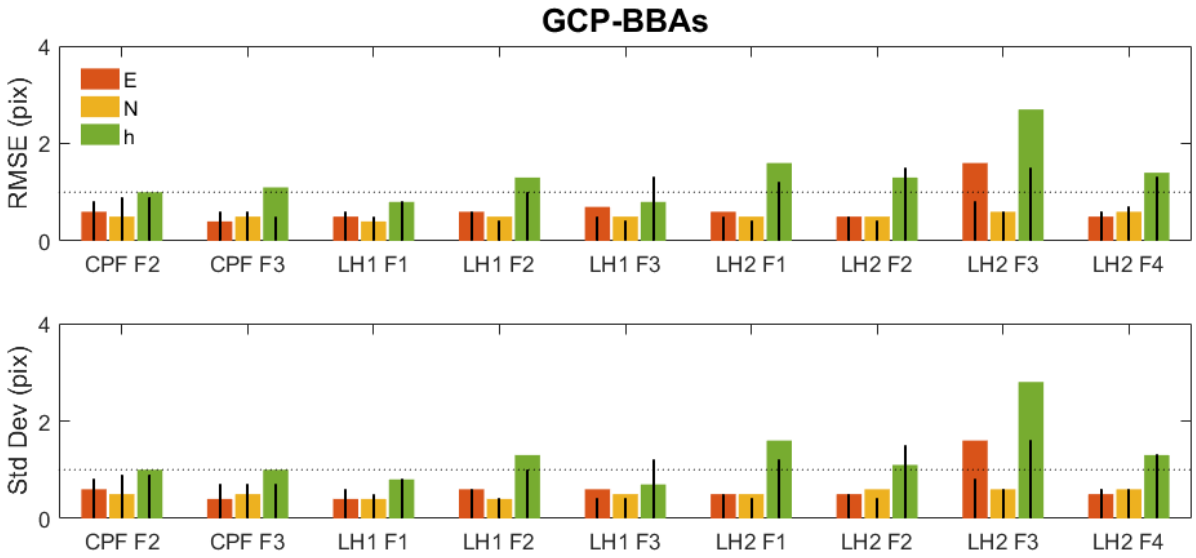

Figure 6-6. Check point RMSEs and standard deviations for GCP-BBAs from APERO software (coloured bars) and PhotoScan software (black bars). 16 GCPs are used for the CPF flights and 19 GCPs are used for LH1 and LH2 flights. Dotted line indicates a 1 pixel value.

Height coordinate RMSEs, however, are noticeably worse for all flights, ranging between c. 1 and 3 pixels for APERO and c. 1 and 1.5 pixels for PhotoScan. Larger height than plan coordinate RMSEs can be expected due to the inherent geometry of the image block, with image orientation error (in particular x-parallax errors) primarily propagating into object point height coordinates (e.g. Kraus, 2007; Harwin *et al.*, 2015). To further inform, Table 6-6 also presents the number of images, images strips, tie points (from APERO and PhotoScan) and average number of image projections per target for each dataset. Noting that vertical block deformation is most evident for the LH2 flights, Table 6-6 shows that these flights have the smallest number of tie points (per software), image strips, and projections per target. Moreover, the lowest respective values for LH2 Flight 3 reflect the largest height coordinate RMSEs in Figure 6-6. Thus it can be inferred that the LH2 flights have the weakest image block configurations. The fewer number of target projections for LH2 Flight 3 also relates to a large number of images being corrupted by a failing SD card which unfortunately fell primarily over the ground targets.

Flight	CPF F2	CPF F3	LH1 F1	LH1 F2	LH1 F3	LH2 F1	LH2 F2	LH2 F3	LH2 F4
Images	663	732	476	423	505	340	277	197	233
Long strips	18	18	15	16	12	14	11	8	13
Cross strips	1	2	0	0	4	0	0	0	0
# of APERO tie points (x10^6)	16.7	16.1	13.6	7.2	13.2	2.5	2.1	1.1	4.8
# of PhotoScan tie points (x10^6)	3.3	3.9	5.0	3.5	5.9	1.8	1.6	1.3	1.6
Av. # of target projections	14	16	19.8	11.4	9.1	7.4	7.2	5.0	6.8

Table 6-6. Image block statistics: number of images and image strips, tie points (from APERO and PhotoScan) and average number of image projections per target

6.6 Camera position determination

In this section, the GPS trajectories are further processed to determine GPS camera positions. This involves time synchronisation and interpolation, and the derivation and application of lever arm corrections (Curry and Schuckman, 1993). Because GPS camera positions with centimetre accuracy are sought, each step is examined for the presented datasets to give a final accuracy estimate of the GPS camera positions prior to implementing GPS-BBAs.

6.6.1 Related literature

Time synchronisation. To obtain a GPS position for each image, image acquisition must be synchronised with GPS data acquisition. Image acquisition times must be recorded in the GPS trajectory time frame, hereafter termed *image time tags*, so that GPS positions may be geometrically interpolated to these times. Any error in image time tags, hereafter termed *camera time synchronisation error*, translates into a GPS camera position offset along the GPS trajectory. In manned aerial photogrammetry, image time tags are typically logged with an accuracy of around 50 µm, equivalent to a position uncertainty of around 4 mm at an 80 m/s aircraft speed (Gruen *et al.*, 1993). On the contrary, fixed wing UAV velocities are relatively low, at around 18-20 m/s, and therefore image time tag accuracy requirements may be reduced. According to Rehak and Skaloud (2017b), there are four methods for the time synchronisation of consumer grade cameras which are hereafter summarised:

1. *Correlating the image acquisition time in the image EXIF with the GPS log* which is typically sufficient for providing approximate camera position values for the BBA.
2. *Time stamping the trigger pulse sent from the autopilot* which has greater accuracy, but is highly sensitive to shutter lag or camera exposure delay errors and is thus only sufficient for slow-moving platforms, such as rotary wing UAVs.
3. *Processing the camera flash signal* which involves recoding the camera flash signal as an event input within the GPS receiver (Jozkow and Toth, 2014). Here the camera flash signal is sent at the precise moment of image exposure via the *hotshoe,* although a small residual error may exist if the flash signal is not sent at the mid-point of image exposure. This method is accurate to 5-10 ms (Eling *et al.*, 2015).
4. *Recording the signals of the mechanical shutter curtains* which is the most accurate, but involves interfacing the camera circuit board directly and thus requires a difficult hardware modification, unlike the former method requiring only a *hotshoe* attachment.

Rehak and Skaloud (2017b) showed that time synchronisation errors can be analysed on the basis of camera position residuals in the BBA. By processing the camera flash *signal*, they calculated a camera exposure delay of 6.2 ms. They devised an adjustment model to account for this synchronisation error in the BBA (without GCPs) but only managed to reduce object point errors by 1-2 cm in plan and primarily in the Y coordinate component owing to the orientation of the image strips. Without the adjustment model, they expected the 6.2 ms exposure delay to be absorbed by the residuals and estimated IOPs (Rehak and Skaloud, 2017b). In addition, Gerke and Przybilla (2016) speculated that camera exposure delays may be minimised by flying image blocks in regular strips and maintaining a constant velocity. Under this configuration, the assumption was made that time synchronisation errors translate to GPS camera position errors with similar magnitude in each strip, but opposite signs respective of the flying direction so that they 'average out'.

Time interpolation. With the recorded image time tags, GPS positions must be geometrically interpolated. However, the suitability of a given interpolation scheme depends on the platform dynamics and the sampling rate of the GPS data (Lichti, 2002). As trajectories of manned aircraft generally exhibit gentle, low frequency variations, purely mathematical approaches have been deemed sufficient (e.g. Gruen *et al.*, 1993). For example, Lichti (2002) tested linear, quadratic and windowed sinc functions for manned aerial platforms. By observing perspective centre residuals for a 1 Hz interpolated trajectory, they showed linear interpolation to out-perform quadratic and windowed sinc interpolation by c. 1 cm (RMSE). With regards to the

data rate, they showed height perspective centre residuals are improved by a factor of 2.5-3 times when interpolating from a 10 Hz trajectory over 1 Hz. In the BBA, however, they showed negligible (< 1 cm) differences in check point errors when using either interpolation approach, or 1 or 10 Hz data rate. They concluded the data rate to be most important over the interpolation method with regard to camera positioning accuracy. The Lichti (2002) study, however, applies only to manned aerial platforms.

In the context of UAV literature, the implications of interpolation scheme have rarely been discussed. For example, Jozkow and Toth (2014) aplied a simple linear interpolation from their 5 Hz GPS positions for a rotary wing UAV traveling at 3 m/s. As the dynamics of UAV trajectories are quite different to that of a manned aerial platforms, for example regarding turning frequency, it is argued here that the UAV case should be considered independently.

Lever arm correction. With GPS positions obtained at image acquisition times (from camera time synchronisation and time interpolation), a so-called lever arm correction is required to reduce antenna reference point (ARP) positions to camera perspective centre positions. Determining lever arm corrections firstly requires knowledge of the physical offset vector (POV) between the ARP and camera perspective centre, and secondly, measurement of the POV instantaneous orientation (heading, roll and pitch) in the mapping frame.

For manned aerial platforms, POV magnitudes are typically large, at the metre-level and are measured pre-flight by conventional surveying techniques (e.g. Gruen *et al.*, 1993). With large POV magnitudes the required accuracy of IMU rotation angles increases because rotation angle errors propagate into a greater positional (lever arm correction) error, although Ackermann and Schade (1993) also suggested (in the manned aerial platform context) that lever arm corrections may be neglected with the exception of applying a constant vertical shift to the camera height if the camera and GPS antenna are vertically aligned. On the contrary, for UAVs, POV magnitudes are usually small, typically at the decimetre level (e.g. Jozkow and Toth, 2014) and thus lower accuracy MEMs-type IMU rotation angles may suffice. For example, for the UAV-determined orthomosaics of Turner *et al.* (2014), the application of lever arm corrections improved check point errors (RMSE) in planimetry from 19.0 cm to 11.5 cm. It is also noteworthy in other examples, that constant vertical offsets are sometimes applied without any IMU-based corrections (e.g. Jozkow and Toth, 2014).

Method and tests. In the following, aspects of time synchronisation, time interpolation and lever arm corrections are implemented and evaluated for the presented datasets. Firstly, expected time interpolation error is evaluated with respect to the interpolation strategy and data

rate. Secondly, lever arm corrections are determined and applied. Finally, an indication of final GPS camera position error is given by comparing with GCP-BBA estimated camera positions, which are independent of errors associated with time synchronisation, time interpolation and lever arm corrections.

6.6.2 Time interpolation strategy

Because UAV GPS logging rates varied between 2 Hz and 10 Hz, different levels of time interpolation error can be expected, whilst also varying from those observed by Lichti (2002) due to differing UAV aerial dynamics. The influence of data rate on expected UAV time interpolation error was investigated by down sampling UAV trajectories before mathematically interpolating back to the initial data rate for the determination of coordinate RMSEs. The influence of the interpolation strategy was investigated by implementing both linear and spline interpolation. Linear interpolation was investigated because of its simplicity and also good performance for 1 Hz manned aerial platform trajectories in Lichti (2002), whilst it was expected that spline interpolation might better accommodate the increased aerial dynamics of the fixed wing UAV.

Time interpolation tests and results. Figure 6-7 shows the interpolation error (RMSE) statistics for data rates of 0.2 s, 0.5 s, 1.0 s, 2.0 s for both linear (Figure 6-7a) and spline (Figure 6-7b) interpolation. As GPS data was logged at 10 Hz for the CPF flights, this was down-sampled from, and evaluated at, a data rate of 0.1 s. However, as GPS data was logged at a lower rate of 2 Hz for the LH1 and LH2 flights, this was down sampled from, and evaluated at a rate of 0.5 s and hence Figure 6-7 does not present data points for data rates shorter than 1 s for these flights.

From Figure 6-7, it is seen that plan interpolation error increases more rapidly with a reduced data rate for linear interpolation over spline interpolation, with RMSEs of c. 50 cm and c. 90 cm when interpolating from a 2 s data rate. However, for data rates of 0.5 s and 0.2 s, plan RMSEs for the linear and spline interpolation errors are in much closer agreement. For linear interpolation, plan RMSEs are 6-8 mm and 40-42 mm for data intervals of 0.2 s and 0.5 s respectively, whilst these values are only 2-4 mm and 5-8 mm cm for spline interpolation. Regarding the height errors, the linear and spline interpolation strategies are approximately equivalent for all data rates. This might be expected due to the smaller UAV height variation compared to that in plan, enabling it to be equally accommodated by either interpolation strategy.

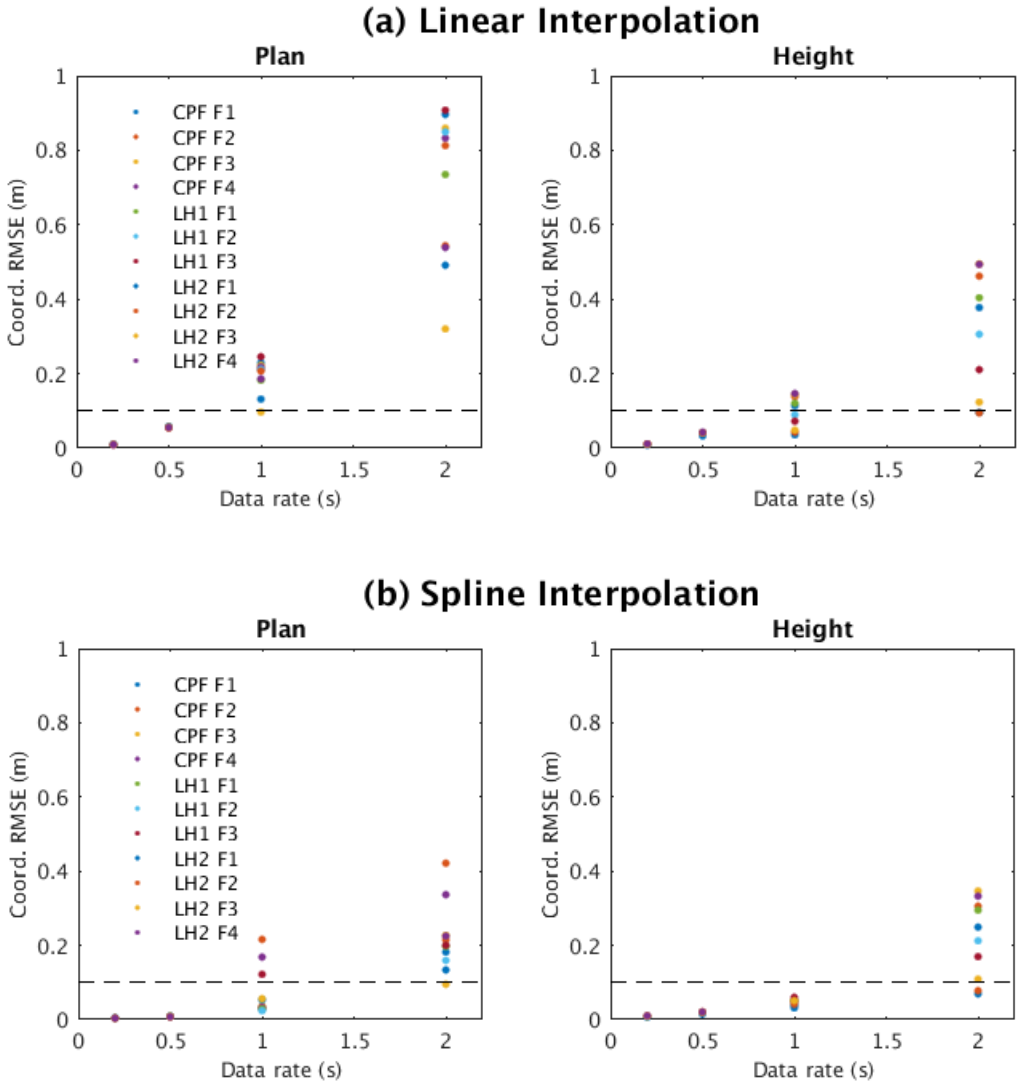

Figure 6-7. Effect of initial (GPS) data rate on interpolation error (shown as coordinate RMSE) when applying (a) linear and (b) spline interpolation.

As spline interpolation outperforms linear interpolation in plan at the 0.2 s and 0.5 s data rates, spline interpolation is adopted for subsequent processing. Accordingly, for the 0.1 s data rate of the CPF flights, interpolation errors are expected to be less than 5 mm, whilst for the 0.5 s data rate of LH1 and LH2 flights, these are expected to be less than 20 mm. Such interpolation errors can thus be considered negligible with respect to possible GPS-related errors. However, had linear interpolation been applied for the LH1 and LH2 flights, interpolation errors of up to 4 cm could have been expected, which might be considered incommensurate with the 2-3 cm expected carrier phase GPS positioning error. For data rates of 1 s, as per Lichti (2002), these results suggest interpolation errors of up to 20 cm could be expected, thus highlighting the difference in the aerial dynamics of a UAV compared to a manned aerial platform.

6.6.3 Lever arm correction strategy

For the determination of lever arm corrections, UAV pitch, roll and heading angles were recorded at 10 Hz and with an assumed accuracy of c. 5 degrees, which is typical of low cost UAVs equipped with a MEMS-based IMU (e.g. Turner *et al.*, 2014). As commercial systems were used, the raw IMU data was not obtainable and thus processed output rotation angles were used. In the UAV log files, the pitch (elevation) angles were given as positive for nose up with zero at the horizontal, the roll (bank) angles were given as positive for right wing down where zero is at the horizontal and heading was given as a whole-circle compass bearing. Lever arm corrections were then derived as follows: Firstly, UAV pitch, roll and heading angles were extracted based on their correspondence with image time tags. Due to their limited expected accuracy, time interpolation of the pitch, roll and heading angles was not performed, but angles recorded closest to the corresponding image time tag were selected. Secondly, the physical offset vector (POV), detailing the ARP to camera perspective centre offset in the UAV body frame, was rotated according to the extracted IMU rotation angles to derive the lever arm correction. Finally, these were added to the GPS coordinates.

With an (assumed) IMU rotation angle accuracy of c. 5 degrees, and maximum POV magnitudes of 12.8 cm for the presented datasets (i.e. for the Q200 flights), IMU rotation angle errors would only propagate to camera position errors of c. 1 cm and are thus commensurate with the 2-3 cm expected carrier phase GPS positioning error. To illustrate the successful application of lever arm corrections, Figure 6-8 shows the corrections for two flight turns of LH2 Flight 2, where the POV is 0.0 cm, 0.0 cm and -12.8 cm in X, Y and Z in the body frame, respectively. The top panel illustrates a right hand turn, where the camera position is seen to swing out to the right of the ARP, whereas the bottom panel illustrates a left hand turn where the camera position is seen to swing out to the left of the ARP. When mid-way through a flight line, the lever arm correction is primarily to the camera position height.

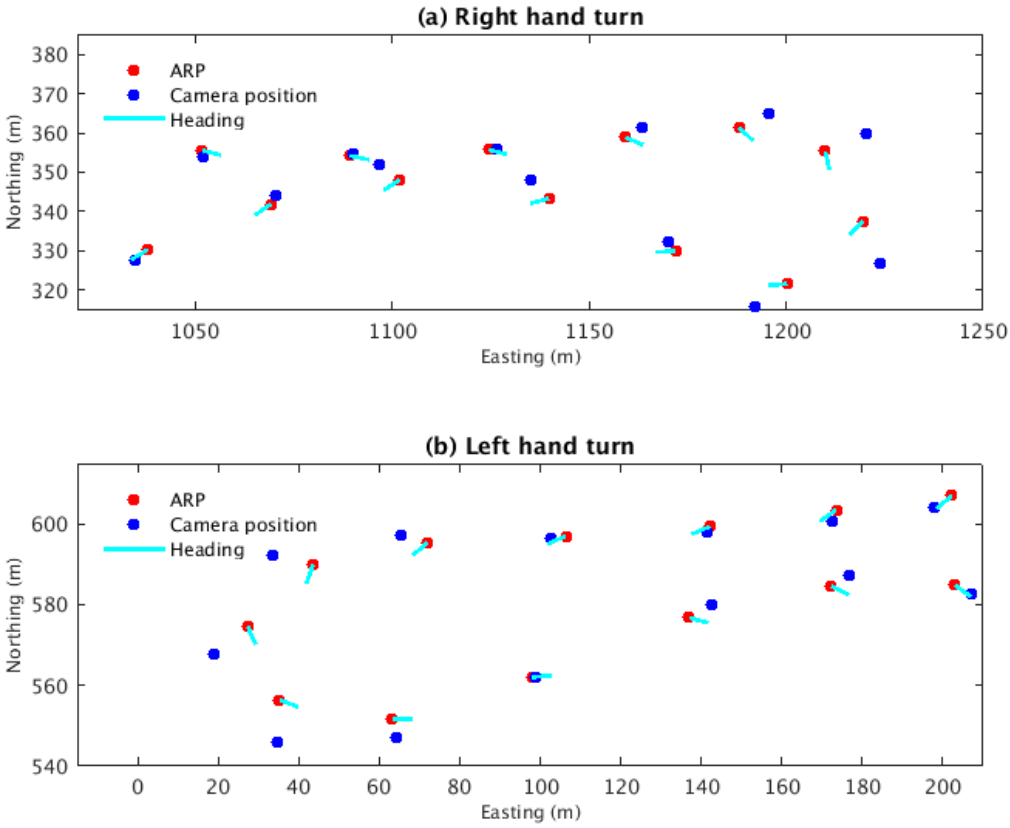

Figure 6-8. Illustration of lever arm correction with data from CPF Flight 2 for a (a) right hand and (b) left hand turn. In this case the camera is vertically offset by 12.8 cm below the ARP, and lever arm corrections have been scaled up 1000 times. POV = [0.0, 0.0, 0.128].

6.6.4 Time synchronisation error

The employed UAVs achieve camera time synchronisation by processing the camera flash signal. Therefore, in accordance with Rehak and Skaloud (2017b), resultant image time tag errors of 5-10 ms could be expected with consequent camera position shifts of 9-18 cm (at an 18 m/s ground speed). To verify the presence of such errors, final GPS camera position solutions were compared to those estimated during the GCP-BBAs. This approach can be used to infer camera time synchronisation errors from the direction of residual differences (Rehak and Skaloud, 2017b).

Table 6-7 presents the RMSEs and standard deviations of the differences between final GPS-determined and reference GCP-BBA estimated camera positions from APERO and PhotoScan for CPF Flights 2 and 3. Additionally, camera position residuals (in plan and height) are plotted in Figure 6-9 for reference GCP-BBA camera positions estimated in both APERO and PhotoScan. This analysis was only performed for the CPF flights because of the more even distribution of GCPs such that reference GCP-BBA estimated camera positions should exhibit a homogenous accuracy. However, because all datasets share the same camera time

synchronisation components (i.e. electronics and software) and strategy (by processing the camera flash signal), results should also be valid for the Low Hauxley flights. Moreover, for these tests, only PPK camera positions were assessed so as not to deteriorate results by the expected PPP errors.

From Table 6-7, it can be seen that the planimetric RMSEs are c. 15-30 cm and c. 10-15 cm for APERO and PhotoScan comparisons respectively. These are similar in magnitude to the expected GPS camera position shifts of 9-18 cm (with possible image time tag errors of 5-10 ms at an 18 m/s ground speed). However, Figure 6-9 indicates little correlation between the direction of the planimetric residuals and any particular image strip for either software, which suggests the absence of such camera time synchronisation errors, and rather camera calibration errors present in the GCP-BBA estimated camera positions. Additionally, the constant height offsets (also evident when comparing camera height coordinate RMSEs and standard deviation magnitudes in Table 6-7) are almost certainly suggestive of focal length error contamination of the GCP-BBA estimated camera positions, as camera height coordinates and focal length are known to be projectively coupled when little height variation exists (Cramer *et al.*, 2000; Lichti *et al.*, 2008).

Software	**Flight**	**RMSE (cm)**			**Std Dev (cm)**		
		E	**N**	**h**	**E**	**N**	**h**
APERO	CPF F1	16.1	27.0	21.5	16.0	26.9	19.5
	CPF F2	20.9	17.3	28.2	20.4	17.3	15.0
PhotoScan	CPF F1	13.4	13.4	25.4	11.8	12.7	8.8
	CPF F2	12.4	10.0	30.5	12.2	9.9	8.4

Table 6-7. RMSEs and standard deviations of the differences between final GPS camera positions and those estimated by the GCP-BBAs (i.e. Indirect Sensor Orientation) in both APERO and PhotoScan for CPF Flights 2 and 3.

Further suggestive of GCP-BBA-estimated camera position errors are the increased magnitude of both planimetric and height residuals to as much as c. 1 m for APERO comparisons (Figure 6-9a) towards the north west of CPF Flight 2. This correlates with the presence of trees, which likely degraded the quality of APERO image tie points and thus reference GPS-BBA estimated camera positions. The PhotoScan comparisons (Figure 6-9b), however, remain relatively unaffected which is a testament to a more consistent quality of PhotoScan image tie points.

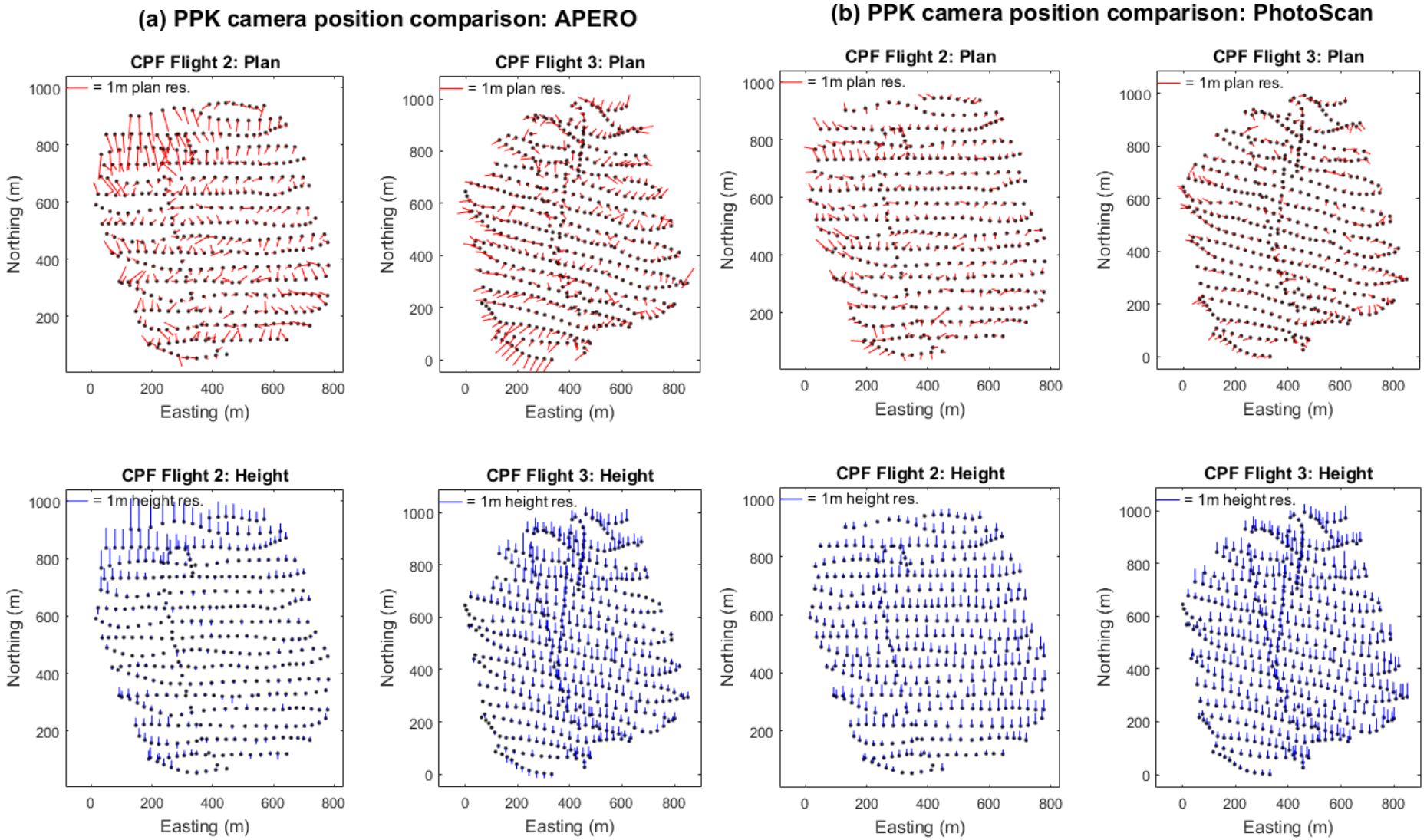

Figure 6-9. Residual plan and height coordinate differences between final GPS camera positions and those estimated in respective (a) APERO and (b) PhotoScan GCP-BBAs for CPF Flights 1 and 2

6.6.5 Summary

In summary, this section discussed procedures for the determination of GPS camera positions from UAV trajectories through time synchronisation, interpolation and lever arm correction. Investigations suggested that errors associated with time interpolation (with a spline interpolation strategy) and lever arm correction are likely to be less than the magnitude of PPK (and therefore PPP) trajectory errors. Time synchronisation errors, however, were more difficult to ascertain, but in accordance with Table 6-5, these are expected to induce camera position errors of no more then c. 10 cm in planimetry, which is in accordance with the study of Rehak and Skaloud (2017b). Although resultant camera height errors could not be verified (due to the likely presence of focal length errors in reference GCP-BBA estimated camera positions) they are expected to be less due to the smaller UAV height variation compared to that in planimetry (Lichti, 2002).

6.7 Results: PPP and PPK-supported BBAs

Having determined PPP and PPK camera positions, PPP-BBAs and PPK-BBAs were implemented. In all cases, the same images, tie points observations and observation weights were used as for the GCP-BBAs, along with the estimation of the same camera models. The only difference was the introduction of GPS camera positions as weighted observations. Assuming PPK camera positions to represent ‘truth’ camera positions, Figure 6-10 presents the mean and standard deviation of the PPP minus PPK camera position differences to denote the expected error in PPP camera positions (except for common time synchronisation errors). This shows mean error magnitudes to range between c. 1 cm and c. 30 cm in planimetry and c. 1 cm and c. 60 cm in height coordinates, whereas median values, are 3.8 cm, 5.1 cm and 10.5 cm in easting, northing and height respectively. The precisions of PPP camera position errors, however, are more consistent at c. 1-5 cm in both planimetry and height coordinates, with median values of 2.1 cm, 1.3 cm and 2.7 cm in easting, northing and height respectively.

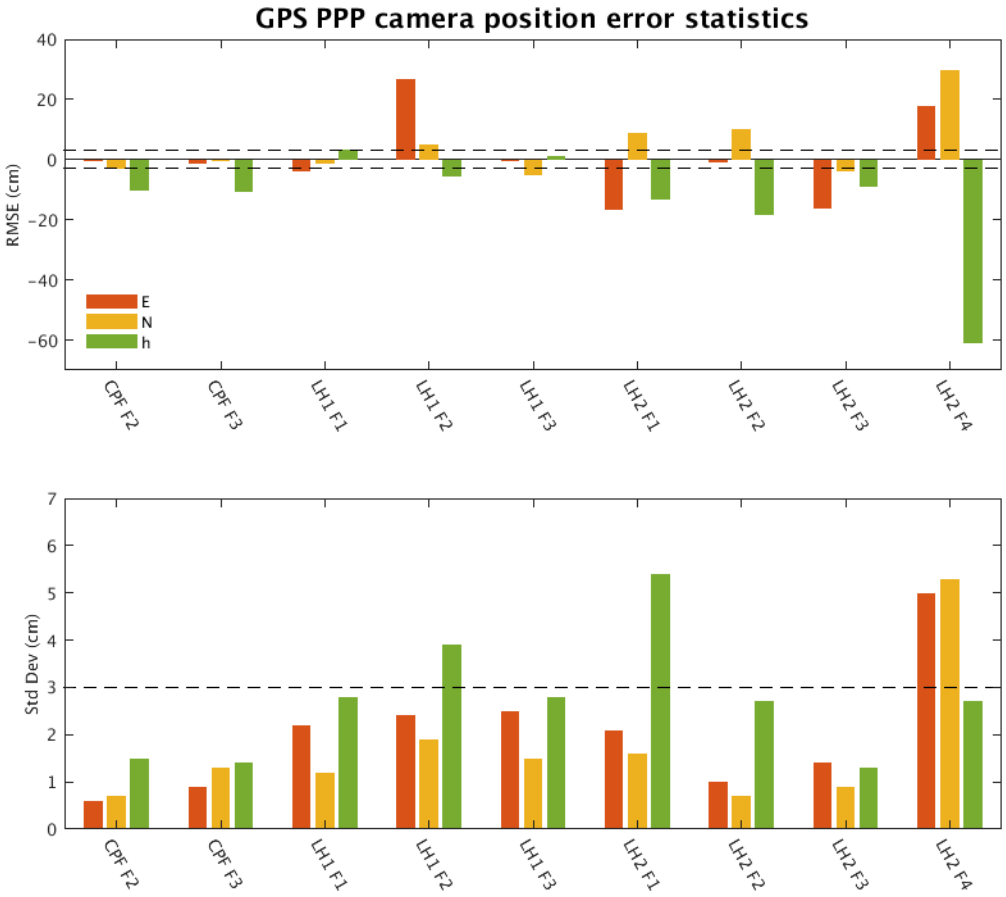

Figure 6-10. Expected PPP camera position error and standard deviation. Dotted line indicates a 1 pixel (equivalent) value.

6.7.1 Camera position weights

Despite the 1-5 cm precision agreement of PPP and PPK camera positions in Figure 6-10, both PPP and PPK camera positions will be equally affected by time synchronisation errors, potentially equivalent to +/- 10 cm in planimetry (as discussed in Section 6.6.4).

Therefore, before evaluating the impact of PPP camera positions over all flights, PPK-BBAs and PPP-BBAs were executed with varied camera position weights (assigned *a priori* standard deviations) to determine appropriate values given the approximately known time synchronisation errors. This analysis was only performed for the CPF flights so as not to deteriorate results by the expected weaker image block configurations for the Low Hauxley flights. Check point RMSEs for PPK-BBA and PPP-BBA are presented in Figure 6-11 with camera position weights varied between 1 mm and 20 cm with 1 cm increments. Such a range of camera position weights was selected because it spans the magnitude of possible camera time synchronisation errors, and has also been used in similar investigations (e.g. Benassi *et al.*, 2017).

Figure 6-11 shows that both PPP and PPK-BBAs responses to the varied camera position weights are similar for either GPS method for the same software. However, APERO check point coordinate RMSEs vary by only c. 1 cm in each coordinate component over all *a priori* camera position standard deviations for both flights. This suggests APERO solutions are relatively insensitive to the camera position weight, as was also shown by Benassi *et al.* (2017) when analysing the performance of PPK-BBAs. This further implies that camera positions with a lower (i.e. up to c. 20 cm) precision could be included in the BBA with similar effect. In contrast, PhotoScan check point coordinate RMSEs are more variable, with planimetric RMSE values spanning c. 5-10 cm and height RMSE values spanning ranges of c. 15 cm for CPF Flight 2 and c. 25 cm for CPF Flight 3 (for both PPK-BBAs and PPP-BBAs). The similar responses for either PPP or PPK-BBAs is suggestive that that both PPK and PPP camera position exhibit a similar precision.

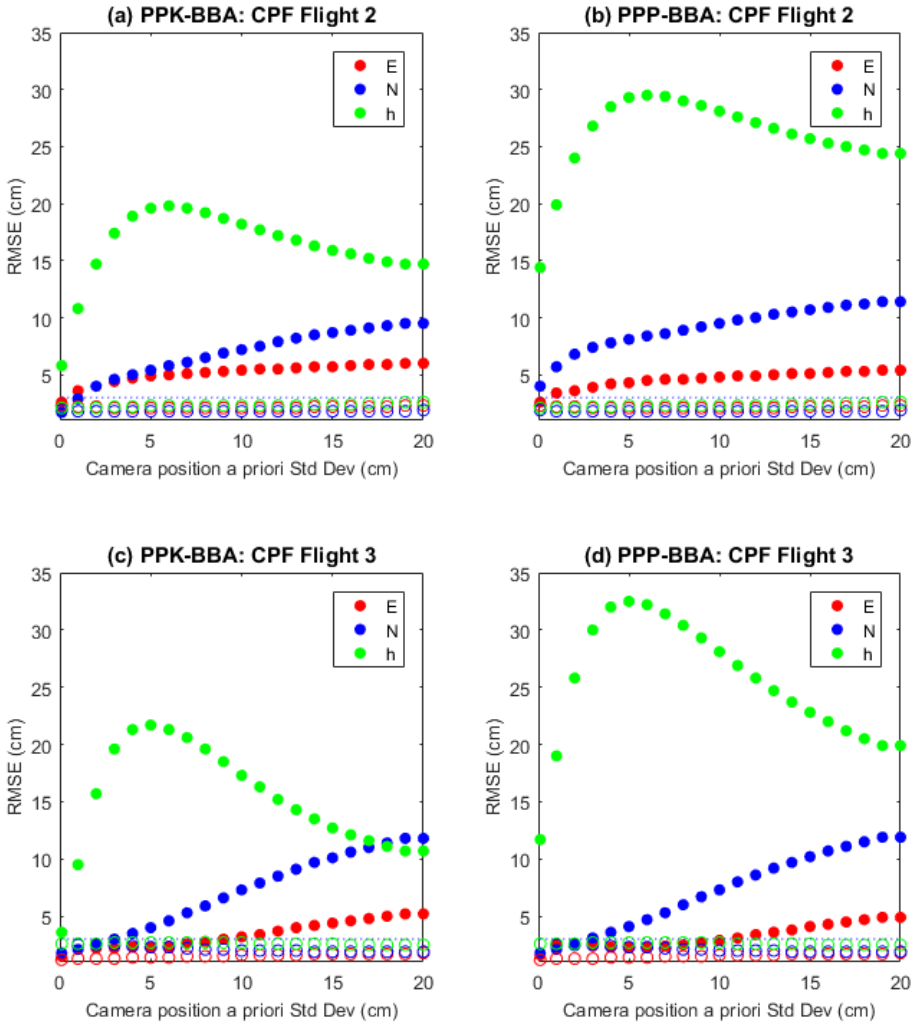

Figure 6-11. PPK-BBA (a, c) and PPP-BBA (b, d) check point RMSEs with camera position weights varied between 1 mm and 20 cm with 1 cm increments from PhotoScan (filled 'o' symbols) and APERO (empty 'o' symbols) for CPF Flights 2 and 3. GCPs are not included.

To accord with Figure 6-11, *a priori* camera position standard deviations of 1 mm are hereafter used in PhotoScan GPS-BBAs, whilst due to the invariance of APERO check point RMSEs, *a priori* camera position standard deviations of 2 cm are hereafter used in accordance with the precision of PPP minus PPK camera position differences in Table 6-7.

6.7.2 PPK-supported BBA with 0, 1 and 4 GCPs

For the generation of reference solutions and to understand the contribution of PPK camera positions towards the elimination of GCPs, PPK-BBAs were first implemented (1) without GCPs, (2) with the inclusion of one GCP and (3) with the inclusion of four GCPs. Coordinate RMSEs and standard deviations for these solutions are shown in Figure 6.12a-c for both APERO and PhotoScan (the APERO results for CPF Flights 2 and 3 are also presented in Grayson *et al.* (2018)).

No GCPs. Without GCPs, easting and northing coordinate RMSEs are c. 1 pixel or better for all flights and both software packages, except for the PhotoScan solution for LH1 Flight 1 where the easting coordinate RMSE is c. 2 pixels. Height coordinate RMSEs, however, are generally worse and range between c. 0.5 and 13 pixels. The variation between software packages for the same flights is important to note as it suggests software dependence and low repeatability of the height coordinate component. Such height errors are likely to result from an inaccurate estimation of focal length which propagates into the height coordinate in the absence of GCPs (e.g. Benassi *et al.*, 2017). Knowing focal length estimation to benefit from variation in image scale, the camera height variation (range and standard deviation) per flight is also given in Table 6-8. Referring to this it can be seen that the smallest height coordinates RMSEs (for the CPF flights) coincide with the largest camera height ranges (of c. 60-80 m) whereas the largest height coordinate RMSEs (for the LH2 flights) coincide with the smallest camera height ranges (of c. 4-7 m). Even the marginally larger camera height range for LH1 Flights 1 and 3 (of c. 11-15 m) over that of LH1 Flight 2 (of c. 6 m) appears to slightly reduce the height coordinate RMSE. The software dependence of height coordinate RMSEs (i.e. for the same flights) can also be explained by the different focal length estimates. For example, regarding CPF Flights 2 and 3 the differences in the APERO and PhotoScan estimated focal lengths were 26 um and 19.8 um respectively. These are equivalent to object point height coordinate differences of 19 cm (6.7 pixels) and 14 cm (4.9 pixels) for the 1:7500 imagery, which account for the respective height estimate discrepancies between software packages.

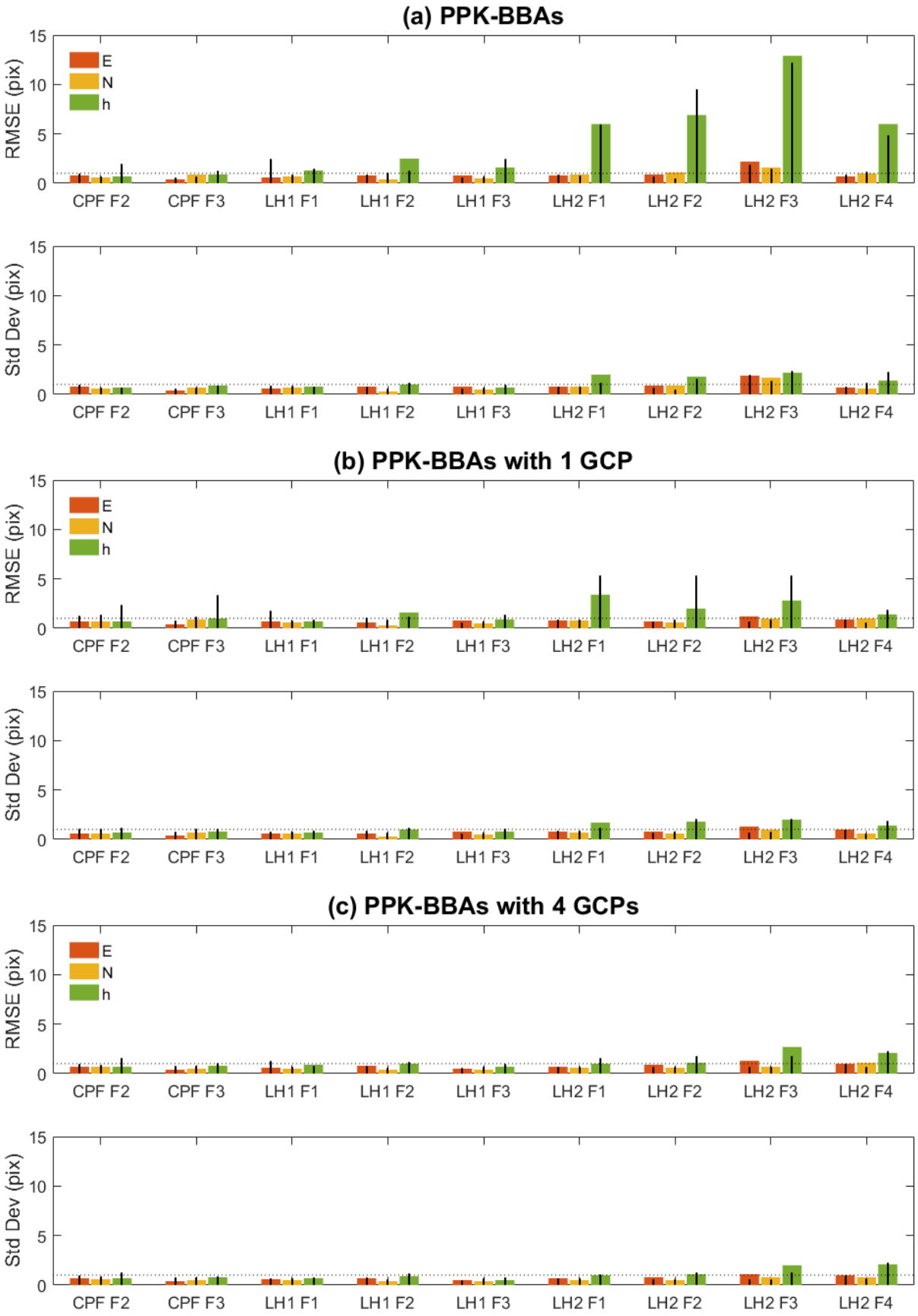

Figure 6-12. Check point RMSEs and standard deviations for PPK-BBAs without GCP inclusion (a), with the inclusion of one GCP (b) and four GCPs (c) from APERO (coloured bars) and PhotoScan (black bars). Dotted line indicates a 1 pixel value.

Aside from the coordinate RMSEs, coordinate standard deviations are c. 1 pixel in easting and northing coordinates and c. 1-2 pixels in height for all flights and both software packages. This confirms both the high precision of PPK camera positions and their appropriate weighting in the BBA with regards to the image tie points. The small (1-2 pixel level) height coordinate standard deviations, relative to the large (up to 13 pixel) height RMSEs suggest that the focal length errors effectively propagate as a height datum error (i.e. the height coordinate error is constant over the image block). Table 6-8 also presents the range and standard deviation of camera roll and pitch angles where it can be seen that angular ranges are c. 50 degrees for all flights. This exceeds the desired 5 degree variability that can mitigate doming deformation errors relating to inaccurate lens distortion modelling as per James and Robson (2014). Such camera attitude variation is therefore also likely to have improved height coordinate precisions.

Flight	**Range**			**Std Dev**		
	Roll (deg)	**Pitch** (deg)	**Height** (m)	**Roll** (deg)	**Pitch** (deg)	**Height** (m)
CPF Flight 2	60.5	49.7	61.0	6.0	6.7	8.6
CPF Flight 3	46.5	61.7	77.4	6.2	6.6	7.8
LH1 Flight 1	56.8	51.7	14.6	8.2	6.8	1.5
LH1 Flight 2	70.7	54.3	5.8	8.9	7.5	0.9
LH1 Flight 3	68.7	69.3	11.2	8.8	8.7	1.4
LH2 Flight 1	58.8	47.3	6.7	8.7	7.0	1.4
LH2 Flight 2	55.3	47.3	6.8	8.6	6.7	1.2
LH2 Flight 3	58.8	47.3	6.7	8.7	7.0	1.4
LH2 Flight 4	46.6	37.5	4.5	8.5	8.3	0.9

Table 6-8. Camera attitude and height value ranges and standard deviations for all datasets

1 and 4 GCPs. When including a single GCP in the PPK-BBA, height coordinate RMSEs for all flights are substantially reduced to between c. 1 and 5 pixels, except for the CPF flights which already exhibited such values without GCPs. With little change (of c. 0.5 pixels) in coordinate precisions, the effect can be summarised as a datum shift of the object point coordinates. Moreover, when including four GCPs rather than one GCP, a further (albeit it small) reduction in height coordinate RMSE to c. 1 pixel is seen for all flights with the exception of LH2 Flights 3 and 4. Furthermore, in this case, RMSEs in all coordinates are approximately equivalent to the respective standard deviations, suggesting that systematic (e.g. datum) errors are now similar in magnitude to random observation errors. In contrast to the solutions without using GCPs, it is important to note that the coordinate RMSE variation between software packages for the same flights is substantially smaller, which suggests software independence and a higher repeatability of the height coordinate component.

Focal length compensation. To explain why additional GCP configurations reduce height coordinate RMSEs, Table 6-9 shows the effective change in object point height coordinates resulting from change in the APERO focal length estimation (hereafter termed focal length height change) with the inclusion of one and four GCPs over not using any. Overall it can be seen that focal length height changes (caused by GCP inclusion) are generally equivalent to, and therefore compensate for, the initial height coordinate RMSEs without GCPs. For example, for LH1 Flight 2, including one and four GCPs result in focal length height change of c. 5 and c. 6 cm respectively, which compensates for the c. 2 pixel height RMSE without GCPs shown in Figure 6-12. For LH2 Flight 2, these values are both c. 18 cm, which again compensates for the c. 6 pixel height coordinate RMSE (equivalent to c. 18 cm) without GCPs shown in Figure 6-12. However, for all CPF flights, and LH1 Flights 1 and 3, height coordinate RMSEs are already c. 1 pixel without GCPs and hence including GCPs results in much smaller focal length height changes of less than 4 cm as shown in Table 6-9. Similar improvements to height coordinate RMSEs with the inclusion of GCPs were also demonstrated by Skaloud *et al.* (2014) and Benassi *et al.* (2017), but they did not show equivalent focal length compensation.

Flight	PPK-BBA	PPK+1GCP	PPK+4GCP
	Nom. correction (cm)	Change (cm)	Change (cm)
CPF Flight 2	-14.5	2.2	0.8
CPF Flight 3	6.5	-0.3	3.3
LH1 Flight 1	50.3	-3.3	-1.5
LH1 Flight 2	55.4	-4.8	-6.2
LH1 Flight 3	0.6	3.7	3.6
LH2 Flight 1	-66.2	-8.9	-15.6
LH2 Flight 2	-28.3	-17.8	-18.4
LH2 Flight 3	-121.8	-23.4	-121.7
LH2 Flight 4	-34.8	-18.3	-14.6

Table 6-9. Effective height change in the object point coordinates from focal length correction for PPK-BBAs, calculated as estimated focal length minus nominal focal length multiplied by image scale.

To summarise, the PPK-BBA reference experiments suggest that a mapping accuracy and precision of c. 1 pixel or less in planimetry can be reliably obtained in the absence of GCPs using highly weighted PPK camera positions. However, an equivalent accuracy and precision in height cannot be obtained with the same reliability in the absence of GCPs due to erroneous focal length estimation. This might be improved with an increase in camera position height variation, although at least four GCPs should be included to reliably compensate, and produce mapping errors that are repeatable and consistent between software packages.

6.7.3 PPP-supported BBA with 0, 1 and 4 GCPs

Examination of the PPK-BBA results has revealed object point errors that are expected due to limitations of the image block configurations (and not the GPS camera positions), whilst applying camera self-calibration in the BBA. In light of these, PPP-BBAs were implemented. As for the PPK-BBAs, to understand the contribution of PPP camera positions towards the elimination of GCPs, PPP-BBAs were also implemented (1) without GCPs, (2) with the inclusion of one GCP and (3) with the inclusion of four GCPs. Check point RMSEs and standard deviations for these solutions are shown in Figure 6-13a-c for both APERO and PhotoScan (the APERO results for CPF Flights 2 and 3 are also presented in Grayson *et al.* (2018)).

No GCPs. Without GCPs, easting and northing RMSEs are substantially larger for LH1 Flight 2 and all LH2 flights (compared to corresponding PPK-BBA solutions), now ranging between c. 1 and 10 pixels. Making reference to Figure 6-10, it can be seen that such easting and northing RMSEs are approximately consistent with the magnitude of expected PPP camera position errors per flight. For example, the LH2 Flight 4 coordinate RMSEs of c. 7 and 10 pixels in easting and northing shown here are almost commensurate with the 17.7 cm and 29.7 cm expected PPP camera position errors in Figure 6-10 (noting the 3 cm GSD). In addition, the LH1 Flight 2 easting RMSE of c. 9 pixels is almost commensurate with the PPP camera position easting error of 26.9 cm. However, for the CPF flights, and LH1 Flights 1 and 3 easting and northing RMSEs are 1-2 pixels, which are again reflective of the centimetre-level magnitude of PPP camera position errors. Such mapping errors are also nearly commensurate with those of the corresponding reference PPK-BBAs. Height RMSEs are also largely variable between flights (and software package), ranging between c. 1 and 11 pixels. However, from the PPK-BBA reference solutions, these are already known to be contaminated by focal length errors and consequently cannot be directly related to the PPP camera position height error magnitudes in Figure 6-10.

Irrespective of coordinate RMSEs, and as per the reference PPK-BBAs, standard deviations are very similar between all flights, at c. 1 pixel in easting and northing, and c. 1-2 pixels in height coordinates for both APERO and PhotoScan. This is even the case for the LH2 flights which exhibit coordinate RMSEs of c. 7-11 pixels (equivalent to c. 20-30 cm). This suggests that PPP camera position observations can enable a high mapping precision, as per the PPK camera positions, and thus equally (to the equivalent PPK solution) contribute to the removal of image block deformation errors. The mapping datum, however, is defined with a variable accuracy per flight in the absence of GCPs.

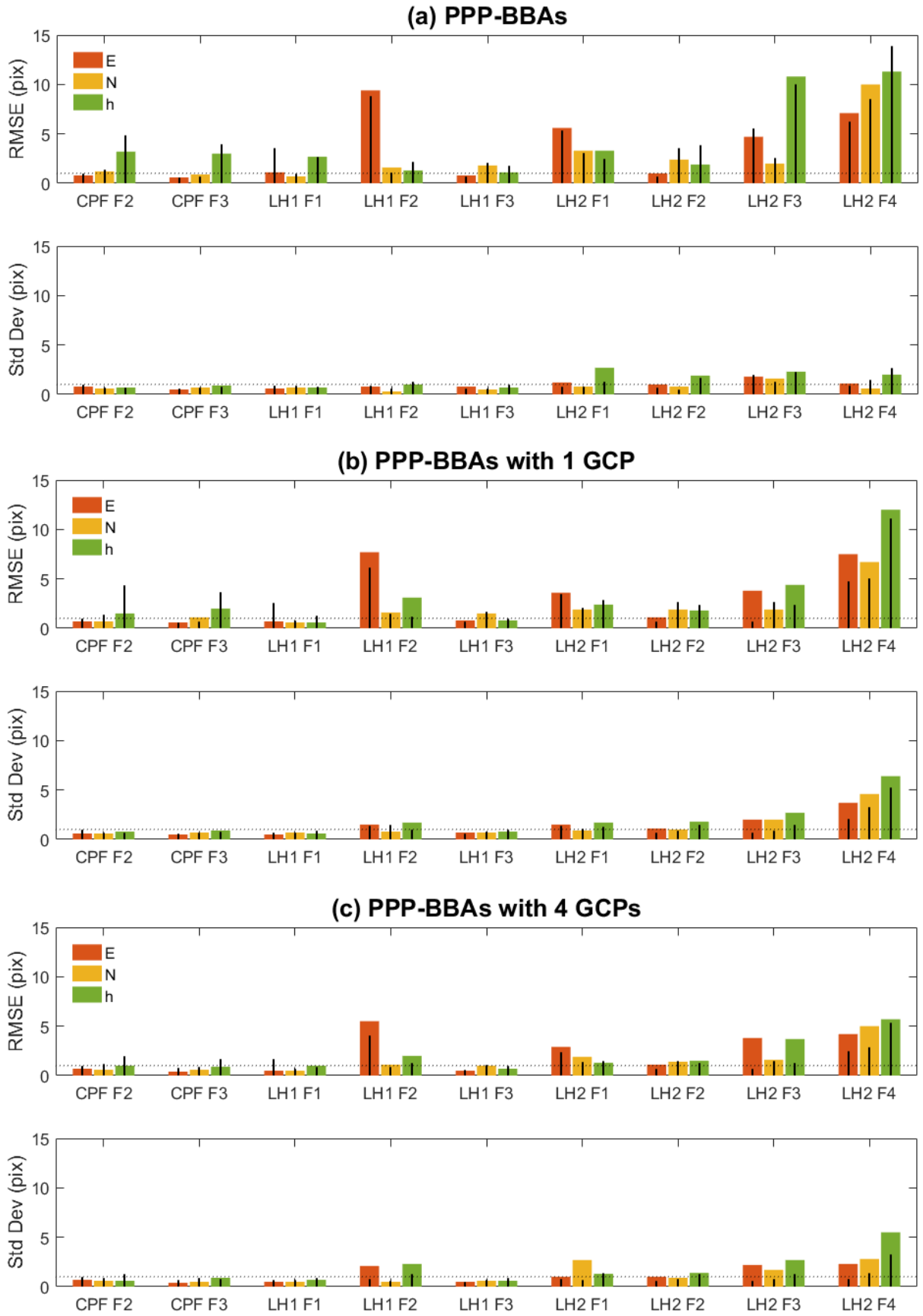

Figure 6-13. Check point RMSEs and standard deviations for PPP-BBAs without GCP inclusion (a), with the inclusion of one GCP (b) and four GCPs (c) from APERO (coloured bars) and PhotoScan (black bars). Dotted line indicates a 1 pixel value.

1 and 4 GCPs. With the inclusion of a single GCP, check point RMSE reductions are generally only c. 2-3 pixels, which is relatively small compared to their initial magnitudes without GCPs. Check point RMSE changes also differ between software packages, for example, as can be seen when comparing APERO and PhotoScan results for the CPF flights. In some cases, the inclusion of a single GCP also degrades coordinate RMSEs, such as for LH1 Flight 2 where the easting RMSE reduces by c. 3 pixels at the expense of a c. 2 pixel increase in the height. The inclusion of a single GCP thus appears ineffective in some cases at reducing the PPP-induced mapping errors.

With the inclusion of four GCPs, the improvement to coordinate RMSEs is more substantial. For instance, for CPF Flights 1 and 2, LH1 Flights 1 and 3 and LH2 Flight 2, all coordinate RMSEs are reduced to c. 1 pixel, with an equivalent precision. Such mapping errors are now commensurate with the equivalent PPK-BBA results, because of the greater BBA constraints incurred from including four GCPs over just one GCP.

However, even with four GCPs, c. 4-5 pixel coordinate RMSEs remain for the easting of LH1 Flight 2, easting and height of LH2 Flight 3, and all coordinate components of LH2 Flight 4. It is also seen for LH1 Flight 2 that coordinate standard deviation increase from c. 1 to c. 2 pixels in both easting and height coordinates, whilst for LH2 Flight 4, coordinate standard deviations increase from c. 1 to 2 pixels in easting, c. 0.5 to 2.5 pixels in northing and c. 2 to c. 5 pixels in height coordinates. Such results are suggestive of tension between the (biased) PPP camera positions and (unbiased) GCP coordinates. Tensions are also indicated by increases in tie point RMSE residual values, such as from 0.79 to 0.97 pixels for LH1 Flight 2 and from 0.78 to 1.19 pixels from LH2 Flight 4 (values taken from APERO). As was also shown by Stöcker *et al.* (2017) and Rupnik *et al.* (2015), such effects usually occur when introducing optimistically weighted observations into the BBA.

Focal length compensation. As for the equivalent PPK-BBA solutions, Table 6-10 again shows the effective change in object point height coordinates resulting from change in APERO focal length estimation with the inclusion of one and four GCPs. With the exception of LH2 Flights 3 and 4, it can be seen that focal length height changes caused by GCP inclusion are generally equivalent to, and therefore compensate for, the PPP-BBA height coordinate RMSEs without GCPs. For example, for the CPF flights, focal length height changes with the inclusion of four GCPs are c. 8-9 cm which are sufficient to accommodate the majority of the c. 3 pixel height coordinate RMSEs respectively. However, noting that focal length is expected to be correctly estimated for these flights (because of the c. 1 pixel height coordinate RMSEs for

corresponding PPK-BBAs without GCPs in Figure 6-12), this is suggestive that the four GCPs force the focal length to compensate for the expected PPP camera position height errors of c. 10 cm. Similarly for LH1 Flight 3, although the focal length height change with four GCPs is small at c. 2 cm, this is sufficient to reduce the former c. 1.5 pixel height coordinate RMSE (without GCPs) to less than 1 pixel.

For LH2 Flight 4, with a former height coordinate bias c. 11 pixels, the focal length height change with four GCPs of c. 31 cm is enough to remove the PPP camera position height error. In this case, however, the height coordinate RMSE (which is also influenced by coordinate precision) is hampered by image block deformations, as indicated by the elevated height coordinate standard deviation of c. 6 pixels. The same can be said for LH1 Flight 2 and LH2 Flights 1-3, although to a lesser extent due to the smaller magnitude of the PPP-induced error. Such results illustrate that with substantial planimetric PPP camera position errors, the inclusion of GCPs becomes less effective because the estimated camera model (and image observation residuals) cannot accommodate the datum inconsistency between (biased) PPP camera positions and (unbiased) GCP coordinates.

Flight	PPP-BBA	PPP+1GCP	PPP+4GCP
	Nom. correction (cm)	Change (cm)	Change (cm)
CPF Flight 2	-12.5	5.4	7.7
CPF Flight 3	10.0	3.2	9.4
LH1 Flight 1	52.6	-6.3	-5.0
LH1 Flight 2	57.2	6.9	-2.7
LH1 Flight 3	1.1	1.7	2.4
LH2 Flight 1	-85.0	11.2	-16.1
LH2 Flight 2	-27.4	-0.8	-0.4
LH2 Flight 3	-110.0	10.7	-109.0
LH2 Flight 4	-25.3	9.1	31.3

Table 6-10. Effective height change at the object point coordinates from focal length correction for PPP-BBAs, calculated as estimated focal length minus nominal focal length multiplied by image scale.

The substantial improvements offered to CPF Flights 1 and 2, LH1 Flights 1 and 3 and LH2 Flight 2 with the inclusion of four GCPs are likely because of the smaller magnitude of PPP camera position errors and thus such errors could be easily compensated by the estimated camera model. However, for the remaining flights, it is evident that some PPP camera position errors are too large for GCPs to have the same effect, and thus they prevail as mapping errors and reduced image block precision.

When larger easting and northing PPP camera position coordinate biases exist, the inclusion of GCP observations in such a way is evidently sub-optimal because the adjustment model cannot accommodate the associated datum error. However, reducing the weight (*a priori* standard deviation) of PPP camera position observations to accommodate the lower accuracy of PPP camera positions would reduce the contribution of PPP camera positions to the image block precision (as shown in the camera position weight tests). In conventional GPS-supported AT, such datum deficiencies are modelled by estimating shift corrections at the camera positions, as discussed in Chapter 3, with the value of these corrections reflecting the GPS camera position bias. As APERO and PhotoScan are not designed to implement such models, the next section investigates the possibility of applying a GCP-based block shift correction in a separate step.

6.7.4 PPP-supported BBA with block shift

As the PPP-BBAs produced object coordinates with c. 1 pixel precision in easting and northing coordinates and c. 1-2 pixel precision in height (shown in Figure 6-13), it can be inferred that the image block shape, scale and rotation (in the mapping frame) has been accurately determined for each dataset. Therefore, all that should be required is a global shift of each image block to mitigate the respective datum errors. Such shifts, comprising a translation in easting, northing and height (three parameters), can be computed from a number of GCPs as the difference between their photogrammetrically determined coordinates and known (surveyed) values. Thus applying such shift corrections effectively minimises the error at the selected GCP(s), but without changing the image block precision.

This was implemented for the former PPP-BBA solutions (computed without GCPs), using the same one and four-GCP configurations (hereafter referred to as one and four-GCP block shifts respectively). Coordinate RMSEs, having applied the one and four-GCP block shifts, are shown in Figure 6-14 for each flight (it should be noted that the Y axis scale has been maintained for cross comparison with Figure 6-13) and that the standard deviations are unchanged from Figure 6-13b and c, respectively.

With a one-GCP block shift, Figure 6-14 shows coordinate RMSEs are now reduced to c. 1 pixel or better in easting and northing, and generally c. 2 pixels or better in height for both APERO and PhotoScan. The only exceptions are remaining height RMSEs of c. 4 and 3 pixels for LH2 Flights 1 and 4 respectively. For LH1 Flight 2 and the LH2 Flights 1 to 4, this marks a substantial improvement on including the same four GCPs as observations in the BBA. In addition, coordinate standard deviations are approximately equivalent (at c. 1-2 pixels) suggesting a maintained image block precision. With a four-GCP block shift, the height RMSEs

for LH2 Flights 1 and 4 are further reduced to c. 2-2.5 pixels, thus suggesting an improved reliability of the block shift correction when computed from with four GCPs rather than just one. For the majority of datasets, however, the one-GCP shift appears sufficient to reduce PPP camera position induced mapping errors to the c. 1 pixel level.

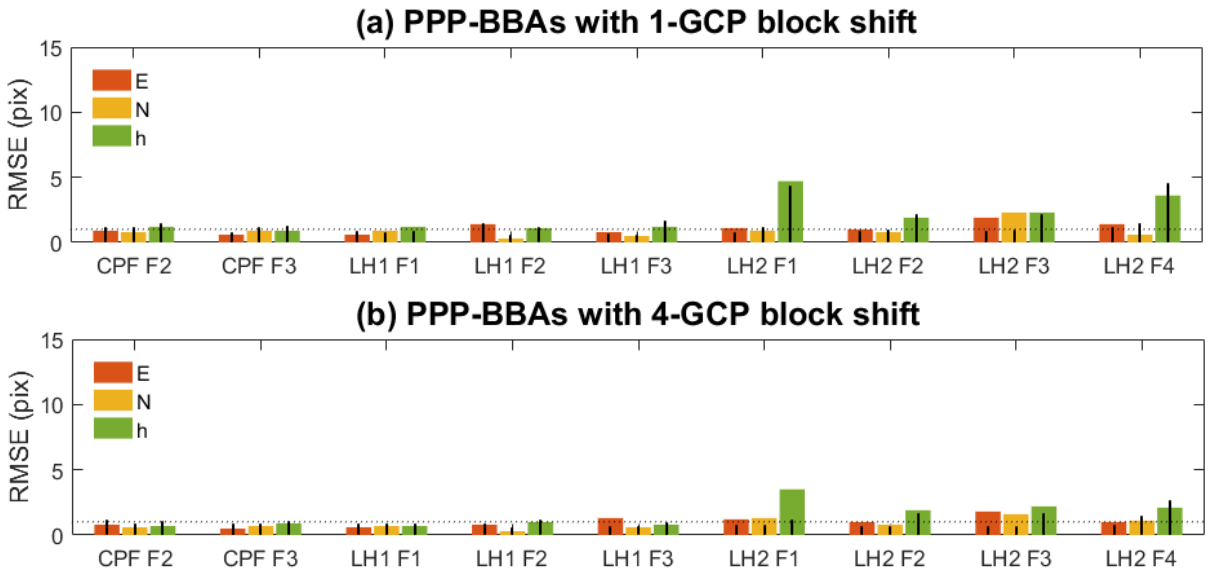

Figure 6-14. Check point RMSEs (standard deviations are unchanged from Figure 6-13b+c, respectively) for PPP-BBAs with (a) one-GCP block shifts and (b) four-GCP block shifts applied, computed in APERO (coloured bars) and PhotoScan (black bars). Dotted line indicates a 1 pixel value.

6.8 Comparison of GCP and GPS-supported BBAs

In this section, PPK and PPP-BBA solutions are compared to the reference GCP-BBA solutions in terms of mapping accuracy, precision and error distribution.

6.8.1 Error ratios

To compare overall mapping error and precision from GCP-BBAs with PPK and PPP-BBAs solutions, ratios were calculated between corresponding check point RMSE and standard deviation error statistics for each flight. In doing so, ratio values of one would represent an equal performance, whilst ratio values exceeding one would represent a better GCP-BBA performance and vice-versa. Such error ratios were calculated for the (1) PPK-BBAs, (2) PPP-BBAs and (3) PPP-BBAs with block translation (computed from four GCPs) and are presented in Figure 6-15.

For the PPK-BBAs (Figure 6-15a), planimetric RMSE ratios are generally between 1 and 2 for all flights, which reflects the similar planimetric accuracy of GCPs and PPK camera positions. Greater variability is however seen for the height RMSEs, where ratio values range from c. 1 to 5 (i.e. the height mapping error can be five times worse for the PPK-BBAs). This can be expected due to the contamination of PPK-BBA height RMSEs with variable focal length errors, which have less effect on the GCP-BBA results. Check point standard deviation ratios, however, are generally consistent at c. 1 for all flights and components, thus suggesting an equal performance of the PPK-BBAs and GCP-BBAs with regards to mapping precision. It is also noted for the APERO solutions for CPF Flights 2 and 3 and all LH1 flights that both check point RMSE and standard deviation ratios are c. 1 in both planimetry and height and thus these solutions can be considered equivalent to the corresponding GCP-BBA workflow.

For the PPP-BBAs (Figure 6-15b), planimetric RMSE ratios range between c. 1 and 17 pixels. This reflects the contamination of PPP-BBAs with PPP camera positions errors which are not present in the GCP control. However, for CPF Flights 2 and 3 and LH1 Flights 1 and 3, planimetric RMSE ratios are c. 1-2 pixels and are thus similar or only slightly worse than the corresponding GCP-BBA solutions. Large and variable height RMSE ratios can be expected due to the contamination of height coordinates by variable focal length errors (as per the PPK-BBA results), but this time in addition to variable PPP camera position errors. As for the PPK-BBA comparisons, such (datum) errors are not present in the GCP-BBA mapping coordinates, and hence height RMSE ratios are elevated. The PPP-BBA coordinate precision ratios, however, are again generally consistent at c. 1 for all flights and components. Moreover, for CPF Flights 2-4, LH1 Flight 2 and LH2 Flight 3, coordinate standard deviation ratios are better

than 1 and thus, as with the PPK-BBAs, suggesting an improved performance of the PPP-BBAs over the GCP-BBAs with regards to mapping precision.

When using four GCPs to compensate for PPP camera position-induced errors (Figure 6-15c), both planimetric and height RMSE ratios are reduced to values between c. 1 and 2 for all flights. Moreover, changes to the coordinate precision ratios from the standalone PPP-BBA solutions are less than c. 0.5. Therefore, using four GCPs is this way, the magnitude of mapping errors (in addition to the precision) is almost consistent with corresponding GCP-BBA workflows for all sites. An equal performance to the GCP-BBAs is thus suggested, but this time with regards to both mapping precision and accuracy, such that PPP has eliminated GCP requirements to only four without a substantial loss in mapping accuracy.

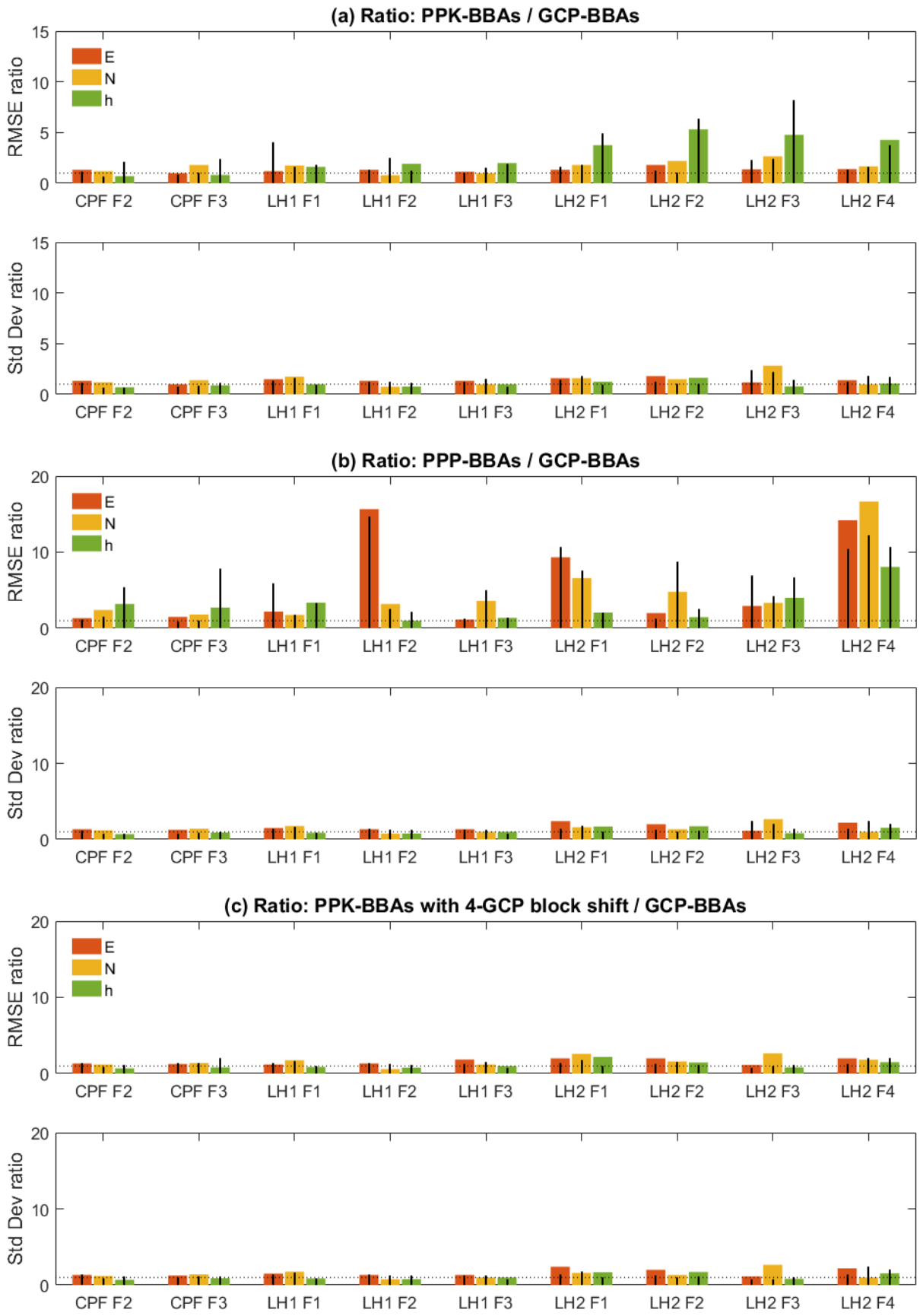

Figure 6-15. PPK-BBA:GCP-BBA (a), PPP-BBA:GCP-BBA (b) and PPP-BBA with block translation:GCP-BBA (c) check point RMSE and standard deviation error statistic ratios for all flights computed from APERO software (coloured bars) and PhotoScan software (black bars) results. Dotted line indicates a ratio value of 1.

6.8.2 Check point residuals

Further to the check point RMSE and standard deviation statistic ratios, the distribution of check point errors for (1) reference GCP-BBAs, (2) reference PPK-BBAs, (3) PPP-BBAs and (4) PPP-BBAs with the four-GCP block shift for the CPF, LH1 and LH2 flights are shown in Figure 6-16, Figure 6-17 and Figure 6-18, respectively.

For all GCP-BBAs and PPK-BBAs (Figure 6-16a-b, Figure 6-17a-b, and Figure 6-18a-b), it is generally seen that check point residuals are randomly orientated in planimetry, which reflects the centimetre-level planimetric accuracy of both GCPs and PPK camera positions. For the PPK-BBAs, however, check point height residuals are often systematically distributed which, as discussed in Section 6.7.2, has been attributed to errors in focal length estimation. This is particularly evident for the LH2 flights (Figure 6-18b), where such residual magnitudes reach 15 pixels. However, due to the varying suitability of each dataset (with respect to camera height variation, as presented in Table 6-8), the magnitude of check point height residuals largely varies between flights, and thus they are not suggestive of variable PPK camera positioning accuracy. For the PPP-BBAs (Figure 6-16c, Figure 6-17c and Figure 6-18c), check point residuals are again often systematically distributed, but this time in both plan and height. This is particularly evident for the LH2 flights, as well as LH1 Flight 2. However, again referring back to Figure 6-10, such check point residual orientations and magnitudes can be related to the direction and magnitude of PPP camera position errors. For example, for LH2 Flight 2, the positive easting PPP camera position bias of c. 25 cm is consistent with the c. 8 pixel, easterly orientated check point residuals, whilst for LH2 Flight 3, the negative northing PPP camera position bias of c. 6 cm corresponds very well with the c. 2 pixel southerly orientated check point residuals.

After applying the four-GCP block shift correction to the PPP-BBAs (Figure 16d, Figure 17d and Figure 18d), check point residuals generally conform to a random orientation in both plan and height for all flights, irrespective of the initial PPP-induced bias. This is most evident for the LH2 flights when comparing Figure 18c and d. The greater localised residual magnitude variations for the LH2 flights, however, may be attributed to the weaker image block configurations (i.e. lower numbers of images, tie points and target projections) as discussed for the GCP-BBAs in Section 6.5.5.

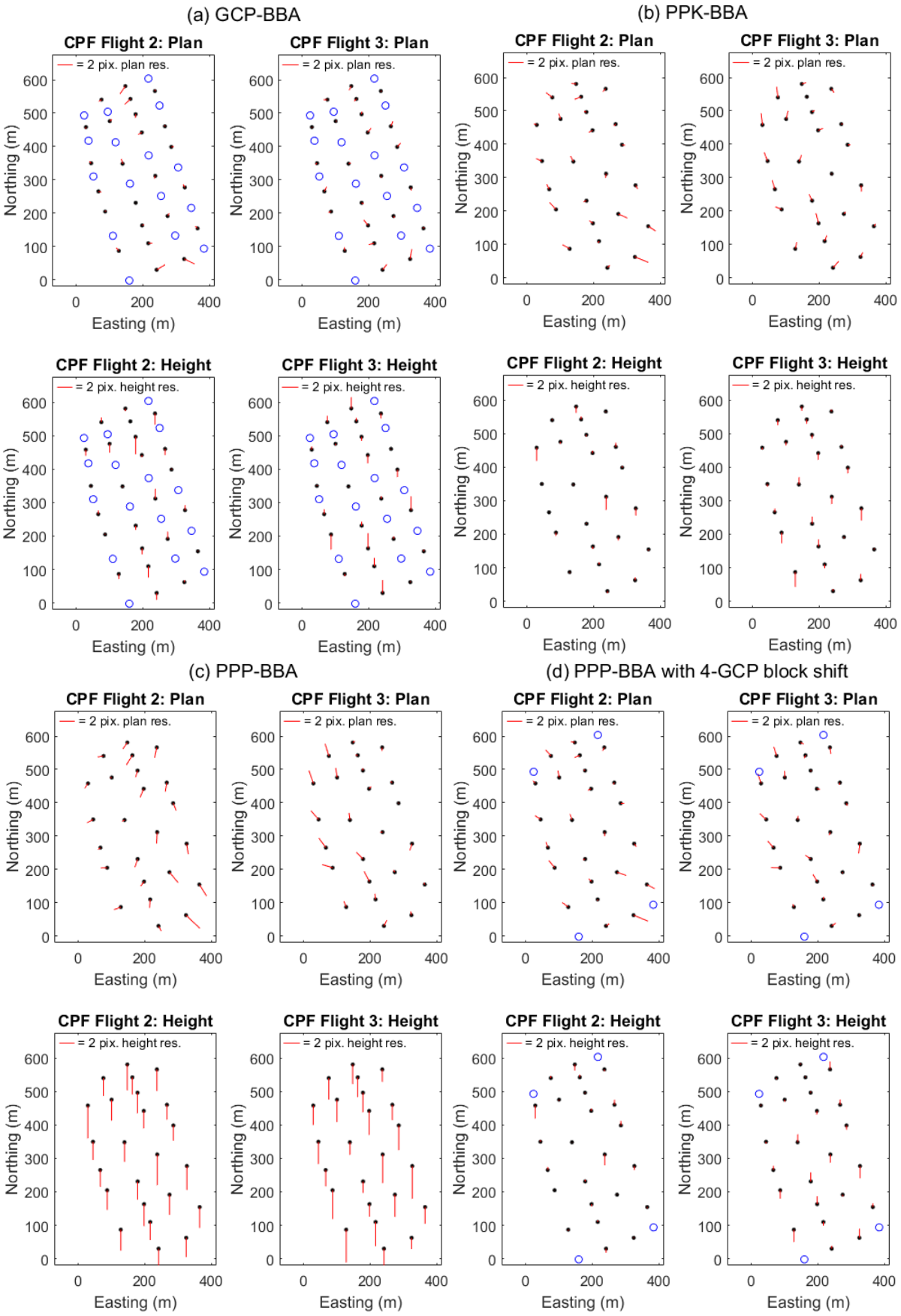

Figure 6-16. Check point error distributions for CPF Flights 2 and 3 for (a) GCP-BBAs, (b) PPK-BBAs, (c) PPP-BBAs and (d) PPP-BBAs with four-GCP block shifts. Blue circles = GCPs used as control.

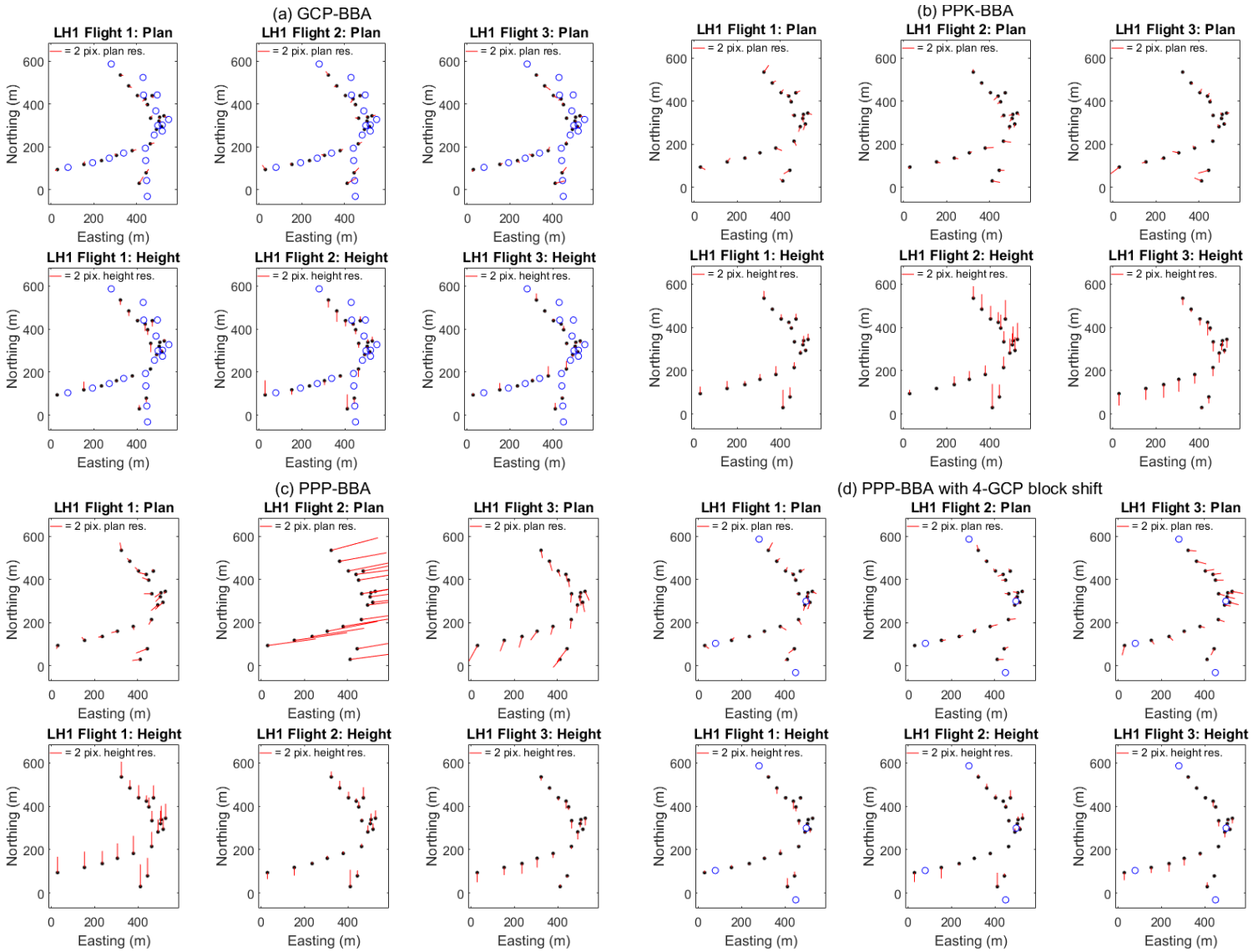

Figure 6-17. Check point error distributions for LH1 Flights 1-3 for (a) GCP-BBAs, (b) PPK-BBAs, (c) PPP-BBAs and (d) PPP-BBAs with four-GCP block shifts. Blue circles = GCPs used as control.

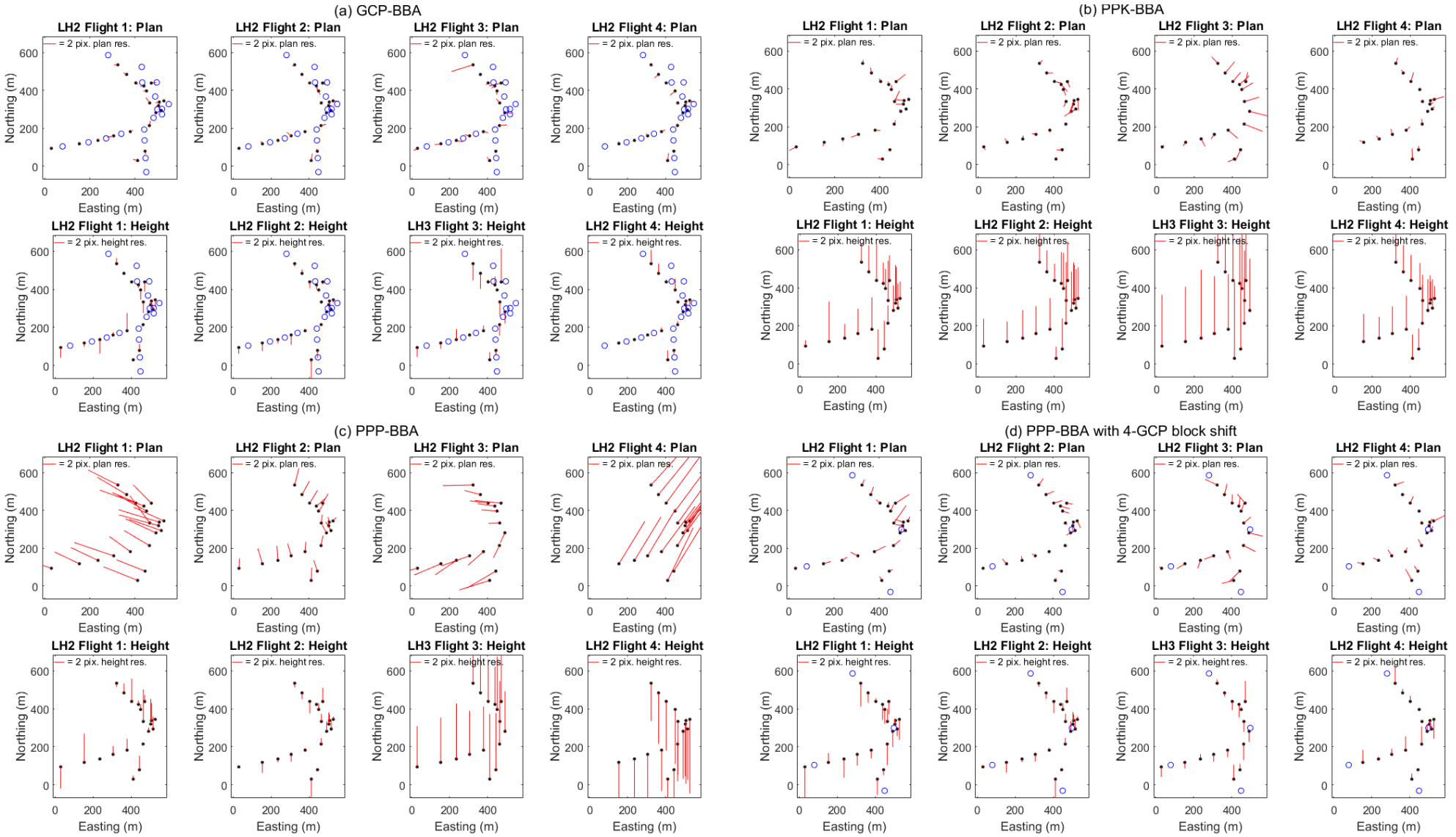

Figure 6-18. Check point error distributions for LH2 Flights 1-4 for (a) GCP-BBAs, (b) PPK-BBAs, (c) PPP-BBAs and (d) PPP-BBAs with four-GCP block shifts. Blue circles = GCPs used as control.

6.8.3 Point cloud comparisons

For the LH1 and LH2 flights, target distributions were limited to narrow corridors, and hence no indication of the mapping error is given elsewhere in the image block. To obtain a more extensive indication of spatial error distributions, object point coordinates of 3D tie points determined from the PPP-BBAs (with four-GCP block shifts) and corresponding GCP-BBAs were compared directly in a cloud-to-cloud comparison. Figure 6-19, Figure 6-20 and Figure 6-21 illustrate these absolute differences in both plan and height for the CPF, LH1 and LH2 flights respectively.

In planimetry, it can be seen that point cloud differences are typically less than 5 cm over the whole of each image block for all flights with exceptions only occurring at the edge of each image block. This is suggestive that the use of PPP camera positions enables a similar planimetric mapping accuracy over the whole of each image bock, and not just at the check point locations.

In height, however, it can be seen that point cloud differences are more systematic in distribution, especially for the LH1 and LH2 flights. For example, such differences are c. 5 cm or less in GCP-containing regions, but elevate with increasing distance from GCPs by up to c. 20 cm. As PPP camera positions are inherently distributed over the whole of each image block, it is suggested that GCP-BBA determined object point coordinates may be deforming with increasing distance from GCPs due to the propagation of unconstrained image orientation errors. This is also supported by the fact that GCPs are better distributed for the CPF flights, such that the systematic height differences are less pronounced. Increasing systematic error with increasing distance from GCPs has also been shown by Rupnik *et al.* (2015) and Goncalves and Henriques (2015). Similar systematic coordinate differences are also evident in planimetry for LH1 (Figure 6-20c).

Unlike the GCPs, due to the complete coverage of PPP camera positions, it is likely that the absolute accuracy of object point coordinates is more consistent over the whole image block. Although such errors cannot be verified in the absence of check points, such a distribution of relative errors is supportive of the use of PPP camera positions in the BBA to improve the image block precision when GCP configurations are sparse, as is consistently shown for these flights.

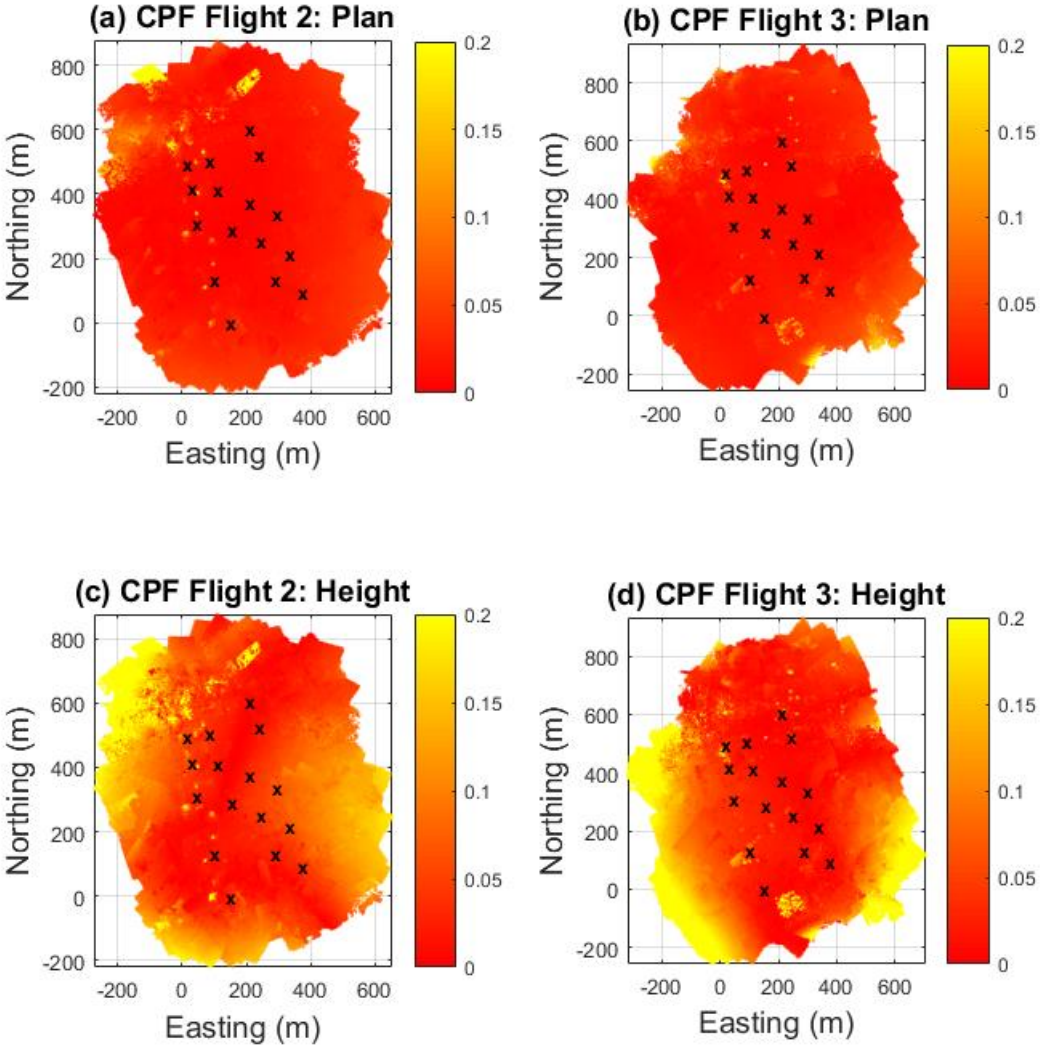

Figure 6-19. Magnitude of the PPP-BBA (with four-GCP block shift) minus GCP-BBA tie point coordinate differences in planimetry and height for CPF Flights 2 and 3. GCP locations for the GCP-BBA are marked by 'x' symbols. Colour ramp units are metres.

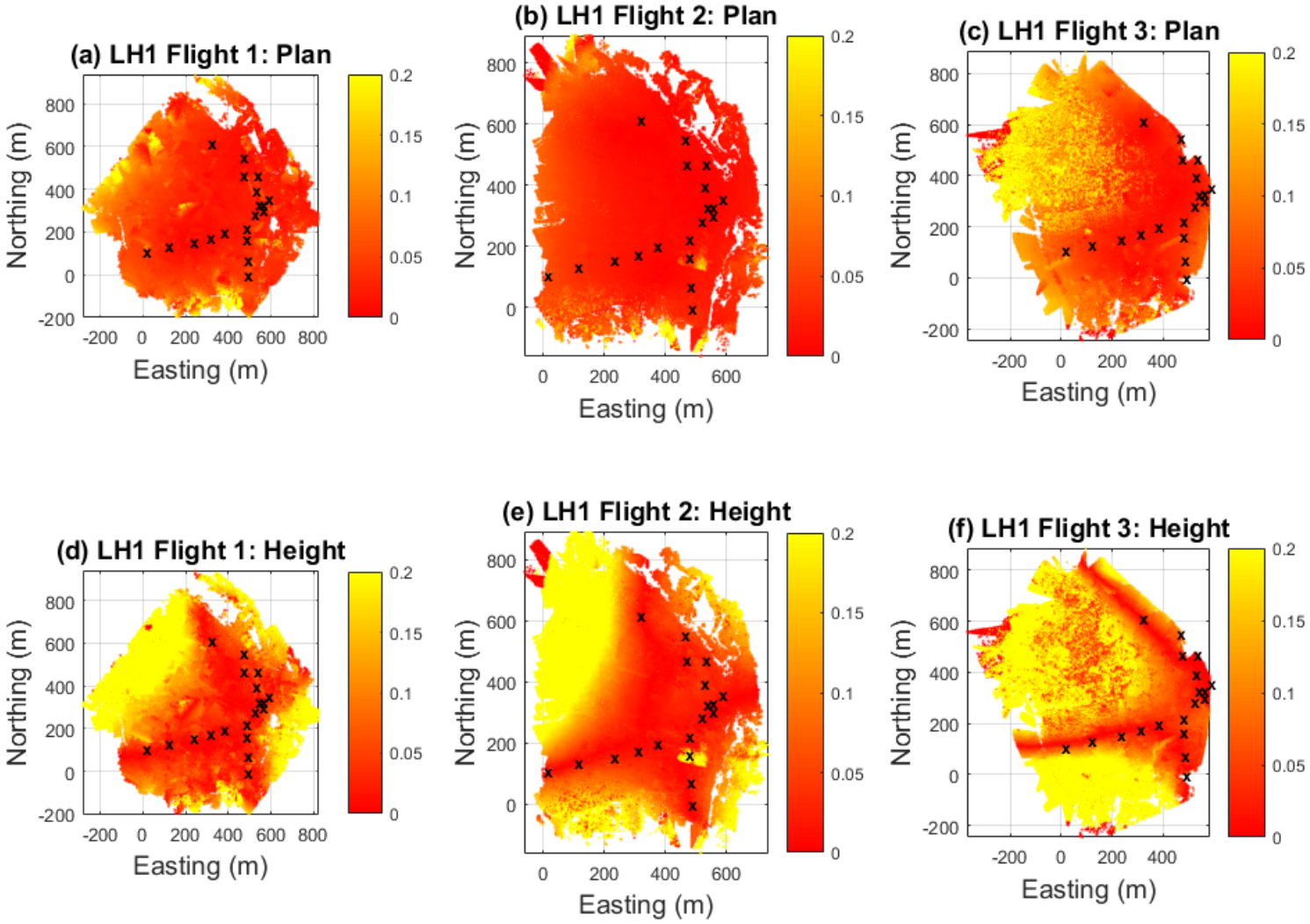

Figure 6-20. Magnitude of the PPP-BBA (with four-GCP block shift) minus GCP-BBA tie point coordinate differences in planimetry and height for LH1 Flights 1-3. GCP locations for the GCP-BBA are marked by 'x' symbols. Colour ramp units are metres.

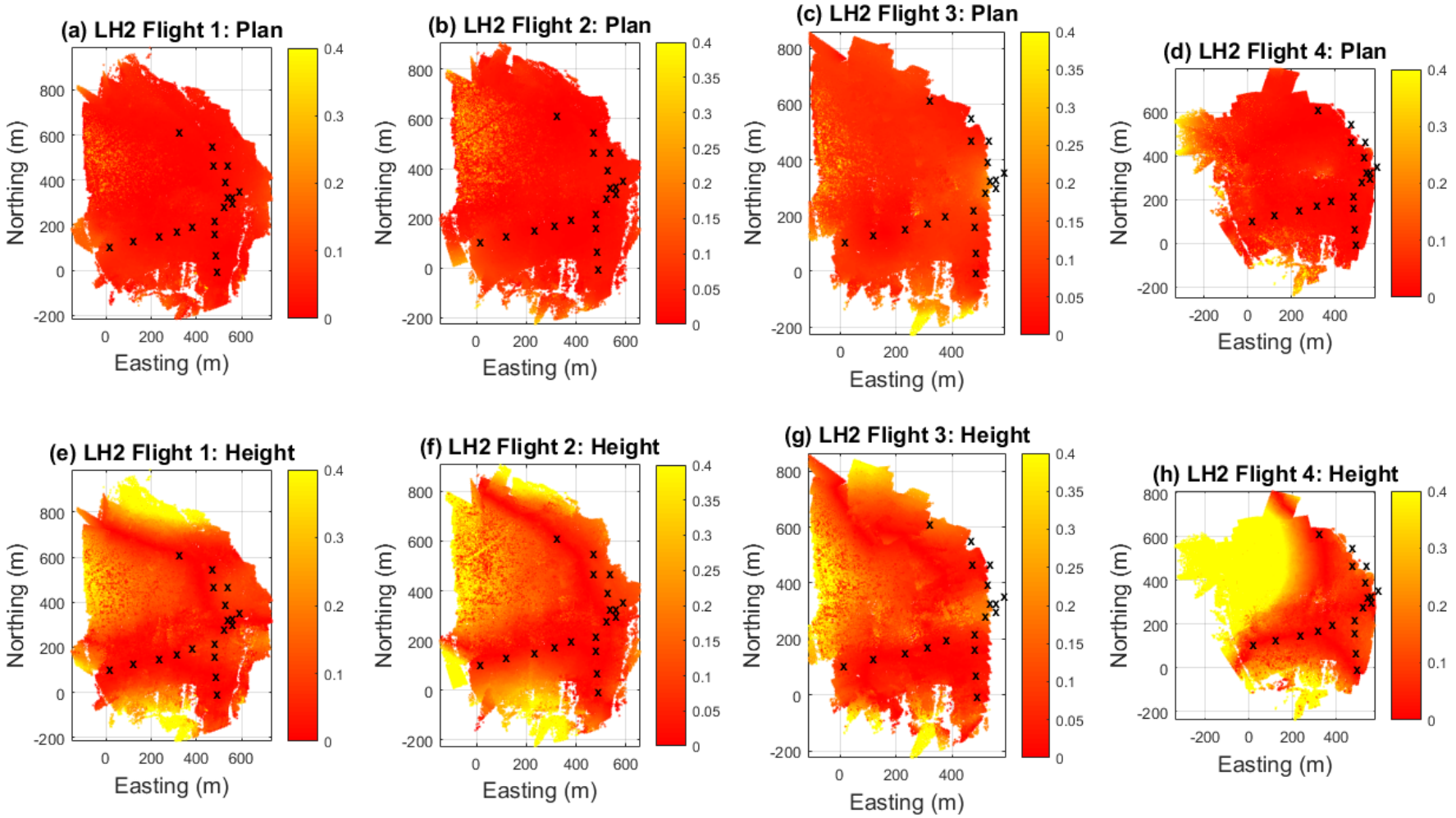

Figure 6-21. Magnitude of the PPP-BBA (with four-GCP block shift) minus GCP-BBA tie point coordinate differences in planimetry and height for LH2 Flights 1-4. GCP locations for the GCP-BBA are marked by 'x' symbols. Colour ramp units are metres.

6.9 Trajectory matching approach

As two of the CPF datasets (Flights 1 and 4) were missing image time tags (due to system failures), it was not possible to determine GPS camera positions and thus implement GPS-BBAs as undertaken for the other datasets. To enable GPS-based image block orientation using only the acquired GPS data, IMU data and the imagery, a different approach was developed, named Trajectory Matching (TM), which is based on the following two principles. Firstly, with GPS and IMU orientation angles, it remains possible to determine the position of the UAV camera at all GPS epochs, hereafter referred to as the *camera trajectory*. With 10 Hz GPS data and c. 18 m/s UAV velocities, a camera trajectory spacing of c. 1.8 m is attainable. This may be further reduced by applying a spline interpolation. Such positions may be regarded as a discrete representation of the continuous UAV camera path, which passes through the locations at which images were acquired in the absolute mapping frame. Secondly, regarding the imagery, a free network adjustment provides estimates of camera positions but in an arbitrary coordinate system. Despite the lack of real-world dimensions, arbitrary camera positions (as hereafter referred) provide a unique solution to each camera position based solely on the image tie points.

The TM approach was therefore developed to combine these two entities (i.e. the absolute camera trajectory and the arbitrary camera positions) to obtain absolute camera positions that may be used as constraints in the BBA. The TM approach is implemented in three main steps comprising:

1. The determination of camera trajectories from GPS positions and IMU rotation angles;
2. An iterative closest point (ICP) adjustment between the camera trajectory and arbitrary camera positions (from the free network adjustment) to deduce a seven parameter similarity (datum) transformation;
3. Selecting the closest camera trajectory point to each of the transformed camera positions, and using these as camera position observations in the GPS-BBA, as before.

The main limitations of this approach are (1) the limited relative accuracy (precision) of arbitrary camera positions due to the quality of tie points and camera model errors, and (2) the discrete representation of the continuous camera trajectory. Regarding the first point, arbitrary camera positions were used from the PhotoScan free network adjustments due to the anticipated better quality of image tie points compared to those from APERO (as found when determining reference GCP-BBA camera positions in Section 6.6.4, see Table 6-7) and thereafter better expected relative accuracy of arbitrary camera positions.

6.9.1 Workflow breakdown

Step 1: Camera trajectory determination. The determination of the camera trajectory is equivalent to applying a lever arm correction to every GPS position (as opposed to just the camera positions previously). Thus, UAV pitch, roll and heading angles were extracted from the UAV log file based on the corresponding GPS epoch times. As the 10 Hz GPS positions would only provide a camera trajectory spacing of c. 1.8 m, these were interpolated to 1000 Hz and thus a camera trajectory spacing of c. 1.8 cm, which is lower than the 3 cm image GSD.

Step 2: ICP adjustment. The ICP adjustment is formulated as a nonlinear least squares adjustment that estimates a seven parameter similarity transformation by minimising the distance between two surfaces (Chen and Medioni, 1991; Besl and McKay, 1992). ICP adjustments have been used in applications such as the registration of successive images acquired from range cameras (e.g. Chen and Medioni, 1991) and more recently terrestrial laser scans (e.g. Grant *et al.*, 2012). However, ICP adjustment is applied here to register the arbitrary camera positions (i.e. the data points) to the absolute camera trajectory (i.e. the model).

The approach described by Chen and Medioni (1991) is followed, where the similarity transformation, G, is found by minimising:

$$e = \sum_{i=1}^{n} (Gp_i - q_i)^2 \tag{6-4}$$

where p and q are the model and (corresponding) data points respectively. However, whereas Chen and Medioni (1991) used point to plane distances for $Gp_i - q_i$, here only simple point-to-point distances are used based on an initial approximation of G, whilst q_i (camera trajectory point selection) is updated with each update of G in the least squares adjustment. A further distinction is that a scale parameter in G is also estimated here. Because coordinate systems are not approximately aligned (evident when comparing Figure 6-22a and b), null values could not be used to approximate G. Thus, to determine suitable approximations, four corresponding arbitrary camera position and trajectory point pairs were coarsely identified per dataset (as illustrated by the green dots on Figure 6-22a and b). These were used to estimate an approximate 2D conformal (four parameter) transformation by solving a linear system of equations in the form:

$$Ax = L + V \tag{6-5}$$

where

$$A = \begin{bmatrix} p_{1E} & -p_{1N} & 1 & 0 \\ p_{1N} & p_{1E} & 0 & 1 \\ p_{2E} & -p_{2N} & 1 & 0 \\ p_{2N} & p_{2E} & 0 & 1 \\ p_{3E} & -p_{3N} & 1 & 0 \\ p_{3N} & p_{3E} & 0 & 1 \\ p_{4E} & -p_{4N} & 1 & 0 \\ p_{4N} & p_{4E} & 0 & 1 \end{bmatrix}$$

$$x = \begin{bmatrix} a \\ b \\ T_E \\ T_n \end{bmatrix}$$

$$L = \begin{bmatrix} q_{1E} \\ q_{1N} \\ q_{2E} \\ q_{2N} \\ q_{3E} \\ q_{3N} \\ q_{4E} \\ q_{4N} \end{bmatrix} \; and \; V = \begin{bmatrix} v_{1E} \\ v_{1N} \\ v_{2E} \\ v_{2N} \\ v_{3E} \\ v_{3N} \\ v_{4E} \\ v_{4N} \end{bmatrix}$$

Here T_E and T_N are the computed approximate easting and northing translations. The linear system of equations may then be solved as:

$$x = (A^T A)^{-1} A^T L \tag{6-6}$$

Also contained in x, the approximate scale s and vertical axis rotation r may be calculated as:

$$s = \sqrt{a^2 + b^2} \tag{6-7}$$

$$r = tan^{-1}\left(\frac{a}{b}\right) \tag{6-8}$$

The result was used to provide approximate values for scale, height axis rotation and easting and northing translations. For the remaining similarity transformation parameters, the height translation was approximated by the difference between the mean arbitrary camera position height and the mean absolute camera trajectory height, whilst easting and northing axis rotations were approximated as null. The transformed (arbitrary) camera positions are illustrated in Figure 6-22c. For the ICP iteration, arbitrary camera positions were initially transformed and corresponding camera trajectory points determined as their closest neighbours. These distances were then minimised in each least squares iteration to determine a new set of transformation

parameters. For subsequent iterations, the arbitrary camera positions were transformed with the new set of transformation parameters to re-select nearest neighbours for q, and the process repeated. In this process, arbitrary camera positions in p were constrained in the direction of their corresponding point in q. However, the movement of this point in the other two degrees of freedom accords with constraints imposed by other point-to-point correspondences (Chen and Medioni, 1991).

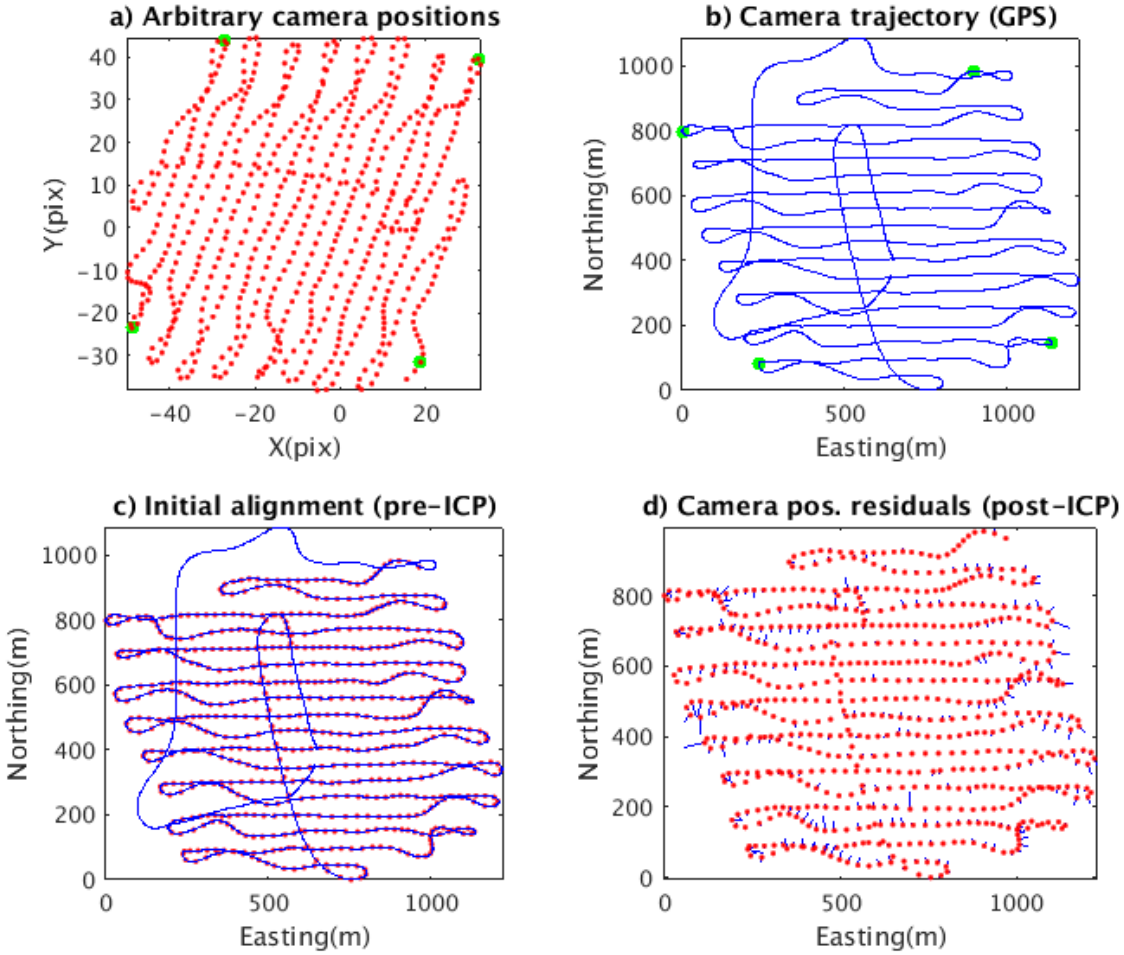

Figure 6-22. Illustration of the trajectory matching ICP adjustment, showing (a) the arbitrary camera positions from the free network adjustment, (b) the densified camera trajectory, (c) the pre-ICP alignment of arbitrary camera positions and camera trajectory, (d) the post ICP residuals at the camera positions (scaled up by 500 for visualisation). Red dots correspond to arbitrary camera positions, blue lines correspond to the GPS camera trajectory and green dots denote the selected seed points.

Step 3: GPS-supported BBA. After the ICP adjustment, arbitrary camera positions are transformed by the final transformation parameters and the final camera positions, hereafter referred to as *TM GPS camera positions*, determined as their closest neighbour on the (GPS) camera trajectory (i.e. the points in q), as illustrated in Figure 6-23. TM GPS camera positions

are then introduced as (weighted) observations in the GPS-BBA implemented through PhotoScan software (although APERO could equally be used). This has the effect of constraining camera position estimates to coincide with the camera trajectory and the constraint is induced primarily in the direction perpendicular to the camera motion. This means camera positions are likely to incur more error in the along-trajectory direction because the arbitrary camera positions are less constrained, and thus it can be expected that coordinate errors will reflect the flight line direction.

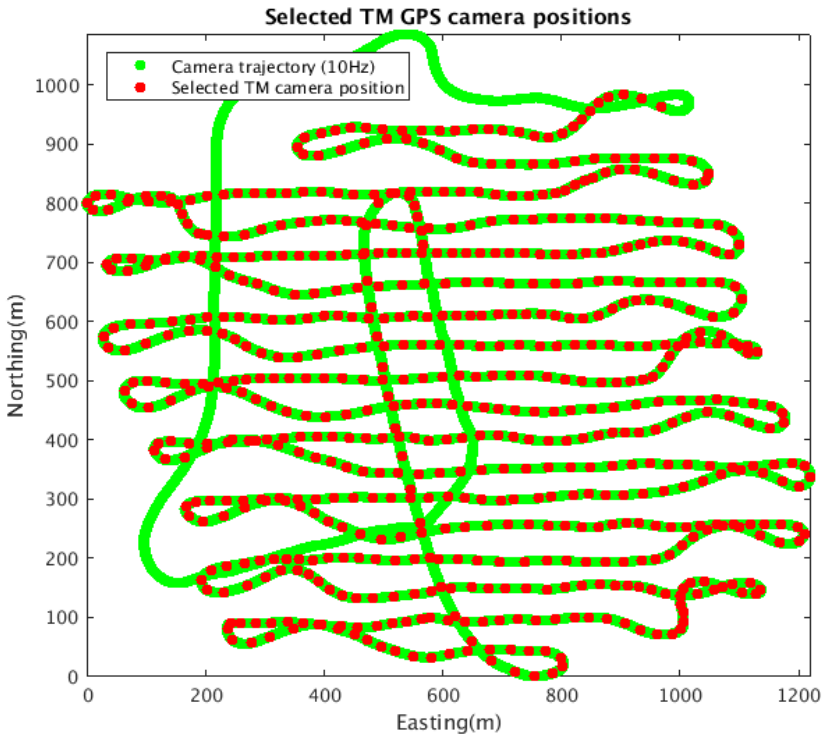

Figure 6-23. Selected points along the camera trajectory after ICP adjustment as TM GPS camera positions.

6.9.2 TM workflow assessment

The performance of the TM approach was primarily assessed through the check point RMSEs and standard deviations after the TM GPS-BBAs, as per the standard GPS-BBAs. However, RMSEs and standard deviations of the camera position residuals were also calculated before and after the ICP adjustment (as shown in Figure 6-22d for the post-ICP adjustment). Camera position residuals before the ICP adjustment refer to the initial $Gp_i - q_i$ differences, whereas those computed after the ICP adjustment refer to the final $Gp_i - q_i$ differences. These are useful to indicate the quality (precision) of the arbitrary camera positions, and general performance of the ICP adjustment.

6.9.3 TM results: pre and post-ICP adjustment

The TM workflow was first undertaken and tested using the PPK-determined camera trajectories, so as not to deteriorate (mapping) results by the PPP trajectory biases. Figure 6-24 shows the RMSEs and standard deviations of the camera position residuals (i.e. the $Gp_i - q_i$ differences) before and after the ICP adjustments for CPF Flights 1-4. Before the ICP adjustment, camera position RMSEs and standard deviations (Figure 6-24a) are c. 5-10 m in easting and northing and c. 20-60 m in height. Large easting and northing RMSEs can be expected due to the use of only four points to calculate initial 2D transformation parameters. However, even larger height RMSEs can be expected because of the very coarse initial approximation used for the height translation (i.e. the difference between the mean arbitrary camera position height and the mean absolute camera trajectory height) and the potentially very inaccurate assumption that easting and northing axis rotations were close to zero. The latter condition will not hold should a highly tilted (non-vertical) image be used to define the arbitrary coordinate system of camera positions estimated in the free network adjustment, and is likely to be the case for CPF Flight 3 where the height coordinate RMSE is c. 60 m.

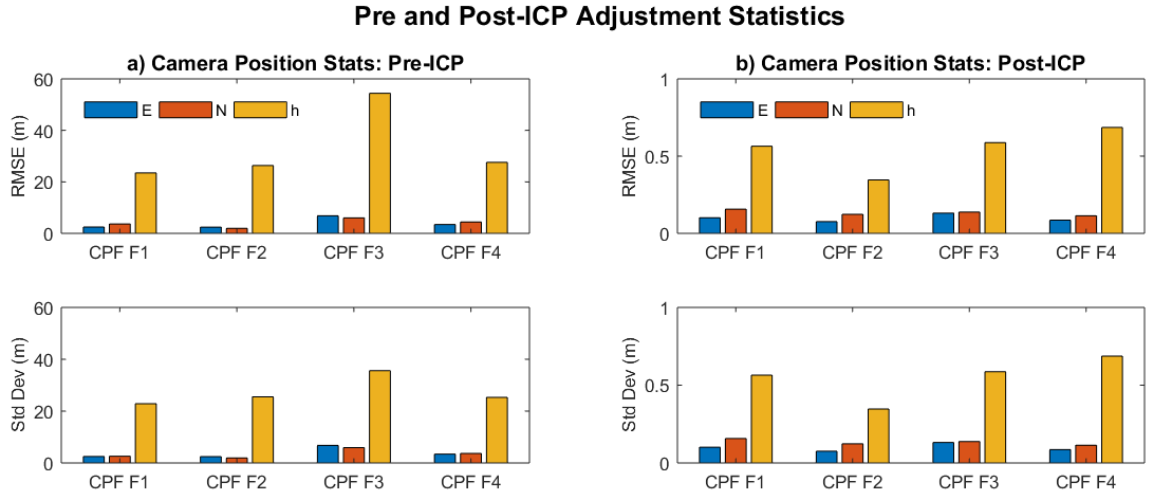

Figure 6-24. RMSEs and standard deviations of the camera position residuals (a) pre- and (b) post-ICP adjustment

In contrast, after the ICP adjustment, camera position RMSEs and standard deviations (Figure 6-24b) are substantially reduced to c. 10-20 cm in easting and northing and c. 30-60 cm in height. Compared to the pre-ICP results, camera position RMSEs from CPF Flight 3 are also now commensurate with the other flights, suggesting that the ICP adjustment has correctly converged despite using low accuracy approximations for the initial transformation parameters. However, the much larger magnitude of camera position RMSEs and standard deviations

compared to the camera trajectory point spacing of c. 1.8 cm, suggests that the transformed (arbitrary) camera positions have a much lower precision.

6.9.4 TM results: TM GPS-supported BBAs

GPS-BBAs were then implemented with both TM PPK and TM PPP camera positions (i.e. using PPK and PPP-determined camera trajectories for the ICP-adjustment, respectively). As the quality of TM camera position precisions was initially unknown, *a priori* standard deviations for camera positions were varied between 10 m and 1 cm. Check point RMSEs and standard deviations after the TM PPK-BBAs for each camera weight setting are presented in Figure 6-25.

With *a priori* camera position standard deviations of 10 m and 1 m, check point RMSEs are consistent for corresponding flights, with variation between flights of 5-10 pixels in easting and northing (equivalent to 15-30 cm) and 5-25 pixels in height coordinates (equivalent 15-75 cm). Being much larger than the expected PPK-determined camera trajectory error suggests that the TM GPS camera positions induce little constraint on the image block for either weight setting. Exceptions to this are the relatively small improvements (of c. 2-5 pixels) to the height coordinate RMSEs for CPF Flights 3 and 4 with a 1 m over 10 m *a priori* camera position standard deviation.

For *a priori* camera position standard deviations of 10 cm and 1 cm, check point RMSEs substantially improve on those obtained after the ICP adjustment (Figure 6-24d). All coordinate RMSEs for all flights are now better than 5 pixels. The best results can be seen for CPF Flight 1, where all coordinate RMSEs are better than 2 pixels (equivalent to c. 6 cm). Regarding check point standard deviations, with an *a priori* camera position standard deviation of 10 cm, these are c. 2 pixels or better for all flights, whilst improving to c. 1 pixel or better with the 1 cm *a priori* camera position standard deviation. This is suggestive that TM GPS camera positions are determined from the ICP adjustment with a sufficiently high precision such that they may be highly weighted in the GPS-BBA (whilst the accuracy relates to that of the PPK camera trajectory).

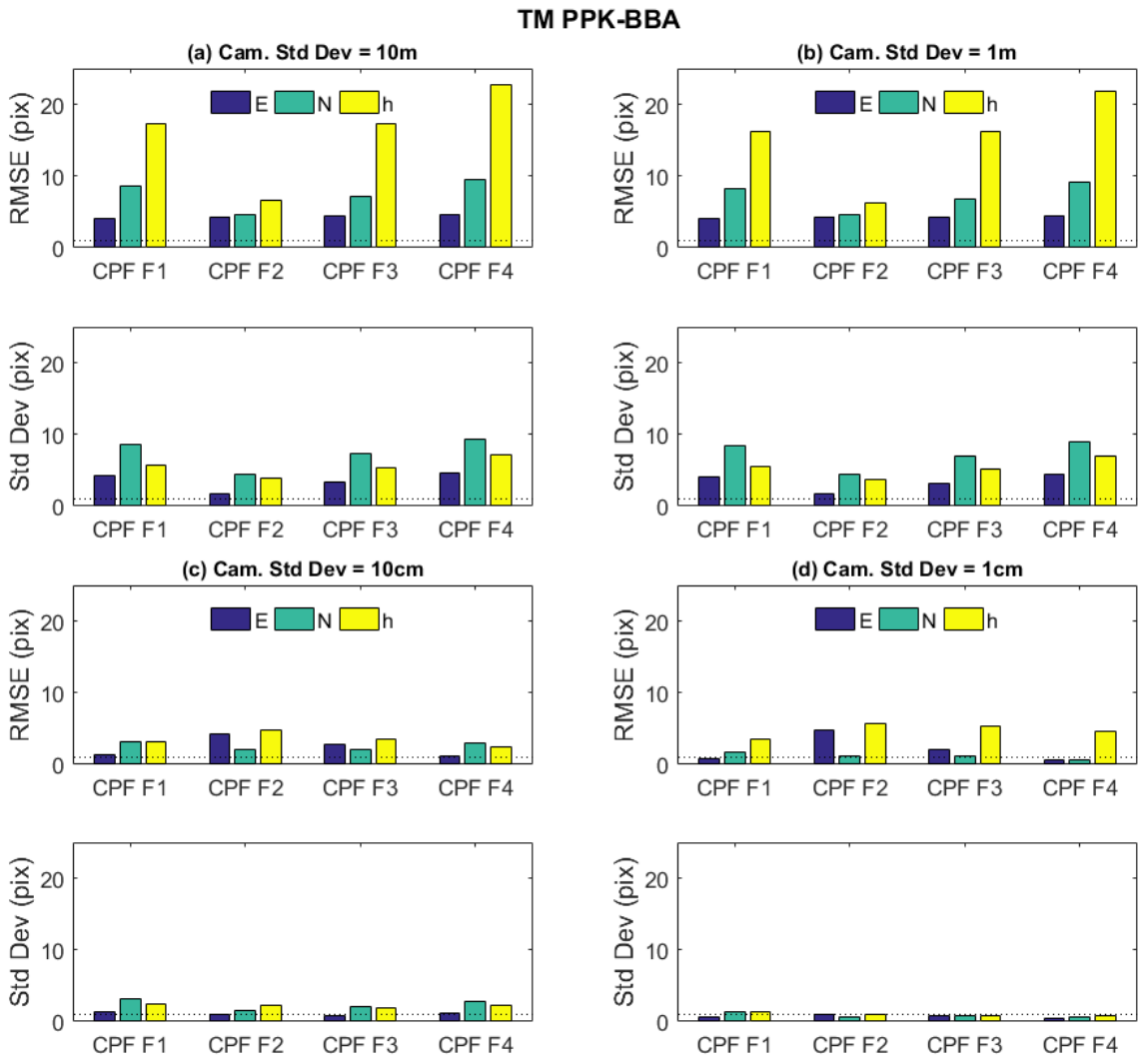

Figure 6-25. Check point RMSE and standard deviation error statistics after TM PPK-BBAs with *a priori* camera position standard deviations of (a) 10 m, (b) 1 m, (c) 10 cm and (d) 1 cm. Dotted line indicates a 1 pixel value.

To compare the performance of the TM PPK-BBA with the standard PPK-BBA workflows (the latter using image time tags to determine PPK camera positions, as presented in Figure 6-12), Figure 6-26 presents check point RMSEs and standard deviations for the corresponding solutions for CPF Flights 2 and 3. The main differences are the c. 5 pixel and c. 2 pixel easting coordinate RMSEs for the TM PPK-BBAs for CPF Flights 2 and 3 respectively, which are only c. 1 pixel for the standard PPK-BBAs. However, northing and height coordinate RMSEs are consistent. This also suggests that the c. 5 pixel height coordinate RMSE for the TM PPK-BBAs are more likely to be an artefact of inaccurate focal length estimation and not the TM approach itself.

The presence of larger easting rather than northing coordinate RMSEs for the TM GPS-BBAs is also noteworthy. As mentioned previously, introducing TM GPS camera positions is likely

to constrain camera positions primarily in the direction perpendicular to the camera trajectory. As flight lines for CPF Flights 2 and 3 comprise east-west running image strips, larger easting coordinate errors could be expected.

Fortunately, both flights also contain image cross strips running north-south, thus offering some constraint in the easting direction. The fact that CPF Flight 3 comprises two cross strips compared to only one for CPF Flight 2, may provide reasoning for the smaller (c. 2 pixel) easting coordinate RMSE for CPF Flight 3 compared to CPF Flight 2.

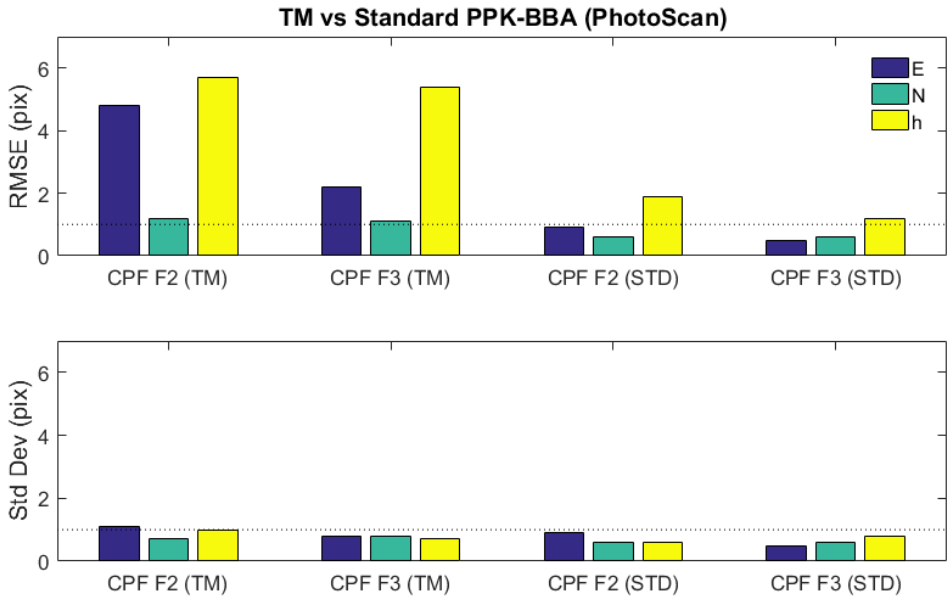

Figure 6-26. Check point RMSE and standard deviation error statistics for TM PPK-BBAs '(TM)' and standard PPK-BBAs '(STD)' for CPF Flights 2 and 3. An *a priori* camera position standard deviations of 1 cm is used for the TM PPK-BBAs. Dotted line indicates a 1 pixel value.

With the TM approach validated using PPK-determined camera trajectories, the same workflow was carried out for PPP-determined camera trajectories. Figure 6-27 shows check point RMSEs and standard deviations for TM PPP-BBAs, with *a priori* camera position standard deviations varying between 10 cm and 1 cm, as before.

For *a priori* camera position standard deviations of 10 cm and 1 cm, check point RMSEs are better than 10 pixels in all coordinate components. Compared to the TM PPK-BBAs, height coordinate RMSEs are around 3 pixels (equivalent to c. 9 cm) larger for CPF Flights 2 and 3, which again reflects the c. 10 cm PPP camera position height error already identified in Figure 6-10. Best results can again be seen for CPF Flight 1, where coordinate RMSEs are better than 1.5 pixels in plan and 2.5 pixels in height (equivalent to c. 4.5 cm and 7.5 cm respectively). This reflects both the good performance of the TM approach, and the centimetre-level accuracy

of PPP-determined camera trajectories. Regarding check point standard deviations, as with the TM PPK-BBAs, these are c. 2 pixels or better for all flights with *a priori* camera position standard deviations of 10 cm, whilst improving to c. 1 pixel or better for a value of 1 cm.

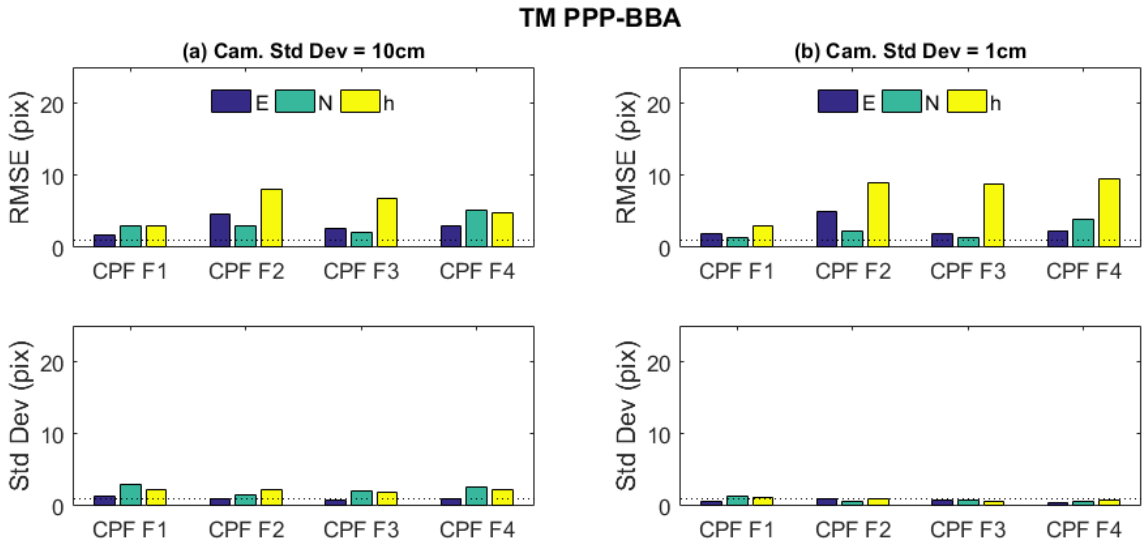

Figure 6-27. Check point RMSE and standard deviation error statistics after TM PPP-BBAs with *a priori* camera position standard deviations of (a) 10 cm and (b) 1 cm. Dotted line indicates a 1 pixel value.

In summary, the TM approach offers a viable solution to GPS-based image block orientation when only the GPS and IMU data are available from the UAV flight (in addition to the imagery). Due to a small drop in mapping accuracy, which evidently correlates with the image block configuration, and noting the ICP adjustments are very sensitive to the shape of the registered objects (e.g. Besl and McKay, (1992)), the TM approach is not as effective as the standard approach of using time tagged GPS camera position observation in the BBA. However, as shown by the TM PPK-BBA results, the error induced is likely to be smaller than that incurred from the absolute PPP error. Further improvement may also be expected by determining a more suitable approximation to the initial similarity transformation, or for more complex image blocks with a greater number of cross-strips.

6.10 Summary

It has been shown that GPS camera positions provide a useful source of control information in BBA and their contribution can be summarised as two-fold. Firstly, both PPP and PPK camera positions contribute equally to the image block precision. This was consistently indicated over all datasets by the achievement of mapping errors with standard deviations of c. 1 pixel in plan and 1-2 pixels in height coordinates. Given the 1-4 cm precision agreement (equivalent to

c. 1 pixel) between PPP and PPK camera positions, this may be attributed to similar constraints on relative image position estimates in the BBAs. The only exceptions, where image block deformations were evidently greater than 1 pixel in magnitude, were for datasets previously identified to exhibit weaker image block configurations when analysing corresponding GCP-BBAs (i.e. LH2 Flights 1-4).

Secondly, both PPP and PPK camera positions contribute to the mapping datum. With PPK camera positions, mapping accuracies of c. 1 pixel or better were consistently achieved in planimetry for all datasets, although the variable height coordinate errors were attributed to inaccurately estimated focal length values. The latter could, however, be anticipated with self-calibration of focal length at a constant flying height. It is thus concluded that PPK camera positions accurately realise the mapping datum. With PPP camera positions, however, mapping accuracies varied between c. 1 and 11 pixels in planimetry, with variable height coordinate errors being a factor of both PPP camera position error and inaccurately estimated focal length values. As planimetric mapping errors were seen to reflect the variable PPP camera position error, it is evident that PPP camera positions did not (reliably) realise the mapping datum with the same accuracy as the PPK camera positions. However, the fact that PPP-BBAs enabled a c. 1 pixel mapping precision in both plan and height coordinates suggested that image blocks were sufficient in scale and orientation and thus equally precise as the equivalent PPK solutions. Based on the utilised software packages, including GCPs (in this case one or four) was only sufficient to remove datum height errors (e.g. as for CPF Flights 2 and 3) whether caused by focal length or PPP error. When planimetric PPP camera position errors were evident, including GCPs caused tensions in BBA because the camera models could not accommodate the conflicting accuracies of the GCPs and PPP camera positions. For this reason it was suggested to use the GCP to calculate a global block shift (translation only) and in doing so, PPP-induced datum errors were mitigated to the 1 pixel level, as per the GCP-BBAs, whilst maintaining an equivalent mapping precision. Therefore, despite UAV PPP positioning errors, PPP-determined camera positions were still leveraged to reduce GCP requirements, as per the UAV PPK positioning technique. Finally, in the absence of image time tags (in this case missing due to system failures for CPF Flights 1 and 4), the developed TM approach remains a viable option for GPS-based image block orientation after the free network adjustment. After the TM GPS-BBA, mapping coordinates were equally precise to the corresponding standard PPK-BBA results, but remained susceptible to coordinate biases of up to c. 5 pixels, which were expected to be a result of ICP registration errors. The difference between PPP and PPK equivalent solution, however, again reflected the PPP error magnitude.

Chapter 7. Discussion and Conclusions

This chapter discusses the overall performance of UAV-based PPP and the PPP-BBA workflow with comparison to published state-of-the-art workflows and relatable achievements. Firstly, the achieved UAV PPP performance is discussed with comparison to the other published kinematic PPP results presented in Chapter 3. Following this, results of the PPP-BBA workflows are evaluated with respect to (1) the theoretically achievable mapping accuracies per dataset, (2) the mapping accuracies achieved by similar published workflows, and (3) the suitability of the PPP-BBA workflow to different applications. Finally, the research aim and objectives are revisited and recommendations for future work are made.

7.1 UAV PPP performance

7.1.1 Relatable achievements

Airborne platforms. Gross *et al.* (2016) present the only UAV-based application of PPP to date. Presented results were based on three UAV flights of only 2.6-5.7 minutes in duration, which are much shorter than the 12 minute or more duration QuestUAV flights presented in Chapter 5. Gross *et al.* (2016) consequently achieved UAV PPP positioning accuracies in the range of 0.61 to 1.39 m. These values are larger than the maximum QuestUAV PPP positioning error of c. 20 cm in planimetry and c. 50 cm in height (from LH2 Flight 4 with a 00:12:19 duration) which can be attributed to the longer QuestUAV flights and thus GPS processing durations, which improved the accuracy of float ambiguity estimation. Moreover, with many QuestUAV flight durations exceeding 30 minutes, the best accuracies obtained were c. 3 cm in planimetry and a decimetre in height coordinates (from CPF Flights 2-3, Grayson *et al.* (2018)), which are considered to be the highest obtained accuracy of UAV PPP positions to date. Further analysis of the QuestUAV results in relation to those at the GNSS reference station (not performed by Gross *et al.* (2016)), showed GPS PPP improvements could be related to improved satellite geometries and greater numbers of satellites (i.e. greater than 9) available to the UAV due to the open sky environment. The QuestUAV results also largely improve on the metre-level PPP positioning accuracies of Yuan *et al.* (2009), which were obtained from a substantially longer manned aircraft flight of 5 hour 43 minutes in duration. However, in the case of Yuan *et al.* (2009), large baselines were used for the generation of reference PPK GPS trajectories, which thus could have been contaminated with residual atmospheric errors.

Ground-based platforms. In order to assess the performance of UAV-based PPP with respect to other published results for ground based platforms, the obtained PPP positioning accuracies (RMSEs) are plotted against their respective processing durations in Figure 7-1, along with those from the case studies discussed in Chapter 3. The latter include the 2-hour land vehicle test of Cai and Gao (2013) (E|N|h errors of 18.2|2.8|9.1 cm), the 2-hour land vehicle test of Yu and Gao (2017) (E|N errors of 4.5|8.5 cm), the 32 minute ground based vehicle test of Anquela *et al.* (2013) (E|N|h errors of 55.2|64.5|82.4 cm) and the 30 minute walking trajectory test of Anquela *et al.* (2013) (E|N|h errors of 12.5|19.8|67.9 cm) as well as results from the three 2.6-5.7 minute UAV flights of Gross *et al.* (2016) and 5 hour 43 minute manned aircraft flight of Yuan *et al.* (2009) (E|N|h errors of 0.8|0.5|1.2 m).

With respect to the PPP processing duration, Figure 7-1 shows the QuestUAV PPP performance to be generally very good, with the majority of coordinate component errors being less than 20 cm for processing durations of under 50 minutes. Such coordinate accuracies are generally either commensurate or improvements on those of the case studies, whilst being obtained for much shorter processing durations.

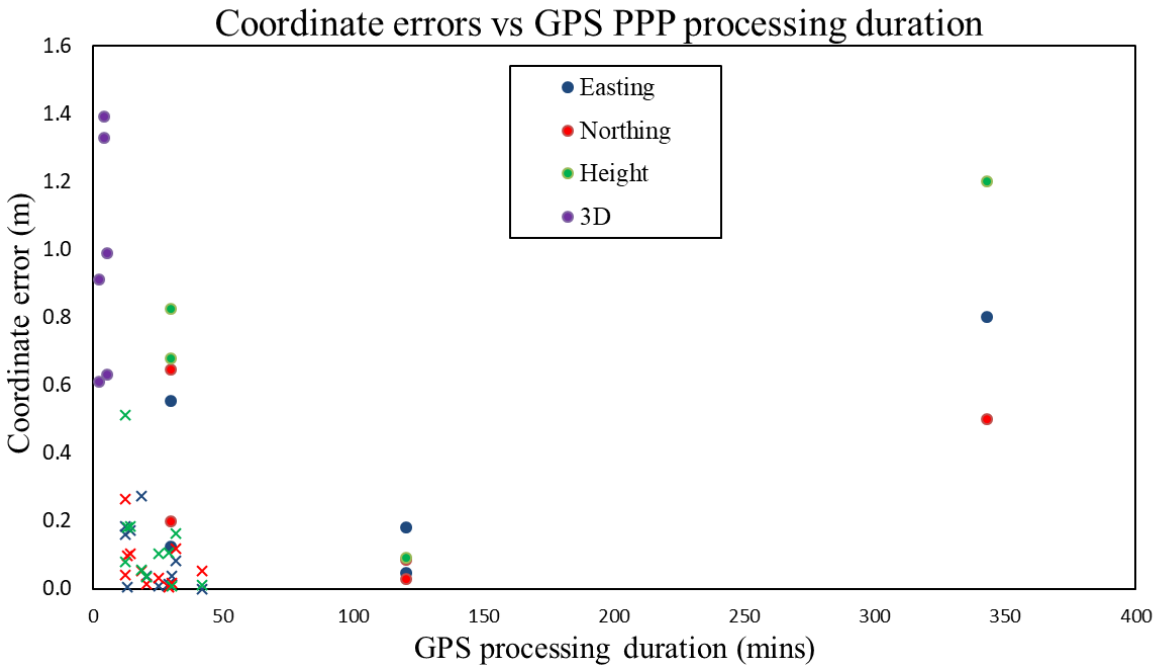

Figure 7-1. PPP coordinate errors obtained from the QuestUAV flights ('x' symbols) and case study examples (filled 'o' symbols) plotted against the PPP processing durations. It should be noted that case study examples include results from both airborne and ground-based platforms. Also, where mean values have been reported in case studies, the absolute mean values have been plotted.

Though not apparent in Figure 7-1, the PPP coordinate precisions obtained in these case studies are also typically much poorer than those obtained for the QuestUAV flights. For example, Yu

and Gao (2017) achieved coordinate precisions of 6.7 cm and 9.1 cm in easting and northing respectively for their 2-hour land vehicle test. Anquela *et al.* (2013) achieved coordinate precisions of 9.0 cm, 8.2 cm and 33.2 cm for their 32 minute ground based vehicle test and 10.1 cm, 4.5 cm and 15.7 cm for their 30 minute walking trajectory test in easting, northing and height respectively. In contrast, the obtained QuestUAV PPP position precisions are at most c. 4 cm for any flights and coordinate components.

7.1.2 Reliability of UAV-based PPP

Flight only processing. Despite the good performance of UAV-based PPP with respect to the case studies discussed in Chapter 3, there remains much variation in the final accuracy of PPP positions between QuestUAV flights (when compared with the PPK positions). The variable performance may be attributed to varied level of ambiguity convergence between flights, which is a contrast to the PPK reference solutions where (double differenced) ambiguities are fixed to their true integer values.

The general assumption was previously made that longer GPS processing durations would facilitate a greater change in satellite geometries such that that accuracy of float ambiguity estimation would be improved (e.g. as per Cai and Gao, 2013 and Li and Zhang, 2014). This was generally confirmed by the better UAV PPP position accuracies obtained for the longer flights (i.e. the CPF and LH1 flights) as opposed to the worse position accuracies obtained from the shorter flights (i.e. the LH2 flights). However, as shown in Chapter 5, the reality was that UAV GPS datasets were contaminated with cycle slips, resulting in the need for multiple ambiguity estimations for the same satellites and thus shorter data spans for these ambiguities. New ambiguity estimation, however, was still assisted by good satellite geometries and numbers (more than 9). As was confirmed by the CPF GPS control experiment at the reference station, coordinate errors for the sub-30 minute UAV flights were also likely to vary between flights depending on the time-of-day satellite geometries, which were unique for each observation period. For these reasons, the obtainable PPP positioning accuracy from UAV flight durations cannot be generally ascertained. However, results suggested it is likely to be c. 0.5 m or better, with the possibility of improving to 10 cm, depending on observation conditions (e.g. PDOPs and the number of satellites). Limited discussion can be found in literature with regards to the presence and consequences of cycle slips on dynamic platforms. Anquela *et al.* (2013) noted the coincidence of PPP coordinate biases with building construction blockages for their ground based vehicle and walking trajectory tests, however, they did not further investigate or specify how many cycle slips occurred. The open sky visibility at the UAV promotes its suitability as a platform for PPP, whilst individual ambiguity resets only

caused small, c. 5 cm coordinate error fluctuations. However, coordinate jumps will prominently happen when cycle slips occur for all satellite observations simultaneously.

The longer QuestUAV flight durations also made it possible to perform GPS processing duration tests. Although Li and Zhang (2014) performed similar kinematic PPP tests for static IGS reference station data, similar tests implemented on dynamic platforms could not be found in literature. Over all flights, GPS processing duration tests showed a substantially larger variation (of c. 40-80 cm, see Figure 5-12 and Figure 5-13) in UAV PPP positioning accuracies for GPS processing durations of less than 10 minutes, which is consistent with the variable positioning accuracies obtained for the three short-duration flights of Gross *et al.* (2016) (noting the 0.61 to 1.39 m range). This has implications for future short-duration UAV flights, as a greater range of coordinate errors can be expected.

Ground logging periods. Gross *et al.* (2016) also suggested the possibility of implementing a ground-based initialisation period to improve ambiguity estimation (although they did not implement such procedures). Results presented here demonstrated the difficulties in effectively implementing such procedures due to the high likelihood of cycle slips, and in most cases, complete loss of lock, during the transition into and out of the flights. This is especially the case for the Quest Q200 and DATAhawk systems, where launch procedures require the UAV (and thus GPS antenna) to be highly tilted, whilst landing procedures involve the UAV being grounded (crashed) at flying speed. During such events, cycle slips were sufficient to prevent any improvement to the UAV PPP positioning accuracy with the extended GPS observation duration. Ground-based initialisation periods may thus be more suitable for runway-based UAV launches and landings as per the Gross *et al.* (2016) fixed wing UAV, or else vertical launches and landings as per rotary wing UAVs, in which cases the GPS antenna would remain upright.

Coordinate precisions. Unlike the UAV PPP positioning accuracy per flight, precisions were generally consistent over all flights at the 1-4 cm level. Consequently, it can be concluded that UAV PPP positions with a centimetre-precision can be obtained with a high reliability (as opposed to accuracy). This was attributed to the two-step estimation approach in PANDA, as described in Chapter 3, such that all GPS observations from the dataset contribute to the determination of coordinates at each epoch, thus maintaining a similar accuracy throughout the computed solution. The fact that PPP position accuracies did not correlate with respective precisions suggests that erroneous satellite ambiguities have predominantly caused coordinate biases. Gross *et al.* (2016) also reported UAV PPP coordinate precisions of c. 3 cm (in 3D) for all flights, which are also consistent with the results presented here.

To summarise, results suggest that UAV PPP positions may be reliably obtained with a precision of a few centimetres. This may be contrasted to the ground vehicle-based PPP trials of Anquela *et al.* (2013), Cai and Gao (2013) and Yu and Gao (2017), where PPP position precisions were a factor of two to three times worse. On the contrary, presented results did not suggest a typical obtainable accuracy of UAV PPP positions due to the inter-flight variability between the centimetre and decimetre-level. However, it was shown that datasets of at least 20 minutes in duration are desirable for the possibility of obtaining UAV PPP coordinate accuracies better than 10 cm. Results for CPF Flights 1-3 and LH1 Flight 1 and 3 illustrated the possibility of obtaining UAV PPP positions with an accuracy of a few centimetres in plan and 5-10 cm in height coordinates. However, for the shorter duration flights (i.e. c. 12-18 minutes), these are more likely to be at least c. 0.5 m.

7.2 Quality of image block orientation

7.2.1 Remarks on block orientation approaches

GPS-BBA implementation in PhotoScan and APERO. Both PhotoScan and APERO allow for the implementation of GPS-BBAs in which residual errors between the observed and estimated camera positions are minimised in the BBA. With centimetre-accurate GPS camera positions (e.g. as produced by all PPK solutions and some of the PPP solutions) and accurately estimated focal length parameters, such GPS-BBAs enabled one pixel-level accuracy mapping without GCPs, as was also achieved by Rehak and Skaloud (2015), Gerke and Przybilla (2016) and Benassi *et al.* (2017). However, when focal length was estimated inaccurately (for example, due to limited image scale variation), regardless of the accuracy of the GPS camera positions, object point height errors prevailed, whilst being software-dependant, which can only be compensated for using a small number GCPs (e.g. one or four). Benassi *et al.* (2017) also demonstrated variable object point height coordinate errors of 0.8-4.0 pixels (c. 2-9 cm) over four near-identical flights, and similarly showed a reduced performance in PhotoScan over APERO. Fortunately for the CPF datasets, the range of camera position height was large (at c. 60 m, equivalent to c. 50% of the flying height), which is known to improve focal length estimation (Gerke and Przybilla, 2016; Luhmann *et al.*, 2016). This was possible for the CPF flights as imagery was acquired on the UAV descent prior to landing, and was sufficient to facilitate the estimation of camera focal length with a pixel-level accuracy in both APERO and PhotoScan, judging by the achieved 1-2 pixel level object point height accuracies. However, in the absence of camera height (and thus image scale) variation, as was the case for the remaining flights, both PPK-BBA and PPP-BBA solutions are equally limited without GCPs and hence such effects should be discounted from the PPP-BBA results.

In addition, the planned acquisition of parallel axis UAV imagery suggested the possibility of doming deformation errors in the photogrammetric model that result from the incorrect estimation of lens distortion parameters (Wackrow and Chandler, 2008; James and Robson, 2014; Eltner and Schneider, 2015; Carbonneau and Dietrich, 2017). However, the high precision (c. 2 pixels or better) of height mapping errors obtained for all flights suggests that such effects are not present in the PPP- or PPK-BBA determined mapping coordinates, or if so, they are small in magnitude relative to the GSD. Moreover, plotted check point height residuals were consistent over the image block and did not show any visually discernible systematic errors. Also assisting the mitigation of doming deformation effects was the natural convergence of UAV imagery due to camera attitude variation exceeding the minimally desired value of +/- 5 degrees (James and Robson, 2014). Overall, it can be concluded that the effects of lens distortion error has been either sufficiently mitigated (to the 1-2 pixel level) in the BBA due to natural image convergence, or otherwise from the equal (relative) constraints offered by both PPK and PPP camera positions observations.

The main limitation of the employed software packages with regards to the implementation of PPP-BBAs, is that they did not allow the modelling of strip-wise or block-wise GPS camera position errors, as per traditional GPS-supported AT. This was particularly problematic when trying to compensate for PPP camera position biases using a small number of GCPs. Simply including the GCPs as direct observations caused tension in the GPS-BBA and consequently block deformation, which was indicated by the increased check point standard deviations and retained magnitudes of the mapping errors. Such problems have not yet been addressed in literature, which is likely because GPS (i.e. PPK) camera position biases are not expected. Moreover, if both GCPs and the UAV camera are positioned with respect to the same GNSS reference station coordinates, a consistent reference frame is guaranteed. On the contrary, when PPP camera position errors were small, and GCPs were included in the PPP-BBA, camera position biases were absorbed by image residuals and estimated camera model parameters. PPP camera position height errors were mostly absorbed by estimated focal length.

GCP-based block shift. To prevent PPP biases prevailing as increased object point errors, the suggested solution was to apply a one- or four-GCP block shift calculated from the same GCPs. This could be implemented without modifying software source code. The high precision of PPP camera positions (with respect to the PPK camera positions) suggested that such observations were sufficient in scale and orientation, but weak in origin, and thus only an origin shift (three translations) was applied to the image blocks. This simplistic approach had the advantage that it could be applied (1) independently of the employed software package and (2) using as little

as one GCP, although four GCPs was more reliable. The (biased) PPP camera positions however retain their contribution to the image block rotation, scale and shape. Dall'Asta *et al.* (2017) also used a similar GCP-based block shift approach for a UAV-based rock glacier survey, where they shifted the image block to have zero discrepancy on a selected GCP. Check point errors prior to the image block shift were not reported, but afterwards values were 4.0 cm, 3.1 cm and 7.2 cm in easting, northing and height respectively. These are comparable to those achieved here for the PPP-BBAs with one- or four-GCP block shifts applied, thus serving as further validation of the approach. In addition to the removal of PPP camera position errors, the block shift also eliminated object point height errors resulting from erroneous focal length estimation.

The relative aerial control approach (as discussed in Chapter 2) is also relatable to the block shift problem in that it eliminates the effects of GPS camera position biases by constraining the BBA with relative (not absolute) camera position observations. Rehak and Skaloud (2017a) showed this to be particularly beneficial when employing low accuracy, yet high precision single frequency (L1 only) PPK positioning, which is similar to the PPP technique with regards to the potential for coordinate biases. As Rehak and Skaloud (2017a) were able to use the relative constraints approach to mitigate the impact of their 10 cm PPK camera position biases, such an approach should also enable the impact of the PPP camera positions biases to be mitigated, with the additional advantage of eliminating the GNSS reference station. The image block shift approach, however, has the additional advantage that it can be implemented using only a single GCP, unlike the minimum of three required for the relative aerial control approach.

TM approach. In addition to the standard approach of using GPS-camera time synchronisation for camera position determination, an alternative solution has been presented which registers arbitrary camera positions (estimated in the free network adjustment) to the GPS-determined camera trajectory, before selecting the nearest trajectory points to each registered camera position for use in subsequent BBAs. This unique approach was conceived so that GPS-based image orientation could be performed for CPF Flights 1 and 4, where image time stamps were not acquired due to UAV system failures. When comparing the standard workflow (GPS-BBA) with the TM workflow for CPF Flights 2 and 3, results suggested a slight drop in mapping accuracy of around 2-4 pixels in plan and height coordinate components. Moreover, the orientation of such errors appeared to be correlate with the direction of the image strips, such that this could be attributed to limitations of the ICP adjustment. The mapping precision, however, was very similar to the standard workflows, at c. 1 pixel in both plan and height

coordinates, and therefore, despite the pixel-level drop in mapping accuracy, the TM remains a feasible option in situations when GPS-camera time synchronisation is not achieved.

7.2.2 Theoretical accuracy

To further evaluate the performance of the PPP-BBAs, the mapping errors were compared to their theoretically achievable values, which may be obtained through error propagation, given approximate dataset parameters (Kraus, 2007; Murtiyoso and Grussenmeyer, 2017). According to Kraus (2007), the theoretical error (RMSE) of object point coordinates from a two-image aerial reconstruction may be calculated as:

$$\sigma_z = m_b . \frac{Z}{B} . \sigma_b \tag{7-1}$$

$$\sigma_x = \sigma_y = m_b . \sigma_b \tag{7-2}$$

where σ_i is the coordinate RMSE for component i, m_b is the image scale, Z/B is the height/base ratio and σ_b is the accuracy of image measurement. The theoretical error ratio may then be calculated as:

$$e_x = \frac{e_m}{\sigma_x} \tag{7-3}$$

where e_x is the theoretical error and e_m is the actual measured error for coordinate component x, and thus values of one suggest an optimal performance.

Table 7-1 presents corresponding theoretical errors (σ_x, σ_y, σ_z) and theoretical error ratios (e_x, e_y, e_z) for results of the PPP-BBAs and PPP-BBAs with four-GCP block shift. From Table 7-1, it can generally be seen that the PPP-BBA mapping errors are between one and five times their theoretical values. Best results are seen for CPF Flights 2 and 3 as well as LH1 Flight 1, where theoretical error ratios are c. 1 for all coordinate components. However, PPP camera position biases in LH1 Flight 2 and LH2 Flight 4 result in theoretical error ratios of 9.4 and 6.0 respectively. In contrast, for the PPP-BBAs with four-GCP block shifts applied, theoretical error ratios are c. 1 or better for all flights and coordinate components with the exception of the easting component of LH1 F3, which is at 1.3. Overall, the range of theoretical error ratio values suggests that PPP-induced mapping errors may be the most limiting with regards to mapping accuracy without GCPs, but may be effectively mitigated with application of the block shift.

Fights	Scale	Theoretical error (cm)	Theoretical error ratio	
			PPP-BBA	PPP-BBA+4GCP
		$\sigma_x, \sigma_y, \sigma_z$	e_x, e_y, e_z	e_x, e_y, e_z
CPF F1 (TM)	7,500	3, 3, 10	1.9, 1.3, 0.9	-
CPF F2		3, 3, 10	0.8, 1.2, 1.0	0.8, 0.6, 0.2
CPF F3		3, 3, 10	0.6, 0.9, 0.9	0.5, 0.7, 0.3
CPF F4 (TM)		3, 3, 10	2.3, 3.8, 0.9	-
LH1 F1		3, 3, 10	1.0, 0.7, 0.8	0.2, 0.7, 0.7
LH1 F2		3, 3, 10	9.4, 1.6, 0.4	0.8, 0.3, 0.3
LH1 F3		3, 3, 10	0.8, 1.8, 0.3	1.3, 0.6, 0.3
LH2 F1	11,550	5, 5, 15	3.4, 2.0, 0.7	0.7, 0.8, 0.7
LH2 F2		5, 5, 15	0.6, 1.4, 0.4	0.6, 0.4, 0.4
LH2 F3		5, 5, 15	2.8, 1.2, 2.2	1.0, 0.9, 0.7
LH2 F4		5, 5, 15	4.3, 6.0, 2.3	0.6, 0.6, 0.4

Table 7-1. Theoretical errors (σ_x, σ_y, σ_z) as per equation (7-1) and theoretical error ratios (e_x, e_y, e_z) as per equation (7-3) for PPP-BBA solutions. Theoretical values assume an 18 m/s UAV velocity with image exposure every 2 s (therefore B = c. 36 m) and image measurement precision σ_b of 1 pixel (equivalent to 4 um).

7.2.3 Applications

Relative errors. As was presented in Table 2-1 for a number of GPS-based case studies, Table 7-2 presents relative errors with respect to viewing distance for the PPP-BBAs (without GCPs) and PPP-BBAs with four-GCP block shifts applied. Also indicated are the best and worst flight performances (in green and red, respectively). Relative errors for the PPP-BBAs are 1:326-1:3698 for plan and 1:354-1:3636 for height coordinates. Referring to Table 2-1, these improve on studies using pseudorange-based GPS, namely Kung *et al.* (2011), Turner *et al.* (2012) and Shahbazi *et al.* (2015), where values are 11:7-1:265 in plan and 1:23-1:299 in height coordinates (also noting that the SPP positioning approach provides an alternative solution that does not require a GNSS reference station). These are also commensurate with studies employing carrier phase-based GPS, where relative errors are 1:137-1:3152 in plan and 1:189-1:1849 in height. Moreover, median values for the PPP-BBAs are 1:1169 and 1:1647 in plan and height respectively, which substantially improve on the values of 1:163 and 1:149 for studies using pseudorange-based GPS and 1:1886 and 1:392 for studies using carrier phase-based GPS. However, when applying the four-GCP block shift to mitigate PPP-induced mapping biases, median values improve to 1:3356 and 1:3528, which further improve on studies based on carrier phase-based GPS. Such median values for the PPP-BBAs also improve on the median (3D)

relative error value of 1:639 determined by Smith and Vericat (2015) from the analysis of 50 RMSE statistics reported in SfM literature.

Flight	PPP-BBA		PPP-BBA+4GCP	
	Plan	h	Plan	h
CPF F2	2774	1250	4000	**5714**
CPF F3	**3698**	1333	4650	4444
LH1 F1	3068	1481	4339	5714
LH1 F2	419	3077	**4682**	4000
LH1 F3	2031	**3636**	2794	5000
LH2 F1	615	1212	2261	**1143**
LH2 F2	1538	2105	3123	2105
LH2 F3	783	370	**1661**	1818
LH2 F4	**326**	**354**	2691	1905
mean	1695	1647	3356	3538
median	1538	1333	3123	4000

Table 7-2. Relative errors for PPP-BBAs and PPP-BBAs with four-GCP block shifts applied

Potential applications. In addition to the relative errors, it is also interesting to recognise which applications the obtained PPP-BBA accuracies may be suitable for. As mentioned in Chapter 1, RICS have provided guidelines in the form of survey detail accuracy bands that specify the required accuracy of object point determination for certain applications (RICS, 2014). Accordingly, the results from the PPP-BBAs and PPP-BBAs with four-GCP block shifts have been classified in Table 7-3. This shows that object point accuracies from the PPP-BBA for eight of the flights (i.e. all CPF flights, LH1 Flights 1 and 3 and LH2 Flights 1 and 2) satisfy survey detail accuracy band *H*, which includes low accuracy topographic surveys, national urban area mapping and geotechnical mapping. However, with only a small improvement to the height coordinate accuracies (e.g. 5 cm for CPF Flights 2 and 3), these results could be classified under survey detail accuracy band *G*, which additionally includes low accuracy measured building surveys, boundary mapping and utility tracing. For PPP-BBAs with four-GCP block shifts applied, obtained object point accuracies generally move up by 1-2 survey detail accuracy bands. For example, six of the flights now satisfy survey detail accuracy band *F*, which includes low accuracy measured building surveys, topographic surveys and high accuracy utility tracing.

Accuracy band	Applications	CPF F1	CPF F2	CPF F3	CPF F4	LH1 F1	LH1 F2	LH1 F3	LH2 F1	LH2 F2	LH2 F3	LH2 F4
Band E **+/-2.5/1.0 cm**	Measured building surveys, topographic surveys, area registration, utility verification, map scales: 1:100											
Band F **+/-5.0/5.0 cm**	Low acc. measured building surveys, topographic surveys, high acc. utility tracing, map scales: 1:200		X	X		X	X	X		X		
Band G **+/-10.0/5.0 cm**	Low acc. measured building surveys, topographic surveys, utility tracing, boundary mapping, map scales: 1:500							X	X			
Band H **+/-25.0/12.5 cm**	Low acc. topographic surveys, national urban area mapping, geotechnical mapping, map scales: 1:1000	X	X	X	X	X			X	X	X	X
Band I **+/-50.0/50.0 cm**	Low acc. topographic surveys, non-urban area mapping, general boundary and asset mapping, map scales: 1:2500						X				X	X

X = PPP-BBA, **X** = PPP-BBA+4GCPs

Table 7-3. Survey detail accuracy bands according to the RICS guidance notes (RICS, 2014) and achieved accuracies for the standalone PPP-BBAs (blue 'x' symbols) and PPP-BBAs with four-GCP block shifts (red 'x' symbols).

Considering the application scenarios presented in Table 1-1, the PPP-BBA technique would be suitable for coastal erosion monitoring, as per Goncalves and Henriques (2015) where surface changes were expected to be 0.2-6 m per year, and for landslide monitoring, as per Lucieer *et al.* (2014) where landslide displacements of up to 6 m were expected. In the context of surface change detection, in accordance with equation (7-4), where t is the t-distribution value of 1.96 to signify a 95% confidence limit and σ_z^n is the vertical uncertainty for DEM n (typically equal to c. 3cm for the GCP-BBAs with 4 GCP block shifts), an associated LoD threshold for surface change detection between DEM epochs of 8.3 cm is attainable.

$$LoD\ threshold = t(\sigma_z^1 + \sigma_z^2)^{1/2} \quad (7\text{-}4)$$

This would suffice for applications such as the landslide monitoring of Dall'Asta *et al.* (2017) where 10 cm monthly displacements were expected, but would not suffice for quantifying sub-centimetre level rill and interrill erosion as per Eltner *et al.* (2015). It is expected, however, that the LoD threshold value would reduce with a smaller GSD (i.e. due to smaller DEM errors).

Using the PPP-BBA technique, it is expected that the 244 GCPs used for the monitoring of the Super Suaze landslide in France (Niethammer *et al.*, 2012; James *et al.*, 2017) could be reduced to only four, representing a substantial reduction in ground survey efforts, as well as the time taken to measure each GCP in the imagery. Further considering that James *et al.* (2017) suggested 47 of these GCPs to be unstable (based on their larger BBA coordinate residuals), PPP camera positions could be used in the BBA to minimise GCP usage such that only the most stable GCPs (i.e. outside the glacier) need be selected.

Scalability. A note should also be made on the scalability of the precision and accuracy of the photogrammetric BBA verses the absolute precision and accuracy of the PPP component. When the flying height increases, so does the GSD, which becomes a limiting factor on the accuracy of object point determination as image measurement errors correspond to greater distances on the ground. Object point errors thus correlate with image scale. Whereas a GSD of 3 cm has been achieved here from a 120 m flying height, largely variable GSDs can be found in literature. For example, Javemick *et al.* (2014) achieved a larger GSD of 16 cm with a flying height of 600-800 m, whereas Eltner *et al.* (2015) achieved a much smaller, sub-cm GSD from a 5 m flying height (noting this comparison is also influenced by differing camera characteristics).

Considering the errors introduced by image scale, in the context of GPS-BBAs, GSD may become more limiting than the accuracy of camera position determination. For example, with a 10 cm GSD, a 3 cm systematic GPS camera position error may not be detected. However, with a 3 cm GSD, it is a likely that a 10 cm systematic GPS camera position error will be detected (also depending on the magnitude of other error sources) as the latter is a multiple of three times the former. Considering the potentially decimetre-level PPP camera position errors, such errors could be easily detected in the object point coordinates (without GCPs) in all cases given the 3 cm GSD. However, had the GSD been larger, for example 10 cm, the image spatial resolution would have remained more limiting on the accuracy of point determination than the PPP camera position errors. Therefore, it should be considered that PPP-BBAs have an increasing applicability to smaller scale (large GSD) imagery as PPP camera position biases become less relevant. It has however, been demonstrated for a number of the UAV flights that 1-pixel level (i.e. c. 3 cm) point determination accuracies are obtainable using the PPP-BBA technique without GCPs, thus confirming the potential for large scale mapping applications.

7.3 Revisiting the aim and objectives

The aim of this research was *to reduce reliance on GCP requirements in large scale UAV-based photogrammetric mapping using high precision GNSS positioning techniques*. This was achieved by satisfying the five research objectives as follows:

The first objective was *to review state-of-the-art digital photogrammetric techniques for UAV image processing and the requirements of external photogrammetric control information*.

This objective was achieved in Chapter 2 by synopsis of close range photogrammetric literature and discussion of the general routines employed in the SfM-photogrammetric workflow. This covered the individual steps that are necessary to facilitate the orientation of close range UAV imagery acquired by consumer grade digital cameras. The typical workflow comprised tie point determination using modern robust feature matching algorithms, followed by direct, SfM-based techniques for the generation of approximate solutions, and finally a rigorous refinement though concepts of photogrammetric BBA. Despite being discussed in the UAV context, such a workflow is synonymous to that adopted for the processing of close range terrestrial imagery.

The latter part of this objective was achieved by discussing the roles and requirements of control information with regards to their effects on the UAV image block orientation, namely to (1) define the mapping datum and (2) compensate for systematic errors. In addition, the consequences when such information may be inadequate, namely that image block deformations can be observed, were discussed. This was followed by discussion of the standard workflow using GCP control and best practices to ensure the requirements of control information were met. Some case study examples were presented to demonstrate the state-of-the-art achievements in terms of mapping accuracy, but also the drawbacks and challenges associated with GCP control implementation, with particular regards to the application.

The second objective was *to review existing, standard techniques for applying GPS positions in the photogrammetric workflow*.

This was achieved by discussing the benefits of including GPS camera position control in the BBA, whilst bearing in mind the problems of GCP control implementation. This initially focused on the first applications in so-called GPS-supported AT on manned aerial platforms (in the 1980s when GPS first became available) and then in the context of UAVs through the GPS-supported BBA, which follows on from the SfM-photogrammetric workflow. Discussion also briefly covered the direct and integrated sensor orientation (DSO, ISO) techniques, although these have yet to be effectively applied on UAVs due to the limited quality of orientation angles

produced by UAV-compatible MEMs-based IMUs. The limitations of GPS-supported BBAs, namely their inability to model strip or block-wise systematic GPS shift errors as per GPS-supported AT, were also highlighted. Example case studies were presented to illustrate attainable mapping accuracies from UAV-based GPS-supported BBAs. This suggested that substantial benefits were only evident when GPS camera positions were both centimetre-accurate, and included as observations in the BBA (and not just to determine a similarity transformation).

Another contribution to this objective was the discussion of basic GPS positioning theory, including the single point, differential pseudorange, carrier phase relative and precise point positioning techniques. It was discussed that the latter two approaches presented the possibility of centimetre-accurate UAV camera positions due to the processing of GPS carrier phase observations. However, whereas the carrier phase relative GPS technique is fast becoming the standard of UAV positioning, the PPP technique had yet to be applied on UAV platforms with a suitable accuracy for effective application in GPS-supported BBA. Moreover, the PPP technique, unlike relative GPS, offered the potential to eliminate the GNSS reference station or need to operate within a permanent GNSS reference station network. Though only one application of PPP on a UAV was found, a review of example case studies which applied PPP technique to other dynamic platforms, such as manned aircraft, ground-based vehicles and walking trajectories, were suggestive of the challenges of determining centimetre-level accuracy PPP positions on a UAV.

The third objective was *to implement PPP on a UAV platform and determine achievable positioning accuracies and precisions given the limitations of UAV-acquired GPS data*.

The PPP technique was successfully implemented on Quest Q200 and DATAhawk fixed wing UAV flights using PANDA software and the CODE orbit product. When processing flight only GPS observations, best UAV PPP positioning accuracies of c. 2-5 and c. 2-10 cm in planimetric and height coordinate components respectively were achieved. These were obtained from UAV flight durations (and therefore GPS processing durations) of 20-30 minutes. However, for flights durations less than c. 20 minutes, UAV PPP positioning accuracies were substantially improved, at around 10-20 cm and 10-50 cm in planimetric and height coordinate components respectively. The attempt to improve the UAV PPP positioning accuracy through ground logging periods did not prove successful due to the presence of cycle slips during UAV launch and landing procedures.

Irrespective of the flight duration and hence UAV PPP positioning accuracy, corresponding precisions were at most c. 4 cm for all components and flights, and typically 1-2 cm. It may therefore be concluded that such centimetre-level precision UAV PPP positioning can be obtained with a high reliability. Centimetre-level accuracy UAV PPP positioning, however, is not guaranteed, but the likelihood increases with longer UAV flight durations (and therefore GPS processing durations), especially beyond 20 minutes.

The fourth objective was *to use UAV PPP positions as external photogrammetric control information in the photogrammetric workflow*.

This objective was achieved firstly by determining camera positions from UAV PPP positions though camera time synchronisation and temporal interpolation and application of lever arm corrections, and secondly, by using these as external camera position observations in the GPS-BBA. Whereas it was estimated that lever arm correction errors would result in only centimetre-level (and thus negligible) GPS camera position errors, it was expected that 5-10 ms camera time synchronisation errors might exist, and subsequently cause 9-18 cm GPS camera position errors. The latter, however, could not be verified because reliable 'truth' camera positions could not be determined. The inclusion of PPP camera positions (as per PPK camera positions) in the BBA proved highly effective at minimising block deformations, shown by the high precision of mapping errors (typically c. 1 pixel in plan and 1-2 pixels in height) although some localised variation remained due to weaknesses in the image block configurations for some flights (i.e. the LH2 flights). Such effects were, however, also present in the corresponding PPK-BBA and GCP-BBA results. In the absence of GCPs, it was found that PPP camera position errors propagated into mapping coordinate errors with an equivalent magnitude. Moreover, due to the magnitude of such errors, and software limitations, these errors could not be mitigated by simply including a small number of GCPs (i.e. one or four). Effective mapping error mitigation could only be achieved by using the same GCPs to determine an independent image block shift, which was equivalent to a mapping datum shift. Moreover, due to uncertainty in focal length estimation which propagates in to height mapping coordinates (and hence a height mapping datum error), a similar number of GCPs was required regardless, even for the control PPK-BBA solutions to eliminate such effects. Consequently, the importance of the mapping datum realised through the GPS camera positions is substantially reduced, in which case the effectiveness of using either error-free PPK camera positions or erroneous PPP camera positions for the implementation of GPS-BBAs is equivalent. Therefore, when using either one or four GCPs, the use of PPP over PPK camera positions enabled the GNSS reference station (or equivalent) to be removed without degrading the accuracy of mapping coordinates, whilst

the similar precision PPP over PPK camera positions enabled a similar mitigation of image block deformations and thus precision of mapping coordinates.

The fifth and final objective was *to rigorously assess the mapping accuracy obtained when using PPP position control and improvements (or degradations) with respect to standard workflows using GCPs.*

This objective was achieved by performing reference GCP-based workflows for each dataset. The centimetre-level accuracy of GCPs, which related to the use of high precision terrestrial GPS survey techniques, facilitated an accurate determination of the image block (mapping) datum, with mapping errors of c. 1 pixel in planimetry and 1-2 pixels in height. However, their effectiveness for mitigating image block deformations (and thus achieving an equivalent mapping precision) highly depended on their number, distribution and strength of the image block configuration, as was indicated by the PhotoScan-Monte Carlo results. Provided PPP camera positions entailed a centimetre-level of accuracy in planimetry (as per the PPK solutions), PPP-BBA mapping errors were generally equivalent to GCP-BBA solutions (i.e. a planimetric mapping RMSE error ratio of around one) as achieved for all CPF and LH1 flights.

However, when PPP-BBA mapping datum errors resulted from PPP camera position errors, the PPP-BBA mapping errors were substantially worse, as such biases were not present in the GCP coordinates. When using one or four GCPs to compensate such biases through an image block shift, however, mapping errors were reduced to commensurate with the GCP-BBA solutions. On the contrary, point cloud comparisons were suggestive that the GCP-BBA-determined object points were deforming outside the GCP-containing regions, whilst this was unlikely to be the case for PPP-BBA-determined object points because of the extensive distribution of PPP camera position control. As a question of whether to adopt PPP over PPK, it has been shown that although standalone PPP-BBA solutions may be susceptible to mapping biases, such that a small number of GCPs is required, the PPK-BBAs also remain susceptible to erroneous focal length estimation, due to the necessitated camera self-calibration in the BBA, such that a similar GCP configuration is still required. After using GCPs in either case, it was shown that the two solutions are equivalent.

7.4 Future work

- The inconsistent performance of PPP on the UAV is a limitation of this work, and thus future work would seek to improve this through better UAV flight control for more

effective implementation of ground logging periods. This should assist the PPP performance on short duration UAV flights.

- Future work would also investigate if PPP performance can be improved using integer ambiguity fixing techniques, such as the PPP-RTK approach (Teunissen and Khodabandeh, 2015) as well as investigating methods for the repair of cycle slips. The latter is expected to improve the utility of the GLPs towards achieving PPP convergence.
- From a photogrammetric standpoint, flights could also be undertaken with improved UAV flight plans that include cross strips flown at different flying heights to improve focal length estimation (Gerke and Przybilla, 2016; Luhmann *et al.*, 2016). Alternatively, performance enhancements may also be offered with the availability of small metric UAV-compatible digital cameras, for which focal length can be pre-calibrated.
- It would also be helpful to develop a SfM-photogrammetric software package with the capability to model systematic strip- or block-wise GPS positioning error in conjunction with GCPs in the BBA. It is expected that this has not yet occurred due to the relatively recent availability of low cost, UAV-compatible carrier phase GPS receivers (Baumker *et al.*, 2013) whilst it is still generally considered that UAVs will only hold pseudorange-based GPS receivers (e.g. James *et al.*, 2017).
- It would finally be interesting to implement the relative aerial control BBA, as per Skaloud *et al.* (2014), but using PPP camera positions. Such an approach, as per the image block shift approach applied here, would be expected to eliminate the effects of remaining PPP camera position biases.

References

Achille, C., Adami, A., Chiarini, S., Cremonesi, S., Fassi, F., Fregonese, L. and Taffurelli, L. (2015) 'UAV-based photogrammetry and integrated technologies for architectural applications - methodological strategies for the after-quake survey of vertical structures in Mantua (Italy)', *Sensors*, 15(7), pp. 15520-15539.

Ackermann, F. and Schade, H. (1993) 'Application of GPS for aerial triangulation', *Photogrammetric Engineering and Remote Sensing*, 59(11), pp. 1625-1632.

Agisoft (2016) *PhotoScan - Professional Edition*. Available at: http://www.agisoft.com/.

Anquela, A.B., Martin, A., Berne, J.L. and Padin, J. (2013) 'GPS and GLONASS Static and Kinematic PPP Results', *Journal of Surveying Engineering*, 139(1), pp. 47-58.

Baumker, M., Przybilla, H.J. and Zurhorst, A. (2013) 'Enhancements in UAV flight control and sensor orientation', *International Archives of Photogrammetry, Remote Sensing and Spatial Information Sciences*, XL(1/W2), pp. 33-38.

Bay, H., Ess, A., Tuytelaars, T. and Van Gool, L. (2008) 'Speeded-Up Robust Features (SURF)', *Computer Vision and Image Understanding*, 110(3), pp. 346-359.

Benassi, F., Dall'Asta, E., Diotri, F., Forlani, G., di Cella, U.M., Roncella, R. and Santise, M. (2017) 'Testing accuracy and repeatability of UAV blocks oriented with GNSS-supported aerial triangulation', *Remote Sensing*, 9(2), pp. 1-23.

Berni, J.A.J., Zarco-Tejada, P.J., Suarez, L. and Fereres, E. (2009) 'Thermal and Narrowband Multispectral Remote Sensing for Vegetation Monitoring From an Unmanned Aerial Vehicle', *IEEE Transactions on Geoscience and Remote Sensing*, 47(3), pp. 722-738.

Besl, P.J. and McKay, N.D. (1992) 'A method for registration of 3-D shapes', *IEEE Transactions on Pattern Analysis and Machine Intelligence*, 14(2), pp. 239-256.

Bisnath, S. and Gao, Y. (2009) 'Current State of Precise Point Positioning and Future Prospects and Limitations', *Observing Our Changing Earth*, 133, pp. 615-623.

Blázquez, M. (2008) 'A new approach to spatio-temporal calibration of multi-sensor systems', *International Archives of Photogrammetry, Remote Sensing and Spatial Information Sciences*, XXXVII(B1), pp. 481-486.

Blázquez, M. and Colomina, I. (2012) 'Relative INS/GNSS aerial control in integrated sensor orientation: Models and performance', *ISPRS Journal of Photogrammetry and Remote Sensing*, 67, pp. 120-133.

Blewitt, G. (1990) 'An automatic editing algorithm for GPS data', *Geophysical Research Letters*, 17(3), pp. 199-202.

Boehm, J., Niell, A., Tregoning, P. and Schuh, H. (2006) 'Global Mapping Function (GMF): A new empirical mapping function based on numerical weather model data', *Geophysical Research Letters*, 33(7), p. 4.

Braasch, M.S. and Van Dierendonck, A.J. (1999) 'GPS receiver architectures and measurements', *Proceedings of the IEEE*, 87(1), pp. 48-64.

Brown, D.C. (1971) 'Close-range camera calibration', *Photogrammetric Engineering*, 37(8), pp. 855-866.

Buyuksalih, G. and Li, Z. (2003) 'Practical experiences with automatic aerial triangulation using different software packages', *Photogrammetric Record*, 18(102), pp. 131-155.

Cai, C.S. and Gao, Y. (2013) 'Modeling and assessment of combined GPS/GLONASS precise point positioning', *GPS Solutions*, 17(2), pp. 223-236.

Carbonneau, P.E. and Dietrich, J.T. (2017) 'Cost-effective non-metric photogrammetry from consumer-grade sUAS: implications for direct georeferencing of structure from motion photogrammetry', *Earth Surface Processes and Landforms*, 42(3), pp. 473-486.

Chen, H., Moan, T. and Verhoeven, H. (2009) 'Effect of DGPS failures on dynamic positioning of mobile drilling units in the North Sea', *Accident Analysis & Prevention*, 41(6), pp. 1164-1171.

Chen, Y. and Medioni, G. (1991) 'Object modeling by registration of multiple range images', *1991 IEEE International Conference on Robotics and Automation*. Sacramento. IEEE, pp. 2724-2729.

Colomina, I. and Molina, P. (2014) 'Unmanned aerial systems for photogrammetry and remote sensing: A review', *ISPRS Journal of Photogrammetry and Remote Sensing*, 92(2014), pp. 79-97.

Cramer, M., Stallmann, D. and Haala, N. (2000) 'Direct georeferencing using GPS/inertial exterior orientations for photogrammetric applications', *International Archives of Photogrammetry, Remote Sensing and Spatial Information Sciences*, XXXIII(B3), pp. 198-205.

Curey, R.K., Ash, M.E., Thielman, L.O., Barker, C.H. and ieee (2004) 'Proposed IEEE inertial systems terminology standard and other inertial sensor standards', in *Position Location and Navigation Symposium 2004*. pp. 83-90.

Curry, S. and Schuckman, K. (1993) 'Practical considerations for the use of airborne GPS for photogrammetry', *Photogrammetric Engineering and Remote Sensing*, 59(11), pp. 1611-1617.

Dai, L.W., Eslinger, D. and Sharpe, T. (2007) *Proceedings of the 2007 National Technical Meeting of The Institute of Navigation*. San Diego, CA, January 2007. Institute of Navigation.

Dall'Asta, E., Forlani, G., Roncella, R., Santise, M., Diotri, F. and di Cella, U.M. (2017) 'Unmanned Aerial Systems and DSM matching for rock glacier monitoring', *ISPRS Journal of Photogrammetry and Remote Sensing*, 127, pp. 102-114.

Dalla Torre, A. and Caporali, A. (2015) 'An analysis of intersystem biases for multi-GNSS positioning', *GPS Solutions*, 19(2), pp. 297-307.

Deseilligny, M.P. and Clery, I. (2011) 'Apero, an open source bundle adjustment software for automated calibration and orientation of set of images', *International Archives of Photogrammetry, Remote Sensing and Spatial Information Sciences*, XXXVIII(5/W16), pp. 269-276.

DigitalGlobe (2018) *The DigitalGlobe Constellation*. Available at: Available: https://dg-cms-uploads-production.s3.amazonaws.com/uploads/document/file/223/Constellation_Brochure_forWeb.pdf (Accessed: 21st May 2018).

Du, S. and Gao, Y. (2012) 'Inertial Aided Cycle Slip Detection and Identification for Integrated PPP GPS and INS', *Sensors*, 12(11), pp. 14344-14362.

El-Sheimy, N. (2009) 'Emerging MEMS IMU and its impact on mapping applications', *Photogrammetric Week*, 9.

El Hazzat, S., Merras, M., El Akkad, N., Saaidi, A. and Satori, K. (2018) '3D reconstruction system based on incremental structure from motion using a camera with varying parameters', *Visual Computer*, 34(10), pp. 1443-1460.

Eling, C., Heinz, E., Klingbeil, L. and Kuhlmann, H. (2014) *Proceedings of the 4th International Conference on Machine Control & Guidance, Braunschweig, Germany*.

Eling, C., Wieland, M., Hess, C., Klingbeil, L. and Kuhlmann, H. (2015) 'Development and evaluation of a UAV based mapping system for remote sensing and surveying applications', *International Archives of Photogrammetry, Remote Sensing and Spatial Information Sciences*, XL(1/W4), pp. 233-239.

Eltner, A., Baumgart, P., Maas, H.G. and Faust, D. (2015) 'Multi-temporal UAV data for automatic measurement of rill and interrill erosion on loess soil', *Earth Surface Processes and Landforms*, 40(6), pp. 741-755.

Eltner, A., Kaiser, A., Castillo, C., Rock, G., Neugirg, F. and Abellan, A. (2016) 'Image-based surface reconstruction in geomorphometry - merits, limits and developments', *Earth Surface Dynamics*, 4(2), pp. 359-389.

Eltner, A. and Schneider, D. (2015) 'Analysis of different methods for 3D reconstruction of natural surfaces from parallel-axes uav images', *Photogrammetric Record*, 30(151), pp. 279-299.

Fang, R.X., Shi, C., Song, W.W., Wang, G.X. and Liu, J.N. (2014) 'Determination of earthquake magnitude using GPS displacement waveforms from real-time precise point positioning', *Geophysical Journal International*, 196(1), pp. 461-472.

Fischler, M.A. and Bolles, R.C. (1981) 'Random sample consensus: a paradigm for model fitting with applications to image analysis and automated cartography', *Communications of the ACM*, 24(6), pp. 381-395.

Fonstad, M.A., Dietrich, J.T., Courville, B.C., Jensen, J.L. and Carbonneau, P.E. (2013) 'Topographic structure from motion: a new development in photogrammetric measurement', *Earth Surface Processes and Landforms*, 38(4), pp. 421-430.

Fraser, C.S. (1997) 'Digital camera self-calibration', *ISPRS Journal of Photogrammetry and Remote Sensing*, 52(4), pp. 149-159.

Fraser, C.S. (2013) 'Automatic camera calibration in close range photogrammetry', *Photogrammetric Engineering and Remote Sensing*, 79(4), pp. 381-388.

Fryer, J., Mitchell, H. and Chandler, J.H. (2007) *Applications of 3D Measurement from Images*. Whittles Publishing.

Gao, Z.Z., Zhang, H.P., Ge, M.R., Niu, X.J., Shen, W.B., Wickert, J. and Schuh, H. (2015) 'Tightly Coupled Integration of Ionosphere-Constrained Precise Point Positioning and Inertial Navigation Systems', *Sensors*, 15(3), pp. 5783-5802.

Geng, J., Teferle, F.N., Meng, X. and Dodson, A.H. (2010a) 'Kinematic precise point positioning at remote marine platforms', *GPS Solutions*, 14(4), pp. 343-350.

Geng, J.H., Meng, X.L., Dodson, A.H., Ge, M.R. and Teferle, F.N. (2010b) 'Rapid re-convergences to ambiguity-fixed solutions in precise point positioning', *Journal of Geodesy*, 84(12), pp. 705-714.

Gerke, M. and Przybilla, H.J. (2016) 'Accuracy analysis of photogrammetric UAV image blocks: influence of onboard RTK-GNSS and cross flight patterns', *Photogrammetrie Fernerkundung Geoinformation*, 2016(1), pp. 17-30.

Goncalves, J.A. and Henriques, R. (2015) 'UAV photogrammetry for topographic monitoring of coastal areas', *ISPRS Journal of Photogrammetry and Remote Sensing*, 104(2015), pp. 101-111.

GPS.gov (2018) *Constellation Arrangement* Available at: https://www.gps.gov/systems/gps/space/#generations (Accessed: 8th May 2018).

Granshaw, S.I. (1980) 'Bundle adjustment methods in engineering photogrammetry', *Photogrammetric Record*, 10(56), pp. 181-207.

Granshaw, S.I. and Fraser, C.S. (2015) 'Computer vision and photogrammetry: interaction or introspection?', *Photogrammetric Record*, 30(149), pp. 3-7.

Grayson, B., Penna, N.T., Mills, J. and Grant, D. (2018) 'GPS precise point positioning for UAV photogrammetry', *Photogrammetric Record*, 33(164), pp. 427-447.

Gross, J.N., Watson, R.M., D'Urso, S. and Gu, Y. (2016) 'Flight-test evaluation of kinematic precise point positioning of small UAVs', *International Journal of Aerospace Engineering*, 2016, pp. 1-11.

Gruen, A. (2012) 'Development and status of image matching in photogrammetry', *Photogrammetric Record*, 26(137), pp. 36-57.

Gruen, A., Cocard, M. and Kahle, H.G. (1993) 'Photogrammetry and kinematic GPS - results of a high-accuracy test', *Photogrammetric Engineering and Remote Sensing*, 59(11), pp. 1643-1650.

Grussenmeyer, P. and Al Khalil, O. (2002) 'Solutions for exterior orientation in photogrammetry: a review', *Photogrammetric Record*, 17(100), pp. 615-634.

Guo, F., Zhang, X.H., Li, X. and Cai, S. (2010) 'Impact of sampling rate of IGS satellite clock on precise point positioning', *Geo-spatial Information Science*, 13(2), pp. 150-156.

Haala, N., Cramer, M., Weimer, F. and Trittler, M. (2011) 'Performance test on UAV-based photogrammetric data collection', *Proceedings of the International Archives of the Photogrammetry, Remote Sensing and Spatial Information Sciences*, 38(1/C22), pp. 7-12.

Hartley, R. and Zisserman, A. (2003) *Multiple view geometry in computer vision*. Cambridge University Press.

Harwin, S. and Lucieer, A. (2012) 'Assessing the accuracy of georeferenced point clouds produced via multi-view stereopsis from Unmanned Aerial Vehicle (UAV) imagery', *Remote Sensing*, 4(6), pp. 1573-1599.

Harwin, S., Lucieer, A. and Osborn, J. (2015) 'The Impact of the Calibration Method on the Accuracy of Point Clouds Derived Using Unmanned Aerial Vehicle Multi-View Stereopsis', *Remote Sensing*, 7(9), pp. 11933-11953.

Heinly, J., Schonberger, J.L., Dunn, E. and Frahm, J.M. (2015) *IEEE Conference on Computer Vision and Pattern Recognition*. New York. IEEE.

Heipke, C. (1997) 'Automation of interior, relative, and absolute orientation', *ISPRS Journal of Photogrammetry and Remote Sensing*, 52(1), pp. 1-19.

Heipke, C., Jacobsen, K. and Wegmann, H. (2002) 'Analysis of the results of the OEEPE test ’Integrated sensor orientation’', *Technical Report 43, OEEPE Official Publications*.

Herring, T.A. (1992) 'Modeling atmospheric delays in the analysis of space geodetic data', *Symposium on Refraction of Transatmospheric Signals in Geodesy*, 36(4), pp. 157–164.

Hofmann-Wellenhof, B., Lichtenegger, H. and Wasle, E. (2007) *GNSS global navigation satellite systems: GPS, GLONASS, Galileo and more*. SpringerWienNewYork.

Hoque, M.M. and Jakowski, N. (2007) 'Higher order ionospheric effects in precise GNSS positioning', *Journal of Geodesy*, 81(4), pp. 259-268.

Hu, G.R., Khoo, H.S., Goh, P.C. and Law, C.L. (2003) 'Development and assessment of GPS virtual reference stations for RTK positioning', *Journal of Geodesy*, 77(5-6), pp. 292-302.

IAC (2018) *GLONASS constellation status*. Available at: https://www.glonass-iac.ru/en/GLONASS/index.php (Accessed: 8th May 2017).

IGS (2018) *GPS Satellite Ephemerides / Satellite & Station Clocks*. Available at: http://www.igs.org/products/data (Accessed: 23rd March 2017).

Immerzeel, W.W., Kraaijenbrink, P.D.A., Shea, J.M., Shrestha, A.B., Pellicciotti, F., Bierkens, M.F.P. and de Jong, S.M. (2014) 'High-resolution monitoring of Himalayan glacier dynamics using unmanned aerial vehicles', *Remote Sensing of Environment*, 150(2014), pp. 93-103.

Ip, A., El-Sheimy, N. and Mostafa, M. (2007) 'Performance analysis of integrated sensor orientation', *Photogrammetric Engineering and Remote Sensing*, 73(1), pp. 89-97.

Jacobsen, K. (2011) 'Recent developments of digital cameras and space imagery', *Proceedings GIS, Ostrava*, p. 8.

James, M.R. and Robson, S. (2012) 'Straightforward reconstruction of 3D surfaces and topography with a camera: Accuracy and geoscience application', *Journal of Geophysical Research-Earth Surface*, 117(F3), pp. 1-17.

James, M.R. and Robson, S. (2014) 'Mitigating systematic error in topographic models derived from UAV and ground-based image networks', *Earth Surface Processes and Landforms*, 39(10), pp. 1413-1420.

James, M.R., Robson, S., d'Oleire-Oltmanns, S. and Niethammer, U. (2017) 'Optimising UAV topographic surveys processed with structure-from-motion: Ground control quality, quantity and bundle adjustment', *Geomorphology*, 280(2017), pp. 51-66.

Jaud, M., Passot, S., Le Bivic, R., Delacourt, C., Grandjean, P. and Le Dantec, N. (2016) 'Assessing the Accuracy of High Resolution Digital Surface Models Computed by PhotoScan and MicMac in Sub-Optimal Survey Conditions', *Remote Sensing*, 8(6).

Javemick, L., Brasington, J. and Caruso, B. (2014) 'Modeling the topography of shallow braided rivers using Structure-from-Motion photogrammetry', *Geomorphology*, 213, pp. 166-182.

Jozkow, G. and Toth, C. (2014) 'Georeferencing experiments with UAS imagery', *ISPRS Annals of the Photogrammetry, Remote Sensing and Spatial Information Sciences*, 2(1), pp. 25-29.

Kasser, M. and Egels, Y. (2002) *Digital photogrammetry*. Taylor & Francis.

Kohoutek, T.K. and Eisenbeiss, H. (2012) 'Processing of UAV based range imaging data to generate detailed elevation models of complex natural structures', *International Archives of Photogrammetry, Remote Sensing and Spatial Information Sciences*, XXXIX(B1), pp. 405-410.

Kouba, J. and Heroux, P. (2001) 'Precise point positioning using IGS orbit and clock products', *GPS Solutions*, 5(2), pp. 12-28.

Kraus, K. (2007) *Photogrammetry: Geometry from Images and Laser Scans*. (459 vols). Walter de Gruyter.

Kung, O., Strecha, C., Beyeler, A., Zufferey, J.C., Floreano, D., Fua, P. and Gervaix, F. (2011) 'The accuracy of automatic photogrammetric techniques on ultra-light UAV imagery', *International Archives of Photogrammetry, Remote Sensing and Spatial Information Sciences*, XXXVIII(1/C22), pp. 125-130.

Lagler, K., Schindelegger, M., Bohm, J., Krasna, H. and Nilsson, T. (2013) 'GPT2: Empirical slant delay model for radio space geodetic techniques', *Geophysical Research Letters*, 40(6), pp. 1069-1073.

Leick, A., Rapoport, L. and Tatarnikov, D. (2015) *GPS satellite surveying*. John Wiley & Sons.

Li, M., Qu, L.Z., Zhao, Q.L., Guo, J., Su, X. and Li, X.T. (2014) 'Precise Point Positioning with the BeiDou Navigation Satellite System', *Sensors*, 14(1), pp. 927-943.

Li, P. and Zhang, X.H. (2014) 'Integrating GPS and GLONASS to accelerate convergence and initialization times of precise point positioning', *GPS Solutions*, 18(3), pp. 461-471.

Li, X.X., Ge, M.R., Dai, X.L., Ren, X.D., Fritsche, M., Wickert, J. and Schuh, H. (2015) 'Accuracy and reliability of multi-GNSS real-time precise positioning: GPS, GLONASS, BeiDou, and Galileo', *Journal of Geodesy*, 89(6), pp. 607-635.

Li, Z.K., Gao, J.X. and Wang, J. (2016) 'Inertial Aided Cycle Slip Detection and Repair for PPP/INS Tightly Coupled Navigation', *Journal of Navigation*, 69(6), pp. 1357-1378.

Lichti, D., Skaloud, J. and Schaer, P. (2008) 'On the calibration strategy of medium format cameras for direct georeferencing', *Proceedings of the International Calibration and Orientation Workshop*. Castelldefels. EuroSDR, pp. 1-9.

Lichti, D.D. (2002) 'The interpolation problem in GPS-supported aerial triangulation', *Photogrammetric Record*, 17(99), pp. 481-492.

Linder, W. (2009) *Digital photogrammetry*. Springer-Verlag.

Lingua, A., Marenchino, D. and Nex, F. (2009) 'Performance Analysis of the SIFT Operator for Automatic Feature Extraction and Matching in Photogrammetric Applications', *Sensors*, 9(5), pp. 3745-3766.

Lowe, D.G. (2004) 'Distinctive image features from scale-invariant keypoints', *International Journal of Computer Vision*, 60(2), pp. 91-110.

Lucieer, A., de Jong, S.M. and Turner, D. (2014) 'Mapping landslide displacements using Structure from Motion (SfM) and image correlation of multi-temporal UAV photography', *Progress in Physical Geography*, 38(1), pp. 97-116.

Luhmann, T., Fraser, C. and Maas, H.G. (2016) 'Sensor modelling and camera calibration for close-range photogrammetry', *ISPRS Journal of Photogrammetry and Remote Sensing*, 115(2016), pp. 37-46.

Luhmann, T., Robson, S., Kyle, S.A. and Harley, I.A. (2006) *Close range photogrammetry: principles, techniques and applications*. Whittles Publishing.

Mader, G.L. (1999) 'GPS antenna calibration at the National Geodetic Survey', *GPS Solutions*, 3(1), pp. 50-58.

Marques, H.A., Marques, H.A.S., Aquino, M., Veettil, S.V. and Monico, J.F.G. (2018) 'Accuracy assessment of Precise Point Positioning with multi-constellation GNSS data under ionospheric scintillation effects', *Journal of Space Weather and Space Climate*, 8(2018), pp. 1-14.

Matese, A., Toscano, P., Di Gennaro, S.F., Genesio, L., Vaccari, F.P., Primicerio, J., Belli, C., Zaldei, A., Bianconi, R. and Gioli, B. (2015) 'Intercomparison of UAV, aircraft and satellite remote sensing platforms for precision viticulture', *Remote Sensing*, 7(3), pp. 2971-2990.

McGlone, J. (2004) *Manual of Photogrammetry*. American Society for Photogrammetry and Remote Sensing.

Micheletti, N., Lane, S.N. and Chandler, J.H. (2015) 'Application of archival aerial photogrammetry to quantify climate forcing of alpine landscapes', *Photogrammetric Record*, 30(150), pp. 143-165.

Mikhail, E.M., Bethel, J.S. and McGlone, J.C. (2001) *Introduction to modern photogrammetry*. Wiley.

Mikolajczyk, K., Tuytelaars, T., Schmid, C., Zisserman, A., Matas, J., Schaffalitzky, F., Kadir, T. and van Gool, L. (2005) 'A comparison of affine region detectors', *International Journal of Computer Vision*, 65(1-2), pp. 43-72.

Murtiyoso, A. and Grussenmeyer, P. (2017) 'Documentation of heritage buildings using close-range UAV images: dense matching issues, comparison and case studies', *Photogrammetric Record*, 32(159), pp. 206-229.

Murtiyoso, A., Grussenmeyer, P., Börlin, N., Vandermeerschen, J. and Freville, T. (2018) 'Open Source and Independent Methods for Bundle Adjustment Assessment in Close-Range UAV Photogrammetry', *Drones*, 2(1), pp. 1-18.

Nex, F. and Remondino, F. (2014) 'UAV for 3D mapping applications: a review', *Applied Geomatics*, 6(1), pp. 1-15.

Niethammer, U., James, M.R., Rothmund, S., Travelletti, J. and Joswig, M. (2012) 'UAV-based remote sensing of the Super-Sauze landslide: Evaluation and results', *Engineering Geology*, 128(1), pp. 2-11.

Nister, D., Naroditsky, O. and Bergen, J. (2006) 'Visual odometry for ground vehicle applications', *Journal of Field Robotics*, 23(1), pp. 3-20.

OS (2018) *A Guide to coordinate systems in Great Britain*. Available at: https://www.ordnancesurvey.co.uk/docs/support/guide-coordinate-systems-great-britain.pdf (Accessed: 12th June 2018).

Penna, N.T., A., M.M.M., Martin, I., Guo, J. and Foden, P.R. (2018) 'Sea Surface Height Measurement Using a GNSS Wave Glider', *Geophysical Research Letters*, *45*, 45(11), pp. 5609-5616.

Peppa, M.V., Mills, J.P., Moore, P., Miller, P.E. and Chambers, J.E. (2016) 'Accuracy assessment of a UAV-based landslide monitoring system', *International Archives of Photogrammetry, Remote Sensing and Spatial Information Sciences*, XLI(B5), pp. 895-902.

Pfeifer, N., Glira, P. and Briese, C. (2012) 'Direct georeferencing with on board navigation components of light weight UAV platforms', *International Archives of Photogrammetry, Remote Sensing and Spatial Information Sciences*, XXXIX(B7), pp. 487-492.

PlanetLabs (2018) *Global monitoring, daily insight*. Available at: https://www.planet.com/products/monitoring/ (Accessed: 21st May 2018).

Pollefeys, M., Nister, D., Frahm, J.M., Akbarzadeh, A., Mordohai, P., Clipp, B., Engels, C., Gallup, D., Kim, S.J., Merrell, P., Salmi, C., Sinha, S., Talton, B., Wang, L., Yang, Q., Stewenius, H., Yang, R., Welch, G. and Towles, H. (2008) 'Detailed real-time urban 3D reconstruction from video', *International Journal of Computer Vision*, 78(2-3), pp. 143-167.

Read, R. and Graham, R. (2002) *Manual of aerial survey*. Whittles Publishing.

Rehak, M., Mabillard, R. and Skaloud, J. (2013) 'A micro-UAV with the capability of direct georeferencing', *International Archives of Photogrammetry, Remote Sensing and Spatial Information Sciences*, XL(1/W2), pp. 317-323.

Rehak, M. and Skaloud, J. (2015) 'Fixed-wing micro aerial vehicle for accurate corridor mapping', *International Archives of Photogrammetry, Remote Sensing and Spatial Information Sciences*, XL(1/W4), pp. 23-31.

Rehak, M. and Skaloud, J. (2017a) 'Performance assessment of integrated sensor orientation with a low-cost GNSS receiver', *ISPRS Annals of the Photogrammetry, Remote Sensing and Spatial Information Sciences*, IV(2/W3), pp. 75-80.

Rehak, M. and Skaloud, J. (2017b) 'Time synchronization of consumer cameras on Micro Aerial Vehicles', *ISPRS Journal of Photogrammetry and Remote Sensing*, 123, pp. 114-123.

Reshetyuk, Y. and Martensson, S.G. (2016) 'Generation of highly accurate digital elevation models with unmanned aerial vehicles', *Photogrammetric Record*, 31(154), pp. 143-165.

Retscher, G. (2002) 'Accuracy Performance of Virtual Reference Station (VRS) Networks', *Journal of Global Positioning Systems*, 1(1), pp. 40-47.

Reussner, N. and Wanninger, L. (2011) 'GLONASS Inter-frequency Biases and Their Effects on RTK and PPP Carrier-phase Ambiguity Resolution', *Proceedings of the 24th International Technical Meeting of The Satellite Division of the Institute of Navigation*. Portland, Oregon. Institute of Navigation, pp. 712-716.

RICS (2014) *Measured Surveys of Land, Buildings and Utilities*. Available at: http://www.rics.org/uk/knowledge/professional-guidance/guidance-notes/measured-surveys-of-land-buildings-and-utilities-3rd-edition/ (Accessed: 25th February 2018).

Rosnell, T. and Honkavaara, E. (2012) 'Point Cloud Generation from Aerial Image Data Acquired by a Quadrocopter Type Micro Unmanned Aerial Vehicle and a Digital Still Camera', *Sensors*, 12(1), pp. 453-480.

Rupnik, E., Nex, F., Toschi, I. and Remondino, F. (2015) 'Aerial multi-camera systems: Accuracy and block triangulation issues', *ISPRS Journal of Photogrammetry and Remote Sensing*, 101(2015), pp. 233-246.

Sauerbier, M., Siegrist, E., Eisenbeiss, H. and Demir, N. (2011) 'The practical application of UAV-based photogrammetry under economic aspects', *International Archives of Photogrammetry, Remote Sensing and Spatial Information Sciences*, 38(1), pp. 45-50.

Schenk, T. (1997) 'Towards automatic aerial triangulation', *ISPRS Journal of Photogrammetry and Remote Sensing*, 52(3), pp. 110-121.

Schmid, C., Mohr, R. and Bauckhage, C. (2000) 'Evaluation of interest point detectors', *International Journal of Computer Vision*, 37(2), pp. 151-172.

Scholtz, A., Kaschwich, C., Kruger, A., Kufieta, K., Schnetter, P., Wilkens, C.S., Kruger, T. and Vorsmann, P. (2011) 'Development of a new multi-purpose UAS for scientific application', *International Archives of Photogrammetry, Remote Sensing and Spatial Information Sciences*, XXXVIII(1/C22), pp. 149-154.

Schonberger, J.L. and Frahm, J.M. (2016) 'Structure-from-Motion Revisited', *2016 IEEE Conference on Computer Vision and Pattern Recognition (CVPR)*. Las Vegas. IEEE, pp. 4104-4113.

Shahbazi, M., Sohn, G., Theau, J. and Menard, P. (2015) 'Development and Evaluation of a UAV-Photogrammetry System for Precise 3D Environmental Modeling', *Sensors*, 15(11), pp. 27493-27524.

Skaloud, J., Rehak, M. and Lichti, D. (2014) 'Mapping with MAV: experimental study on the contribution of absolute and relative aerial position control', *International Archives of Photogrammetry, Remote Sensing and Spatial Information Sciences*, XL(3/W1), pp. 123-129.

Smith, M.W. and Vericat, D. (2015) 'From experimental plots to experimental landscapes: topography, erosion and deposition in sub-humid badlands from Structure-from-Motion photogrammetry', *Earth Surface Processes and Landforms*, 40(12), pp. 1656-1671.

Snavely, N., Seitz, S.M. and Szeliski, R. (2008) 'Modeling the world from Internet photo collections', *International Journal of Computer Vision*, 80(2), pp. 189-210.

Stamatopoulos, C. and Fraser, C.S. (2014) 'Automated Target-Free Network Orientation and Camera Calibration', *ISPRS Annals of the Photogrammetry, Remote Sensing and Spatial Information Sciences*, 2(5), pp. 339-346.

Stöcker, C., Nex, F., Koeva, M. and Gerke, M. (2017) 'Quality assessment of combined IMU/GNSS data for direct georeferencing in the context of UAV-based mapping', *International Archives of Photogrammetry, Remote Sensing and Spatial Information Sciences*, XLII(2/W6), pp. 355-361.

Stumpf, A., Malet, J.P., Allemand, P., Pierrot-Deseilligny, M. and Skupinski, G. (2015) 'Ground-based multi-view photogrammetry for the monitoring of landslide deformation and erosion', *Geomorphology*, 231, pp. 130-145.

Teunissen, P.J.G. and Khodabandeh, A. (2015) 'Review and principles of PPP-RTK methods', *Journal of Geodesy*, 89(3), pp. 217-240.

Toth, C. and Jozkow, G. (2016) 'Remote sensing platforms and sensors: A survey', *ISPRS Journal of Photogrammetry and Remote Sensing*, 115, pp. 22-36.

Triggs, B., McLauchlan, P.F., Hartley, R.I. and Fitzgibbon, A.W. (1999) 'Bundle Adjustment - A Modern Synthesis', *International Workshop on Vision Algorithms*. Corfu, Greece. Springer, pp. 298-372.

Turner, D., Lucieer, A. and de Jong, S.M. (2015) 'Time Series Analysis of Landslide Dynamics Using an Unmanned Aerial Vehicle (UAV)', *Remote Sensing*, 7(2), pp. 1736-1757.

Turner, D., Lucieer, A. and Wallace, L. (2014) 'Direct georeferencing of ultrahigh-resolution UAV imagery', *IEEE Transactions on Geoscience and Remote Sensing*, 52(5), pp. 2738-2745.

Turner, D., Lucieer, A. and Watson, C. (2012) 'An Automated Technique for Generating Georectified Mosaics from Ultra-High Resolution Unmanned Aerial Vehicle (UAV) Imagery, Based on Structure from Motion (SfM) Point Clouds', *Remote Sensing*, 4(5), pp. 1392-1410.

Tyc, G., Tulip, J., Schulten, D., Krischke, M. and Oxfort, M. (2005) 'The RapidEye mission design', *Acta Astronautica*, 56(1-2), pp. 213-219.

Ullman, S. (1979) 'The interpretation of structure from motion', *Proceedings of the Royal Society of London*, 203(1153), pp. 405-426.

Wackrow, R. and Chandler, J.H. (2008) 'A convergent image configuration for DEM extraction that minimises the systematic effects caused by an inaccurate lens model', *Photogrammetric Record*, 23(121), pp. 6-18.

Waegli, A., Skaloud, J., Guerrier, S., Pares, M.E. and Colomina, I. (2010) 'Noise reduction and estimation in multiple micro-electro-mechanical inertial systems', *Measurement Science and Technology*, 21(6), pp. 1-11.

Wallace, L., Lucieer, A., Malenovsky, Z., Turner, D. and Vopenka, P. (2016) 'Assessment of Forest Structure Using Two UAV Techniques: A Comparison of Airborne Laser Scanning and Structure from Motion (SfM) Point Clouds', *Forests*, 7(3), pp. 1-16.

Wanninger, L. (2004) *Introduction to Network RTK*. Available at: http://www.wasoft.de/e/iagwg451/intro/introduction.html (Accessed: 30th November 2017).

Wanninger, L. (2012) 'Carrier-phase inter-frequency biases of GLONASS receivers', *Journal of Geodesy*, 86(2), pp. 139-148.

Weiss, S., Scaramuzza, D. and Siegwart, R. (2011) 'Monocular-SLAM-Based Navigation for Autonomous Micro Helicopters in GPS-Denied Environments', *Journal of Field Robotics*, 28(6), pp. 854-874.

Weng, J.Y., Ahuja, N. and Huang, T.S. (1993) 'Optimal motion and structure estimation', *IEEE Transactions on Pattern Analysis and Machine Intelligence*, 15(9), pp. 864-884.

Wester-Ebbinghaus, W. (1980) 'Aerial photography by radio controlled model helicopter', *Photogrammetric Record*, 10(55), pp. 85-92.

Westoby, M.J., Brasington, J., Glasser, N.F., Hambrey, M.J. and Reynolds, J.M. (2012) "Structure-from-Motion' photogrammetry: A low-cost, effective tool for geoscience applications', *Geomorphology*, 179, pp. 300-314.

Wolf, P., Dewitt, B. and Wilkinson, B.E. (2014) *Elements of Photogrammetry with Application in GIS*. McGraw Hill.

Yang, B.S. and Chen, C. (2015) 'Automatic registration of UAV-borne sequent images and LiDAR data', *ISPRS Journal of Photogrammetry and Remote Sensing*, 101, pp. 262-274.

Yastikli, N. and Jacobsen, K. (2005a) 'Direct sensor orientation for large scale mapping - Potential, problems, solutions', *Photogrammetric Record*, 20(111), pp. 274-284.

Yastikli, N. and Jacobsen, K. (2005b) 'Influence of system calibration on direct sensor orientation', *Photogrammetric Engineering and Remote Sensing*, 71(5), pp. 629-633.

Yu, X.D. and Gao, J.X. (2017) 'Kinematic precise point positioning using multi-constellation Global Navigation Satellite System (GNSS) observations', *ISPRS International Journal of Geo-Information*, 6(1), pp. 1-15.

Yuan, X.X. (2009) 'Quality assessment for GPS-supported bundle block adjustment based on aerial digital frame imagery', *Photogrammetric Record*, 24(126), pp. 139-156.

Yuan, X.X., Fu, J.H., Sun, H.X. and Toth, C. (2009) 'The application of GPS precise point positioning technology in aerial triangulation', *ISPRS Journal of Photogrammetry and Remote Sensing*, 64(6), pp. 541-550.

Zhang, X.H., Guo, F. and Zhou, P.Y. (2014) 'Improved precise point positioning in the presence of ionospheric scintillation', *GPS Solutions*, 18(1), pp. 51-60.

Zhang, X.H. and Li, X.X. (2012) 'Instantaneous re-initialization in real-time kinematic PPP with cycle slip fixing', *GPS Solutions*, 16(3), pp. 315-327.

Zumberge, J.F., Heflin, M.B., Jefferson, D.C., Watkins, M.M. and Webb, F.H. (1997) 'Precise point positioning for the efficient and robust analysis of GPS data from large networks', *Journal of Geophysical Research-Solid Earth*, 102(B3), pp. 5005-5017.